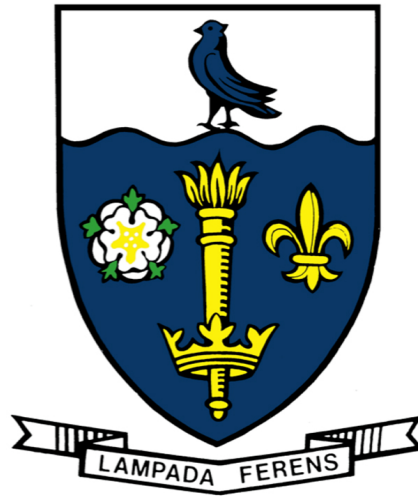# THE UNIVERSITY OF HULL

The Motions of Galaxies within Large-Scale Structures

being a Thesis submitted to the University of Hull in accordance
with the requirements of the Degree of DOCTOR OF PHILOSOPHY
IN PHYSICS in the Faculty of Science & Engineering.

by

Lawrence Edward Bilton, M.Phil (Open), BSc (Hons) (Open)

Submitted October 2020

"If you're not prepared to be wrong, you'll never come up with anything original."

– Sir Ken Robinson, *The Element (2009)*

Abstract

Galaxy clusters represent one of the largest-scale structures in the Universe, with their environments of varying density being ideal for inducing an increase in activity of the cluster galaxy members and the pervading Intracluster Medium (ICM) between them. However the precise drivers, thereby the inferred consequences, of differing states of galaxy cluster activity have not been adequately disentangled. If one can procure a sufficient dichotomic sample of cluster galaxies of differing sub-populations from relaxed and unrelaxed galaxy cluster dynamical states, one could analyse how these sub-populations 'move' as a function of both radius and dynamical state. Specifically, using velocity dispersion profiles (VDPs) that weight against cluster galaxies across all radii with a Gaussian window function, one can determine how cluster galaxies of properties that pertain to galaxy evolutionary indicators respond to the cluster environment as a function of the clustocentric radius. In addition, analysing the rotational profiles of these sub-populations as a function of the clustocentric radius can help identify where the bulk of the kinetic energy lies. In view of these points, we have pooled data of galaxies from the Sloan Digital Sky Survey (SDSS) two composite galaxy clusters are assembled into unrelaxed and relaxed states, which are compared with one another through splitting their cluster galaxy populations by their evolutionary proxies (i.e. morphology, colour, mass and AGN), thus analysing their resultant VDPs and rotational profiles. It is therefore found that unrelaxed galaxy clusters possess increased interaction between cluster galaxies as the radius increases, driven by blue and red elliptical galaxies, suggesting an induction of activity by pre-processed groups. AGN-hosting cluster galaxy sub-populations within these unrelaxed environs however present increased activity as $R \rightarrow 0$, indicating these are recent infallers, potentially triggered due to interactions with the ICM. Rotational profiles of unrelaxed clusters build upon the VDPs, showing significant bulk rotation of cluster galaxies with prominent core rotation driven by redder sub-populations.

Acknowledgements

Declaration of Originality

The contents of this document proffers a thesis being submitted for examination in order to fulfil the conditions required for the degree of Doctor of Philosophy from the University of Hull. The binding of this thesis is accomplished via the collation of published peer-reviewed journal articles that have been led and authored by myself; modern astronomy is publish-driven and collaborative by nature, therefore, the publishing of results and having multiple co-authors is commonplace. Specifically, Chapter 2 has been published as Bilton & Pimbblet (2018) MNRAS 481, 1507, Chapter 3 has been published as Bilton et al. (2019) MNRAS 490, 5017, while Chapter 4 presents the most recent work accepted for publication as Bilton et al. (2020) MNRAS 499, 3792. The full details as to the nature of the contributions made by myself–along with full lists of my co-authors–to these works are described in the prologues of the relevant Chapters.

This is typically the result of large consortia involved within the design, implementation and operation of large-scale facilities such as multi-national telescope surveys and their ancillary data reduction tools required to conduct our research, or, the result of interactions between the observing community with the simulation community. The observational data used here were the result of observations conducted by others as part of large scale surveys, and the data products from these observations are explicitly referenced.

I therefore declare that the following work presented within this thesis is original and of my own volition while under the supervision of Dr. Kevin Pimbblet & Dr. Elke Roediger. Where work, results, or ideas have been procured from other sources, those sources are explicitly referenced.

CANDIDATE'S SIGNATURE: ......*Lawrence E. Bilton*...... DATE: ......09/10/2020......

Contents

List of Figures

List of Tables

1.   Introduction

"I have gathered a posie of other men's flowers, and nothing but the thread that binds them is my own."

– Michel de Montaigne, *The Essais: Book III (1595)*

1.1   The Era of the "Island Universe"

By the turn of the 20th century observational astronomy, with thanks to the advancement of telescopic engineering, had already revealed to us the more unusual and seemingly ethereal structures that inhabit our Universe (see catalogues Messier 1781; Herschel 1802). One such category of object known at the time as *Spiral Nebulae* had eluded astronomers with their hosting of peculiarly high luminosity novae. This abnormality from current thinking ultimately led to questioning the true scale of the Universe; the high luminosity novae were simply too bright to be considered an object that did not lie within the Milky Way. This was the pretext for *The Great Debate* on 26 April 1920 between Harlow Shapley and Heber Curtis in an attempt to formally settle the question, 'What is the true scale of the Universe?', based upon the evidence at the time the total diameter of the Universe (Milky Way) was thought to be $\lesssim 30000$ light years across (see Shapley & Curtis 1921). Shapley was in favour of the Milky Way encompassing the entire Universe; spiral nebulae, such as the 'Great Spiral of Andromeda', are but mere structures that inhabit our Milky Way. Whereas Curtis pursued the antithesis, with his rhetoric stated the Milky Way was itself merely but one among many other such "island universes", a phrase coined by Immanuel Kant ~ 160 years prior (Kant, 1755; Curtis, 1917).

Shapley had additional observational evidence following the work conducted by van Maanen (1916), a well-established Dutch-American Astronomer, presenting the pinwheel spiral nebula (M101) to be ostensibly rotating. The immediate implication was that due to the finite speed of light, and for there to be such short timescales involved in observing such rotation in M101, the spiral nebula must be confined to a space inside the Milky Way. However, this result was specious due to van Maanen mistakenly not accounting for
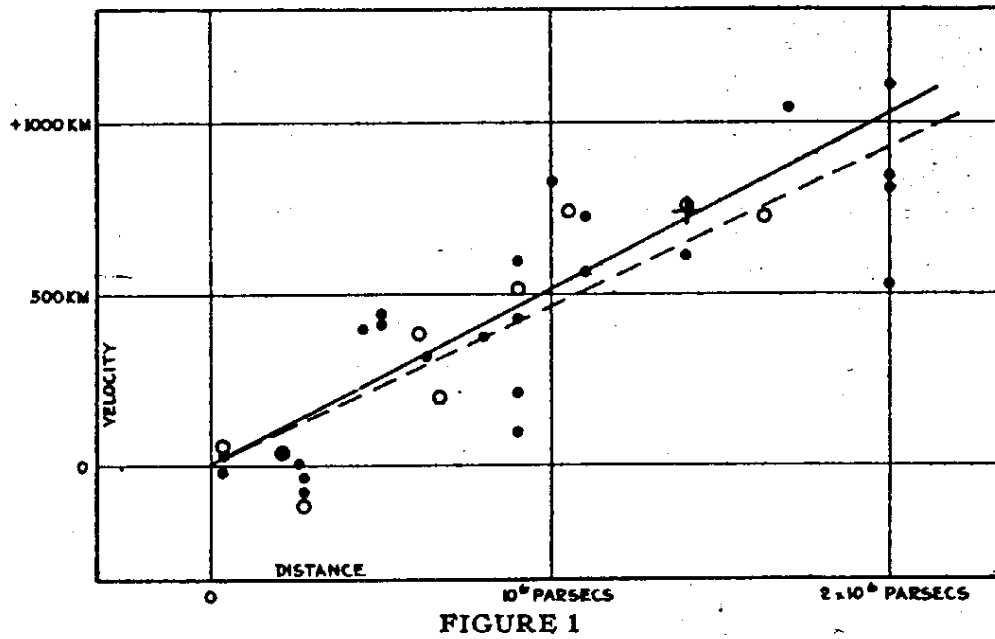
Figure 1.1: The observed relation between galaxy recession velocity and their distance, considered the first direct observational evidence of an expanding Universe. Obtained from Hubble (1929a).

edge-effects of his field stars between each of the photographic plates. In contrast, Curtis questioned, 'if Andromeda were within the Milky Way, then how could such a significant number of novae be found localised to a small volume of the Galaxy?' (Curtis, 1917). This question was in direct response to Shapley's comments between the distances and high luminosity of these novae, in which Curtis countered that if the distance of spiral nebulae is extended to extragalactic scales, the number of novae per comoving volume becomes approximately equivalent to that of the Milky Way (Curtis, 1920). Towards the end of the 1920s Edwin Hubble determined the distance to the spiral nebula of Andromeda through the study of member *Cepheid Variables*[1], which act as standard candles, and found conclusively that Andromeda was indeed its own island universe; the spiral nebula of Andromeda is an independent galaxy (Hubble, 1929b). Thus, placing the final nail into the coffin in the argument and debate of scale in this context.

Although, even with the Universe becoming bigger than what was once initially prescribed it continued to provide astronomers controversial revelations from both theory and observation, such as the expanding Universe theory and the standard model of cosmology

---

[1]Cepheid Variables are stars that act as standard candles. Standard candles are objects that possess a common luminosity which allow one to determine a luminosity distance with an observer-measured apparent brightness to the standard candle and, if applicable, the candle's host.

(Friedmann, 1922; Lemaître, 1927, 1931; Robertson, 1935; Walker, 1937). In that vein Edwin Hubble, continuing his observations of these extragalactic galaxies, determined more distances of more galaxies using Cepheid Variables while simultaneously recording their recession velocities (see Slipher 1915). Hubble (1929a) presents the result of these observations, highlighting a positive correlation between a galaxy's recession velocity and its distance relative to our frame of reference, which led to the direct observational evidence the Universe is expanding (see Figure 1.1). These few decades swiftly caused a significant shift in our paradigm on the scale and physics of the Universe, ultimately, leading to the birth of extragalactic astronomy.

1.1.1   The Hubble-Lemaître Law & Cosmological Redshift

While considering the recent discussion of distance and scale, one might anticipate the light we see from extragalactic objects lying within an expanding space to suffer a *Doppler Effect*. This expanding space, which is commonly referred to as the Hubble flow (e.g. Gorski 1988; Regos & Geller 1989; Coles & Lucchin 2002; Freedman & Madore 2010), does indeed induce a Doppler-like effect that correlates with the distance between the observer and the extragalactic object; the expansion of space is intrinsic to the cosmology of the Universe, not an object's own motion, therefore the separation induced by the cosmological parameters defines what we observe as *Cosmological Redshift*. The effect of cosmological redshift is what enabled Hubble to determine the recession velocities for his aforementioned work on the expansion of the Universe, which is now known today as the *The Hubble-Lemaître Law*, to posthumously recognise the equivalent contributions made by Georges Lemaître. The calculation of these redshifts is fairly trivial in the knowledge that there are known fixed atomic energy transitions that either emit or absorb light at specific wavelengths, therefore, the observed emission or absorption from varying atomic species can be compared to the laboratory values to give $(1 + z) = (\lambda_{obs}/\lambda_{em})$. The resultant relationship between the effect of cosmological redshift and the distance to an extragalactic object is therefore expressed as,

$$cz \approx H_0 d, \tag{1.1}$$

where $H_0 \approx 70\,\mathrm{km\,s^{-1}\,Mpc^{-1}}$ is the Hubble constant, d is the distance which is proportional

to the redshift z and the consequential recession velocity defined as $v = cz$. Although, the determination of cosmological distances to extragalactic objects in this manner possess a slight caveat in that the observable redshift is not only a result of the Hubble flow; an object's measured redshift is entangled with contributions from the Hubble flow and the peculiar velocity of the object itself. The consequence of these impure measures of recession velocity through redshift lead to the appearance of stretched clumps of galaxies in clusters of galaxies along z-space from the contributions of local galaxy motions due to gravity in addition to the expansion of space (see Figure 1.2). However, it should be noted that the non-relativistic nature of equation 1.1 is only applicable for small redshifts and any values determined this way start to deviate from the comoving distance at around $z \sim 0.1$, where the comoving distance is assumed to be equivalent to the proper distance for a flat ΛCDM universe to provide equation 1.2 (see Hogg 1999; Coles & Lucchin 2002; Lambourne 2010; Serjeant 2010),

$$d_{\text{comoving}} = \frac{c}{H_0} \int_0^z \frac{dz'}{\sqrt{(1+z)^3 \Omega_{\text{m}} + \Omega_{\Lambda}}}. \tag{1.2}$$

Current observational ideas and theories rely upon these fundamental, and historic, discoveries which have led to the systematic progress in bettering our understanding of galaxies with their evolution; the indirect observations of a dark matter; assembly into clusters of galaxies; the cosmology of the Universe itself. Therefore, this Chapter aims to introduce the key underlying concepts, and the necessary background knowledge, for the subsequent scientific Chapters of this thesis from our current comprehension of the Universe and its cosmology down to the galactic scale. Building upon the opening historical perspective this Chapter will discuss the current understandings of cosmology, including the influences of 'dark matter', that drive for the formation of the observed large-scale structures; the current observations and understandings of large-scale structure; the properties and evolution of the constituent galaxies that assemble into these large-scale structures. It is therefore anticipated this Chapter will prepare the reader for appreciating the questions attempted to be answered within this thesis; How do cluster galaxy sub-populations respond to their environment and sub-structuring activity? Can we infer the evolutionary history of a galaxy cluster through their angular momentum histories? Can we perform a kinematic analysis of AGN-hosting cluster galaxies in hostile environments

to infer the triggering mechanisms of AGN?

1.2   The Presence and Assembly of Large-Scale Structure

The Universe is commonly described to possess a flat cosmology, where the overall density parameters for the matter ($\Omega_m(t)$), radiation ($\Omega_r(t)$) and 'dark energy' ($\Omega_\Lambda(t)$) it holds provide the curvature parameter to be $k = \Omega_m(t) + \Omega_r(t) + \Omega_\Lambda(t) - 1 = 0$ (e.g. de Bernardis et al. 2000; Percival et al. 2002; Blake et al. 2011). This holds true for parameters deduced for $t = 0$ (i.e. at our current epoch) since the Universe is not so finite that we can see an infinitely luminous sky full of objects, nor is there a relatively shallow cosmic horizon preventing us to see objects at greater lookback times. The apparent tuning of the individual cosmological parameters (see *The Fine Tuning Problem*; Dicke 1961) has allowed for the existence of the elements, molecules, gas, dust, stars, black holes and galaxies through the underlying nature of this Universe obeying the *cosmological principle*; the Universe is isotropic and homogeneous, implying the laws of physics that drive the nuclear processes of the stars are the same as those that form galaxies (e.g. Saadeh et al. 2016). However, the observation of this principle is not pronounced until we reach ~ 100Mpc in scale (Scrimgeour et al., 2012). In other words, we can clearly observe that galaxies themselves are not randomly distributed across the sky but are structured into a 'cosmic web' of matter. This structure can be seen from optical surveys of galaxies – the Centre for Astrophysics redshift survey (CfA; Davis et al. 1982), the 2 degree Field Galaxy Redshift Survey (2dFGRS; Colless et al. 2001), the 6 degree Field Galaxy Survey (6dFGS; Jones et al. 2004) or the Sloan Digital Sky Survey (SDSS; York et al. 2000) – without the need to observe too deeply into z-space.

Figure 1.2 illustrates the observed web-like distribution of galaxies from the 2dFGRS run, where regions of space highly dense with galaxies can be seen to coalesce into node points, these are galaxy clusters and are themselves interconnected by filaments of galaxies to provide the observed web-like structure (Bond et al., 1996). These clusters of galaxies, while connected by the filaments, are also met with great voids where the galaxy number density is at its lowest and can act as chasms of up to diameters[2] of ~ 30Mpc h^{-1} (Pan et al., 2012; Schneider, 2015). Furthermore, the distribution of these varying sources of

---

[2]We parameterise our length-scales with the Hubble parameter $h = H_0/100$km s^{-1} Mpc^{-1}
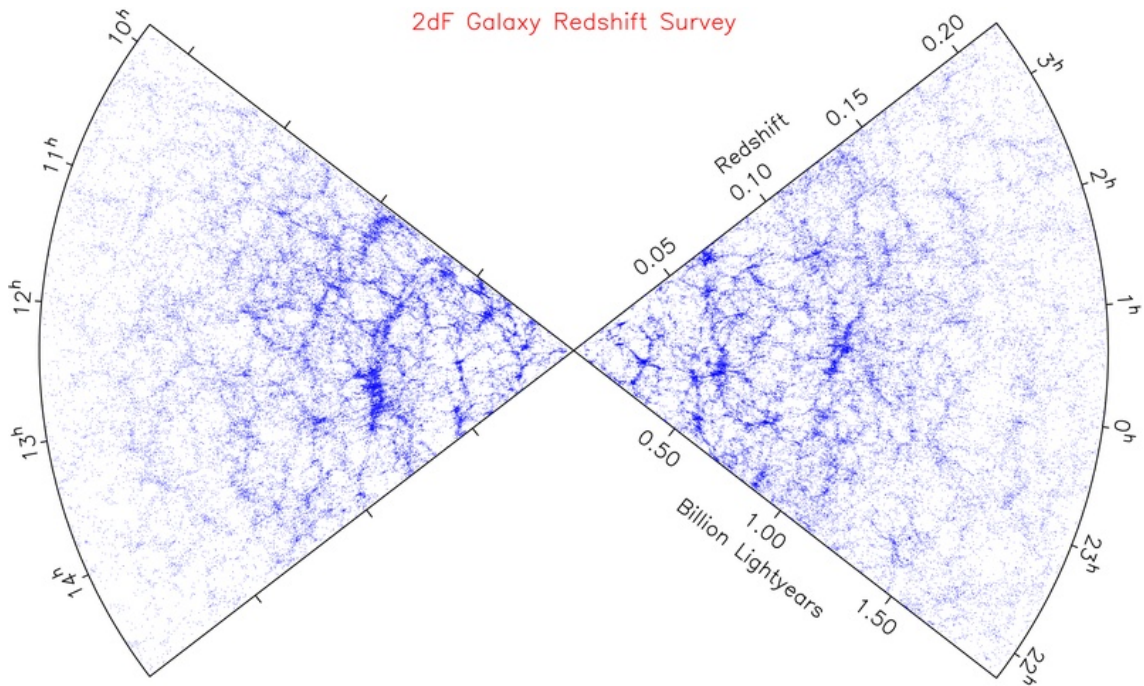
Figure 1.2: The 2dF Galaxy Redshift Survey (2dFGRS) highlighting the distributions of galaxies and the presence of structure within the Universe. The clustering of galaxies is apparent, forming nodes that stretch in redshift-space to produce what is known as the 'Fingers of God' effect, and combined with the Kaiser (1987) effect, illustrate the dynamical nature of these systems. Obtained from Colless et al. (2001).

mass in the Universe compared to the volumes that host them is stark, to the point where a tiny fraction of the Universe is inhabited by a significant fraction of the mass (see Figure 1.3).

1.2.1 Galaxy Clusters

The clustering of galaxies into the observed nodes of Figure 1.2 are believed to be the result of the confluence of two or more independent filaments of galaxies, collapsing onto a common potential, and thus feeding into growth of galaxy clusters (Springel et al., 2005b; Kravtsov & Borgani, 2012). This origin makes galaxy clusters dynamically active systems, this is evident if we analyse the distribution of the member cluster galaxies and pay close attention to the elongation, ostensibly pointed in the direction of the observer, we notice the distribution of cluster galaxies about each cluster's centre. Commonly known as *The Fingers of God* effect, this elongation is a Doppler effect caused by the peculiar velocities of the cluster galaxies themselves (Jackson, 1972). On average, an assembled regular cluster with assumed spherical symmetry (e.g. the Coma cluster), has a radial velocity dispersion of galaxies of $\sigma_{cz} \sim 1000 \mathrm{kms}^{-1}$ within a diameter of $d_{\mathrm{clu}} \sim 2\mathrm{Mpc}$
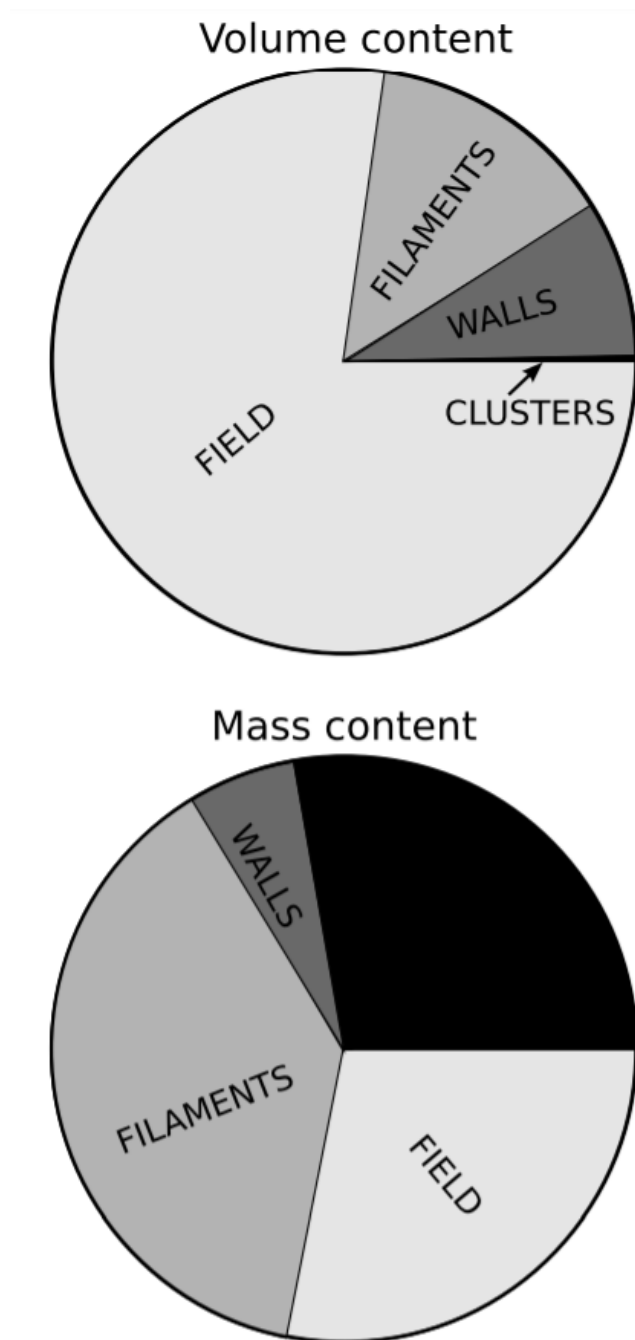
Figure 1.3: Pie charts of the volume and mass distributions of the different large-scale structures and features that pervade the Universe. The stark contrast between these charts profoundly indicates how much mass occupies the smallest fractions of the Universe. Obtained from Aragón-Calvo et al. (2010).

h^{-1}. With this we can say something about the dynamical timescales of these massive objects – estimated as the time it takes for cluster galaxy to move across the diameter of the system – which happen to operate to the order of $t_{\mathrm{dyn}} \sim d_{\mathrm{clu}}/\sigma_{cz} \sim \times 10^9$yr. Considering the Universe has been determined to be around $\sim 14 \times 10^9$ yr old (Planck et al., 2018) this means clusters themselves are still relatively young cosmologically and most are still relaxing into equilibrium; we can still learn about the evolution of the dynamical states of these systems. The cluster galaxy population can still grow further, with the potential for field population galaxies to be perturbed from their occupation of the Hubble flow and consequently start an infall journey to the potential's centre (Regos & Geller, 1989).

The cluster galaxies are not the only contributors to these very deep potential wells. As well as the galaxies themselves, there is also a diffuse hot plasma that pervades the space in-between the galaxies known as the Intracluster Medium (ICM), with typical temperatures of $\sim \times 10^7 - \times 10^8$K. X-ray observations of galaxy clusters inform us that these large structures are the densest concentrations of baryons in the Universe (White & Fabian, 1995) and play host to their own many intriguing insights into the internal dynamics of these systems with the existence of ICM shockwaves, shock fronts and cold fronts (e.g. Markevitch et al. 2002; Owers et al. 2009; Ghizzardi et al. 2010; Botteon et al. 2018). The ICM itself may therefore be the more ideal component to study in relation to the dynamical histories of a galaxy cluster since it carries a greater contribution to the baryonic mass and also leaves behind lasting imprints allowing for easier observations; cluster galaxies are statistically collisionless compared to the ICM on comparable timescales (Roettiger et al., 1997). The 'Bullet Cluster' – a remnant merger event between a cluster and a smaller sub-cluster (Tucker et al., 1998) – illustrates the collisionless nature of cluster galaxies, in which the cluster galaxies within the sub-cluster appear to be unaffected by the passage, compared to the highly interactive ICM emitting X-rays as a byproduct of these interactions (Barrena et al., 2002). Figure 1.4 illustrates these interactions with the X-ray data highlighting the hot diffuse ICM in pink compared to the optical image it is overlaid onto depicting the galaxies and their spatial positions. Moreover, the mapping of gravitational lensing effects–highlighted in blue–is indicative of an unusual offset in the positioning of the ICM centre of mass compared to the total centre of mass with the sub-cluster's ICM lagging behind the collisionless galaxies. The lensing effects lying coincident with those galaxies helped to further confirm the existence of an invisible 'Dark
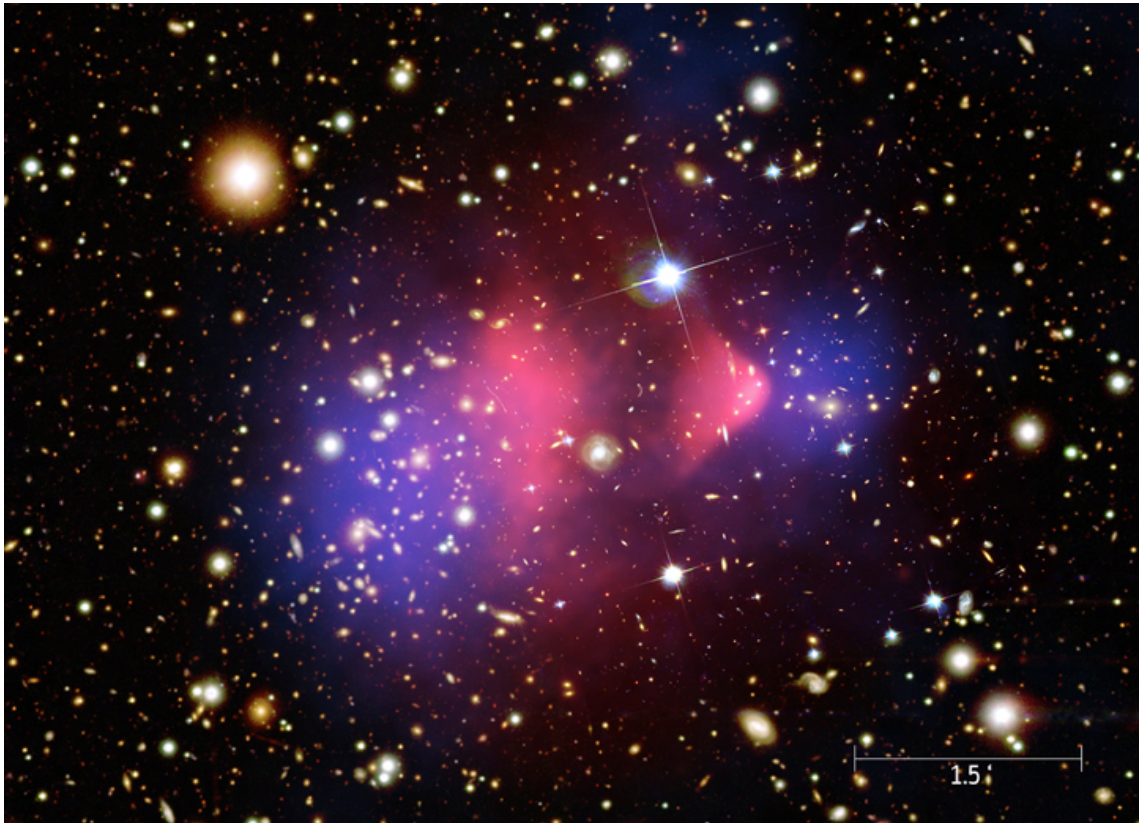
Figure 1.4: Composite image of the cluster system 1E 0657-56, commonly known as the 'Bullet Cluster', depicting the remnant interactions between the ICM gas (pink) of the cluster and sub-cluster with respect to the collisionless galaxies coincident with the mapped concentration of gravitational lensing (blue). The spatial dissociation of the baryonic ICM mass, the 'bullet', from the total mass of the system indicates the presence of a large concentration of mass not directly visible via known means. Obtained from https://chandra.harvard.edu/photo/2006/1e0657/more.html

Matter' (Clowe et al., 2004; Markevitch et al., 2004; Clowe et al., 2006).

1.2.2 The Introduction of Dark Matter

Galaxy clusters contain large concentrations of baryonic matter in the form of galaxies and a hot diffuse gas known as the ICM, with the latter forming the larger mass fraction to each system. However, as it was also shown in Figure 1.4, the concentration of gravitational lensing being spatially shifted away from the more massive ICM indicates there must be a more massive form of non-baryonic matter diffusely spread as a halo around the cluster and sub-cluster of galaxies. In fact, this deficit of matter has been noted since the early days of extragalactic astronomy. Zwicky (1933) studied the Coma cluster and found the radial dispersion of velocities to be $\sigma_{cz} \sim 1000 \text{ kms}^{-1}$, as stated earlier, with the aim to find the escape velocity of the cluster. In order to accomplish this, Zwicky (1933) would

proceed to calculate the mass of the cluster through the visible light of its member cluster galaxies. This is achievable through the knowledge that stars possess a mass-luminosity relation (Eddington, 1924), therefore, the integrated luminosity across a galaxy of stellar light should inform us of its mass; the more luminous, the more massive the galaxy. Specifically, if we assume there is an average mass-to-light ratio for a galaxy of Sun-like stars (e.g. $M_\odot/L_\odot$), then we could determine the mass to be $M_{gal} = (M_\odot/L_\odot)L_{gal}$. However, elliptical galaxies are found to be the common galaxy type in the Coma cluster, which are very luminous due to their large quantities of lower mass stars. Thus, our earlier estimate has to be improved to meet this average by a factor of 10, thereby giving $M_{gal} = 10(M_\odot/L_\odot)L_{gal}$. Applying this to each cluster member allowed Zwicky (1933) to determine the mass of Coma, then utilising the virial theorem, he realised that the escape velocity was considerably smaller than the velocity dispersion of Coma; the cluster galaxies should be unbound and flung out of the system entirely. This led to Zwicky (1933) concluding the existence of a 'dunkle materie', or, dark matter.

This dark matter could not be simply the hot diffuse ICM however, which can be tested by means of formulating homology relations. We know that the X-ray luminosity increases in the ICM due to increased frequency of collisions, implying that the X-ray luminosity would be related by a number density of ICM gas n within the cluster of radius r_{clu}, giving the X-ray luminosity of the cluster to be $L_X \propto n^2 r_{clu}^3$. From this gas within the cluster volume we can deduce the ICM gas to be $M_{gas} \propto n r_{clu}^3$, which relates to the X-ray luminosity as $M_{gas} \propto L_X^{1/2} r_{clu}^{3/2}$. Finally, considering the total mass will result from the hydrostratic equilibrium, isothermal pressure balances result in $M_{total} \propto r_{clu}$ which leads to the fraction of gas to be $M_{gas}/M_{total} \propto L_X^{1/2} r_{clu}^{1/2}$. The gas mass fraction within galaxy clusters averages to being roughly $M_{gas}/M_{total} \sim 0.10$ (White et al., 1993; Lubin et al., 1996), which adds further credence to the existence of a non-baryonic, collisionless dark matter. Additional observational evidence of dark matter came to light with the advent of superior spectroscopic technology that allowed for higher precision studies of galaxy rotation curves, which were shown to be constant throughout their disks (Rubin & Ford, 1970). With dark matter further concreted into our paradigm of the Universe after successive observations on large-scale structures over several decades such as the 'Bullet Cluster', as described above.

1.2.3   Cosmology & the Nature of Dark Matter

From the key observational evidence indicated previously we now know that dark matter operates on different scales and pervades the Universe in a collisionless manner; maintaining constant rotational curve velocities within galaxies to providing the deepest potential wells and acting as one of the most overt weak lenses in the Universe. There is a consequence to this realisation however; what is the nature of dark matter? How does it scale with the Universe? How can we model it to astrophysical objects? The first of these questions being the most elusive to the scientific community to this day.

Current dark matter models focus on *Cold Dark Matter* (CDM) halos as opposed to *Hot Dark Matter* (HDM) models. The full mathematical reasoning for this will not be explored here, however, we can start with knowing models on the formation of the Universe and its constituents need to coincide with current observations. HDM models show that the matter power spectrum–the density discrepancy between local and mean matter densities as a function of scale, providing the scale-invariant power law $P(k) = Ak^n$–becomes dampened for increasingly large values of k, meaning the early Universe small-scale fluctuations in local density required to form structure are smoothed out completely. This 'smoothing' is the result of the 'free streaming movement' of the HDM particles since they would possess relativistic velocities and would only coalesce on very large scales in order for non-relativistic velocities to be met, where the implications are top-down hierarchical structure formation (see Bond et al. 1982; Blumenthal et al. 1982; Peebles 1982). Considering the plethora of deep observations showing galaxies existing at a redshift $z \gtrsim 6$, lookback times of $\sim$ 12Gyr, we can immediately conclude that small-scale structures existed early in the universe not long after the epoch of recombination; the surface of last scatter containing the small density fluctuations that prelude the large-scale structures in the Universe, commonly known as the *Cosmic Microwave Background* (CMB) (Blumenthal et al., 1984). Therefore, dark matter cannot be hot in nature but is in fact cold, which is in accordance with observation due to the allowance of CDM particles to self-gravitate on small scales as $P(k)$ becomes undampened. For the CDM to collapse into *halos* and *subhalos* (e.g. galaxy clusters and individual galaxies respectively), those initial perturbations in the CMB have to grow from small to large mass scales over a period of time. This is shown in the Press & Schechter (1974) model of spherical collapse; the

initial density fluctuations that have reached above a certain threshold density within a volume correlate with regions of collapsed mass, allowing for the distribution of mass to be written as a function of time.

The Press & Schechter (1974) model applied to a CDM-hosting universe allows for small-scale low mass structures to form at earlier epochs. This indicates that galaxy mass scales will form first and lead to *hierarchical structure formation*, with larger structures forming through evolution from the gradual assembly of the smaller structures. However, there are limitations to modelling a universe analytically, especially when trying to introduce gravitational effects of multiple mutually interacting bodies. Thus, numerical simulations of dark matter particles given certain initial conditions are an ideal way to see how the Universe evolved from the density perturbations. One of the largest and well documented recent simulation runs on dark matter evolution within the Universe is the *Millennium Simulation*, with a staggering 2160^3 dark matter particles, each representing $\sim \times 10^9 M_\odot$ (Springel et al., 2005b). Figure 1.5 illustrates the results of the Millennium-II simulation utilising a flat cosmology of $\Omega_m = 0.25, \Omega_\Lambda = 0.75$ and a baryonic matter contribution of $\Omega_b = \Omega_m - \Omega_{dm} = 0.045$, where the evolution of the dark matter particles are shown at different epochs (z) and different scales. The results of such numerical simulations clearly run parallel with observations of hierarchical structure formation. They are found to conform to what we refer to as a ΛCDM model, or 'standard model', of cosmology where the Λ term refers to the cosmological parameter of the expansion of the Universe.

1.2.4   Dark Matter Halos

For the formation of structures, such as those from the spherical collapse models of Press & Schechter (1974), there has to be the modelling of dark matter halos, since baryonic matter will be found to clump where dark matter halos are formed. These are simply clumps of dark matter that have overcome the cosmic expansion, due to the density perturbations in the CMB, and may also contain subclumps or 'subhalos' (e.g. a galaxy cluster containing cluster galaxies). The simplest definition for a spherically symmetric dark matter halo is where average density reaches ~ 200 times the critical density of the universe meaning it being equivalent to the radius $R_{halo} \sim r_{200}$. However, simulations typically use 'friends-of-friends' algorithms since dark matter halos are not trivially spherically symmetric.
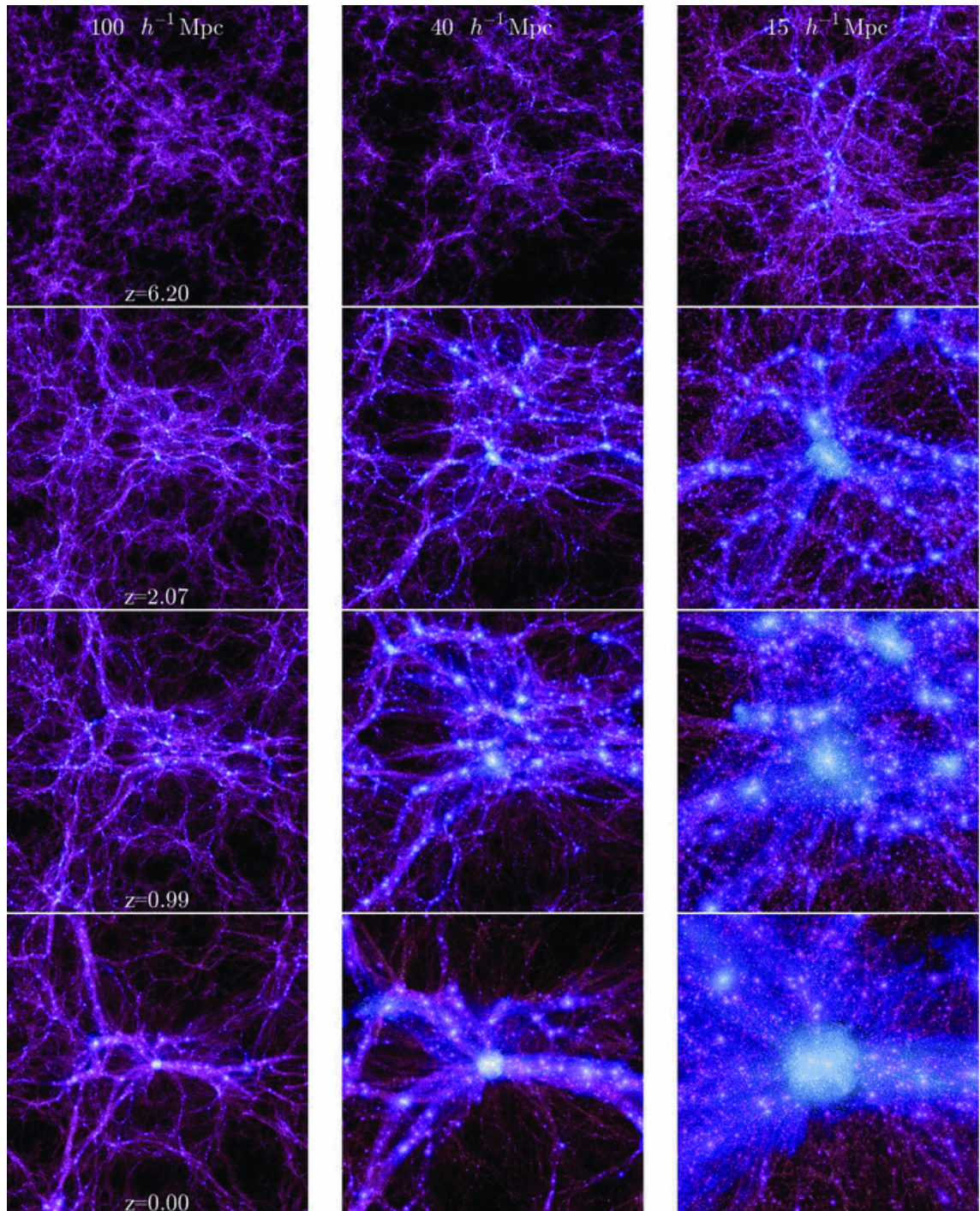
Figure 1.5: The Millennium-II simulation of structure formation and evolution with dark matter. Where each row indicates a unique epoch ($z = 6.20, 2.07, 0.99$ and 0.00) with each column visualising each epoch from different scales (at 100, 40 and 15 Mpc h^{-1}). Obtained from Boylan-Kolchin et al. (2009)

Friends-of-friends algorithms work via relying upon connecting all particles that are below a mean particle separation $\sqrt{1/n}$, where $n = N/r^3$ is the number density of the particles (e.g. Colberg et al. 2000; Springel et al. 2005b; Boylan-Kolchin et al. 2009.

If we can resolve enough dark matter particles within a halo, then we can determine the radial density profile of a dark matter halo, which is useful for constraining the mass distribution of different halos against our observations. One mathematical description of such dark matter halo profiles is the Navarro, Frenk & White (NFW; Navarro et al. 1997) profile, which is denoted in Equation 1.3. This was found to be a 'Universal Profile', since it was discovered that the radial profile of the halo did not change shape across 4 orders of magnitude of mass (Navarro et al., 1996). The NFW profile was initially proposed by Navarro et al. (1995) and represents the halo density for N-body dark-matter simulations as a function of radius below as,

$$\frac{\rho(r)}{\rho_{\text{crit}}} = \frac{\rho_c}{(r/r_s)(1+r/r_s)^2}, \tag{1.3}$$

where $\rho_{\text{crit}} = 3H^2/8\pi G$ is the critical density of the Universe–defined as the density required to halt the expansion of the Universe– with r_s defined as a scale radius weighted by a dimensionless parameter and ρ_c is a dimensionless characteristic overdensity that maintains the mean halo density to be $200 \times \rho_{\text{crit}}$. Despite having been a powerful tool this so-called universal profile does not operate at all scales of halo effectively, as with dwarf galaxy halos it leads to a steeply rising radial density profile as $r \to 0$ making the halo 'cuspy', which goes against observed density profiles that show dwarf halos to be flat (e.g. Moore 1994; Oh et al. 2015). These cuspy halos could possibly be the result of the increased resolving power of dark matter particles in N-body simulations, which have led to determining that a more suitable determination of dark matter density would be the Einasto-profile,

$$\rho(r) = \rho_s \exp\left(\frac{-2}{\alpha}\left[\left(\frac{r}{r_s}\right)^\alpha - 1\right]\right), \tag{1.4}$$

where ρ_s is the density at the scale radius and α determines the shape of the slope. The Einasto profile therefore reduces the cuspy nature by not responding so strongly as $r \to 0$.

1.2.5   The Extrema of Large-Scale Structures

Galaxy clusters, within the mass scales they operate on, are large-scale structures that would be considered an intermediate level. To elaborate, there are smaller structures that exist at $\sim \times 10^{13} M_\odot$ mass scales known as *Galaxy Groups*; the predecessors to galaxy clusters through hierarchical structure formation. If one for the moment considers that there is an observed presence of galaxies 'clumping' in some galaxy clusters/groups at relatively low redshifts, this would therefore imply the cluster/group has undergone a recent merger with another cluster or group. These substructures also subtly highlight the tendency for galaxies to coalesce to form a larger structure, by extension, large collections of galaxies in groups or clusters to coalesce to form an even larger structure. The concept of hierarchical structure formation is fully realised with the work of Lacey & Cole (1993) and is depicted schematically in Figure 1.6. In light of the hierarchical With the galaxy groups on the lower end of the large-scale structure scale, the upper end is occupied by structures that hold masses at $\sim \times 10^{16} M_\odot$ known as *Superclusters*; collections of galaxy groups and galaxy clusters clumped into a larger-scale single structure. These structures are explored in greater detail in the following subsections.

Galaxy Groups

Considered the starting point for galaxy assembly and virialisation into structure, galaxy groups are but small seeds compared to their elder equivalents; typically contain $\lesssim 50$ galaxies, possess a radius of $R \lesssim 0.5 \text{Mpc}$ and have estimated dispersion velocities approximately $\sim 150 \text{kms}^{-1}$. Although, there are exceptions to these ostensibly fluid criteria with some classified groups having greater masses (see Paul et al. 2017). As well as this basic definition, there are further sub-categories, such as proto-groups, compact groups, and fossil groups. Proto-groups are those that are undergoing formation, whereby independent galaxy and proto-galaxy halos are in the process of forming a singular dark matter halo (Diener et al., 2013). Compact groups are, as their name implies, very compact collections of galaxies that are strongly virialised and have typically $\lesssim 5$ galaxies (Hickson, 1982). The need for dark matter is apparent in these objects, since the visible mass present in these relatively tiny ensembles does not meet the necessary threshold to keep its members gravitationally bound to one another (see Hickson 1997). Fossil groups are old systems

that have not harassed additional galaxies to infall onto their potential, however, do have a history galaxy-galaxy merging processes between members of the group and therefore are useful indicators of galaxy evolution within isolated systems. The result of this leaves behind an X-ray halo relic of the intra-merging events (Hickson, 1997; Mulchaey, 2000).

Superclusters

The next echelon in the hierarchy of structure formation above galaxy clusters are superclusters, which were originally postulated as 'second-order clusters' by Abell (1958). Superclusters are defined to be a collection of two or more galaxy clusters above a certain spatial density threshold (Bahcall, 1988). Although, unlike galaxy clusters, they are not virialised, are less dense, and are objects on a very large scale lying on the Hubble flow (Chon et al., 2015). Aside from the 'Sloan Great Wall', superclusters are the largest collections of galaxies which provide a plateau in the mass-to-light ratios when compared to their smaller progenitors within the observable Universe. The mass-to-light ratios of superclusters do not deviate much greater than the values commonly found from galaxy clusters, thus, dark matter cannot contribute more to the mass of the Universe beyond that of galaxy clusters. The application of the aforementioned consequences of these structures leads one to be able to constrain the cosmological parameters of the Universe to a greater accuracy.
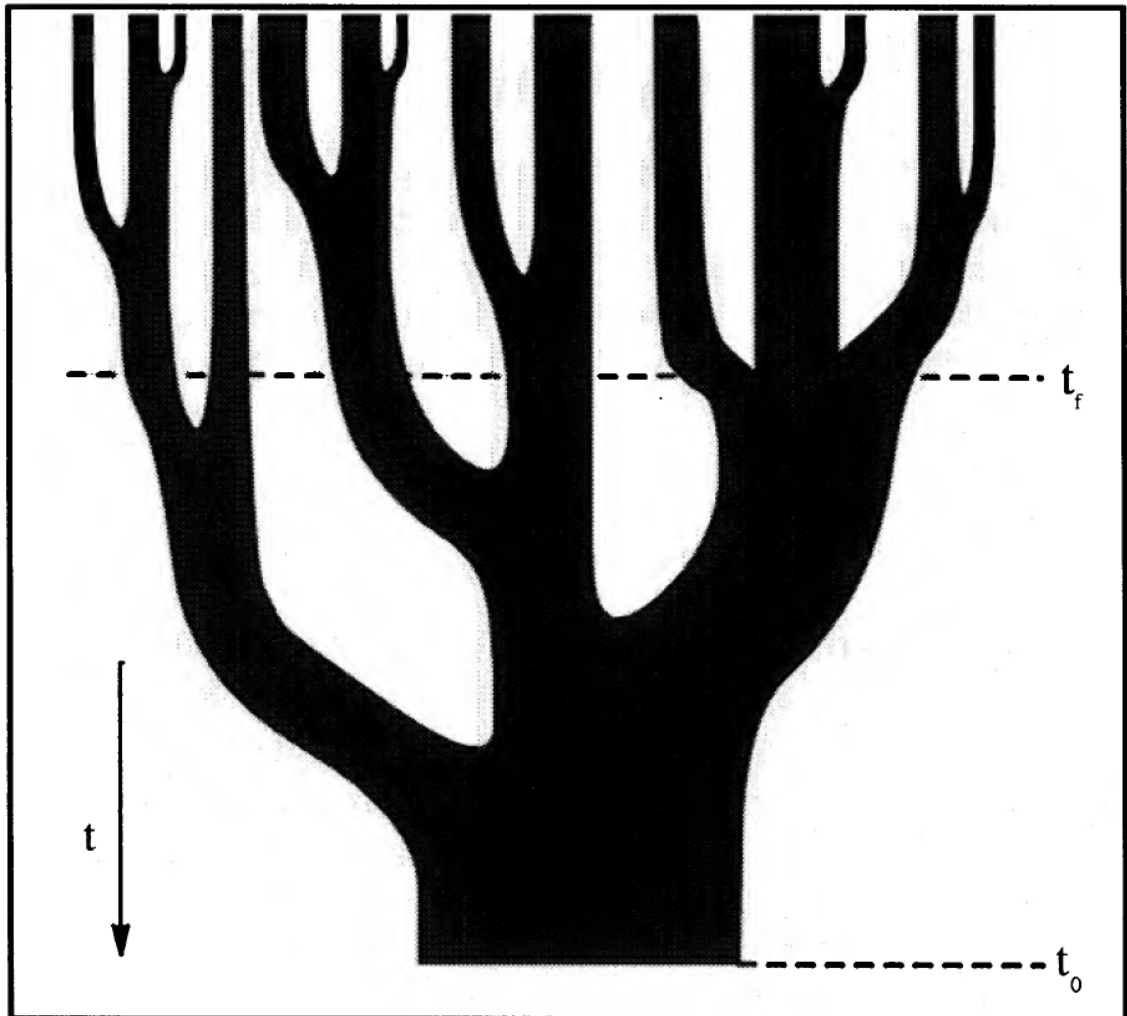
Figure 1.6: Hierarchical merge tree resembling the growth of a halo. Time increases from top to bottom where t_0 is the current epoch. The width of each branch resembles the evolution of mass assembly throughout time t. Obtained from Lacey & Cole (1993).

1.3 Galaxy Evolution and the Effects of Large-Scale Structure

So far we have discussed the clustering of galaxies, how they form large-scale structure and how modelling their dark matter halos can constrain cosmology. However, we are yet to elaborate on the namesake of these objects, the cluster galaxies themselves.

1.3.1 Observable Indicators of Galaxy Evolution

As the study outward to our Universe advanced at a relatively fast pace throughout the 20th century, it was soon realised that galaxies express themselves and their ages through a variety of indicative markers; imprints of extragalactic histories are detailed through their catalogued morphologies, by extension, galaxy luminosities and colours can indicate their ages as well as that of the stellar population that are responsible for the luminosities that we can see in the visible spectrum. We explore the markers of a galaxy's evolution in the following subsections below as a prelude to how these are important for determining the evolutionary histories of galaxy clusters.

Morphology

Referring back to the initial realisation in subsection 1.1 with the Universe containing many galaxies that lie at great extragalactic distances from our own, Hubble (1926) also noted the large variety of common 'shapes' of galaxies. These morphological differences presented galaxy populations that possessed spiral arms, which could be further sub-divided by the presence–or the lack thereof–of a barred core as well how tightly wound their spiral features were; galaxy populations without spiral arms were noticeably sub-divided by differing scales of eccentricity. Thus, Hubble (1926) categorised galaxies into three broad population groups of 'spiral', 'elliptical' and 'lenticular'. Together, these categories formed *The Hubble Sequence* and was depicted graphically into what it is colloquially called as the 'Hubble tuning fork' diagram. It was the placing of these varying morphological groupings onto this diagram that initially caused confusion by some astronomers, believing it to represent an evolutionary sequence on how a galaxy's shape may evolve. However, Hubble never stated this to be the case, going so far as to explicitly outline that his classification had no intent of going beyond being empirical to the simple categorisation of galaxy morphologies (Hubble, 1927). As a peculiar

consequence of the old way of thinking towards galaxy morphological evolution that plagues older publications, it is worth briefly noting that 'early-type' galaxies are those that fall under elliptical and lenticular categories, with 'late-type' galaxies allotted to spirals and irregulars. Therefore, a modified version of the Hubble sequence can be seen in Figure 1.7, which in addition supplies a fourth class of galaxy named as 'irregulars'.
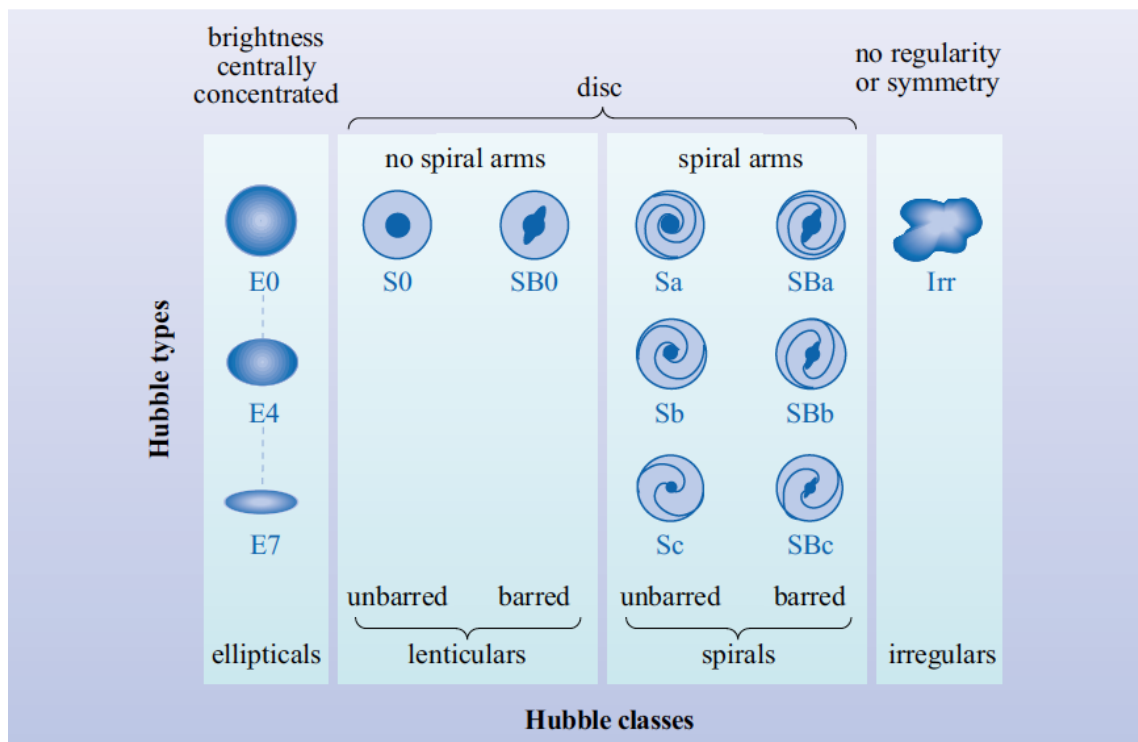
Figure 1.7: Modified Hubble Sequence Diagram demonstrating the four classes in four separate columns. Ellipticals show an increasing eccentricity down the column; lenticulars are simply defined between barred and non-barred; spirals decrease in their arm tightness down the column with a sub-division between barred and non-barred; irregulars represent anything that has asymmetry or no regularity. Obtained from Jones et al. (2015).

Brightness & Luminosity

One of the most empirical concepts within observational astronomy is the ability to observe the objects we study in the night sky, which, can only be achieved if the astronomical body is bright enough and our instrumentation is sensitive enough. The brightness of these objects vary in accordance with their distance from an observer, this is found to operate as an inverse-square law. Therefore, implying that we can determine an object's intrinsic brightness, which is referred to as the luminosity and is defined as $L = F/4\pi r^2$, where F represents the flux of the object. In addition, the study of a galaxy's luminosity, for example, can inform to us a great deal about the age of its stellar population; strength of their luminosities in differing passbands giving us their colours, giving us an insight into their total masses and their relative star formation rates.

We can quantify the luminosity variations that exist in a population of galaxies through the determination of a luminosity function, and by extension, the stellar mass function of those galaxies. The first understandings of these distributions of galaxy by luminosity was determined by Schechter (1976) through assembling a volume limited sample of galaxies from 13 clusters into a composite to minimise a *Malmquist Bias* (Malmquist, 1925). The result of this allowed for Schechter (1976) to formulate the expression,

$$\Phi(L) = \Phi^* \left(\frac{L}{L^*}\right)^{-\alpha} \exp\left(-\frac{L}{L^*}\right), \tag{1.5}$$

where Φ^*, L^* and α represents the free parameters of a normalisation factor in units of number density, a characteristic break luminosity and the slope of the gradient respectively. In reality the total luminosity function masks the luminosity functions of the sub-classes of galaxies by morphology that contribute to the observed total distribution of galaxies, this can be seen in Figure 1.8, where ellipticals and spirals generally dominate the within the same high regions of L with the low L regions primarily occupied by dwarf and lenticular galaxies. The resulting data is useful in providing a picture of the distributions of differing mass scales of galaxies.

Colour

All galaxies host a population of stars and these stellar populations contribute the majority of the optical luminosities we observe in each galaxy. The stellar populations themselves
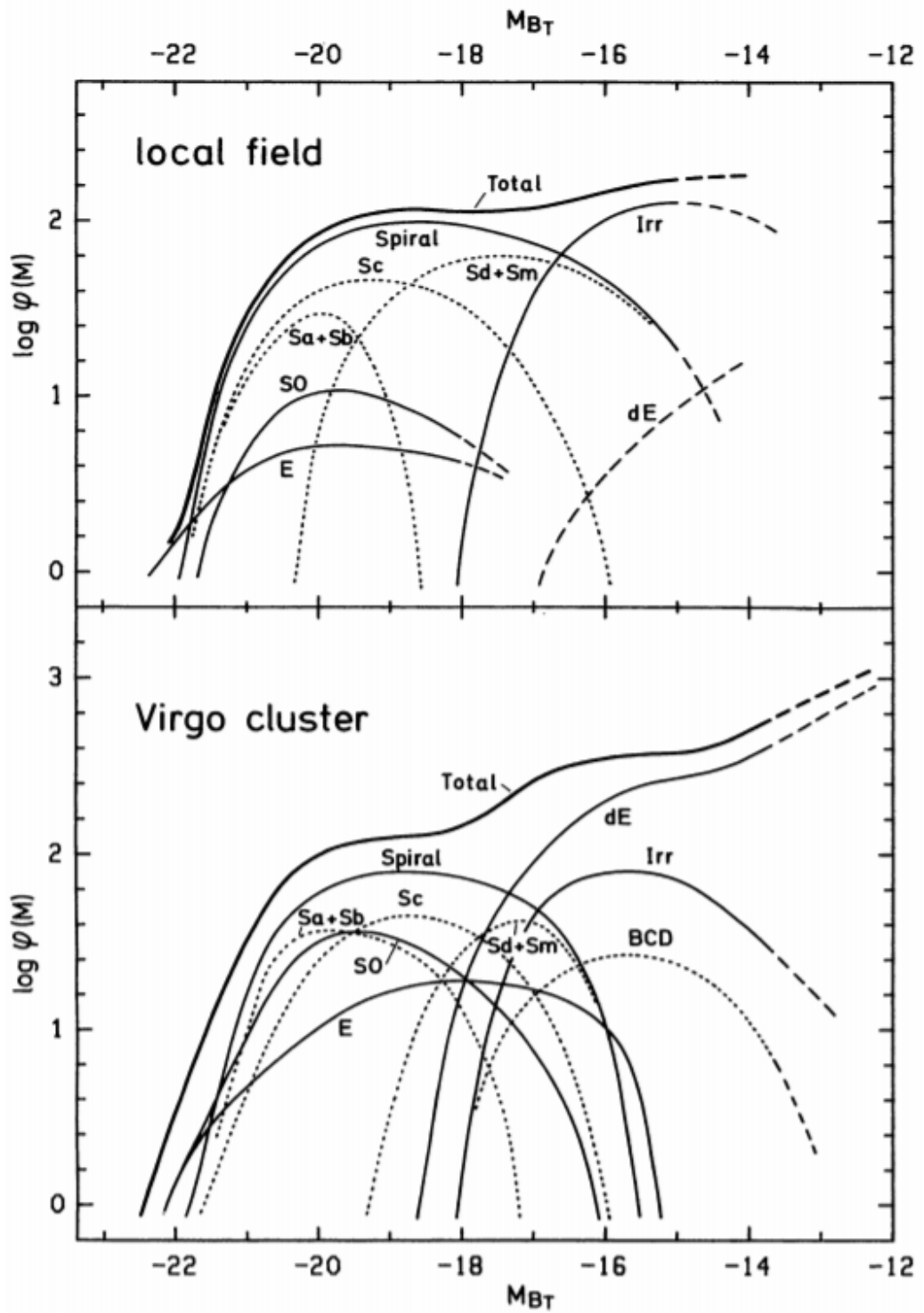
Figure 1.8: A comparison of luminosity functions by galaxy morphology between a sample of local field galaxies (*top*) and galaxies that lie within the Virgo cluster (*bottom*). An interesting consequence of the clustered environments is an increase in the number density of luminous lenticulars (S0) and ellipticals (E), with the surge in number density of dwarf ellipticals at lower luminosities. Obtained from Binggeli et al. (1988).

exhibit varying degrees of colour, which relates to their relative masses, ages, temperatures and luminosities as per the Hertzsprung-Russell diagram (HR; Hertzsprung 1909; Russell 1914). The HR diagram is famous in astronomy for allowing us to understand stellar evolution through a simple observation of the stellar colours (e.g. B-V) against their magnitudes (e.g. M_V). Thus, by extension, colour-magnitude diagrams can be used to analyse the colour distributions of a sample of galaxies and considering the relation between luminosity and mass we can see how galaxies of different masses correspond to their total integrated colours (Strateva et al., 2001; Bell et al., 2004). Galaxy colours are therefore useful indicators of the age of a galaxy; according to the HR diagram we know bluer stars (e.g. O, B and A stars) are associated with more massive and short-lived populations of stars compared to redder stars that live long lives on their main-sequence. It was found from galaxy surveys that the distribution of galaxy colours are predominantly bimodal; a 'red-sequence' principally consisting of early-type galaxies with a 'blue cloud' of predominantly late-type galaxies and a sparser region in-between coined the 'green valley' (Bell et al., 2004). Figure 1.9 illustrates this bimodality along the with green valley of galaxies. It should be noted that these colour distribution diagrams do not inform us of the intrinsic properties of a galaxy, but, merely described the stellar populations hosted by the galaxy.

Star Formation Rate

The stellar populations hosted by galaxies are important constituents, which typically co-evolve with their galaxies as they build mass, this can be seen by analysing star formation histories of galaxies whereby cosmic star formation peaks at redshift $z \sim 1.6$ (Madau et al., 1998). From fundamental principles the act of star formation itself requires an input of some sort of 'fuel' as well as the physical mechanisms themselves that drive star formation. As a consequence of this galaxies can be simplified as reservoirs of fuel, in this case, the fuel is the gas that is found to pervade within galaxies. A simple relation of the surface density of the star formation rate to this reservoir of gas can be approximated as a power-law to the surface density of gas available,

$$\Sigma_{\text{SFR}} = A\Sigma_{\text{gas}}^n, \tag{1.6}$$
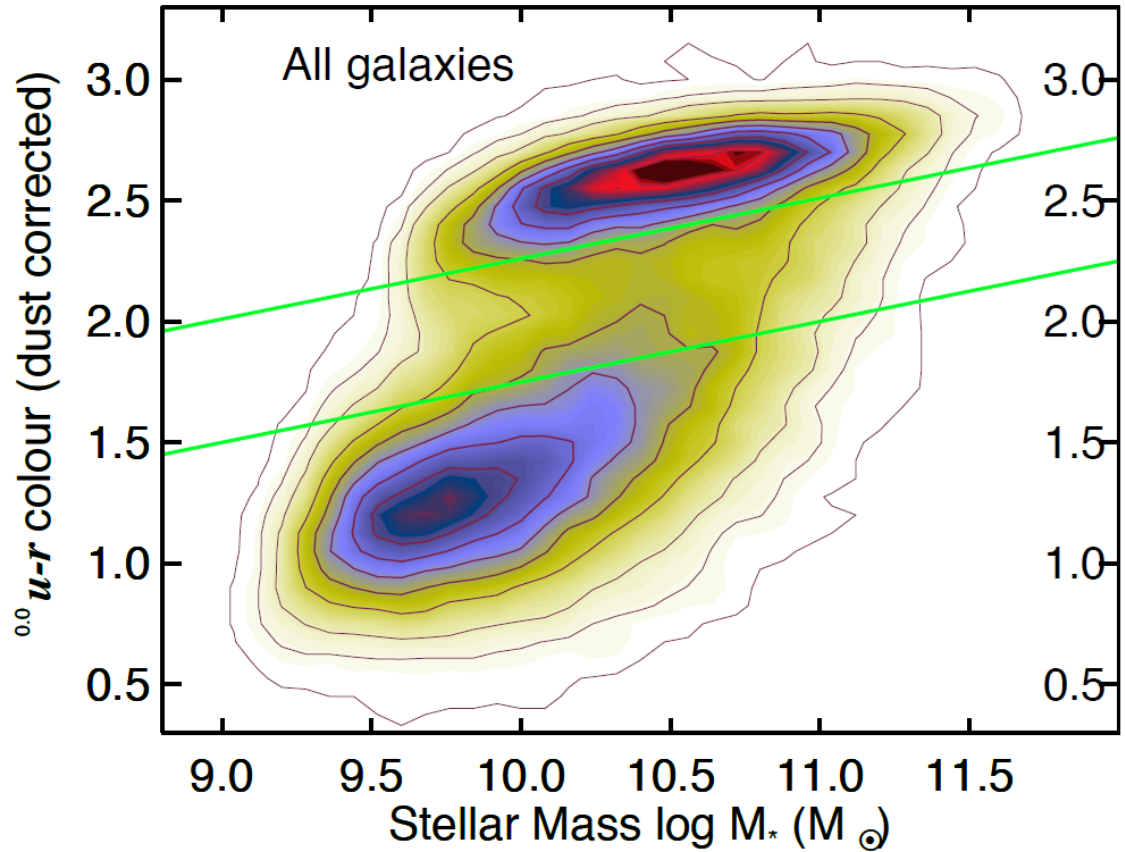
Figure 1.9: The $u - r$ colour distribution of galaxies taken from SDSS, GALEX and Galaxy Zoo survey data in a $z = 0.0$ restframe. The dense distribution of galaxies near the top of the plot resembles the 'red sequence' of galaxies, whereas the more spherical-like distribution close to the bottom of the plot depict the 'blue cloud'. The distribution of galaxies that lie in between the green lines highlights the so-called 'green valley' region of galaxies. Obtained from Schawinski et al. (2014).

where Σ_{SFR} is the surface density of star formation, A is a proportionality constant and Σ_{gas} is the surface gas density, this is referred to as the *Schmidt Law* (Schmidt, 1959). Observations show the value of the gradient n to vary in value between 1 and 2. For example, the work of Kennicutt (1998b) finds $n = 1.4$.

In order to ascertain a value for the rate of star formation of a particular galaxy, however, we need to rely upon spectroscopic measurements to infer these values indirectly. We start with the knowledge that the physically closest analogue for a galactic stellar population is our own Milky-Way galaxy. Furthermore, we know that the local and young populations of stars, which are formed in more recent epochs, are typically O and B type stars that lie within H II regions. These stars ionise their surrounding gas with UV photons, thereby resulting in a dominant $H\alpha$ Balmer line emission, the luminosity of this emission can be used to infer the rate of star formation of these young stellar populations (Kennicutt & Kent, 1983; Kennicutt, 1998a; Kennicutt & Evans, 2012). Assuming all young stellar UV photons are absorbed by the surrounding gas with a known Salpeter (1955) initial mass function and that star formation is constant within the timescales for young stars of masses $10 \leq \mathrm{M}_\odot \leq 20$ we can determine the star formation from the $H\alpha$ luminosity as outlined by Kennicutt (1998a),

$$\frac{\mathrm{SFR}}{\mathrm{M}_\odot \mathrm{yr}^{-1}} = 7.9 \times 10^{-42} \frac{L(H\alpha)}{\mathrm{ergs\ s}^{-1}}. \tag{1.7}$$

$H\alpha$ is a commonly used optical tracer of star formation, however, as an optical tracer $H\alpha$ luminosity can be attenuated due to the local interstellar dust absorbing the stellar light (Lonsdale Persson & Helou, 1987). It is possible to correct for this attenuation for a particular atomic line if one can resolve the star formation region itself (Dopita et al., 2002). Other wavelengths have their own spectroscopic tracers of star formation, for example, in the infrared polycyclic aromatic hydrocarbons are shown the tightly correlate with the total infrared luminosity, which is in turn shown to correlate with extinction-corrected $H\alpha$ luminosity (see Kewley et al. 2002; Peeters et al. 2004; Farrah et al. 2007). This expands to a menagerie of multiwavelength photometric and spectroscopic observations in the ultraviolet, optical, radio and infrared (e.g. Yun et al. 2001; Schmitt et al. 2006; Elbaz et al. 2011).

1.3.2   Observed Galaxy Cluster Population Effects

The aforementioned observable indicators of natural galaxy evolution are commonly indicative of the passive ageing a galaxy undergoes if we assume it has experienced little-to-no interaction with its immediate external surroundings. In the following subsection we briefly discuss the impact a galaxy's local environment has on these evolutionary indicators, and by extension, the effects on the evolution of a galaxy within the context of galaxy-dense galaxy clusters. Cluster galaxy evolution, and its relationship to the local cluster environment, is a theme explored throughout this thesis and is elaborated on further in each of the three main science Chapters 2, 3 and 4 as a function of cluster dynamical state and projected radius from their host cluster's centres.

Morphology-Density

Galaxies are very dynamic objects within the space they inhabit despite their relatively long dynamical timescales; galaxies experience galaxy-galaxy merging commonly throughout their evolutionary process and goes someway to help indicate and explain why the morphologies and compositions vary from galaxy to galaxy (e.g. Moore et al. 1996, 1999; Owers et al. 2012). With this in consideration observations of cluster galaxies present an overt dichotomy of cluster galaxy morphologies as a function of the projected radius from the their respective cluster centres (Oemler, 1974; Dressler, 1980; Houghton, 2015). Dressler (1980) first illustrated this apparent environment-induced galaxy evolution through fractions of different morphological types; early-type morphologies dominate the space towards the cluster centre with late-type morphologies found to be diffusely spread at larger radii (see Figure 1.10).

Colour-Density

The observed contrast in galaxy populations within clusters as a result of their relative clustocentric radii is not limited solely to galaxy morphologies. Hogg et al. (2003, 2004) highlight a colour-density relation with redder galaxies found towards the centres of galaxy clusters and vice versa for bluer galaxies, in addition, this colour-density relation is found to be an even stronger and tighter relation than the morphology-density relation (Balogh et al., 2004; Bamford et al., 2009). The colour-density dichotomy ties in well with that

of morphology-density since early-type galaxies are typically found to be redder galaxies with late-types being commonly married to bluer populations. The colour-density relation is illustrated in Figure 1.11 where increasing density leads to a significant decrease in the fraction of blue galaxies and an increase in fraction of red galaxies.

Star Formation-Density

With the prior density-based relations of galaxy properties it is rather unsurprising that there is a resultant relation between galaxy star formation and their environment through density. The relationship maintains the rolling consistency with the previous density relations with early-type, red and quenched star forming galaxies associated with older galaxy populations are found at higher fractions towards a cluster core; late-type, blue and star forming galaxies representing younger galaxy populations are found at higher fractions at higher radii from a cluster core (Lewis et al., 2002; Gómez et al., 2003; von der Linden et al., 2010; McGee et al., 2011; Wetzel et al., 2012). Figure 1.12 continues the trend of presenting increasing density as the clustocentric radius reduces to zero with galaxies predominantly possessing low star formation rates against higher fractions of higher star formation rates shown at larger radii and lower densities.

1.3.3 Active Galactic Nuclei

Active Galactic Nuclei (AGN) are highly luminous sources of radiation in the Universe ($\sim \times 10^{40} - \times 10^{47}$erg s^{-1}) powered by supermassive black holes ($\gtrsim \times 10^5 M_\odot$), hosted by a galaxy, as a consequence of the accretion of matter and the formation of an accretion disc surrounding the accreting black hole within a tiny region of up to $\sim$ 10AU (Kolb, 2010; Serjeant, 2010). An example of the power and energy emitted by an AGN can be seen in Figure 1.13, where the active nucleus present in Centaurus A is driving a jet that is interacting with the surrounding intergalactic medium. AGN are classified into four broad groups: Quasars, Seyferts, Blazars and Radio Galaxies. These objects are all currently believed to be all one of the same, with their distinctions determined by the observer's line-of-sight, and therefore dependence on the orientation of the objects themselves (more in-depth discussions can be found in the following and references therein Tadhunter 2008; Jones et al. 2015; Netzer 2015). This consequence leads to the 'unified model' of AGN, with two types of AGN unification: radio loud and radio quiet (see Figure 1.14). Only
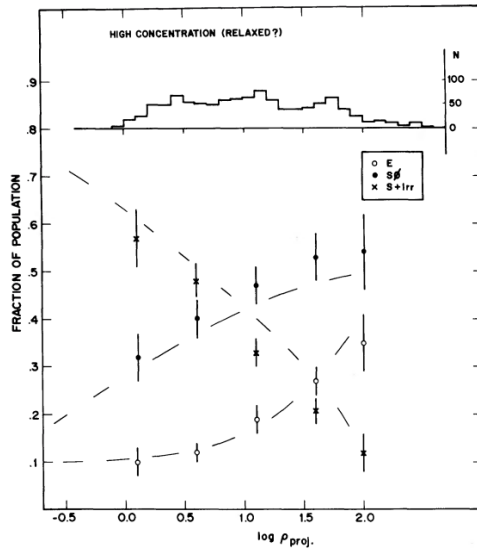
FIG. 8.—High-concentration clusters (A151, A539, A957, A1656, A1913, A2040, A2063, 0247−31, 0428+53, 1842−63).
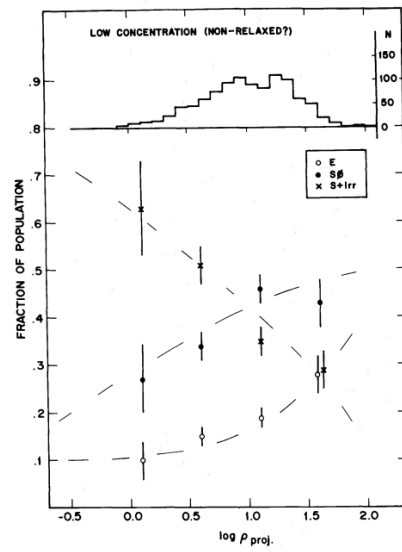
FIG. 9.—Low-concentration clusters (A76, A119, A168, A978, A979, A1644, A1736, A2151, 0030−50).

Figure 1.10: The observed morphology-density relation as depicted by Dressler (1980). A comparison of the fractions of galaxy populations split by their relative morphologies is made between dense (*left* and less dense (*right*) clusters. In both cases fractions of ellipticals increase as the projected density (ρ_{proj}) increases, with spirals populations dramatically declining with the increase in projected density.
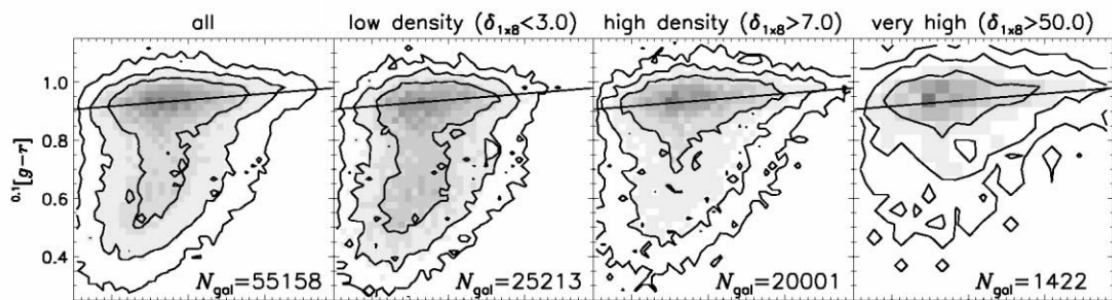
Figure 1.11: The observed colour-density relation as depicted by Hogg et al. (2004). Galaxy colour-magnitude plots are shown where the entire colour distribution of galaxies (*far left column*) is compared against the adjacent columns that each successively represent increasing density from left to right. As we approach higher densities it can be observed that the distribution of galaxy colour shifts to a dominance of a red sequence of galaxies. Where the overdensity $\delta_{1\times8}$ is equal to zero in a mean density environment, i.e. there is no overdensity.
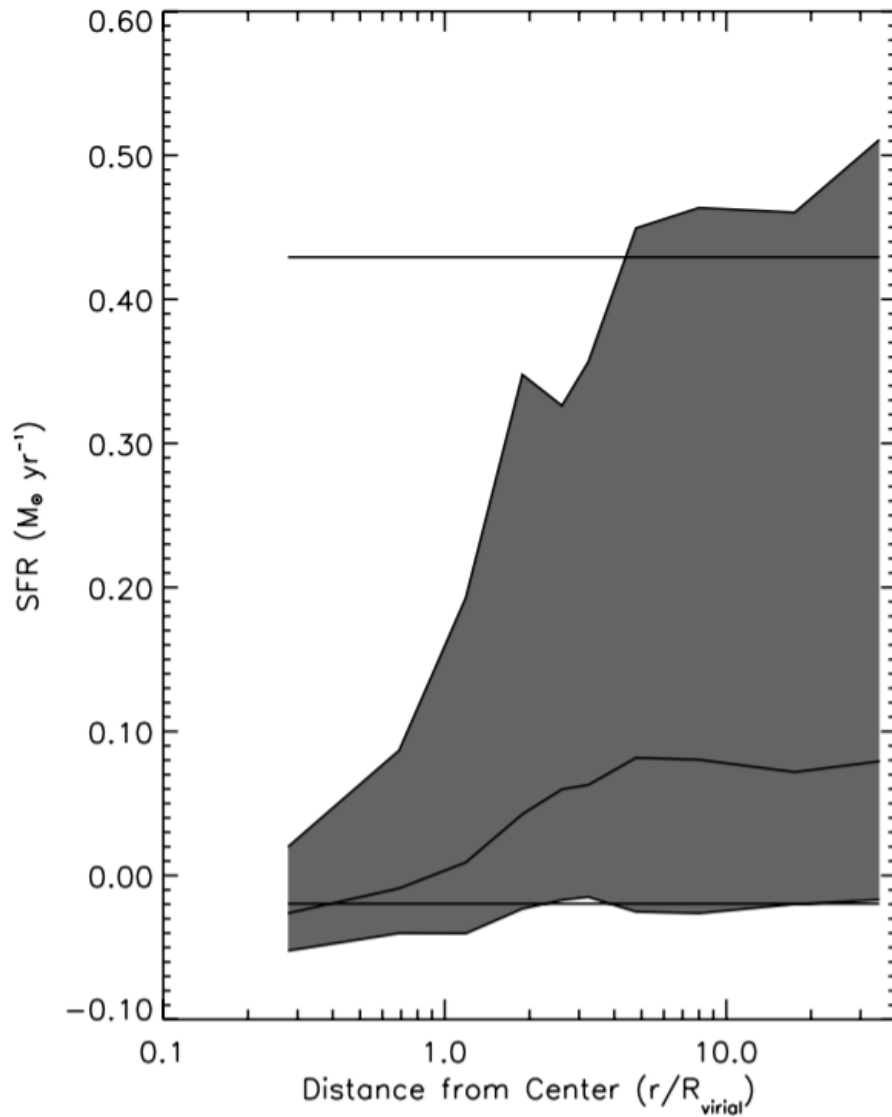
Figure 1.12: The star formation rate- density relation as observed by Gómez et al. (2003). The shaded regions represent the distribution of star formation rates for each projected radial bin in units of the virial radius R_{virial}, where each bin holds ~ 180 galaxies. The variable line in the centre represents the median of the distribution, with the shaded regions above and below representing the 75th and 25th percentiles respectively. The top and bottom fixed horizontal lines illustrate the 75th and 25th percentiles of the field population respectively. It can be seen here that as the projected radius increases, leading to a decrease in density, the distribution of star formation rates widens to higher values, indicative of quenching at smaller clustocentric radii.

$\sim 10\%$ of AGN are found to be radio loud and the precise reasoning for this is still relatively unclear (Hooper et al., 1995).

The $M - \sigma$ Relation and AGN Feedback

One of the most fascinating revelations in the recent history of AGN studies is the observed influences AGN have on their host galaxies. Magorrian et al. (1998) studied a sample of galaxies and determined a scattered correlation between the luminosities of their central galactic bulges and the estimated black hole mass. However, this surprising result was strengthened with the remarkably tight correlation found between galaxy supermassive black hole masses and the velocity dispersions of the stellar bulge population at approximately $M_{\mathrm{BH}} \propto \sigma_e^4$ (see Figure 1.15; Ferrarese & Merritt 2000). Any possible cross-contamination between the black hole mass estimates and velocity dispersion estimates that could invalidate such a correlation is also negated (Gebhardt et al., 2000). The immediate consequence of such a result is that there is some sort of feedback mechanism at play between the back hole mass and bulge velocity dispersion (and bulge mass) that leads to the growth of mass observed in order to maintain such a tight relation. If we assume that AGN resemble earlier epochs in the co-evolution between supermassive black hole growth and that of the host galaxy, then the AGN could be the likely candidate responsible for regulating and constraining this growth, for example, the AGN quenching of stellar mass growth (Springel et al., 2005a; Croton et al., 2006; Schawinski et al., 2007). Such attempts to model this have identified the requirement of AGN driven winds that are generated during high redshifts and resemble the bulk of the supermassive black hole mass assembly that results from a collapse of mass that leads to a momentum-driven outflow (see Silk & Rees 1998; King 2003; Fabian 2012).

AGN and their Environment

Not all galaxies host an AGN, which therefore leads to the implications that AGN are not constants throughout a galaxy's lifespan and either become quiescent as a result of the depletion of fuel or via the retardation of some sort of fuelling mechanism. The source of the fuel can come from the host galaxy through the perturbation of material during galaxy-galaxy mergers that will inflow into the black hole engine (Di Matteo et al., 2005).
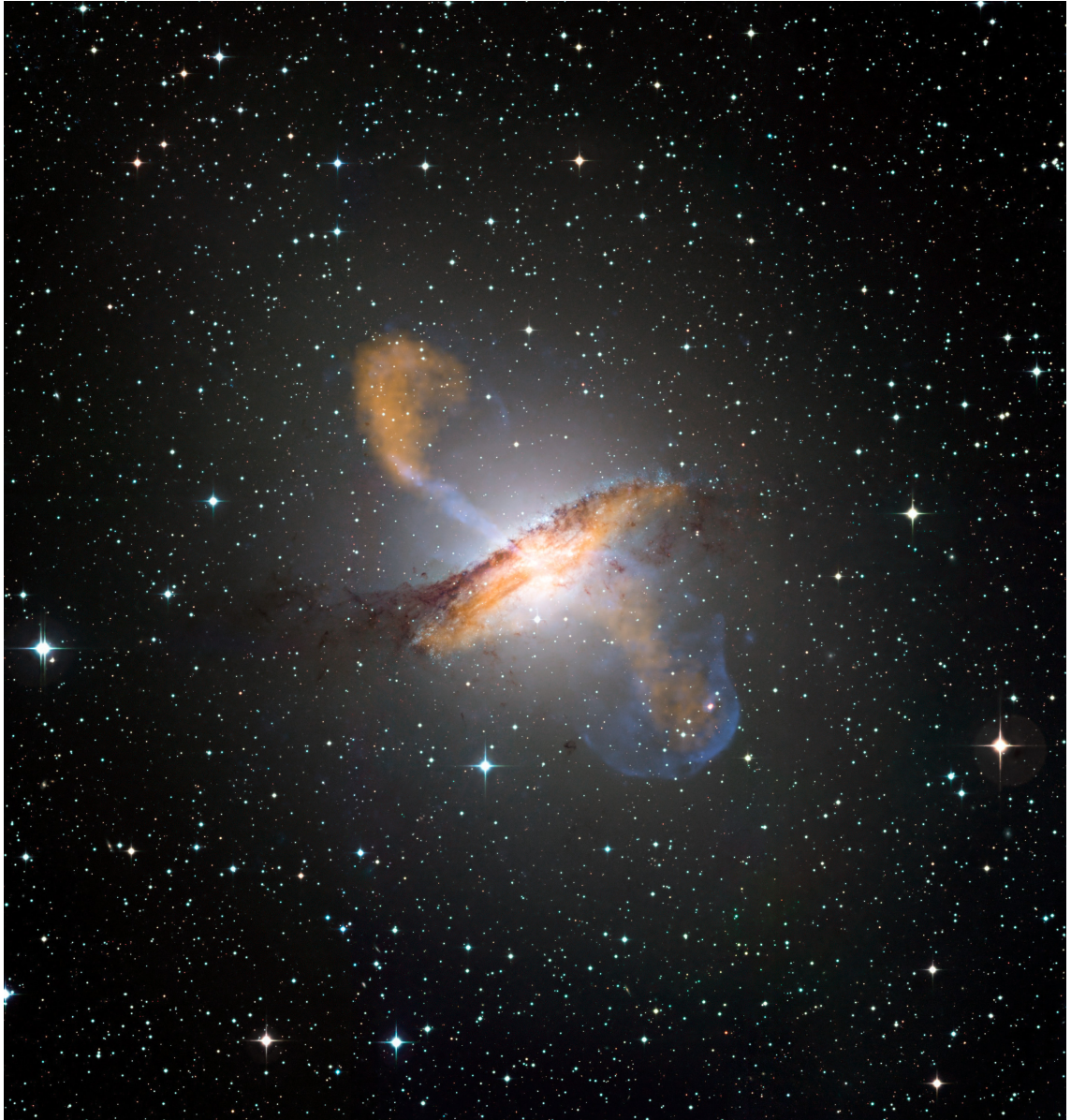
Figure 1.13: A composite image of Centaurus A highlighting the jets emanating from the AGN and interacting with its environment. The orange depicts the lobes with submillimetre data from the LABOCA instrument on APEX. The blue illustrates the shock fronts and jets with X-ray information from the Chandra X-ray Observatory. Visible light data from the Wide Field Imager (WFI) on the MPG/ESO 2.2 m telescope at La Silla, Chile, show the stars and the galaxy's characteristic dust lane. Image copyright ©ESO.
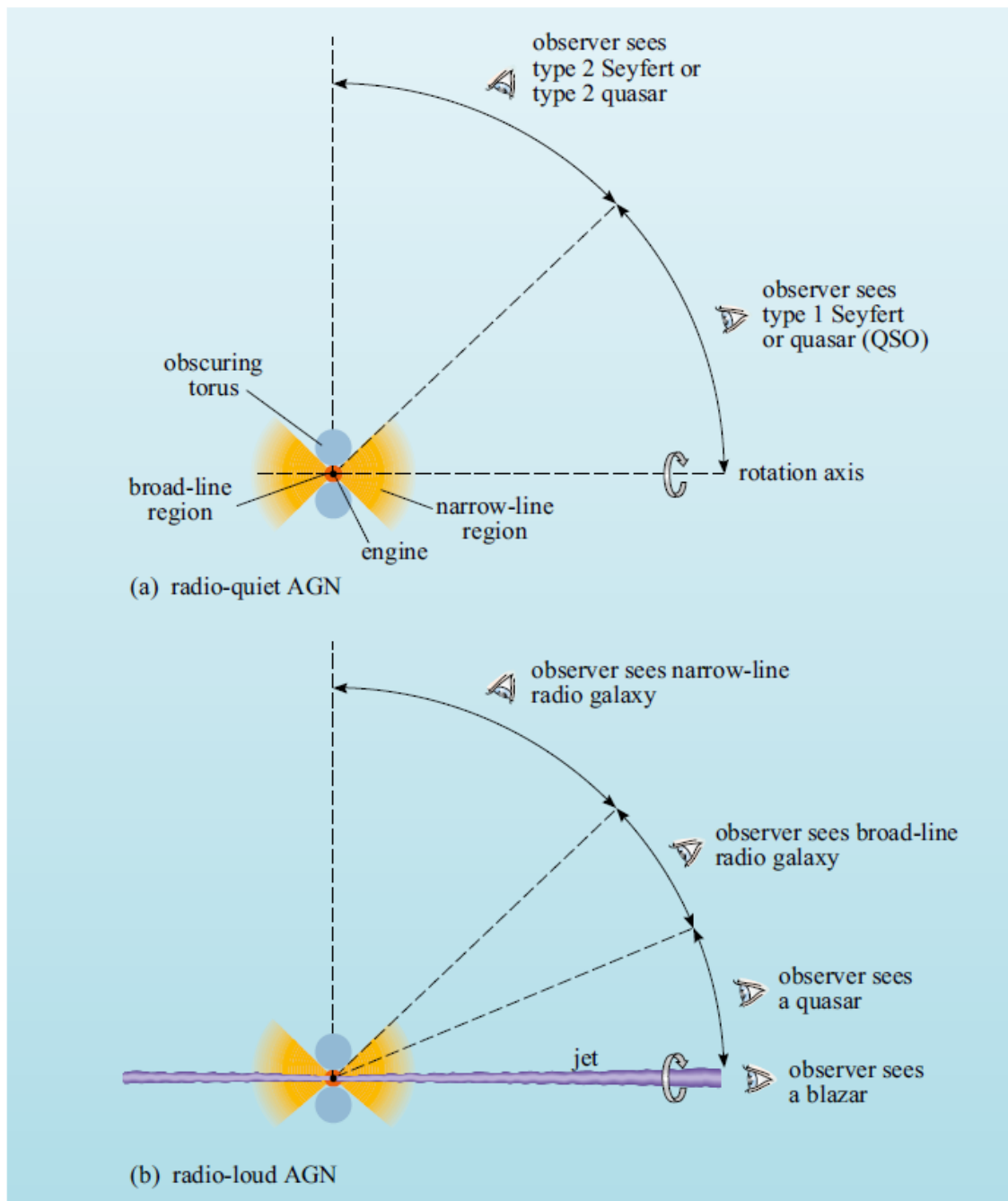
Figure 1.14: The AGN unification model between radio-loud and radio-quiescent galaxies. Within this model different classifications of AGN are dependent on the observer's line-of-sight; a dusty torus obscuring incident photons from an accretion disk will attenuate doppler broadened lines and vice versa. Obtained from Jones et al. (2015).
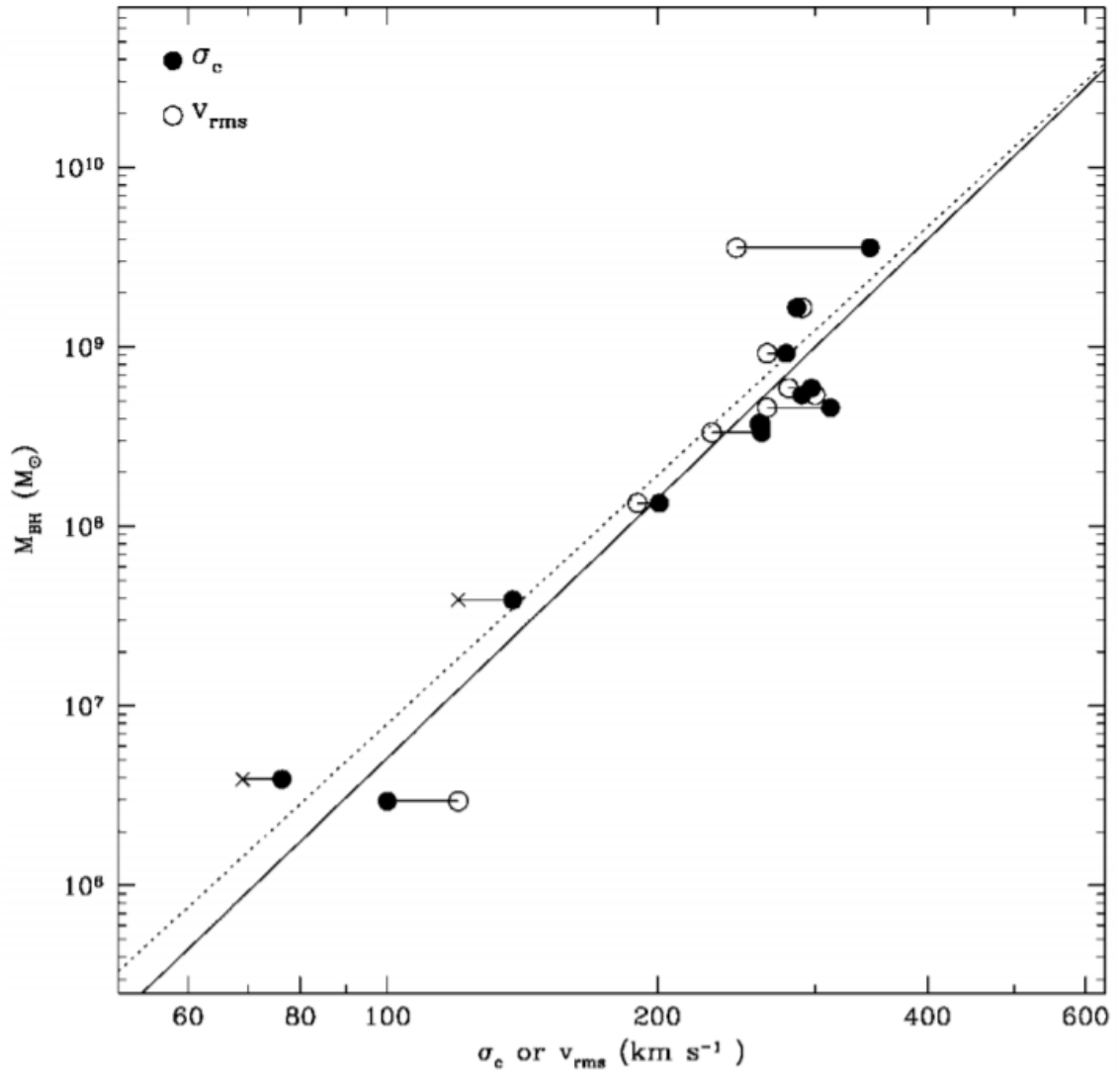
Figure 1.15: The masses of black holes are plotted against their host galaxy's intrinsic velocity dispersion σ_c (filled circles) or rms velocity v_{rms} (open circles) with any applicable lower limits ($\times$). It is remarkable how extremely tight this relationship between the black hole and stellar bulge is with a cursory glance. Considering that bulge velocities correlates strongly with the bulge mass, this implies there must be a feedback mechanism by which black hole and bulge masses grow together. Obtained from Ferrarese & Merritt (2000).

By extension, the harassment of a galaxy by a galaxy cluster and its consequential infall into it increases the probability of galaxy-galaxy tidal interactions that strip and distort material that could lend aid to the triggering of AGN (Moore et al., 1996, 1999). In fact, it is indeed established that AGN are more commonly found within these infall regions (Haines et al., 2012; Pimbblet et al., 2013), which are not limited to clusters, but are also prevalent in low mass groups (Gordon et al., 2018). As well as the increasing density of galaxies to interact with, there is the influence and interaction with the ICM to consider, especially with the potential for ram-pressure stripping as the ICM comes into contact with the infalling galaxy's cold gas, producing so-called 'jellyfish galaxies' (Gunn & Gott, 1972). It has been found that these ram-pressure stripped galaxies preferentially host an AGN (Poggianti et al., 2017). AGN outflows also contribute to the observed cavities present within cluster galaxies (see Figure 1.16). Radio jets from these AGN hosted by a massive central galaxy can interact with the hot diffuse ICM, pushing and heating the gas, generating a shock front that quenches the cooling flow of the ICM collapsing onto the central galaxy (McNamara et al., 2005).

1.4   Wide-Field Survey Astronomy and the Scope of this Work

1.4.1   A Historical Perspective on Wide-Field Survey Astronomy

Telescopic observations of the many objects in the night sky have deepened our understanding over time, and through greater resolving power, we have analysed their light through finer spectroscopic and photometric methods. In the early 20th century these studies were focused on gathering data from specific objects at a time, which was ideal for honing precision, however not ideal for gathering a representative sample of the objects populating the sky. This was in part due to the limitations of the optics available, whereby any larger aperture reflecting telescopes suffered with astigmatism and comas leading to unrefined and blurry extended objects.[3] Bernhard Schmidt resolved this during his development of what is now known as the *Schmidt Telescope*, resulting in an era of coma-free wide-field optics (Schmidt, 1938). Fritz Zwicky quickly saw an opportunity to influence decision makers at the Californian Institute of Technology to procure an 18" telescope

---

[3]Reflecting telescopes of the time, such as those hosted by the Lick Observatory, were therefore restricted to small apertures and narrower fields of view ($\sim 1 \text{deg}^2$). Considering the high number of sky pointings required it would take up to $\sim 10,000$ years to survey the available sky!
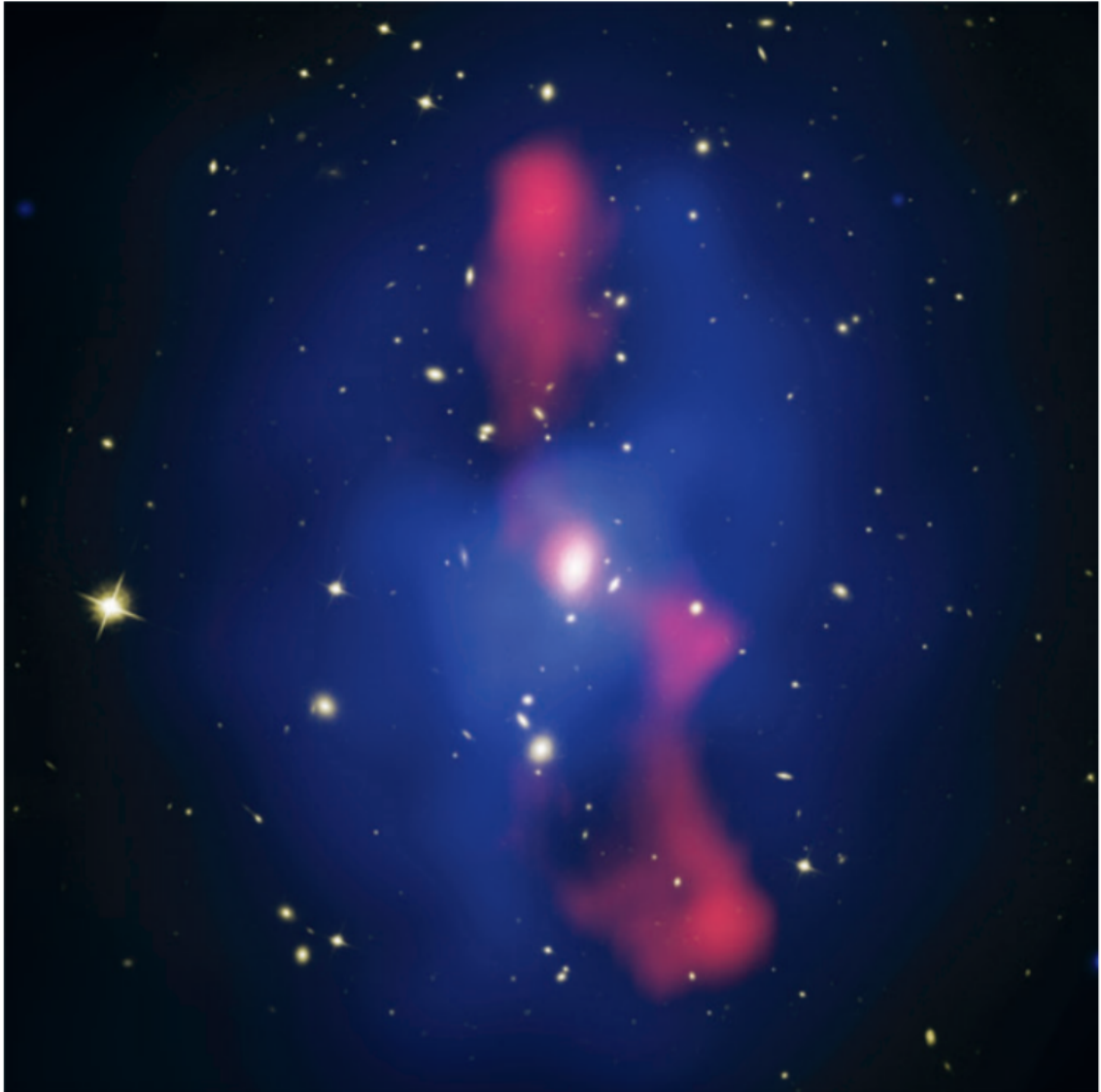
Figure 1.16: A composite image of the MS0735.6+7421 galaxy cluster. The optical field image of the cluster is taken from the Hubble Space Telescope, the blue regions are taken from the X-ray overlay from Chandra that represent the ICM halo and the red shows the radio jets from an AGN taken from the VLA at 330MHz. The AGN radio jets are observed here to be displacing the ICM mass and generating cavities in the ICM halo. Obtained from McNamara & Nulsen (2007)

with the new Schmidt (1938) design for their new observatory on Palomar Mountain to increase observational efficiency (Dyson, 2005). Zwicky, along with peer Walter Baade, was interested in using this new telescope in conducting an extensive search for Supernovae to utilise its wider-field of view and faster optics. The wider field of view enabled the ability to catalogue such transient objects through the fewer pointings required to survey the sky and fast optics that allow for reducing photography time, which resulted in the first catalogue of Supernovae (Baade & Zwicky, 1934).

The quality and depth of data acquired from this relatively small telescope was an impressive feat, which led to the building of the successor 48" Schmidt telescope with the first photographic plate exposure in 1949 (Nature, 1949). The astronomical community believed the best use of the 48" Schmidt was to perform an all-sky survey, the expense of which was alleviated in securing of additional funding leading to forming the *National Geographic Society – Palomar Observatory Sky Survey* programme (Abell, 1959). The programme surveyed 3/4 of the sky down to $\delta \sim -27°$ in 879 fields with each covering an area of 6.6 deg^2 to a brightness depth of 21 mag and garnered representative population samples of stars, galaxies large-scale structures of galaxies on blue and red sensitive photographic plates (Abell, 1958, 1959; Minkowski & Abell, 1963; Zwicky & Rudnicki, 1963). Survey astronomy has since become the standard means by which we sample extragalactic populations, with modern survey instrumentation employing multiple observational techniques with a variety of photometric filters and spectroscopic measurements of atomic lines from a multitude of wavelengths.

Spectroscopy in particular aided to build depth to the objects projected on our 2D plane of sky with a plethora of programmes such as the aforementioned CfA, 2dFGRS and SDSS surveys in subsection 1.2. As well as measuring the composition, star formation rates and masses of large samples of galaxies we can determine the redshifts of the galaxies in these surveys from the observed emission lines of known rest frame wavelength. The comparison between observed and rest frame wavelengths, using Hubble's Law, ultimately allows for the calculation of distances to galaxies. The 3D projection provided for large samples of galaxies with their ancillary data allows to visualise the structures these galaxies form, to learn the histories of the sub-populations of galaxies that reside within these structures and how they compare to those populations not virialised to any large-scale structure. Redshift surveys have provided astronomers with plentiful quantities of data and can provide a

continuous stream of new scientific analysis as more novel ways to use the data come to fruition. The data used within the body of this work is acquired from the observations made by SDSS, one of the most comprehensive photometric and spectroscopic surveys of the northern hemisphere, in which its specifications, advantages and disadvantages are listed below.

1.4.2 The Sloan Digital Sky Survey

The SDSS (see Figure 1.17) consists of a 2.5 m primary mirror positioned at Apache Point Observatory, New Mexico in the USA and is the largest and most comprehensive astronomical survey to have been undertaken thus far with a variety of projects and upgrades added to the original scope of the programme (e.g. Gunn et al. 2006; Yanny et al. 2009; Dawson et al. 2013; Majewski et al. 2017). The main run of these survey programmes involved the imaging of $\sim 35\%$ of the sky with a coverage of $\sim 14,500 \ \text{deg}^2$, obtaining photometric data between 1998-2011 with 'Data Release 8' being the last containing new imaging photometric data (Aihara et al., 2011). The photometry of SDSS ranges from blue to red across 5 different passband filters *u, g, r, i* and *z* with median wavelengths of 3551, 4686, 6166, 7480 and 8932 Å respectively down to $r \lesssim 22.2$ mag. The original legacy spectrographic instrument installed in SDSS for phases I-II could simultaneously record 640 spectra within its field via the use of optical fibres positioned and 'plugged' into drilled aluminium plates that matched the targets on the sky (Newman et al., 2004). The spectroscopic data covers $\sim 9,400 \ \text{deg}^2$ of sky to a shallower *r*-band depth at $r \lesssim 17.7$ mag (Strauss et al., 2002), however, it did provide the community with 1.6 million spectra of which $\sim \times 10^6$ galaxies benefited (Abazajian et al., 2009).

1.4.3 The Scope of this Thesis

The main scientific body of work begins with Chapter 2, whereby the kinematics of sub-populations of cluster galaxies are compared between clusters with substructuring and those without as delineated by Dressler & Shectman (1988). Here the test is to see how the varying cluster galaxy sub-populations respond to their environment in each of these different cluster states. While velocity dispersion measurements of clusters is fairly common place (e.g. Danese et al. 1980; Zabludoff et al. 1990; Beers et al. 1990; Pimbblet et al. 2006), their usefulness is restricted to cluster core radii since they are not sensitive
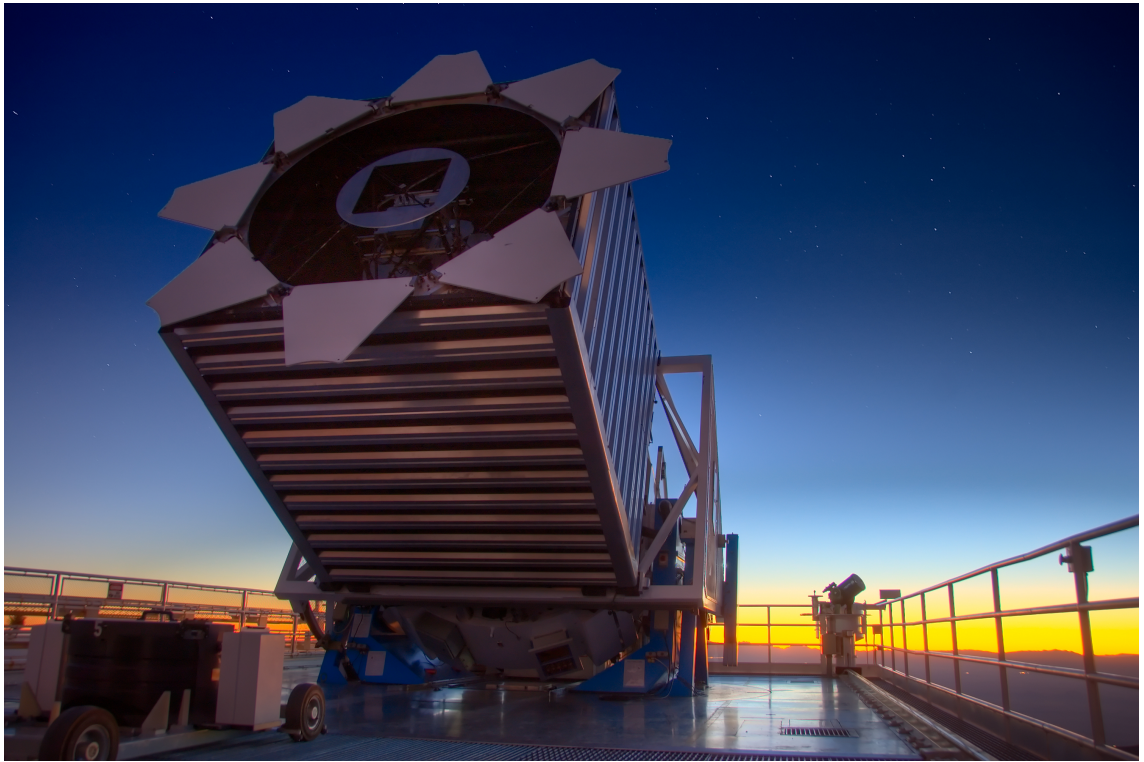
Figure 1.17: The Sloan Digital Sky Survey 2.5m telescope at Apache Point Observatory in New Mexico USA. Image copyright ©SDSS.

to any potential kinematic response with discrete, incremental bins of radius. Utilising the velocity dispersion profiles methodology initially devised by Bergond et al. (2006) the velocity dispersion is determined at incremental bins of radius and weighted across all radii (see Hou et al. 2009, 2012). Taking advantage of the photometric and spectroscopic data of SDSS, two cluster samples of substructured and non-substructured cluster galaxies were stacked and the velocity dispersion profiles for cluster galaxies of distinct galaxy property values of mass, colour and morphology were computed. Chapter 2 therefore uses this particular method to uniquely determine how differing populations of cluster galaxies in different cluster epochs respond to their environment. The work presented in Chapter 2 is published under Bilton & Pimbblet (2018).

Chapter 3 continues the theme by testing the dynamic response of cluster sub-populations to their environment between clusters with substructure and those without. The aim is to discover the how the angular momenta of different cluster sub-populations differ between different cluster epochs in their merger histories as a function of radius. The main workhorse in this Chapter is the application of the Manolopoulou & Plionis (2017) method to calculate rotational velocities and infer the presence of rotation of a cluster via

the radial velocities of the cluster galaxies. By continuing to exploit the public data suite offered by SDSS, and additionally, the NASA extragalactic database three cluster samples were procured; substructured and non-substructured cluster samples were stacked similarly to Chapter 2 with SDSS data and a sample of clusters hosting a dumbbell core were also stacked. The body of work in Chapter 3 therefore implements a unique procedure of using cluster galaxies as a proxy for the production rotational profiles of cluster galaxies at alternate merger states as a function of their environment. The scientific output of Chapter 3 is published under Bilton et al. (2019).

In Chapter 4, the final science Chapter of this thesis, the strength and fraction of AGN are tested against their kinematic response to the environment. Considering how merging environments ostensibly demonstrate an increase in AGN fraction and general activity along with the of ram-pressure feeding of supermassive black holes (e.g. von der Linden et al. 2010; Poggianti et al. 2017; Kim et al. 2020) with the aim to observe the kinematic consequences of AGN hosting cluster galaxies at differing cluster epochs as a function of their environment. The science within Chapter 4 involves the now uniquely ubiquitous administration of the velocity dispersion profiles procedure to observe this kinematic response. The public SDSS spectrograph data are employed and AGN hosting galaxies from our existing cluster samples defined within Chapters 2 and 3 are obtained by using the WHAN diagram definitions (Cid Fernandes et al., 2010, 2011). The current presentation of the work in Chapter 4 is currently under peer-review after being submitted to the Monthly Notices of the Royal Astronomical Society.

Chapter 5 of this thesis summarises the key outcomes of the work conducted across the three science Chapters as well as outlining the prospects for future work with advancing technologies in wide-field surveys. For example, the possibility to continue the work carried out here with an enhanced sampling of galaxies that would allow for an improved SNR and for more clusters to be selected is possible with the upcoming Vera Rubin Observatory[4] (formally the Large Synoptic Survey Telescope).

---

[4]http://www.lsst.org

2. Cluster Galaxy Kinematics via VDPs

"The only way to make frequentist methods comprehensible is to lie about them,

and the only way to be fully accurate is to make them incomprehensible."

– Unknown

2.1 Prologue

The Chapter presented here is the published work entitled "*The kinematics of galaxies via velocity dispersion profiles*", under MNRAS **481**, 1507 (Bilton & Pimbblet, 2018). This article was written and led by myself and co-authored with Kevin Pimbblet. As lead author of this article and the research contained within, I was the principal contributor to this work in terms of research and writing of the article, with my co-author assisting through their supervisory role and seeding the idea that drove the science questions that were intended to be answered within this very Chapter. The article has been slightly altered to fit the format of a thesis, therefore to this end, the abstract has been omitted to avoid repetition of the whole thesis.

2.2 Introduction

Galaxies are known to follow a morphology-density relation, which is pronounced in clusters of galaxies (Oemler 1974; Dressler 1980; Smith et al. 2005b). Late-type galaxies are found to dominate at large radii from a galaxy cluster centre, predominantly within the field population. Conversely, early-type galaxies are found to pervade the denser regions at smaller radii, well within galaxy clusters. There are further observable environmental side-effects that follow similar patterns, such as the apparent bimodality of the colour-density relation (Hogg et al., 2003, 2004), where denser regions are populated with quenched, red and elliptical galaxies. Contrarily star-forming, blue and spiral morphologies are found out towards the field population (e.g. Lewis et al. 2002; Gómez et al. 2003; Bamford et al. 2009).

Galaxy clusters are consequently an epicentre for environmental interactions. The comparative accretion histories of cluster galaxies between galaxy clusters and the field population can be determined as a function of their environment, indicated by their membership's morphology, colour and star-formation assuming a fixed stellar mass (e.g. Postman & Geller 1984; Hogg et al. 2004; von der Linden et al. 2010). The evolutionary transformation of cluster galaxies could have transpired prior to a galaxy's accretion onto a cluster's potential, since the field population's morphologies, colours and rate of star-formation are mixed (e.g. Kauffmann et al. 2004; Blanton et al. 2005). Or, it is possible that the harassment and accretion of a galaxy by a cluster leads onto a transformation of blue to red; star-forming to non-star-forming; spiral to elliptical (Moore et al., 1996). This metamorphosis during the infall of a galaxy into a cluster is considered to be the result of an increased probability of tidal galaxy-galaxy interaction mechanisms, or, even the tidal field of the cluster itself. The former being more likely to give rise to the stripping of material, and distortion of a galaxy's structure (Moore et al., 1999). Further observations ostensibly show the shifting of morphologies from late-type to early-type are chiefly to be the result of mergers between two galaxies (e.g. Owers et al. 2012).

The volume between cluster galaxies contains a sea of hot diffuse gas that represents an intracluster medium (ICM), another form of environmental interaction. An infalling galaxy approaching a cluster centre at higher velocities relative to the ICM will experience ram pressure stripping (Gunn & Gott 1972; Abadi et al. 1999; Quilis et al. 2000; Sheen et al. 2017). The disc of cold gas surrounding an infalling galaxy will be stripped away over small timescales, however, as the ICM density increases during infall so do the time scales of this process (Roediger & Brüggen, 2007). The result of this process retards rates of star-formation to where the infalling galaxy will be quenched completely. The diffuse nature of any hot gas haloes surrounding infalling galaxies lends to their increased likelihood of being ejected from the galaxy's potential. Therefore, the removal of any surrounding haloes of hot gas around an infalling galaxy will inhibit the replenishment of their cold gas reservoirs through radiative cooling, slowly strangling galaxy star-formation, with any remaining cold gas being exhausted (Larson et al., 1980). Ram pressure stripping has been found to be prevalent in the dense cores of clusters through observations of tails with H I and Hα emission lines that are associated with a parent galaxy (e.g. Gavazzi et al. 2001; Cortese et al. 2007).

With galaxy cluster environments hosting extended ICM haloes that interact significantly with field and infalling galaxies, consideration of a cluster's size is therefore needed in order to understand where the boundary between these environments lie. One common definition of a cluster's size is the virial radius, commonly approximated as $R_{vir} \sim r_{200}$. r_{200} represents the radial point at which the average density is ~ 200 times the critical density (e.g. von der Linden et al. 2010; Pimbblet & Jensen 2012; Bahé et al. 2013; Pimbblet et al. 2014). However, the proposed splashback radius may represent a more physical boundary, extending farther than r_{200} (e.g. More et al. 2015; More et al. 2016; Baxter et al. 2017). The splashback radius represents the first apoapsis of an observed accreted galaxy that has already passed through its first periapsis or turnaround (Sanchis et al. 2004; Pimbblet et al. 2006). Despite both of these definitions for a potential cluster boundary, they do not extend to the radii observed with harassed galaxies infalling to the cluster centre; colour-densities and effects on star-formation can continue beyond these defined boundaries (e.g. Balogh et al. 1999; Haines et al. 2009; von der Linden et al. 2010; Haines et al. 2015). A plethora of observations and simulations appear to indicate that there is a natural fluidity between the local cluster environment and the field population of late-type star-forming galaxies. Such simulations have shown the entire cluster boundary to expand even grander scales with ICM haloes extending out to radii of ~ 10 Mpc from the cluster centre (Frenk et al., 1999).

The existence of these large-scale structures therefore indicates the presence of smaller scale clumping of galaxies; more layers of substructure within galaxy clusters are expected (Dressler & Shectman 1988). It is more likely that any accreted galaxies from the field population will undergo 'pre-processing' into smaller galaxy groups that help form the substructure within a cluster (e.g. Berrier et al. 2009; Bahé et al. 2013), inducing evolutionary changes prior to traditional cluster galaxy infall and accretion. In the simulation work of Haines et al. (2015) it is found that star-forming galaxies are unexpectedly quenched at large radii from the cluster centre, models can only account for this if the galaxies have undergone pre-processing into a substructure prior to any further interaction. There is an alternative variant of pre-processing in rarer cluster-cluster merger events, the most famous example of such an event is the Bullet Cluster (Tucker et al., 1998). X-ray observations of the Bullet Cluster show a smaller sub-cluster of galaxies colliding with a larger cluster, thereby ram-pressure stripping causing the removal of the surrounding

hot gas (Markevitch et al., 2002). Other 'bullet-like' events are shown to effect the local galactic environment in equivalent ways (e.g. Owers et al. 2011; Owers et al. 2012).

This leads on to potential ways to make a comparison between these different environments via their varying dynamical states. We can therefore probe the variation in cluster environments via analysis of the cluster kinematics as a function of radius with Velocity Dispersion Profiles. VDPs represent how the radial velocity dispersions vary from the dense area of accreted early-type galaxies within r_{200}, out to sparser star-forming late-types on their infall journey to the centre (see Hou et al. 2009, 2012). It is therefore possible to test how the shape of a VDP is affected by binning a profile based on different cluster galaxy properties. As an example, Pimbblet & Jensen (2012) splits the VDP of Abell 1691 into individual high and low mass profiles. It is found that there is a large disparity in the velocities between the high and low mass samples, Pimbblet & Jensen (2012) argues the large high mass sample velocities could be due to the presence of substructure, or recent arrivals to the system. The shape of the VDP could, however, be affected by any evolutionary change due to the cluster environment.

In this work, we aim to test how the average cluster VDP's shape can be altered as a function of radius, parameterised by its member's different evolutionary stages through proxies of varying masses, colours and morphologies, in order to explore the varying dynamics between merging, dynamically active and non-merging, relaxed environments. We therefore present galaxy data taken from the Sloan Digital Sky Survey (SDSS) to form a membership from a defined cluster sample determined from an X-ray catalogue. Details on how the data was acquired can be found in section 2.3. Details on the derivation and production of the VDPs can be found in section 2.4. A discussion of the data, results and their consequences are outlined in section 2.5, followed by a summary of our conclusions in section 2.6.

Throughout the work presented here we assume a ΛCDM model of cosmology with $\Omega_{\mathrm{M}} = 0.3$, $\Omega_{\Lambda} = 0.7$, $H_0 = 100h$ km s^{-1} Mpc^{-1}, where $h = 0.7$.

2.3   The Data

We define a sample of galaxy clusters using the X-Ray Galaxy Clusters Database (BAX, Sadat et al. 2004), a comprehensive catalogue of X-ray emitting clusters from multiple

literary sources in the 0.1-2.4 keV band. For each galaxy cluster we obtain members from SDSS Data Release 8 (DR8, Aihara et al. 2011) with complementary data from MPA-JHU Value Added Catalogue (Kauffmann et al. 2003; Brinchmann et al. 2004; Tremonti et al. 2004). We use data from Galaxy Zoo 2 (GZ2, Willett et al. 2013; Hart et al. 2016) to provide morphological information on member galaxies.

2.3.1   Defining the Cluster Sample and their Membership

To select our cluster sample, we adopt an X-ray luminosity range of $3 < L_X < 30 \times 10^{44}$ ergs s^{-1}. These limits ensure we are selecting the most massive clusters from the BAX catalogue across a range of dynamically relaxed and perturbed states. Although, it is worth noting that the most diffuse of ICM will possess a low surface brightness at x-ray wavelengths, thus galaxy clusters healthy with galaxies may be alienated from the selection if they do not happen to fall within our defined range of luminosities. We impose a redshift range of $0.0 < z < 0.1$, which serves to help make the final sample of galaxies making each cluster complete. The imposed limits with BAX output a base sample size of 68 clusters.

For each of the clusters in the sample a 10 Mpc h^{-1} upper radial limit of DR8 galaxies is applied from the BAX-defined centres to the appropriate scales, using the flat cosmology prescribed in section 2.2 (Wright, 2006). However, there is a caveat to using the BAX-defined centres in that the x-ray centres–from which they are derived–can be dissociated from the true centres if they are in a heavily disturbed system, which leads to an offset that can lead to not capturing true galaxy cluster members. Each candidate cluster have their global means ($\overline{cz}_{glob}$) and velocity dispersions (σ_{glob}) calculated for galaxies ≤ 1.5 Mpc h^{-1}, the latter are determined by the square root of the biweight midvariance (see Beers et al. 1990). Due to a willingness to observe the effect infall galaxies have on velocity dispersion profiles beyond r_{200}, a constant line boundary applied in velocity space is not ideal to distinguish an infaller from the field, since a cluster's potential varies with increasing R from the centre. Using the mass estimation method of caustics (Diaferio & Geller 1997; Diaferio 1999), we produce surface caustics with velocity limits of $\Delta V = \pm$ 1500 kms^{-1} and a radial limit of $R \leq 10$ Mpc h^{-1}, where $\Delta V = c[(z_{gal} - z_{clu})/(1 + z_{clu})]$. The surface caustics help determine the final membership that considers the varying potential as a function of R (Gifford & Miller 2013; Gifford et al. 2013). The resultant

caustic mass profiles allow for an estimation of r_{200} with the application of a varying enclosed density profile, $\rho(r) = 3M(r)/4\pi r^3$, until $\rho(r) = 200\rho_c$, where ρ_c is the critical density of the universe for our flat cosmology. An example of these surface caustics are shown in Figure 2.1 and are discussed in Section 2.5.2.

The final values for σ_{glob}, $\sigma_{r_{200}}$ for galaxies $\leq r_{200}$ and $\overline{cz}_{glob}$ are determined. The uncertainties for these parameters are calculated following the methodology of Danese et al. (1980). In order to maximise the number of DR8 galaxies per cluster while maintaining a mass-complete sample across our redshift range, we impose a stellar mass limit of $\log_{10}(M_*/M_\odot) \geq 10.1$. Candidate clusters are then cross-checked with the Einasto et al. (2001) catalogue of superclusters to help eliminate those structures that overlap with one another. A final check we employ before a cluster is added to the final master sample is to test if the cluster is sufficiently rich in its membership of cluster galaxies. We define the richness limit here as clusters with >50 galaxies at $\leq r_{200}$, any clusters not meeting this requirement are ignored. This leads to a resultant sample size of 14 galaxy clusters.

2.3.2   Merging Cluster Sample

For the thesis of this work, we create subset samples of merging and non-merging galaxy cluster systems in order to compare how their respective environments affect the kinematics of their members. To determine whether or not a cluster is merging we employ the Δ test of substructure devised by Dressler & Shectman (1988) on galaxies ≤ 1.5 Mpc h^{-1} from the BAX defined cluster centre. The Δ test methodology takes the local mean radial velocity ($\overline{cz}_{local}$) and local standard deviation of the radial velocity (σ_{local}) of a galaxy and its $N_{nn} = \sqrt{N_{glob}}$ nearest neighbours, where N_{glob} is the number of galaxies < 1.5 Mpc h^{-1}. These are then compared to the global values of the cluster they are the members of, as shown in equation 2.1.

$$\delta_i^2 = \left(\frac{N_{nn}+1}{\sigma_{glob}^2}\right)[(\overline{cz}_{local} - \overline{cz}_{glob})^2 + (\sigma_{local} - \sigma_{glob})^2], \tag{2.1}$$

where δ measures the deviation in the small region around the galaxy compared to the global cluster values at ≤ 1.5 Mpc h^{-1}. This process is iterated through each galaxy to produce the sum $\Delta = \sum_i \delta_i$. Pinkney et al. (1996) has shown the Δ test to be the most sensitive for indicating the presence of substructure, demonstrating a $\geq 99\%$ significance
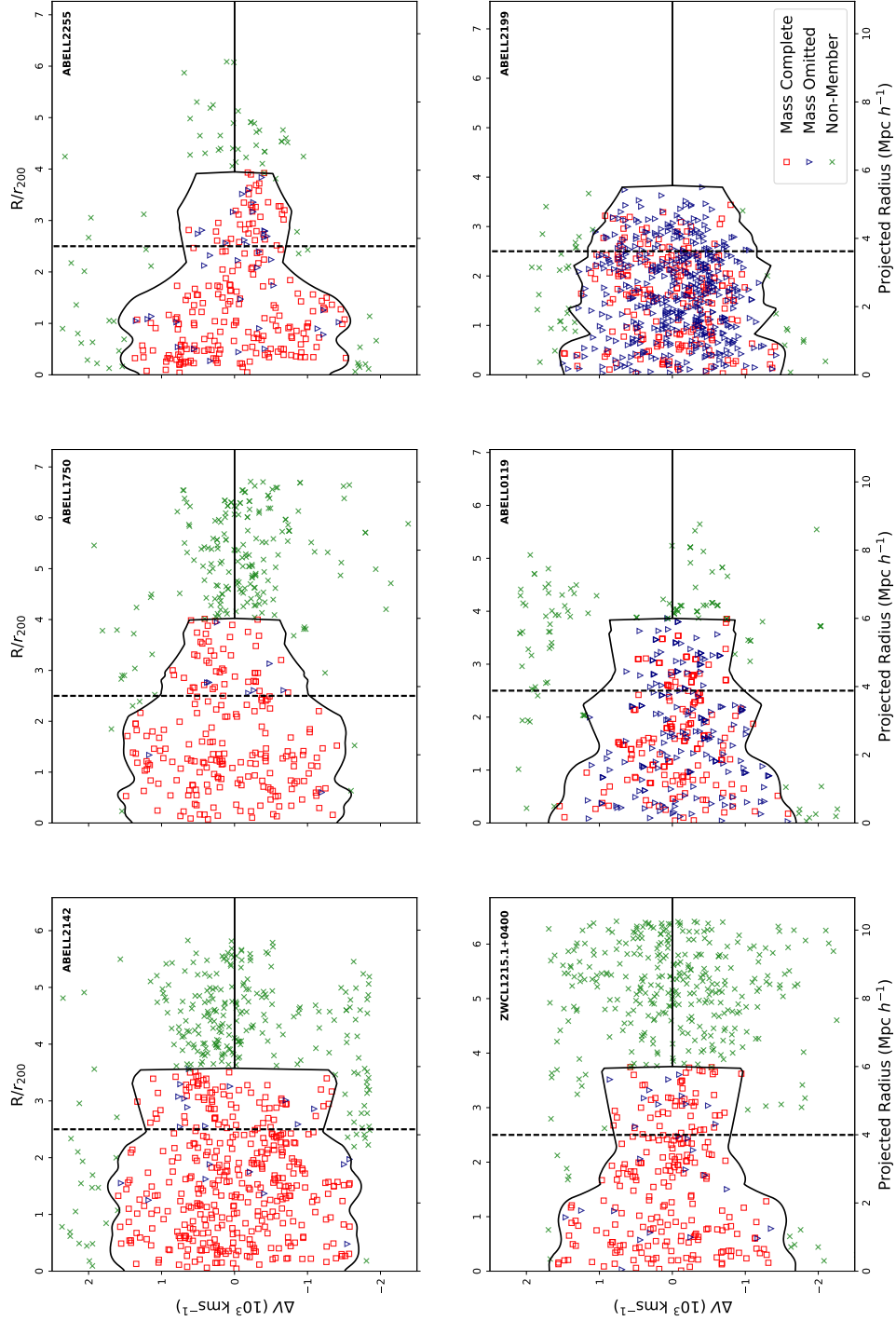
Figure 2.1: A selection of example surface caustics (the black curves) from the final merging cluster sample (top row) and non-merging cluster sample (bottom row). Where the red squares represent the galaxies that make a complete sample at $\log_{10}(M_*/M_\odot) \geq 10.1$, with the blue triangles representing omitted galaxies that are at $\log_{10}(M_*/M_\odot) < 10.1$. Galaxies that lie within the surface caustics are considered to be cluster members. Here the radial velocity (ΔV) with respect to the cluster's mean recession velocity is plotted against the projected radius in units of Mpc h^{-1} and R/r_{200}. The black dashed vertical lines represent the 2.5 R/r_{200} radial cut of each cluster. Only galaxies of ≤ 2.5 R/r_{200} within the caustics are used in the production of the stacked VDPs.
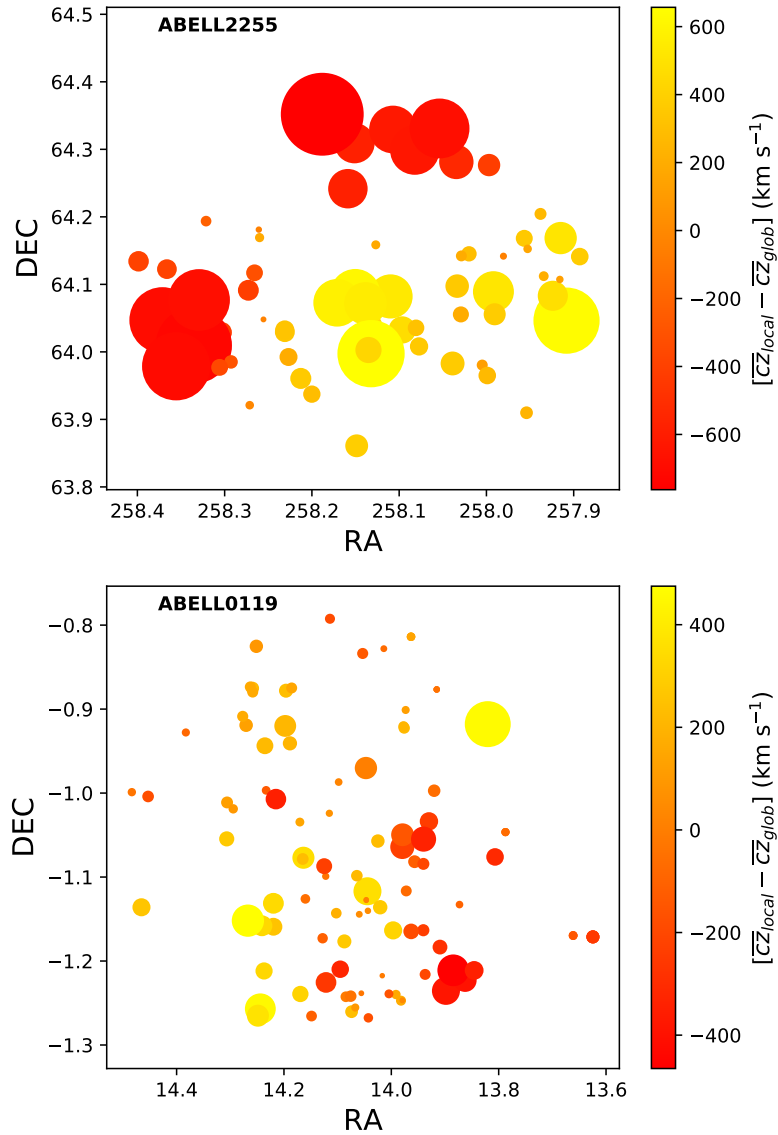
Figure 2.2: Example bubble plots from the Δ test, where the total area of each circle is proportional to the deviation e^{δ_i}, and the colours representing varying radial velocity differences $[\overline{cz}_{local} - \overline{cz}_{glob}]$. Cluster Abell 2255 (top) shows significant sub-clustering with a greater number of substantial deviations from the global values, as demonstrated by the overlapping larger area circles with large radial velocities. Cluster Abell 0119 (bottom) in comparison demonstrates weak sub-clustering, with fewer numbers of significantly strong deviations from the global values.

Table 2.1: The mass complete merging cluster subset sample. The J2000 coordinates and X-ray luminosity values are taken from BAX. $\sigma_{r_{200}}$ is determined from a biweight estimator, as noted by Beers et al. (1990). The uncertainties for the mean recession velocities and velocity dispersions are calculated following the method by Danese et al. (1980). The σ_{ref} values are reference velocity dispersions from the literature. The $P(\Delta)$ values testing for substructure follow the methods of Dressler & Shectman (1988) with equation 2.1, those values that are $\ll 0.01$ strongly reject the null hypothesis and have values smaller than to three decimal places.

Name	RA	Dec	L_x	$N_{r_{200}}$	$\overline{cz}_{glob}$	$\sigma_{r_{200}}$	σ_{ref}	$P(\Delta)$
	(J2000)	(J2000)	($\times 10^{44}$ erg s^{-1})		(km s^{-1})	(km s^{-1})	(km s^{-1})	
Abell 426	03 19 47.20	+41 30 47	15.34[a]	97	5155±59	827^{+40}_{-47}	1324[1]	0.010
Abell 1750	13 30 49.94	-01 52 22	5.98[b]	72	25614±92	782^{+56}_{-72}	657[2]	$\ll 0.01$
Abell 2142	15 58 20.00	+27 14 00	21.24[a]	132	26882±84	816^{+52}_{-63}	1193[8]	0.005
Abell 2255	17 12 31.05	+64 05 33	5.54[a]	72	24075±98	788^{+60}_{-79}	1009[4]	$\ll 0.01$

[1] Struble & Rood (1999)

[2] Einasto et al. (2012)

[8] Munari et al. (2014)

[4] Akamatsu et al. (2017)

[a] Reiprich & Böhringer (2002)

[b] Popesso et al. (2007)

in determining its occupancy. Therefore, a cluster will be classified as merging when substructure is detected at $P(\Delta) \leq 0.01$. All clusters that reject the null hypothesis are added to the subset merging cluster sample. We discuss some of the caveats of this approach in section 2.5.4. The resultant merging subset sample contains 4 galaxy clusters, detailed in Table 2.1, leaving the non-merging subset outweighing the mergers with 10 galaxy clusters, detailed in Table 2.2. Example bubble plots of a merging and non-merging cluster from both samples are shown in Figure 2.2, where the area of each circle is proportional to e^{δ_i}, indicating the level of sub-structuring through the magnitude of deviations from the global values.

Table 2.2: The mass complete non-merging cluster subset sample is presented here, noting the null hypothesis is accepted where $P(\Delta) \geq 0.01$. All values and uncertainties are obtained and determined as detailed in Table 2.1.

Name	RA	Dec	L_x	$N_{r_{200}}$	$\overline{cz}_{glob}$	$\sigma_{r_{200}}$	σ_{ref}	$P(\Delta)$
	(J2000)	(J2000)	($\times 10^{44}$ erg s^{-1})		(km s^{-1})	(km s^{-1})	(km s^{-1})	
Abell 85	00 41 37.81	-09 20 33	9.41[a]	70	16709±71	719^{+45}_{-55}	979[5]	0.853
Abell 119	00 56 21.37	-01 15 46	3.30[a]	59	13279±74	752^{+47}_{-59}	619[6]	0.579
Abell 1650	12 58 46.20	-01 45 11	6.99[a]	50	25087±98	671^{+58}_{-78}	498[2]	0.636
Abell 1656	12 59 48.73	+27 58 50	7.77[a]	145	6995±39	798^{+27}_{-29}	973[7]	0.087
Abell 1795	13 49 00.52	+26 35 06	10.26[a]	70	18754±87	794^{+56}_{-69}	662[2]	0.265
Abell 2029	15 10 58.70	+05 45 42	17.44[a]	127	23382±103	932^{+63}_{-79}	973[7]	0.415
Abell 2061	15 21 15.31	+30 39 16	4.85[d]	90	23311±69	719^{+43}_{-53}	898[3]	0.183
Abell 2065	15 22 42.60	+27 43 21	5.55[a]	93	21565±92	882^{+57}_{-72}	1286[3]	0.211
Abell 2199	16 28 38.50	+39 33 60	4.09[a]	67	9161±55	737^{+36}_{-42}	722[6]	0.586
ZWCL1215	12 17 41.44	+03 39 32	5.17[a]	97	23199±98	671^{+58}_{-78}	889[9]	0.873

[2] Einasto et al. (2012)

[3] Pearson et al. (2014)

[5] Agulli et al. (2016)

[6] Rines et al. (2003)

[7] Sohn et al. (2017)

[9] Zhang et al. (2011)

[a] Reiprich & Böhringer (2002)

[d] Marini et al. (2004)

2.4 Velocity Dispersion Profiles

The kinematics of each cluster within the sample are analysed from their respective velocity dispersion profiles, denoted as $\sigma_P(R)$. These VDPs can depict, with reasonable clarity, how dynamically complex or simple a cluster is. In this work we derive the VDPs computationally from the method prescribed by Bergond et al. (2006) for globular clusters. This has since been adapted to galaxy groups and clusters by Hou et al. (2009, 2012). The VDPs are produced from bins of the radial velocities through a Gaussian window function that is weighted exponentially as a function of radius across all radii. However, in line with Harris (private communication), we note here the presence of a typographical error in the original notation of this function by Bergond et al. (2006), in which the exponential component should be denoted to be negative rather than positive. This error appears to have been perpetuated into further works cited here (e.g. Hou et al. 2009; Hou et al. 2012; Pimbblet et al. 2014). We therefore present the corrected version of this window function in equation 2.2, which can be seen in the body of the work by Woodley et al. (2007) under equation 3. The correct window function is written as

$$\omega_i = \frac{1}{\sigma_R} \exp - \left[\frac{(R - R_i)^2}{2\sigma_R^2} \right], \tag{2.2}$$

where the kernel width σ_R determines the size of a window that the radial velocities are binned against with the square-difference in radius $(R - R_i)^2$. The window is chosen to be $0.2R_{max}$ in units of r_{200}. This is to avoid the window being too large, thereby smoothing out features in the profile, or too small where spurious shapes in the profile could be produced by outliers. The window function ω_i is then applied to the projected VDP, which is written as

$$\sigma_P(R) = \sqrt{\frac{\sum_i \omega_i(R)(x_i - \bar{x})^2}{\sum_i \omega_i(R)}}, \tag{2.3}$$

where x_i represents the radial velocity of each galaxy inputted taken as a difference from $\bar{x}$, which represents the mean recession velocity of the cluster. The uncertainties for $\sigma_P(R)$ are determined by reshuffling the velocities 1000 times per bin, calculating a monte-carlo version of $\sigma_P(R)$ for each reshuffle, before determining the standard deviation for each of these 1000 reshuffles.

The in-putted cluster data ideally should not have fewer than 20 galaxy members, this is to ensure the resultant projected VDPs are not specious (Hou et al., 2009). This can potentially pose problems for wanting to observe the dynamics of a cluster based on varying galactic parameters due to the inadvertent biasing to smaller bin sizes. Applying the cluster richness criterion of 50 galaxy members at $\leq r_{200}$ provides an adequate safeguard against this problem while determining cluster membership. An example of the full non-split VDPs from each sub-sample are presented in Figure 2.3. From this we can see the bins that reside within 1.5 Mpc h^{-1} marry closely with the results from the Δ test for substructure, however, this is not found to be consistent across the entire the sample of determined merging and non-merging systems. A problem which was noted by Pimbblet et al. (2014), and could reflect the homogenisation of certain clusters where the weighting of the Gaussian moving window function causes a rise in response to more significant groupings of galaxies at larger radii.
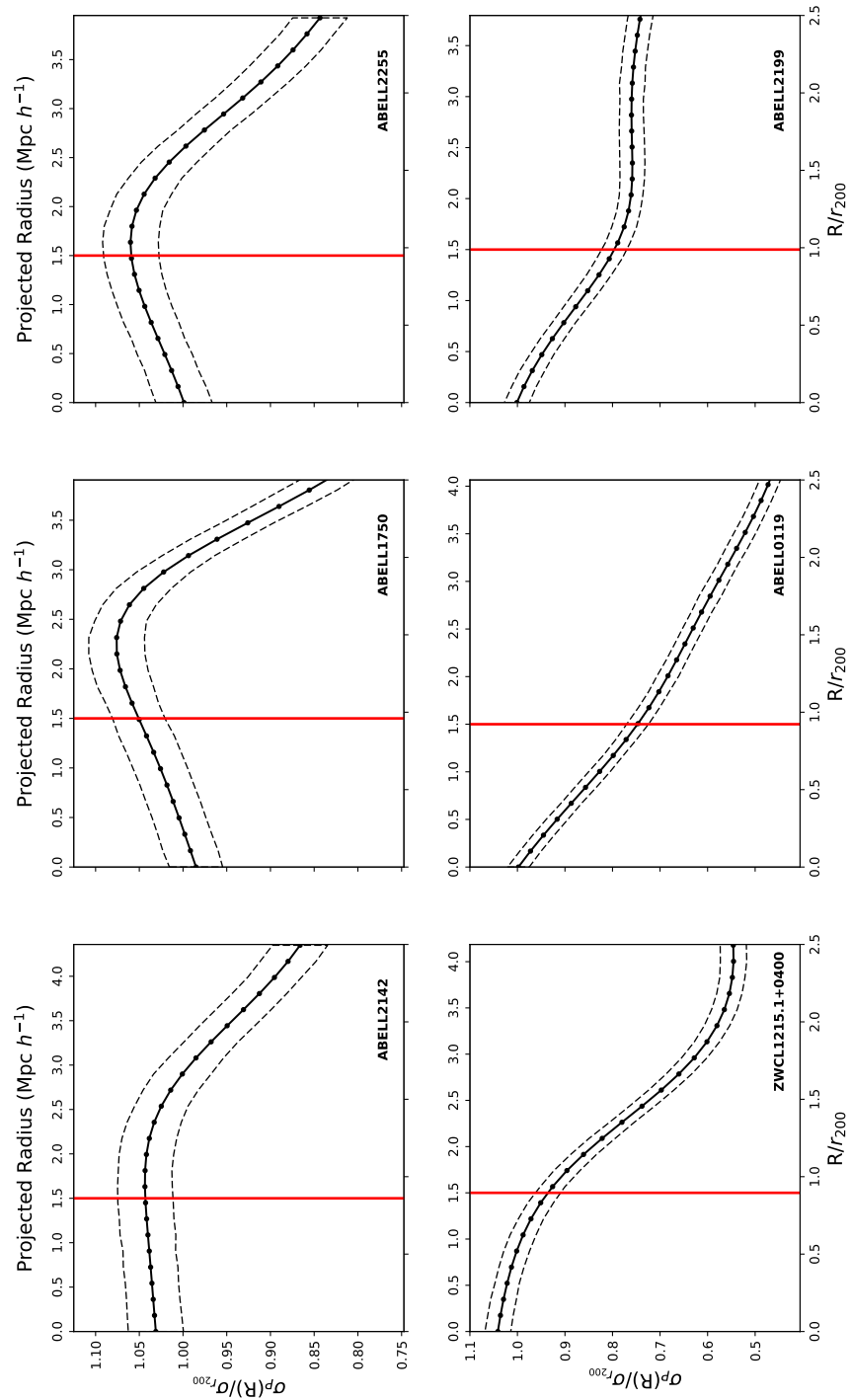
Figure 2.3: Example VDPs, consistent with those in Figure 2.1, from the merging (*top row*) and non-merging (*bottom row*) sub-samples plotted as a function of the projected virial radius r_{200} and normalised to their respective $\sigma_{r_{200}}$ values. The red vertical line indicates 1.5 Mpc h^{-1} from the cluster centre where the global values and Δ test for sub-structuring are calculated. The dashed lines represent the 1σ uncertainty of 1000 monte carlo resamples. Note the rising profiles within 1.5 Mpc h^{-1} in the merging clusters compared to the decreasing-to-flat profiles for the non-merging clusters within 1.5 Mpc h^{-1}.

In order to address the aims of this work we compare the cluster environments between merging and non-merging systems with the kinematics of their member cluster galaxies through varying limits of different intrinsic cluster galaxy parameters. We therefore compute a series of VDPs with equations 2.2 and 2.3 outlined in section 2.4 using the following methodology: Cluster galaxies are split between specific limits of varying galaxy properties of mass, morphology and colour. These splits are passed through each cluster from both samples, with each cluster galaxy co-added to a normalised fixed grid of line of sight velocity ΔV, and projected radius R between $0 - 2.5\ r_{200}$. Resulting in a stack for each of the merging and non-merging samples. Stacking for each sub-sample allows for a general picture of each environment to be built, to ascertain how the kinematics of differing sub-populations of galaxies within each environment are affected.

2.4.1 Mass

The MPA-JHU stellar mass estimates that are used in this work are predominantly produced from the methodology laid down by Salim et al. (2007). This follows a procedure of fitting template photometric spectral energy distributions (SEDs) of model galaxies to the SEDs of galaxies observed in the SDSS *ugriz* passbands. The template SEDs are produced from stellar population synthesis models through estimating the spectral energy output as a function of time and, in the case of MPA-JHU, is initialised with the Chabrier (2003) initial mass function. These models allow for the determination of the M/L ratios for each galaxy SED template, therefore, the determination of the MPA-JHU observed stellar masses used here can be ascertained through the model stellar luminosities of the template SEDs. The analysis of varying stellar mass limits allows for basic inference of how differing galaxy populations may vary depending on its environment at incremental radii from its centre (e.g. see Mitchell et al. 2013). Fixed limits are chosen for 3 profiles of different masses: $\log_{10}(M_*/M_\odot) \geq 10.8$, $10.5 \leq \log_{10}(M_*/M_\odot) < 10.8$ and $\log_{10}(M_*/M_\odot) < 10.5$. These limits are selected arbitrarily in order to maintain parity between the bin sizes of each range.

Figure 2.4 shows the resultant stacks of the merging, and non-merging, clusters split via different stellar masses present in the DR8 data. In the merging stack, there is a prominent illustration of a dynamic environment, especially between the $\log_{10}(M_*/M_\odot) < 10.5$ and $\log_{10}(M_*/M_\odot) \geq 10.8$ profiles. The $\log_{10}(M_*/M_\odot) \geq 10.8$ mass profile shows a steadily

increasing profile to having the highest dispersion of velocities at ~ $1.5r_{200}$, in tandem with the $\log_{10}(M_*/M_\odot) < 10.5$ profile. The former commonly denoted as members of an accreted older population of galaxies, with the latter commonly associated with an accreted younger population. The $\log_{10}(M_*/M_\odot) \geq 10.8$ profile represents an increasing intensity of interacting, or merging, galaxies at $\lesssim 1.5\ r_{200}$. The same can be determined with the $\log_{10}(M_*/M_\odot) < 10.5$ mass profile, which demonstrates a level of merging activity that is in tandem with the 'All Galaxies' profile peaking at ~ $1.5\ r_{200}$. These are clearly the two prominent sub-populations that drive the dynamic nature of the merging stack. The 'All Galaxies' profile shows a parity with the $\log_{10}(M_*/M_\odot) < 10.5$ profile throughout, suggesting the lower mass galaxies dominate the kinematics of the stack. At ~ $1.5\ r_{200}$ it appears there is a high level of mixed substructuring between the $\log_{10}(M_*/M_\odot) < 10.5$ and $\log_{10}(M_*/M_\odot) \geq 10.8$ populations. Where the 'All Galaxies' profile seems to indicate it is primarily composed of the two aforementioned sub-populations at larger radii. This is indicative of the occurrence of pre-processing by accretion of galaxies onto groups prior to cluster accretion. The intermediate profile of $10.5 \leq \log_{10}(M_*/M_\odot) < 10.8$ is the flattest, therefore, least dynamic of the populations within the stack.
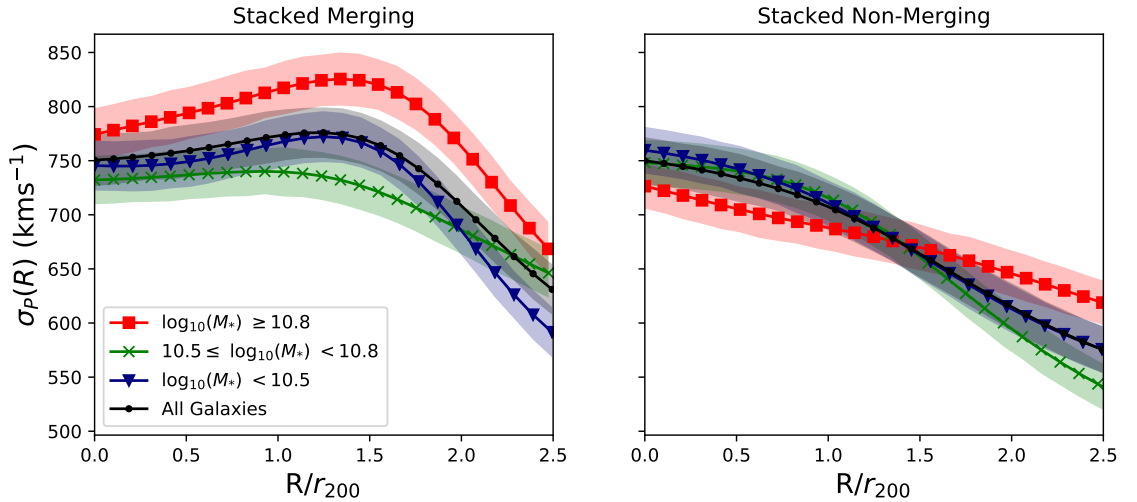
Figure 2.4: Co-added VDPs split by stellar mass for each cluster. Each profile represents a split by different intervals of $\log_{10}(M_*/M_\odot)$ as a function of radius (R/r_{200}), with the black profile representing all available galaxies within the sample. Shaded regions represent the 1σ uncertainty of 1000 monte carlo resamples.

The non-merging sample is comparatively dynamically relaxed with smaller dispersions and declining profiles that are not too dissimilar to the trend shown by Girardi et al. (1996). The $\log_{10}(M_*/M_\odot) < 10.5$ shows the closest parity with the 'All Galaxies' profile

stack, again, suggesting low mass galaxies dominate the kinematics. This profile possess the highest dispersion of velocities within r_{200}, indicative of a young infalling population of galaxies. Whereas the $\log_{10}(M_*/M_\odot) \geq 10.8$ profile has the lowest dispersion within r_{200}. This could be an indicator of an old population of galaxies slowly sloshing with the recently collapsed members onto cluster potentials. The $10.5 \leq \log_{10}(M_*/M_\odot) < 10.8$ profile blends in with the 'All Galaxies' and $\log_{10}(M_*) < 10.5$ profiles, suggesting there is little diversity between these populations of galaxies.

2.4.2   Colour

The cluster galaxies of each sample are passed through a colour limit gradient as a function of stellar mass. This is determined through the residuals of the bimodal distributions of colour in quartile increments of stellar mass (see Jin et al. 2014). This results in the following linear relation

$$(u - r)_{z=0} = 0.40[\log_{10}(M_*/M_\odot)] - 1.74, \tag{2.4}$$

which as a consequence allows for an adequate boundary between red and blue galaxies that accounts for the biasing of galaxy colour distributions between low and high stellar masses. The resultant boundary line and the galaxy distributions can be seen in Figure 2.5.

It should be noted that not all galaxies possess complete 'modelMag' DR8 photometry in all passbands due to insufficient signal, therefore, some clusters experience a slightly reduced bin size compared to the principle MPA-JHU derived parameters. The galaxy colours are k-corrected to $z = 0$ prior to computing the VDPs with the imposed variable limit (see Chilingarian et al. 2010; Chilingarian & Zolotukhin 2012). Figure 2.6 depicts the merging sample to have a consistently high dispersion profile for the blue cloud stack at $\leq 1.5\ r_{200}$, where the red sequence presents a shallow rising VDP with radius. However, there is a rising kinematic parity of the red sequence profile with the 'All Galaxies' profile throughout $\leq 1.5\ r_{200}$. This behaviour could be an indicator the population of blue, presumably star-forming, galaxies are kinematically active due to pre-processing of galaxies within the merging substructure with gradual infall onto the potential; Haines et al. (2015) highlights the need of pre-processing galaxies into groups to account for
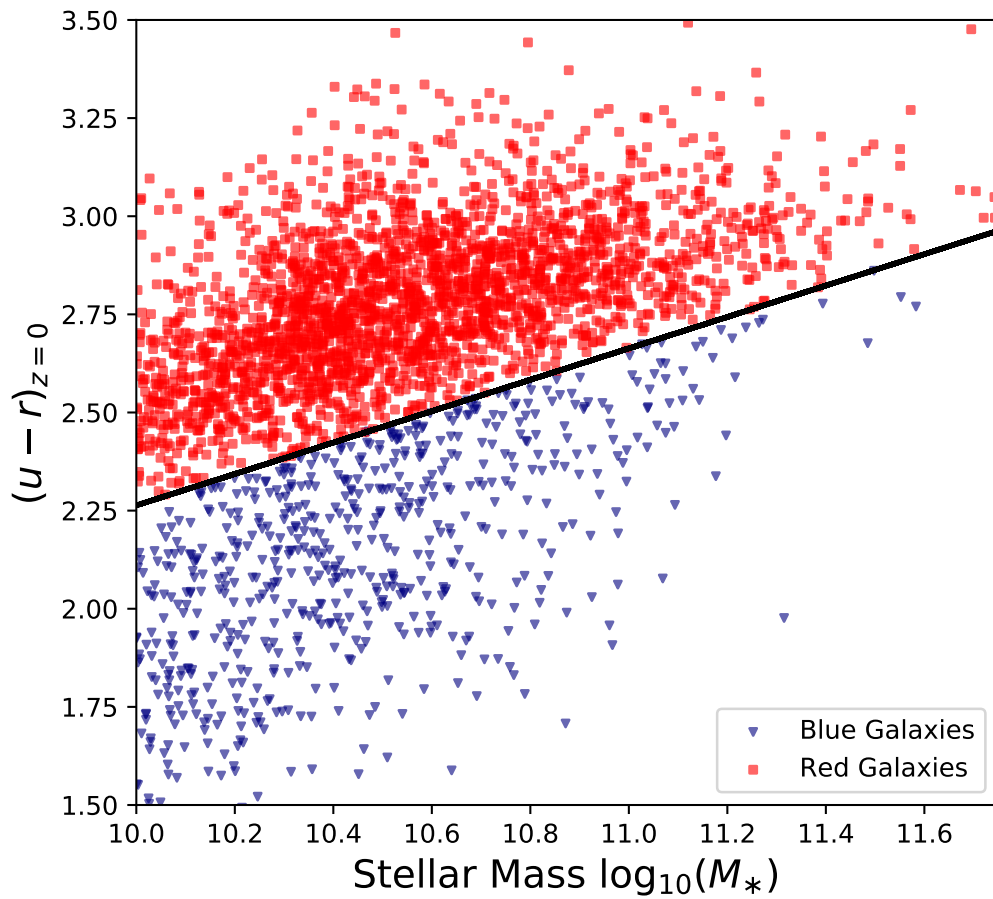
Figure 2.5: $(u - r)_{z=0}$ plotted as a function of $\log_{10}(M_*/M_\odot)$. The black line resembles the linear fit of the centre of the bimodal distribution at quartile increments of $\log_{10}(M_*/M_\odot)$; red galaxies are above the fitted line denoted as red squares; blue galaxies are below the fitted line denoted as blue triangles.

the level of quenching of star formation observed in cluster galaxies at large clustocentric radii. The rising profile of the red population with radius potentially demonstrates another environment of interacting galaxies, the profile leads to a rising VDP, indicating groupings of red galaxies at larger radii. These results evince a mixed population of merging blue galaxies alongside already pre-processed red galaxies in sub-groupings at larger radii from the cluster centre.
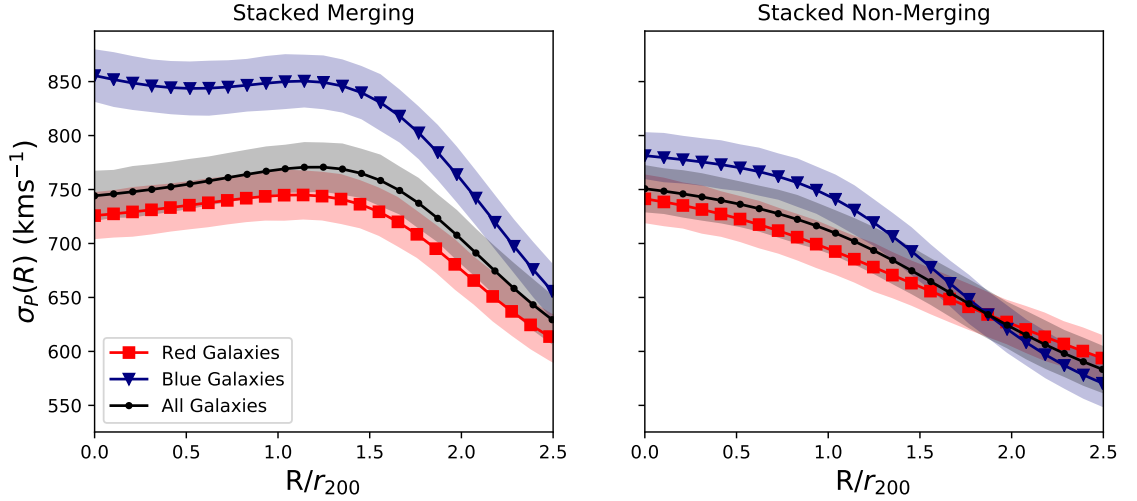
Figure 2.6: Stacked galaxy cluster VDPs split by their colour with the same axes as Figure 2.4. Where the blue triangle and red square profiles represent the blue cloud and red sequence respectively, with the black dot profiles representing all cluster galaxies available with colour data. Shaded regions represent the 1σ uncertainty of 1000 monte carlo resamples.

The non-merging sample shows less dynamical variation, where all of the profiles present a shallow-to-flat variance with R/r_{200}. The shallow rising of the blue galaxy profile at $\sim 1.5\ r_{200}$ could be an indicator of an infalling population of blue galaxies, that have not tidally interacted with other cluster members to the same degree as the merging counterpart. Comparatively, the red population profile presents gradual decrease from faster velocity dispersions at $\leq r_{200}$. There is the conspicuous observation of the merging red VDP in Figure 2.4 representing high mass galaxies in that it does not marry with what we would anticipate in comparison the merging red VDP in Figure 2.6 representing red galaxies. However, the mass limits in section 2.4.1 are independent of colour, therefore, there is a mix of red and blue galaxies in the high mass sample of galaxies. This is combined with a discrepancy in the sample sizes between a bi-modal colour split and that of stellar mass which can be seen in Figure 2.5, which is indicative that the red low-to-

intermediate mass galaxies contribute to lower velocity dispersions. This behaviour does match with what Girardi et al. (1996) believe to indicate a neighbouring system or grouping of galaxies at larger radii. The direct comparison between the merging and non-merging samples in Figure 2.6 demonstrates a more diverse variation of colour in dynamically relaxed clusters when compared to those that are dynamically complex, which has been discussed with recent observations made by Mulroy et al. (2017).

2.4.3   Morphology

The morphological classification of galaxies in clusters can be used as a proxy on how the local environment can lead to an alteration of their structure and shape. Therefore, utilising the debiased morphological classification data of GZ2, this is married with the data of both merging and non-merging samples split by the same colour limits noted in 2.4.2. The samples are separated between umbrella spiral and elliptical morphologies, which is determined using the string classifier of 'gz2_class' by whether or not a galaxy possessed any number of spiral arms in its structure. It should be noted, however, that the relatively small number of galaxies classified within GZ2 ($\sim 300,000$) means the average cluster membership can drop significantly. As a result the two clusters, Abell 0426 and Abell 0085, are not added to the stack for not meeting the richness criteria highlighted in section 2.3. This drop in membership could lead to the average profiles being spurious due to the lack of a more complete data set. For each morphology in each environment, the cluster galaxies are then split into the same colours via the same linear relation as noted in section 2.4.2.

Figure 2.7 presents the resultant morphology-colour split. The merging spiral stack shows a declining blue population profile, that then converges with the 'All Galaxies' profile. This coincides with a near flat profile of the spiral red population that starts to decline at $\sim r_{200}$. It is clear the merging spiral blue and red populations equally contribute to the total dispersion of merging spirals of the 'All Galaxies VDP. However, there is a discrepancy from the conspicuously high dispersion of blue spirial galaxies within r_{200}, suggesting there is an infalling, or recently accreted, high velocity population of blue spirals. The blue population profile of the merging ellipticals is fairly dynamic, leading to bulk rise at $\sim 1.5\, r_{200}$. This is indicative of a strongly interacting sub-population of cluster galaxies, potentially as the result of tidal-tidal interactions through substructuring. The red
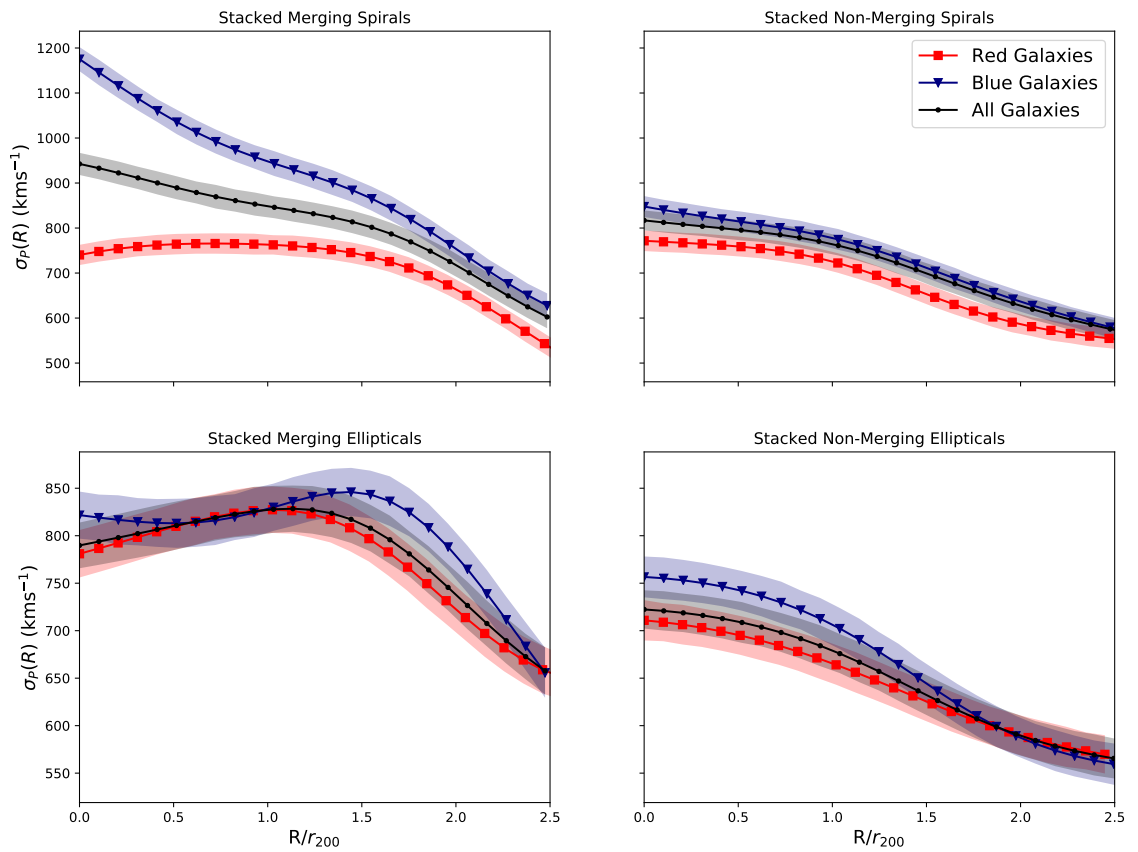
Figure 2.7: Co-added VDPs of spirals and ellipticals for each of the individual environments, which are then split by their bi-modal colours as per Figure 2.6. Shaded regions represent the 1σ uncertainty of 1000 monte carlo resamples.

elliptical profile, which shows a bulk rise at $\sim 1.2\ r_{200}$, reaching close parity with the 'All Galaxies' profile, indicating the red ellipticals be the main contributor to the 'All Galaxies' profile. The red ellipticals, like the blue ellipticals, present an interacting sub-population within a merging environment, potentially these could be older pre-processed galaxies that were harassed into substructures at a subtly earlier epoch. The merging elliptical VDPs consist of mixed blue and red elliptical galaxies that have gone through pre-processing interactions beyond r_{200} Both colour sub-populations in the merging elliptical stack are consistent with the blue and red merging sub-populations in Figure 2.6, insinuating that ellipticals are the dominant contributors to a merging cluster environment.

In contrast with the non-merging sample, the spiral galaxies of both colour sub-populations steadily decline with radius. The non-merging ellipticals present a similar uniform of profiles that steadily decline with radius, aside from the slight increase in the dispersion of blue ellipticals at $\lesssim r_{200}$ suggesting they are recent members to collapse onto the cluster potential. The general slow decline observed with these non-merging profiles indicates a comparatively mixed ambient system of cluster galaxies. The merging VDPs are overtly dynamic, especially with the high dispersions in blue spiral cluster galaxies, or the variable profile shapes in the ellipticals, when compared to their non-merging counterparts. This is a clear indication of the differences in dynamical ages of the two environments; active feeding of a cluster potential through substructuring and infall compared to one which has reached a relaxed dynamical equilibrium.

2.5   Discussion

The work presented here shows that across all intrinsic galactic parameter splits, the merging samples possess some form of rising profile. Hou et al. (2009) argues that such a rise indicates an interacting, or merging, system based on a correlation between a sample of non-Gaussian galaxy groups, coinciding with previous work by Menci & Fusco-Femiano (1996). However, these earlier works did not explicitly delineate which class(es) of galaxy are driving this.

2.5.1   Interpreting the VDPs

When analysing the 'All Galaxies' profiles for each split of the merging stacks, it can be deduced that these results seemingly back the argument made by Menci & Fusco-Femiano (1996) and Hou et al. (2009). With the non-merging samples generally showing a flat-to-declining series of profile. These results could corroborate recent work by Mulroy et al. (2017) that finds different cluster evolutionary histories must have played a part to explain the prominent colour variation observed in non-merging systems compared to that of merging systems. Deshev et al. (2017) is consistent with this, observing a significant decrease in the fraction of star-forming galaxies in the core of the merging Abell 520 system compared against their non-merging sample, with evidence of a smaller group of galaxies, possessing a higher fraction of star forming galaxies, feeding the merger. One explanation for this observation suggests a non-merging galaxy cluster is formed on long timescales by their haloes inducing the infall, and accretion, through harassment of galaxies from the surrounding field population that leads to the gradual variation from red to blue colours with increasing radius from the centre seen in Mulroy et al. (2017). Whereas the merging systems are formed primarily from the accretion of pre-processed galaxy groups, meaning the galaxies have undergone heavy interactions leading to evolutionary changes, and are virialised to their local groupings.

We find the red populations of the merging stacks are the main contributors to the rising profiles, which illustrates a common and significant amount of interactions occurring at $\sim 1.5\ r_{200}$ radii. Although, consideration should be taken into account that red galaxies could overshadow the total colour distribution of the cluster galaxy sample by numbers alone due to the Malmquist bias (Malmquist, 1925), along with the making the sample complete, thereby impeding a true indication on how these two sub-populations behave kinematically. In comparison to the non-merging profiles that clearly illustrate a more relaxed environment with a possible suggestion of infalling blue galaxies, this married with the merging profiles showing the dominant driver of the rising profile shape to be a mix of red and blue elliptical sub-populations. The diverse dynamics between merging and non-merging systems provide further affirmation to the idea of a galaxy infall and accretion bi-modality between merging and non-merging systems.

Considering the epochs of differing events that occur in a typical cluster (e.g. infall,

accretion, splashback), we can use the timescales between them to try and infer the current physical processes occurring and how they relate to their kinematics. Haines et al. (2015) simulate the accretion paths of multiple galaxies onto a massive cluster from various epochs and classify the infall regions to start $\lesssim$ 10 Mpc h^{-1}, or $\lesssim 5r_{200}$. It is calculated that the timescales from infall to accretion to be $\sim$ 4Gyr, a galaxy then becomes accreted once it reaches r_{200} and passes its first pericentre on timescales of $0.5 - 0.8$Gyr, followed by a significantly slower of $2 - 3$Gyr for the galaxy to reach its first apocentre (splashback radius). Collectively, the VDPs demonstrate a period of infall in the merging stacks at $\leq r_{200}$, alongside a culmination of interactions occurring as a result of the domination of pre-processed groups. This is corroborated with the merging colour and morphology VDPs, where mixed blue and red populations of galaxies assumed to be undergoing pre-processing are infalling to be accreted onto the cluster, reaffirming the suggestion by Haines et al. (2015) that pre-processing is required to explain star formation being quenched at larger radii from the cluster centre. Furthermore, the VDPs representing spiral morphology could be indicating the galaxies at $\gtrsim 1.25\ r_{200}$ are the start of a $\sim$ 4Gyr long journey onto the cluster potential, leading to their accretion and possible splashback, thus accounting for the larger surface density of spirals at smaller clustocentric radii (see Wetzel et al. 2012; Haines et al. 2015; Cava et al. 2017).

In any case, there are increasingly more observations and simulations that appear to occasionally contradict, where many authors suggests a need for pre-processing (Haines et al. 2015; Roberts & Parker 2017; de Carvalho et al. 2017). Mulroy et al. (2017) argues for a bi-modality on infall and accretion histories with similar accretion rates, one with pre-processing and one without, in order to explain the variations in colour found in non-merging systems. Further simulations could possibly help to build on this picture for these bi-modal, kinematic outcomes.

2.5.2   Phase-Space Caustics

In Section 2.3 we calculate velocity dispersions through a biweight method (Beers et al., 1990) and the phase-space surface caustics to determine cluster membership (Diaferio & Geller 1997; Diaferio 1999). The phase-space caustics produced from the chosen methodology follow a trumpet-shape pattern as we move away from the cluster centre, which is a result from galaxies infalling onto the cluster when the potential inundates the

Hubble flow (Regos & Geller, 1989). Diaferio & Geller (1997) and Diaferio (1999) both demonstrate the amplitudes of these surface caustics to be a product of random non-radial motions from substructuring, indicating a diverging caustic to be illustrative of a cluster with increasing interactions. Therefore, these caustics represent an escape velocity of the cluster potential. The key benefit, aside from powerfully indicating cluster boundaries, is that these caustics can be produced on redshift data alone. Unlike the rest of the literature, we allow the surface caustics to stretch to a ΔV velocity limit of ± 1500 kms^{-1}. This is to allow infallers to be added into the sample of cluster galaxies for each cluster, although, we wish to note that this method involves the risk of adding interloping larger scale structures to the sample. Many of the clusters compiled within this sample have been well studied, with calculated surface caustics and velocity dispersions. Reference values for the latter are presented in both Tables 2.1 and 2.2. The calculated $\sigma_{r_{200}}$ velocity dispersions are fairly consistent with the reference literature, however, there will be differences dependent on which method was used to estimate the velocity dispersions, at what radial point and how many galaxies are available for the membership of the cluster at $\leq r_{200}$ in this work. What follows is a comparison of our phase-space surface caustic analysis with that of the literature.

Abell 85

Abell 85 is a well studied cluster, with multiple calculations of its dispersion of velocities, along with phase-space surface caustics presented within Rines & Diaferio (2006). The value of $\sigma_{r_{200}}$ from this work is ~ 200 kms^{-1} offset from the calculated literature values. The primary driver of this offset is due their cluster membership being significantly greater with 497 galaxies within 1.7 r_{200} compared to 234 galaxies within 2.5 r_{200} from the data used here. The vast difference in galaxy membership can induce a slight alternate shape between the resultant surface caustics. Agulli et al. (2016) do not publish the surface caustics on their phase-space diagrams, leaving the surface caustics of Rines & Diaferio (2006), which indicate a strong constraint in ΔV-space at low radii. Despite the lack of sharp, sudden changes in the surface caustic with increasing R, there are still similarities in the membership from the caustic presented here against that of Rines & Diaferio (2006). This indicates there is consistency between the two independent calculations of the caustic

surface that allows for a more liberal inclusion of galaxies into the membership.

Abell 119

Abell 119 possesses multiple surface caustics in the literature alongside calculations of their velocity dispersions (Rines et al. 2003; Rines & Diaferio 2006). There is, again, an offset of ~ 100 kms^{-1} in the calculation of $\sigma_{r_{200}}$, for which similar reasoning is applied from that of our discussion on Abell 85; the radial point at which the velocity dispersion is calculated can push the gaps between the literature further. Additionally, the techniques used for calculating the velocity dispersion from this work varies from that of Rines & Diaferio (2006), where sigma clipping is used (Zabludoff et al., 1990), this will lead to an underestimating of the velocity dispersion when directly compared to a biweight estimator. The phase-space caustics are the most consistent with the CAIRNS cluster study of Rines et al. (2003), with very similar profiles. These caustics only deviate where there are discrepancies in the number of galaxies within ≤ 10 Mpc h^{-1}. The recalculated caustics presented in Rines & Diaferio (2006) focus on constraining the cluster membership by limiting galaxies in ΔV-space to ≤ 1000 kms^{-1}, creating a surface caustic that is not as smooth, but is effective in the elimination of infallers and the encompassing large scale structure.

Abell 426

Abell 426, commonly known as the 'Perseus cluster', does not presently possess any phase-space caustic analysis in the literature. Although, the phase-space surface caustics determined here are relatively simple, and the population of galaxies accumulated does not extend beyond ~ 2 Mpc h^{-1}, providing a smooth distribution with several groupings of member galaxies. The limited and immediate break in the available data, due to the survey's limitations in observing the north galactic cap, lends to an artificial increase in the VDP at larger radii. However, this affect should be reduced when stacked against the other clusters that extend beyond the projected radii of Abell 426. The velocity dispersions of Abell 426 determined within this work are not consistent with those determined within the literature, showing an offset of ~ 500 kms^{-1} (Struble & Rood, 1999). The lack of consistency is a result of the significant loss of galaxy members compared to the true scale

and size of Abell 426, which contains close to ~ 1000 galaxy members.

Abell 1650

Abell 1650 is an atypical cluster with a radio quiet cD cluster galaxy at its centre. The surface caustics presented in the literature follow (Rines & Diaferio, 2006) a similar shape and profile to our surface caustics, with a slight difference to the radial cut used on the sample of galaxies and a wider velocity window to allow for the addition of galaxy infallers. The velocity dispersions produced within this work are consistent with those of Einasto et al. (2012), within a slight discrepancy of ~ 200 kms^{-1}. Although, the discrepancy in these values is expected due to differing methods used in calculating the dispersion.

Abell 1656

Abell 1656, commonly referred to as 'Coma', is a well studied cluster with close to ~ 1000 members. It has such a strong presence within the literature primarily due to its relatively close proximity ($z \sim 0$), which results in a greater sacrifice of cluster galaxies when maintaining completeness. However, this is offset by the extremely high number density of cluster galaxies. The phase-space caustics of the coma cluster presented in this work are the most consistent with Sohn et al. (2017), this is the result of a more relaxed ΔV-space limit to accommodate the very large nature of the cluster. This consistency is lost at ~ 4 Mpc h^{-1} due to a sudden drop in galaxies present within our MPA-JHU sample. However, an assumption can be made based the consistency is valid due to the trend of the caustic profile following that of Sohn et al. (2017) closely. The same consistency exists for the values of the velocity dispersion with very small offsets when compared to values from the literature (Rines et al. 2003; Sohn et al. 2017).

Abell 1750

Abell 1750 is a complex triple subcluster system in a pre-merger state, which is briefly discussed in 2.5.3. The phase-space surface caustics presented here are the most consistent with produced by Rines & Diaferio (2006), with the exception of allowing infallers at ~ 2 Mpc h^{-1} to form the cluster membership. The literary values of the velocity dispersion show a discrepancy of ~ 100 kms^{-1} from the values calculated in this work (Rines &

Diaferio 2006; Einasto et al. 2012). What does remain consistent is the reasoning that alternative, less robust, methods were used to calculate a value for σ. As well as this, there is a lack of clarity on the exact methodology used to calculate the dispersions of velocities within some of the literature where alternative limits could have been used within their calculations that are otherwise unstated.

Abell 1795

Abell 1795 is a cool core galaxy cluster with an unusually large cavity with no counterpart (Walker et al., 2014). There is currently no phase-space surface caustic analysis within the literature that can be aided to check consistency. However, from our own determined caustics we can see there is a roughly even distribution of member galaxies close to the centre of the cluster, as expected from a typical relaxed cluster. Our calculated velocity dispersion is consistent with those values found in the literature (Zhang et al. 2011; Einasto et al. 2012).

Abell 2029

Abell 2029 is a massive cluster that possess a powerful cD galaxy at its centre, forming part of a supercluster with complex dynamical interactions within the ICM (Walker et al., 2012). Sohn et al. (2017) has produced surface caustics of Abell 2029 that are inconsistent with our own. There are gaps in the galaxy population size within the phase-space diagram due to the redshift limitations of the MPA-JHU DR8 data. These limitations make our data incomplete for this cluster, whereas Sohn et al. (2017) has used complementary sets of data, and therefore, does not possess the same restrictions as those found in this work. However, the bulk of the galaxies present within the imposed limits of this work match those defined as members within the phase-space surface caustic diagrams of Sohn et al. (2017) that include infallers. The calculated velocity dispersion is calculated in this work is consistent with other determined values within the literature despite the variances in galaxy membership.

Abell 2061

Abell 2061 is a double subcluster system with complex dynamics that is in close proximity to Abell 2067, this is highlighted in more detail in 2.5.3. The comprehensive CIRS survey by Rines & Diaferio (2006) presents consistent phase-space surface caustics when in consideration for the discrepancy in the range of velocities used. The only discrepancy of note is the the presence of strong foreground substructuring at ~ 3.5 Mpc h^{-1} inducing the caustic profile to maintain a consistent velocity of ~ 1000 kms^{-1}, which causes the VDP to slight increase beyond the $\sigma_{r_{200}}$ values. The literary values for Abell 2061's velocity dispersion are consistent with our own where Pearson et al. (2014) presents an offset of ~ 100 kms^{-1}, however, this is primarily due to the tighter distribution of galaxies, as well as differing methodologies for calculating the dispersion.

Abell 2065

Abell 2065, at present, does not have any detailed phase-space analysis within the literature for direct comparison. However, from our own analysis, Abell 2065 possesses what appears to be a strong bi-modal distribution, which can be attributed to a complex dynamical system of multiple substructures. This would provide consistency, since Abell 2065 is stated in the literature to possess an unequal core merger, for which the full nature of this is detailed in 2.5.3. We believe the relatively flat velocity offset at ~ -2000 kms^{-1} with increasing R to be the smaller of the two cores. The state of initial merger makes it difficult for the surface caustics to discern where the cluster ends and begins. However, the string of flat galaxies implies something akin to the Kaiser effect (Kaiser, 1987), where a flat radial separation against a non-flat separation in the plane of the sky leads to the inference of infallers.

Abell 2142

Abell 2142 is a notorious cluster for its smooth and symmetric X-ray emission, indicative of a post core-merger event, which occurred ~ 1 billion years ago (Markevitch et al., 2000). The phase-space surface caustics of Abell 2142 vary within the literature, as well as in comparison to the work done here. Munari et al. (2014) presents surface caustics within the confines of ~ 3 Mpc h^{-1} and appear to be constant with increasing R. Again,

with Rines & Diaferio (2006) demonstrating a more dynamic and tighter caustic due to differing limits applied in both velocity-space and radial-space alongside data visualisation effects. As usual, the shapes of these caustics are determined by the numbers of galaxies present within the field and how closely, or sparsely, they are distributed as we increase R from the cluster centre. Again, the calculated velocity dispersions from Munari et al. (2014) are inconsistent with our own value, offset by ~ 300 kms^{-1}. This is due to the spread, number and density of the cluster membership determined in the work of Munari et al. (2014) being equally greater.

Abell 2199

Abell 2199 is a relatively local galaxy cluster and provides a good testing-bed for large scale structure formation thanks to its close proximity, this is akin to Abell 1656, another relatively local cluster. The cluster is well studied, possessing several phase-space surface caustics in the literature. The phase-space caustics in this work are the most consistent with Song et al. (2017) and Rines et al. (2003), where the shape and profile closely matches despite a lower membership. The velocity dispersions calculated here are consistent with those found within the literature (Rines et al., 2003).

Abell 2255

Abell 2255 is a merging galaxy cluster with a complex X-ray distribution, which has yielded a variety of studies to better understand the mechanisms of diffuse radio emission Akamatsu et al. (2017). The total membership of Abell 2255 in this work is considerably less than that of other literature. However, the surface caustics of this work are still reasonably consistent with the caustics determined by Rines & Diaferio (2006), if lacking in definition. The velocity dispersion profiles determined here are consistent with those in the literature, despite offsets of ~ 200 kms^{-1}, the drivers are variations in galaxy membership (Zhang et al. 2011; Akamatsu et al. 2017).

ZWCL1215

The phase-space caustics of galaxy cluster ZWCL1215 determined in this body of work is consistent with those that are produced by Rines & Diaferio (2006), with only slight

variations in the definition of the shape of the surface caustics. The calculated velocity dispersions are also consistent with those determined by Zhang et al. (2011), with an offset of ~ 200 kms^{-1}, as a result of the reduced membership of galaxies presented within this work.

2.5.3   Interloping Structures

The clusters that form our sample are not purely isolated potentials, therefore we should take into consideration potential interloping structures as a result of a cluster being a member of supercluster. As an example, during the data accumulation stage of section 2.3, the clusters are cross matched against the Einasto et al. (2001) catalogue of superclusters to determine any significant contamination between clusters. Abell 2244 and Abell 2249 are eliminated from the samples due to their strong interloping/overlap in RA-DEC space and z-space within the regions being investigated in this work. Although, their removal from the samples has not altered to shape of the final stacked VDPs to any significant degree.

There are also other clusters within the sample that possess unusual substructures. The phase-space diagram of Abell 2065 in Figure 2.1 clearly presents two seemingly independent structures. However, Abell 2065 has been documented in the literature to be at the late stage of an ongoing merger (Markevitch et al., 1999). Further X-ray observations with XMM-Newton indicate more specifically the presence of an ongoing compact merger between two subclusters within Abell 2065, where the two cores are at an epoch of initial interaction (Belsole et al., 2005). Higher resolution X-ray observations from Chandra show a surviving cool core from the initial merger, with an upper limit merger velocity of $\lesssim 1900$ kms^{-1}, adding to the argument that Abell 2065 is an unequal core merger (see Chatzikos et al. 2006). This provides an explanation to the slightly off-centre line-of-sight mean velocity distribution of galaxies, with a second, smaller core averaging out to ~ -1500 kms^{-1} found in the phase-space diagram of Abell 2065, and naturally will affect the shape of the VDP at larger radii. Abell 1750 is a triple subcluster system with the north subcluster separated from the central subcluster by a velocity offset of -900 kms^{-1} and are all currently in a stage of pre-merger to the point where the plasma between the substructures is significantly perturbed (Molnar et al. 2013; Bulbul et al. 2016). In contrast Abell 2061, which resides within the gravitationally bound Corona Borealis supercluster

with Abell 2065 (see Pearson et al. 2014), possesses two optical substructures that will affect the VDP similarly to Abell 2061 (van Weeren et al., 2011). It should be noted that Abell 2061 potentially forms a bound system with the smaller cluster/group Abell 2067 (Marini et al. 2004; Rines & Diaferio 2006), with line-of-sight velocity separation of ~ 725 kms^{-1} (Abdullah et al., 2011). Observations hint at a likely filament connecting the two systems (Farnsworth et al., 2013) aiding to the suggestion of cluster-cluster interloping. There is ~ 30′ of sky separation and with the prescribed cosmology in section 2.2 this provides a rough projected distance of ~2.7 Mpc h^{-1} from the centre of Abell 2061. Yet, this confirms to the cluster-cluster overlapping suggestion with the criteria used to develop cluster membership. Therefore, it is very likely the membership of Abell 2061 is contaminated with the infalling Abell 2067 cluster's member galaxies as we approach 2.5 R/r_{200}.

2.5.4 The Delta Test

The process of determining whether or not a cluster is merging involved the use of the Δ test for substructure, devised by Dressler & Shectman (1988). Whereby the presence of any substructure to a $\geq 99\%$ significance is recorded as a merging cluster environment. The Δ test, while a powerful and sensitive tool, is limited in its power to test for substructure since it only concerns itself with the sum of the deviations of a local velocity dispersion and mean recession velocity with global cluster values. This could lead to a greater probability of false positives for sub-structuring, along with omissions of those clusters that genuinely possess it. The problem becomes more apparent if an appropriate radial cut-off is not applied when calculating Δ, otherwise the test will classify nearly every cluster to contain substructure. This is a consequence of the varying numbers of cluster galaxies that are added into the calculation of Δ; greater numbers of cluster galaxies help decrease the value of $P(\Delta)$, thereby artificially increasing the significance of subclustering and vice versa. Pinkney et al. (1996) highlights in their comparison of substructure tests how the sensitivity of the Δ test is affected measurably by the projection angle of the member galaxies, this can lead to a potential loss of genuine merging systems from our sub-sample when their velocities run along 0° or 90°. One way to potentially alleviate this could be the introduction of more spatial parameters. For example, the *Lee Three-Dimensional Statistic* adapted by Fitchett & Webster (1987), took into consideration angles derived

from the projected space and velocity. This test can help to eliminate any potential false positive with its ability to be insensitive to genuine non-merging systems (Pinkney et al., 1996).

There are also methods for testing dynamical activity that involve measuring the Gaussianity of the velocity distributions, such as the 'Hellinger Distance' measuring the distance between a set of observational and theoretical distributions (see Ribeiro et al. 2013; de Carvalho et al. 2017). Other novel approaches, such as one presented by Schwinn et al. (2018), test to see whether 2D mass maps can be used to find mass peaks using wavelet transform coefficients. Highlighting discrepancies between definitions of substructure. In contrast, tried and tested methods are evaluated by Hou et al. (2009), comparing different approaches to analysing the dynamical complexity to groups of galaxies. The authors find a χ^2 goodness-of-fit is not best suited for determining a transition away from a Gaussian distribution of velocities. The principles upon which the Δ test is built upon is a frequentist χ^2, which may indicate there is some form of decoupling in the link between sub-structuring and dynamical activity. This apparent decoupling is most likely a result of the limitations of using a singular technique to define if a merging system of cluster galaxies is present, as the Δ test is only sensitive to average deviations from observed line-of-sight velocities. This is a problem that extends to the VDPs, since they rely on a weighted grouping of objects in velocity-space with a moving Gaussian window function. Therefore, care has to be taken when classifying a galaxy cluster as merging or non-merging based on using the methodology of Bergond et al. (2006) and Hou et al. (2009). Despite these caveats, the nature of determining substructure with classical statistical testing is simple, sensitive and allows for fast computation on determining our sub-samples. However, there is room to consider how one can accurately define a cluster to be merging or not based solely on limiting velocity-space tests for substructure/grouping of galaxies. For example, there are relic mergers with non-thermal emissions that represent an afterglow of a merging event, or, represent a pre-merging environment as a result from the interactions between intra-cluster media (e.g. Giovannini et al. 2009; Bulbul et al. 2016). These environments would be insensitive to our traditional statistical testing for substructure due to its constrained application on using the clustering of galaxies as the sole proxy for a merging system. Utilising other parts of the spectrum highlight strong interactions between particles of the ICM, or, of two interacting ICMs from two initially

independent systems, and the lack of a comprehensive study can call into question how we best define what is and is not a merging cluster.

The VDPs produced here could potentially mask any further variability within the kinematics that would otherwise be visible on a smaller scale 'window width'. It is apparent from this work there is some form of sub-layer to the profiles that inhibit a clearer picture being formed in the dynamical nature of galaxies with differing properties. It is a notable possibility that, within some clusters, there is still an inclusion of interloper field galaxies towards $\sim 2.5\, r_{200}$ that distort our final view on the key drivers of these seemingly interacting galaxy sub-populations. The differing merging and non-merging sample sizes present problems of their own that lead to biasing the final stacked VDPs. For example the smoothing kernel, along with the chosen width of the kernel, used will cause a decrease in the sensitivity in how the VDPs respond to substructuring. This problem continues with the stacking procedures, which decrease the sensitivity to the presence of mergers due to each cluster possessing unique environments with different position angles and separations. This problem is further extended when clusters possess limited numbers due to spectroscopic limitations of the survey in the MPA-JHU data. Therefore, unless there is a significant number of galaxies inputted to the calculation of a VDP, the risk of spurious features appearing is still a powerful one. In some cases this is purely a limitation of the data available from marrying the MPA-JHU with DR8 photometry or GZ2 morphologies, in others, an indicator to the limitations in using VDPs as a tool to present the dynamical overview of galaxy clusters.

2.6   Summary

In this work we have produced a base line cluster galaxy membership that marries the MPA-JHU DR8 archival data with the BAX limits of $(3 < L_X < 30) \times 10^{44}$ ergs s^{-1} and $0.0 < z < 0.1$, which is complete at $\log_{10}(M_*) > 10.1$. The sample of galaxy clusters are sub-categorised into a merging or non-merging samples of galaxy clusters depending on the outcome of the Dressler & Shectman (1988) test. Stacks of VDPs are computed for differing galactic parameters in order to determine what drives the shape of the VDP. The key results are summarised as follows:

(i) In common with previous literature, our merging cluster sample demonstrates a

steeply rising VDP. The bulk of this rise happens at $\sim 1.5\ r_{200}$. On the other hand, non-merging clusters generally exhibit a declining-to-flat VDP.

(ii) In merging systems, a mix of red and blue elliptical galaxies appear to be driving the rising VDP at these radii. This may be the result of pre-processing within galaxy groups.

(iii) Non-merging systems commonly display little variation in kinematics throughout their VDPs, however, there are consistently higher $\sigma_P(R)$ values from the VDPs associated with a younger population of galaxies.

(iv) Spiral galaxy VDPs in merging systems present a dichotomy in their dispersion of velocities, with the blue spiral galaxies possessing a high velocity dispersion that is indicative to an infalling sub-population of field galaxies.

(v) The global VDP of an individual cluster must be treated with care since a rising or falling VDP may be driven by a subpopulation of the cluster members.

Acknowledgements

3. The Dynamics of Cluster Galaxies

"I can calculate the motions of the heavenly bodies, but not the madness of people."

– Isaac Newton, *Comments on the 'South Sea Bubble' (1720, adapted 2019)*

3.1 Prologue

The Chapter presented here is the published work entitled "*The rotational profiles of cluster galaxies*", under MNRAS **490**, 5017 (Bilton et al., 2019). This article was written and led by myself and co-authored with in the following order: Matthew Hunt, Kevin Pimbblet and Elke Roediger. As lead author of this article and the research contained within, I drove the direction, scientific aims, data handling and analysis as well as leading the co-authors to provide their contributions. Subsection 3.5 of this Chapter introduces complementary N-body simulations computed with `FLASH`-code, which was written and analysed by Matthew Hunt. Contributions made by the remaining co-authors include scientific feedback on draft versions of this work and making suggested corrections where applicable. My total workload and contributions to this article thus amount to $\sim 80\%$. The article has been slightly altered to fit the format of a thesis, therefore to this end, the abstract has been omitted to avoid repetition of the whole thesis.

3.2 Introduction

Galaxy clusters are large and dense realms in space which anistropically coalesce along the convergence of independent filaments through hierarchical merger events, resulting in the induction of random motions in their member galaxies (e.g. Bond et al. 1996; Springel et al. 2005b; Kravtsov & Borgani 2012). These large collections of matter are home to strong gravitational potentials that cause the further perturbation of galaxies from the Hubble flow (Regos & Geller, 1989). As a result, galaxy clusters seemingly play host to environmental effects that are pivotal in the understanding of the evolution of galaxies through an assumption of fixed stellar mass: the transition from late-type to early-type

galaxies towards the cluster's centre with the morphology-density relation (e.g. Oemler 1974; Dressler 1980; Postman & Geller 1984); the observed bimodality of the colour-density relation (Hogg et al., 2003, 2004); the consistent decrease in the fraction of star forming galaxies in cluster cores (e.g. Lewis et al. 2002; Gómez et al. 2003; Bamford et al. 2009; von der Linden et al. 2010); a galaxy infalling onto a cluster potential experiencing ram-pressure stripping due to interacting with the intracluster medium (ICM) (e.g. Gunn & Gott 1972; Sheen et al. 2017; Poggianti et al. 2017).

The hierarchical nature of galaxy cluster formation lends itself to the existence of physical substructures (Geller & Beers, 1982; Dressler & Shectman, 1988). Therefore, the aforementioned environmental effects on galaxy evolution can be scaled down to the smaller substructure environments within a cluster. We can use the presence and strength of this sub-structuring within the cluster to delineate differing environments (i.e. merging or non-merging). The substructures that reside at larger radii from the cluster centre are smaller galaxy groups that cause 'pre-processing' (Berrier et al., 2009; Bahé et al., 2013); smaller-scale premature evolution of galaxies due to localised galaxy-galaxy interactions (see Moore et al. 1999). Pre-processing is considered to be a common occurrence in order to account for the swift changes in star formation and colour fractions as galaxies transition from the field (e.g. see Haines et al. 2015; Bilton & Pimbblet 2018).

Perhaps one of the striking features of many galaxy clusters is the presence of overtly bright giant early-type galaxies, commonly with an extended diffuse region, that lie within the dynamical centres of their host cluster (Quintana & Lawrie, 1982), otherwise known as the brightest cluster galaxy (BCG). The formation mechanism for BCGs has been key point of contention. One such model is galactic cannibalism (Ostriker & Tremaine, 1975), whereby galaxies infall and accumulate at the bottom of the potential well through dynamical friction. An alternatively favoured model is rapid hierarchical galaxy-galaxy merging into an ensemble of sub-groupings of galaxies of similar size prior to collapse onto the bottom of the potential (Merritt, 1985). Testing of these models has often yielded mixed results; galactic cannibalism is deemed too slow in order to build a BCG within a reasonable timescale with the observed luminosities (e.g. Lauer 1988; Dubinski 1998); hierarchical galaxy merging events alone do not assemble enough sub-groupings with calculations to our current epoch (Collins et al., 2009). However, despite these shortfalls, there is evidence for clusters to have had merger events over their histories with the

observations of BCGs with multiple cores (e.g. Oegerle & Hill 1992; Laine et al. 2003). There is also convincing evidence of core-core pre-merger; on-going merger; post-merger activity between two originally independent potential wells, with high peculiar velocities of BCGs, that indicate perturbations from their original geometric and kinematic centres (e.g. Quintana et al. 1996; Smith et al. 2005a; Pimbblet et al. 2006; Shan et al. 2010; Lakhchaura et al. 2013; Caglar & Hudaverdi 2017). These systems with multiple-core BCGs are sometimes known as 'Dumbbell Clusters'.

If we assume these dumbbell clusters arise from two originally independent sub-clusters interacting off-axially, then the strength and presence of their resultant momenta could leave an imprint onto their line-of-sight velocities, producing some sort of 'global cluster rotation' (Ricker, 1998). Due to the apparent random motions of cluster galaxies, the idea of galaxy clusters supported by rotational energies was excused for a pressure-based model. However, once thought indistinguishable from the cluster galaxy kinematics, there have since been several works that have observed global rotation (e.g. Materne & Hopp 1983; Oegerle & Hill 1992; Hwang & Lee 2007; Tovmassian 2015; Manolopoulou & Plionis 2017). One could argue that the source of cluster rotation is from the Universe possessing its own angular momentum and donating it onto celestial bodies during their formation (Li, 1998; Godłowski et al., 2003, 2005). However, to account for the strong peculiar velocities from relatively recent histories, galaxy cluster rotation could be derived from the merging processes between two clusters (Peebles, 1969; Ricker, 1998); off-axis tidal interactions from two independent deep potential wells. Observations of such events/relics would only be pragmatic by observing the ICM due to the high collisional probability of particles that produce X-rays, where the more sparse cluster galaxies are found to be collisionless on equal timescales; global angular momentum observed via the galaxies is transient (White & Fabian, 1995; Roettiger et al., 1997; Roettiger & Flores, 2000). Indeed, recent simulation studies show how the ICM could be used to determine bulk cluster rotation dynamics (see Baldi et al. 2017, 2018). In addition, there is the very sensible notion that the accretion of mass through the filaments during cluster assembly is the primary driver of momentum donation to these systems (see Song et al. 2018). One immediate method that could be used to infer a cluster's global rotation is the use of a geometrical technique known as 'perspective rotation'; peculiar motion measurements taken from the mean radial velocities to determine the transverse motion by artificially

rotating the galaxy cluster on the plane of the sky (Feast et al., 1961).

Therefore, in this paper we aim to establish whether or not the global rotational dynamics of clusters correlate with their sub-populations and if the presence of a dumbbell BCG core imprints a cluster evolutionary mechanism onto the global rotational profile. This will be achieved by utilising a 'perspective rotation' technique, which infers the presence of cluster rotation through the comparative radial velocity differences between two semi-circles divided by the cluster centre (see Manolopoulou & Plionis 2017; MP17 hereafter). We present a complementary suite of galaxy data from the Sloan Digital Sky Survey (SDSS) and NASA/IPAC Extragalactic Database (NED) to form a membership of clusters into two samples of those that do, and do not, host a dumbbell nucleus. An elaboration on how these data were acquired can be found in section 3.3. An explanation of the methods used to output our global rotation profile analysis, along with our results, are outlined in section 3.4. In addition to our array of observational data, we utilise 3D hydrodynamics and N-body simulations to determine the impact of idealised binary cluster mergers on global rotational profiles. The comparison of our observational rotational analysis with our 3D hydrodynamic and N-body simulations are elaborated in section 3.5. Concluding with a discussion and summary of our findings in this work with section 3.6.

Throughout this work we assume a flat ΛCDM model of cosmology with $\Omega_M = 0.3$, $\Omega_\Lambda = 0.7$, $H_0 = 100h$ km s^{-1} Mpc^{-1}, where $h = 0.7$.

3.3   The Data Suite

We compile two samples of clusters to allow for a more comprehensive study of the affects of cluster rotation; a sample of bright X-ray selected clusters utilising the X-ray Cluster Database (BAX; Sadat et al. 2004), a curated repository linking X-ray data from multiple instrumental sources; a sample of dumbbell clusters catalogued by Gregorini et al. (1992, 1994) Each X-ray selected cluster is then built from the BAX centre and defined by galaxies from SDSS Data Release 8 (DR8; Aihara et al. 2011) cross-matched with the MPA-JHU Value Added Catalogue (Kauffmann et al., 2003; Brinchmann et al., 2004; Tremonti et al., 2004). The dumbbell clusters are assembled via the procurement of NED galaxies that lie within 30 arcminutes of the NED-defined centres of the 12 dumbbell clusters, similarly to the work presented by Pimbblet (2008).

We initialise our cluster sample with the BAX database by employing an X-ray luminosity range of $1 < L_X \leq 20 \times 10^{44}$ ergs^{-1} that lie within the redshift range of $0.0 < z \leq 0.15$. These limits ensure we are selecting the most massive clusters; that we garner a significant number of clusters; sampling across a variety of dynamical states in z-space from a finite epoch range. Once parsed through BAX, the applied limits provide an initial sample size of 481 clusters. For each of the BAX clusters an initial radial limit of ≤ 10 Mpc h^{-1} is applied to DR8 galaxies from the cluster centre, calculated with our outlined cosmology (Wright, 2006). The cluster sample is iterated through to have their global mean recession velocities ($\overline{cz}_{\mathrm{glob}}$) and velocity dispersions (σ_{glob}) calculated for galaxies ≤ 1.5 Mpc h^{-1} from the cluster centre by computing the square root of the biweight midvariance (Beers et al., 1990). We then proceed to define the cluster boundary in velocity space as a function of projected radius R with surface caustics, in accordance with the methodology of Diaferio & Geller (1997); Diaferio (1999). Velocity limits of $\Delta V = \pm 1500$ kms^{-1} are imposed upon each cluster in the sample as a conservative threshold to increase confidence against interlopers contaminating the DR8 assembled clusters, with

$$\Delta V = c \left(\frac{z_{\mathrm{gal}} - z_{\mathrm{clu}}}{1 + z_{\mathrm{clu}}} \right). \tag{3.1}$$

However, it should be noted that this limit can potentially omit genuine members from those systems that are actively relaxing onto a cluster potential due to their greater dispersion of galaxies, acting as an echo from two originally independent sub-clusters coalescing onto each other. The surface caustic profiles are then determined with the remaining galaxies for each cluster, allowing for estimations of M_{200} and r_{200}, the cluster masses and radii for when the density is 200 times the critical density of the universe for our flat cosmology (Gifford & Miller, 2013; Gifford et al., 2013). Cluster candidates are ignored if their initial richness is < 50 at $\leq r_{200}$, or, if they are found within the Einasto et al. (2001) supercluster catalogue to possesses overlapping structures. The resultant cluster sample size provided by the BAX-DR8 galaxies is 33, which is found to be mass-complete at $\log_{10}(M_*/\mathrm{M_\odot}) \geq 10.2$. The final compilation of BAX-defined clusters built from DR8 galaxies can be found in Table 3.1.

The 12 dumbbell clusters are initialised with the NED galaxies that reside within 30 arcminutes from the NED defined centres. The NED galaxies associated with each cluster

are then run through the same process as the DR8 galaxies above. The NED-defined clusters built from the NED galaxies, along with their calculated values, can be found in Table 3.2.

3.4   Cluster Rotation & Environmental Effects

It has already been noted in section 3.2 how one might expect galaxy clusters to have gained their momentum. To study how different cluster activity states drive the dynamical side-effects onto cluster galaxy sub-populations we utilise the BAX-selected clusters to compile two sub-samples, those that possess substructure against those without, as determined by the Dressler & Shectman (1988) test (Δ-test hereafter) which is outlined in section 3.4.1 below. The methodology outlined by MP17, elaborated in section 3.4.2, is applied to construct the rotational curves determined through their artificial transverse rotation on the plane of the sky to study how the cluster galaxy sub-populations respond to global cluster rotation and level of sub-structuring. From this method, we determine the rotational profiles as a function of projected radius of the clusters from both our samples, as well as producing composite profiles for merging and non-merging (i.e. level of activity) sub-samples for the BAX-selected clusters (see sections 3.4.3 and 3.4.4). Allowing for us to compare the angular momentum of galaxy clusters between different possible states of merger activity and how cluster galaxy sub-populations drive the resultant profiles.

3.4.1   The Delta Test

The use of a geometric perspective motion effect can lead to spurious detections of ambient cluster rotation in the presence of strong galaxy-galaxy merger activity from a merging cluster. However, within this work, we aim to establish the rotational velocities (see 3.4.2) as a function of radius to determine how the strength of the global cluster rotation varies between merging and non-merging environments. Therefore, to test how cluster activity can alter the rotational dynamics of clusters and thereby, affect the evolution of the cluster galaxies, we incorporate the Δ-test for substructure on galaxies within 1.5 Mpc h^{-1} (defined as N_{glob}) of the BAX and NED defined cluster centres in order to delineate between merging and non-merging environments. The Δ-test is a commonly used and very robust tool for indicating substructure, with substructure detections reaching $> 99\%$
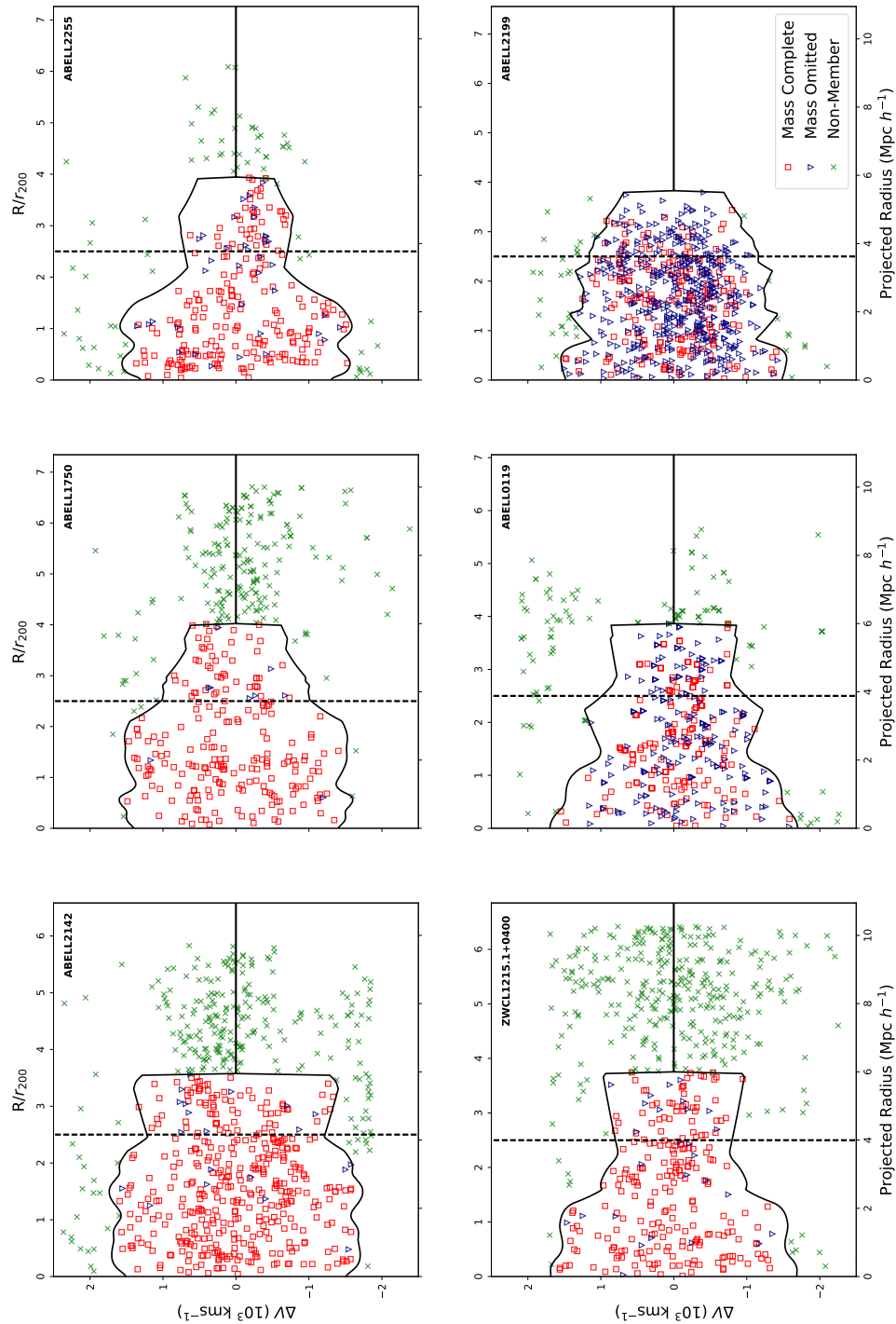
Figure 3.1: Example surface caustics (the black curves) from the final merging cluster sample (*top row*) and non-merging cluster sample (*bottom row*). Where the red squares represent the galaxies that make a complete sample at $\log_{10}(M_*/M_\odot) \geq 10.2$, with the blue triangles representing omitted galaxies that are at $\log_{10}(M_*/M_\odot) < 10.2$. Galaxies that lie within the surface caustics are considered to be cluster members. Here the radial velocity (ΔV) with respect to the cluster's mean recession velocity is plotted against the projected radius in units of Mpc h^{-1} and R/r_{200}. The black dashed vertical lines represent the 2.5 R/r_{200} radial cut of each cluster; galaxies ≤ 2.5 R/r_{200} within the caustics produce the rotational profile stacks.

Table 3.1: The mass-complete BAX cluster sample. The J2000 coordinates and X-ray luminosity values are taken from BAX. The methodology for the determination of kinematic and global rotational values can be found in sections 3.3 and 3.4.2. χ^2_{id}/χ^2_{rd} is the ratio of the χ^2 statistic between ideal and random rotation curves with $P(KS)$ being the two-sample Kolmogorov-Smirnov test of significance in rotation. MP17 defines a strict criterion as $P(KS) < 0.01$ and $\chi^2_{id}/\chi^2_{rd} \leq 0.2$, alongside a loose criterion as $P(KS) < 0.01$ and $\chi^2_{id}/\chi^2_{rd} \leq 0.4$, for determining the presence of cluster rotation. The $P(\Delta)$ values represent the significance of sub-structuring with respect to the Δ-test in equation 3.2. Where $P(\Delta) \ll 0.01$ and $P(KS) \ll 0.01$ is strongly indicative of substructure and rotation with values smaller three d.p.

Cluster	RA (J2000)	DEC (J2000)	L_x ($\times 10^{44}$ erg s^{-1})	$\overline{cz}_{\mathrm{glob}}$ (km s^{-1})	$N_{r_{200}}$	$\sigma_{r_{200}}$ (km s^{-1})	v_{glob} (km s^{-1})	θ_{glob} (°)	χ^2_{id}/χ^2_{rd}	$P(KS)$	$P(\Delta)$
				Merging							
Abell 426	03 19 47.20	+41 30 47	15.34[a]	5396±62	106	831^{+40}_{-46}	271±68	100	0.26	0.007	0.010
Abell 1552	12 29 50.01	+00 46 58	1.09[d]	25782±111	75	809^{+64}_{-84}	366±129	260	0.12	0.083	0.003
Abell 1750	13 30 49.94	-01 52 22	3.19[c]	25482±95	70	726^{+55}_{-71}	512±121	100	0.08	≪0.01	≪0.01
Abell 1767	13 36 00.33	+03 56 51	2.43[c]	20985±78	126	770^{+47}_{-58}	326±90	320	0.12	≪0.01	0.002
Abell 1991	14 54 30.22	+01 14 31	1.42[d]	17687±61	57	535^{+37}_{-47}	287±78	270	0.07	0.044	≪0.01
Abell 2033	15 11 28.19	+00 25 27	2.56[b]	24582±90	53	589^{+51}_{-69}	571±100	300	0.15	≪0.01	≪0.01
Abell 2147	16 02 17.17	+01 03 35	2.87[a]	10492±48	95	688^{+30}_{-35}	226±60	300	0.15	≪0.01	≪0.01
Abell 2255	17 12 31.05	+64 05 33	5.54[a]	24283±107	112	817^{+62}_{-80}	317±92	60	0.36	0.011	≪0.01
				Non-Merging							
Abell 85	00 41 37.81	-09 20 33	9.41[a]	16488±73	71	709^{+44}_{-55}	103±106	120	0.17	0.063	0.853
Abell 119	00 56 21.37	-01 15 46	3.30[a]	13190±77	60	760^{+47}_{-58}	222±92	220	0.18	0.091	0.579
Abell 602	07 53 19.02	+01 57 25	1.12[b]	18587±94	34	626^{+55}_{-75}	147±112	110	0.69	0.484	0.163
Abell 1066	10 39 23.92	+00 20 41	1.20[c]	20985±91	62	714^{+53}_{-69}	363±116	130	0.09	0.011	0.020
Abell 1190	11 11 46.22	+02 43 23	1.75[d]	22484±87	66	669^{+51}_{-66}	140±98	30	0.23	0.309	0.194
Abell 1205	11 13 22.39	+00 10 03	1.77[c]	22784±106	49	748^{+61}_{-82}	440±126	20	0.18	0.013	0.026
Abell 1367	11 44 29.53	+01 19 21	1.25[a]	6595±49	48	660^{+31}_{-37}	200±72	320	0.06	0.007	0.026
Abell 1589	12 41 35.79	+01 14 22	1.53[e]	21585±88	74	751^{+52}_{-66}	140±103	160	0.17	0.316	0.124
Abell 1650	12 58 46.20	-01 45 11	6.99[a]	25182±100	51	670^{+57}_{-77}	268±109	0	0.10	0.215	0.636
Abell 1656	12 59 48.73	+27 58 50	7.77[a]	6895±40	150	817^{+26}_{-29}	37±57	350	0.41	0.229	0.087
Abell 1668	13 03 51.41	+01 17 04	1.71[d]	18886±89	47	639^{+52}_{-69}	112±115	40	0.28	0.540	0.336
Abell 1773	13 42 08.59	+00 08 59	1.37[c]	22784±96	68	687^{+55}_{-73}	149±114	260	0.19	0.289	0.336
Abell 1795	13 49 00.52	+26 35 06	10.26[a]	18587±92	72	785^{+55}_{-69}	246±108	180	0.13	0.031	0.265
Abell 1809	13 53 06.40	+00 20 36	1.69[e]	23683±80	64	618^{+46}_{-60}	43±95	270	0.17	0.101	0.420
Abell 2029	15 10 58.70	+05 45 42	17.44[a]	23084±102	117	893^{+60}_{-76}	79±111	10	0.29	0.370	0.415
Abell 2052	15 16 45.51	+00 28 00	2.52[a]	10492±65	38	619^{+40}_{-50}	48±71	320	0.21	0.129	0.663
Abell 2061	15 21 15.31	+30 39 16	4.85[f]	23383±69	91	630^{+41}_{-51}	154±91	210	0.09	0.043	0.183
Abell 2063	15 23 01.87	+00 34 34	2.19[a]	10492±78	58	785^{+48}_{-59}	163±93	330	0.35	0.170	0.016
Abell 2065	15 22 42.60	+27 43 21	5.55[a]	21884±98	113	873^{+58}_{-73}	422±125	10	0.07	0.002	0.211
Abell 2069	15 23 57.94	+01 59 34	3.45[g]	34775±139	69	910^{+77}_{-104}	363±178	150	0.21	0.089	0.179
Abell 2107	15 39 47.92	+01 27 05	1.41[e]	12291±62	42	615^{+38}_{-47}	159±74	280	0.15	0.021	0.151
Abell 2124	15 44 59.33	+02 24 15	1.66[f]	19786±103	53	751^{+60}_{-80}	38±130	150	0.45	0.705	0.873
Abell 2199	16 28 38.50	+39 33 60	4.09[a]	8993±52	75	649^{+33}_{-39}	156±59	10	0.13	0.008	0.586
Abell 2670	23 54 10.15	-00 41 37	2.28[c]	22784±89	92	799^{+53}_{-66}	232±104	220	0.11	0.085	0.523
ZWCL1215	12 17 41.44	+03 39 32	5.17[a]	22484±86	87	760^{+51}_{-64}	58±118	240	0.40	0.888	0.873

[a] Reiprich & Böhringer (2002)   [b] Ebeling et al. (1998)   [c] Popesso et al. (2007)

[d] Böhringer et al. (2000)   [e] Jones & Forman (1999)   [f] Marini et al. (2004)

[g] David et al. (1999)

Table 3.2: The volume-limited NED cluster sample as per Pimbblet (2008). The descriptors for the NED cluster kinematic values can be found in Table 3.1.

Cluster	RA (J2000)	DEC (J2000)	$\overline{cz}_{\mathrm{glob}}$ (km s^{-1})	$N_{r_{200}}$	$\sigma_{r_{200}}$ (km s^{-1})	v_{glob} (km s^{-1})	θ_{glob} (°)	χ^2_{id}/χ^2_{rd}	$P(KS)$	$P(\Delta)$
Abell 533	05 01 30.79	-01 30 27	14000±171	22	751^{+99}_{-153}	951±319	270	0.09	0.002	0.026
Abell 2860	01 04 20.62	-02 39 17	31718±48	14	229^{+27}_{-39}	131±60	210	12.92	0.035	0.878
Abell 2911	01 26 04.60	-02 31 54	24223±85	31	484^{+49}_{-68}	250±118	50	0.19	0.058	0.129
Abell 3151	03 40 27.71	-01 54 49	20265±115	50	753^{+67}_{-91}	278±168	10	0.09	0.227	0.041
Abell 3266	04 31 24.10	-04 05 47	17657±54	281	825^{+34}_{-38}	55±81	200	0.13	0.219	0.356
Abell 3391	06 26 22.80	-03 34 47	15409±114	81	931^{+69}_{-88}	525±151	240	0.08	0.003	≪0.01
Abell 3528	12 54 18.20	-01 56 05	15829±71	103	674^{+43}_{-53}	48±89	140	3.61	0.663	0.834
Abell 3570	13 46 52.50	-02 31 29	10972±50	16	233^{+30}_{-45}	110±81	150	1.09	0.023	0.612
Abell 3535	12 57 48.55	-01 53 57	19546±53	28	291^{+31}_{-43}	87±69	30	1.15	0.402	0.319
Abell 3653	19 53 00.90	-03 28 07	32647±84	43	565^{+48}_{-63}	261±114	170	0.10	0.094	0.115
Abell 3716	20 51 16.70	-03 30 47	13850±76	117	767^{+47}_{-57}	200±110	220	0.06	0.152	0.586
Abell 3744	21 07 12.29	-01 41 45	11422±60	64	481^{+37}_{-47}	61±76	320	0.17	0.928	0.028

confidence when applied on cluster galaxy sample sizes of $N_{\mathrm{glob}} \geq 60$ (e.g. Pinkney et al. 1996; Pimbblet 2008; Song et al. 2018; Bilton & Pimbblet 2018). Therefore, we apply the Δ-test onto each galaxy and their $N_{nn} = \sqrt{N_{\mathrm{glob}}}$ nearest neighbours. The localised kinematics are determined and then compared against the global values,

$$\delta_i^2 = \left(\frac{N_{nn} + 1}{\sigma_{\mathrm{glob}}^2}\right)\left[(\overline{cz}_{\mathrm{local}} - \overline{cz}_{\mathrm{glob}})^2 + (\sigma_{\mathrm{local}} - \sigma_{\mathrm{glob}})^2\right], \tag{3.2}$$

where δ measures the deviation in the small region around the galaxy compared to the global cluster values at ≤ 1.5 Mpc h^{-1}. The application of the Δ-test to the BAX sample leads to a merging sub-sample size of 8 clusters and a non-merging sub-sample size of 25 clusters, the resultant values for which can be found in Table 3.1. Example phase-space diagrams, along with their respective caustics, produced from each sub-sample of clusters are presented in Figure 3.1 to illustrate the membership and spread of galaxies for each cluster and their local environments.

3.4.2   The Manolopoulou & Plionis Method

In order to determine our averaged cluster galaxy rotational profiles, we employ the methodology of MP17, which utilises the geometrical 'Perspective Rotation'. Assuming an ideal case where the rotational axis of a cluster is perpendicular to our line-of-sight

(i.e. $\phi = 0°$), we split our cluster into two semicircles vertically down the X-ray defined centre and determine their line-of-sight velocities of the member galaxies with respect to their angle μ from the origin. The mean velocity of each semicircle ($\langle v_1 \rangle$, $\langle v_2 \rangle$) is then determined in equation 3.3. Enabling observations in how the difference in the mean velocities of each semicircle ($v_{\text{diff}} = \langle v_1 \rangle - \langle v_2 \rangle$) vary as we project the average proper motions of the galaxies through the transverse rotation of galaxies in $\theta = 10°$ increments. Therefore, for each semicircle we apply iteratively

$$\langle v_{1,2} \rangle = \frac{1}{N} \sum_{i=1}^{N} \Delta V_i \cos(90° - \mu_i), \tag{3.3}$$

where ΔV_i is the line-of-sight velocity from equation 3.1 for the galaxy $z_{\text{gal},i}$, and the angle from the origin μ_i operates between $0°$ and $180°$ for each semicircle. This means that v_{diff} can be determined for each angle θ. Leading to the uncertainties of each semicircle being propagated through for each angle θ as

$$\sigma_\theta = \sqrt{\frac{\sigma_{v,1}^2}{n_1} + \frac{\sigma_{v,2}^2}{n_2}}, \tag{3.4}$$

where σ_v is the velocity dispersion and n is the galaxy number for each semicircle 1 and 2 at each angle of θ.

Finally, we assume the maximum $v_{\text{diff}}(\theta)$ is the rotational velocity $v_{\text{rot}} = \text{MAX}[v_{\text{diff}}(\theta)]$, which consequently, provides the angle of the rotational axis in the plane of the sky θ_{rot}. Therefore, for our global cluster definition, we determine rotational values for each cluster from our BAX and NED samples that are computed using equation 3.3 with galaxies that lie ≤ 1.5 Mpc h^{-1} from their respective cluster centres. Thus, providing the final cumulative global cluster rotational velocities and angle of the rotational axes for each, which are denoted as v_{glob} and θ_{glob} respectively. The statistical significance of the presence of rotation from our global definition is calculated for galaxies from both our BAX and NED cluster samples. Following the methodologies of MP17 we determine the ideal (χ_{id}^2) and random (χ_{rd}^2) χ^2 statistic in Equation 3.5 as a by-product of our analysis, formulated as

$$\chi^2 = \sum_{\theta=0}^{360} \frac{(v_\theta - v_{m,\theta})^2}{\sigma_\theta^2 + \sigma_{m,\theta}^2}, \tag{3.5}$$

where v_θ and $v_{m,\theta}$ are the data and model velocity differences per interval θ respectively. The outputted values from Equation 3.5 can be found within Table 3.1. Figure 3.2 presents
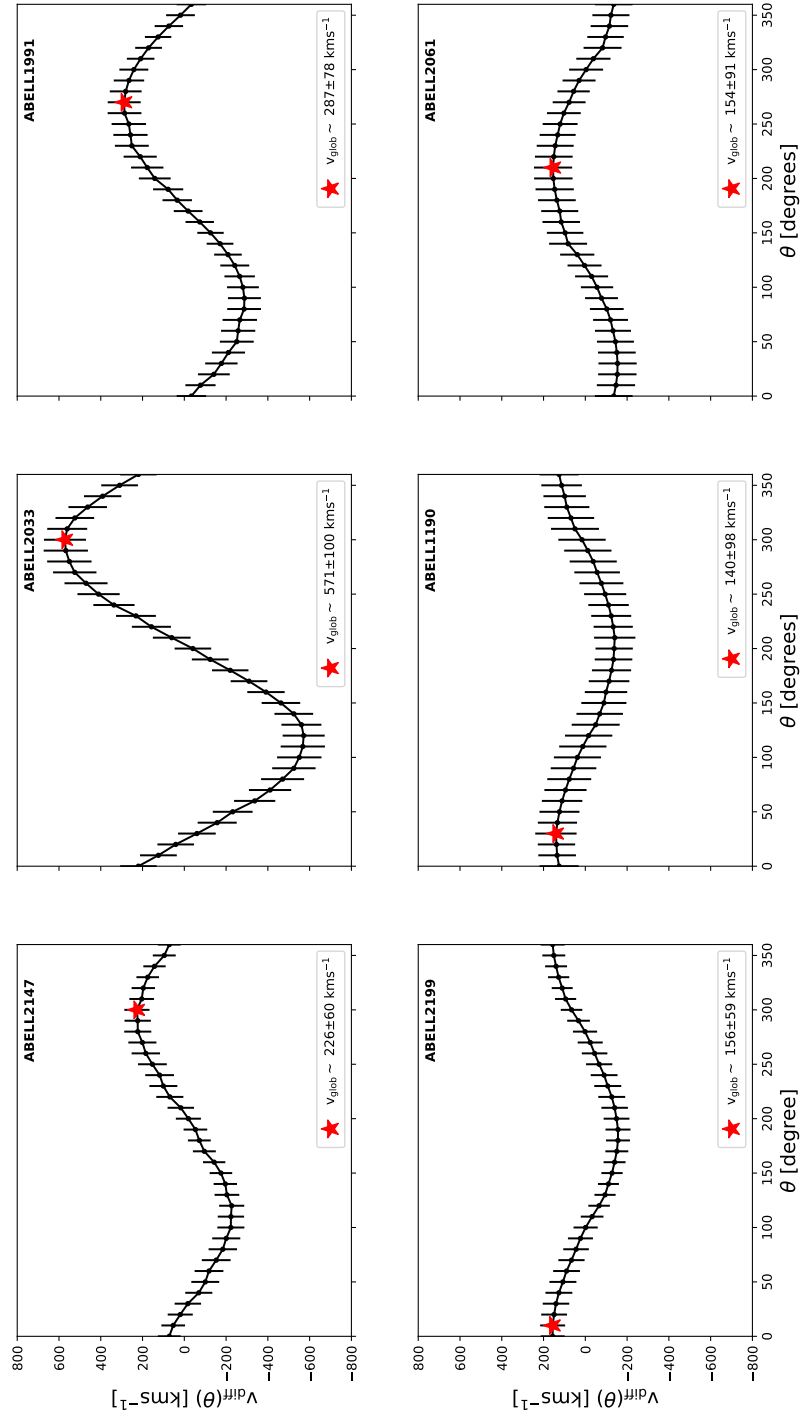
Figure 3.2: A selection of example BAX cluster sinusoidal rotational curves of merging (*top row*) and non-merging (*bottom row*) clusters, as determined by the Δ-test for substructure with galaxies that lie ≤ 1.5 Mpc h^{-1} from the cluster centre, with v_{diff} as a function of θ as per the MP17 methodology outlined in section 3.4.2. The red star marks the point at which $v_{\text{glob}} = \text{MAX}[v_{\text{diff}}(\theta)]$. The uncertainties on the real data curve are derived by the propagation of the standard error as denoted in Equation 3.4.

an example of the MP17 methodology with our BAX merging and non-merging cluster sub-samples (consistent with the examples in Figure 3.1) to determine cluster rotation in the form of the sinusoidal curves produced by artificially rotating the clusters in the plane of the sky.

The thesis presented here is focused on how v_{diff} is dependent on the cluster galaxy sub-populations as a function of cluster radius at different epochs; core-merging events between two originally independent clusters; sub-structuring of galaxies relaxing from a core-merger event; older and relaxed clusters that are homogeneous to our tests of substructure. We therefore, using the calculated global cluster defined values, determine how v_{glob} varies as a function of radius from the cluster centre in incremental units of $0.1r_{200}$ with a coverage of $0 < R \leq 2.5r_{200}$ by fixing our theta to the rotational axis θ_{glob}. An example of the application of this methodology to the individual BAX-defined clusters between merging and non-merging environments, as defined previously by the Δ-test, is depicted in Figure 3.3.

Here we find the merging clusters demonstrate rising profiles from the cluster centre that lead to consistently high $v_{\text{diff}}(\theta_{\text{glob}})$ values throughout to $2.5r_{200}$. In contrast, non-merging clusters possess dampened core-rotational velocities, with Abell 2199 showing a consistent profile out towards $2.5r_{200}$, most likely as a result of the outer galaxy members homogenising with the cluster's angular momentum. The behaviour observed here between the two sub-samples runs parallel to the Δ-test for substructure; increasing core-rotational velocities show correlation with merging environments. This response of environment to the rotational velocities is not completely surprising considering both methodologies are constrained to the same projected radii and radial velocity measurements. It should be noted that this effect is not completely consistent to every Δ-test defined merging cluster, which highlights the limitations of analysing 3D motions through a projected 2D-plane of sky.
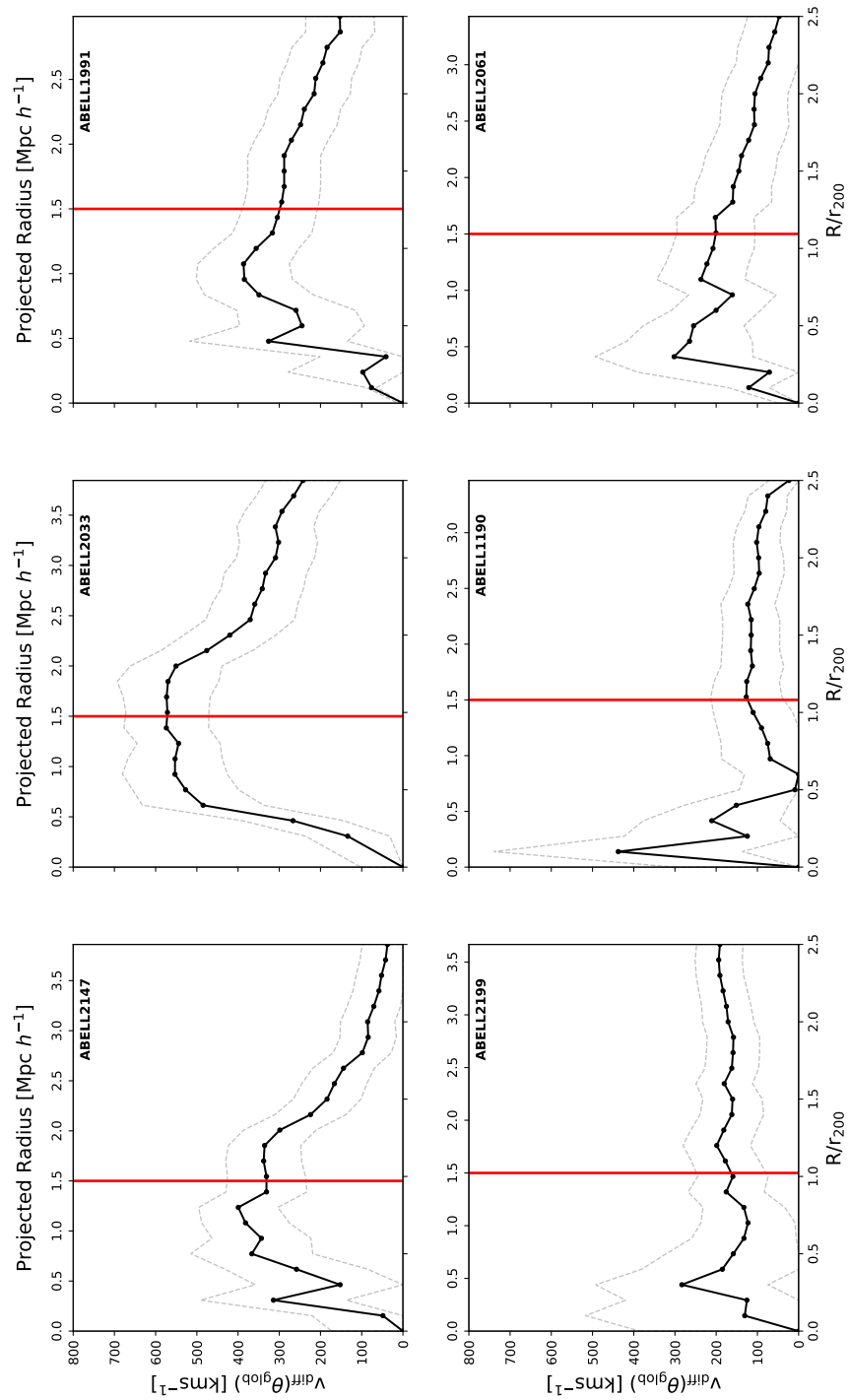
Figure 3.3: A selection of example $v_{\mathrm{diff}}(\theta_{\mathrm{glob}})$ rotational profiles consistent with Figure 3.2, as a function of the projected virial radius R/r_{200} in increments of 0.1, of merging (*top row*) and non-merging (*bottom row*) as determined by the Δ-test for substructure. The red vertical lines represent the point at which the global cluster values are determined and the statistical tests for both substructure and rotation are calculated with galaxies that ≤ 1.5 Mpc h^{-1} from the cluster centre. Note the consistency of higher rotational velocity throughout the merging clusters in comparison to the dampened profiles for the non-merging clusters. The dashed lines represent the uncertainties derived from the propagated standard error as denoted in Equation 3.4.

3.4.3 Dumbbell BCG Clusters

If we assume that the evolution of angular momentum within clusters originates from the off-axial interaction between two smaller clusters, then this could potentially be detected through line-of-sight measurements that are sensitive to determining rotation. Hence, we consider clusters that host multiple BCG components with significant velocity offsets could be the result of recently merged sub-clusters that are relaxing onto a common potential. Therefore, we elected to study a sample of dumbbell BCG clusters for their global rotational profiles with the aim to test if their offset peculiar velocity BCG cores are an indicator of higher levels of merger activity; resembling earlier epochs of post-merger relaxation. Using the volume-limited sample as outlined in section 3.3 with the NED galaxies we perform the Δ-test for substructure from the NED centres to ≤ 1.5 Mpc h^{-1} (see 3.4.1). A comparison between the statistical results, alongside the bubble plots, and the global rotational profiles, as determined in section 3.4.2, of each dumbbell BCG cluster is made. An example of these results for our dumbbell BCG hosting clusters can be found in Figures 3.4, 3.5 and 3.6.

   We, unsurprisingly, do not find a significant correlation between sub-structuring and the presence of multiple off-set velocity BCGs, consistent with the findings of Pimbblet (2008). This is in despite of the use of a standard, more loose, criteria where in this work substructure is deemed significant at $P(\Delta) \leq 0.01$. It is more likely that substructure would not play a key role in the instance of dumbbell cluster BCG cores due to the collisionless nature of galaxies on the timescales presented, especially if the dumbbell cores are in the early stages of a merger between two initially independent potential wells. Abell 3391 is the only cluster in the dumbbell sample found to possess substructure, the bubble plot is presented, along with the rotational profile, in Figure 3.4. It is interesting to note how the rotational profile of Abell 3391 decreases to a minimum at ~ 1.0 Mpc h^{-1}, before rising back to previous v_{glob} values within the same projected radial separation. This, compared with the substantial sub-structuring observed with the bubble plot, illustrates a strong double-component system of rotating galaxies; a fast rotating core and a fast rotating outer region as a result of an on-going active merging event between two originally independent BCGs and their host galaxy clusters. This inference is exacerbated by comparing the same analysis the dumbbell hosting clusters of Abell 3716 and Abell 3653, which can

Figure 3.4: Top: bubble plot of Abell 3391 from the Δ-test, where the size of each circle is proportional to $\pi(e^{\delta_i})^2$, the black cross represents the NED-defined centre and the colours representing varying radial velocity differences $[\overline{cz}_{\mathrm{local}} - \overline{cz}_{\mathrm{glob}}]$. Bottom: the rotational profile of Abell 3391.

Figure 3.5: Top: bubble plot of Abell 3716 from the Δ-test, where the size of each circle is proportional to $\pi(e^{\delta_i})^2$, the black cross represents the NED-defined centre and the colours representing varying radial velocity differences $[\overline{cz}_{\text{local}} - \overline{cz}_{\text{glob}}]$. Bottom: the rotational profile of Abell 3716.
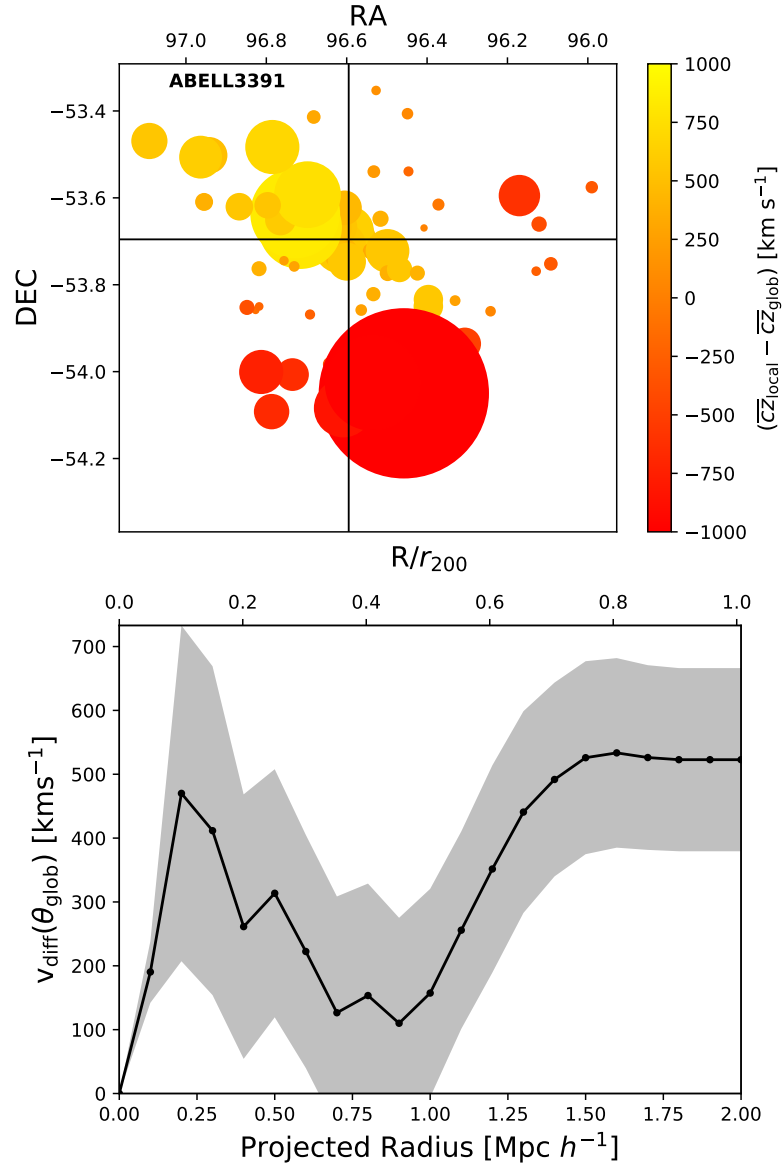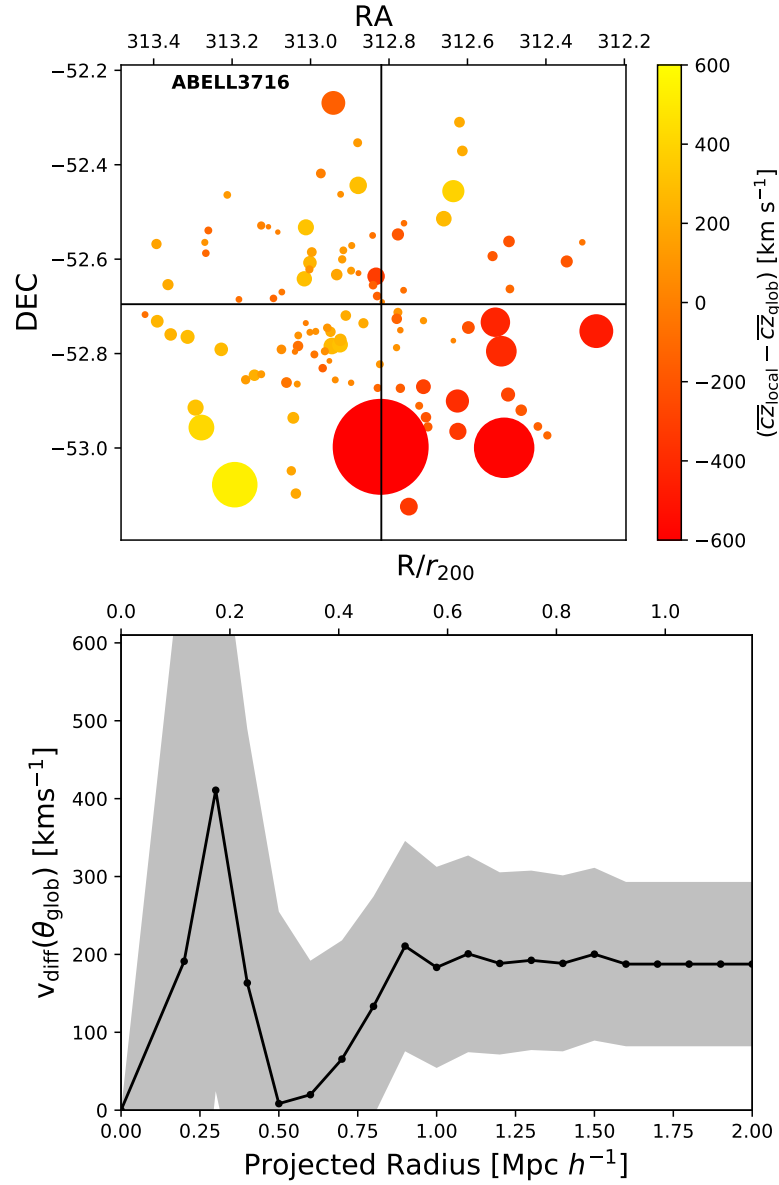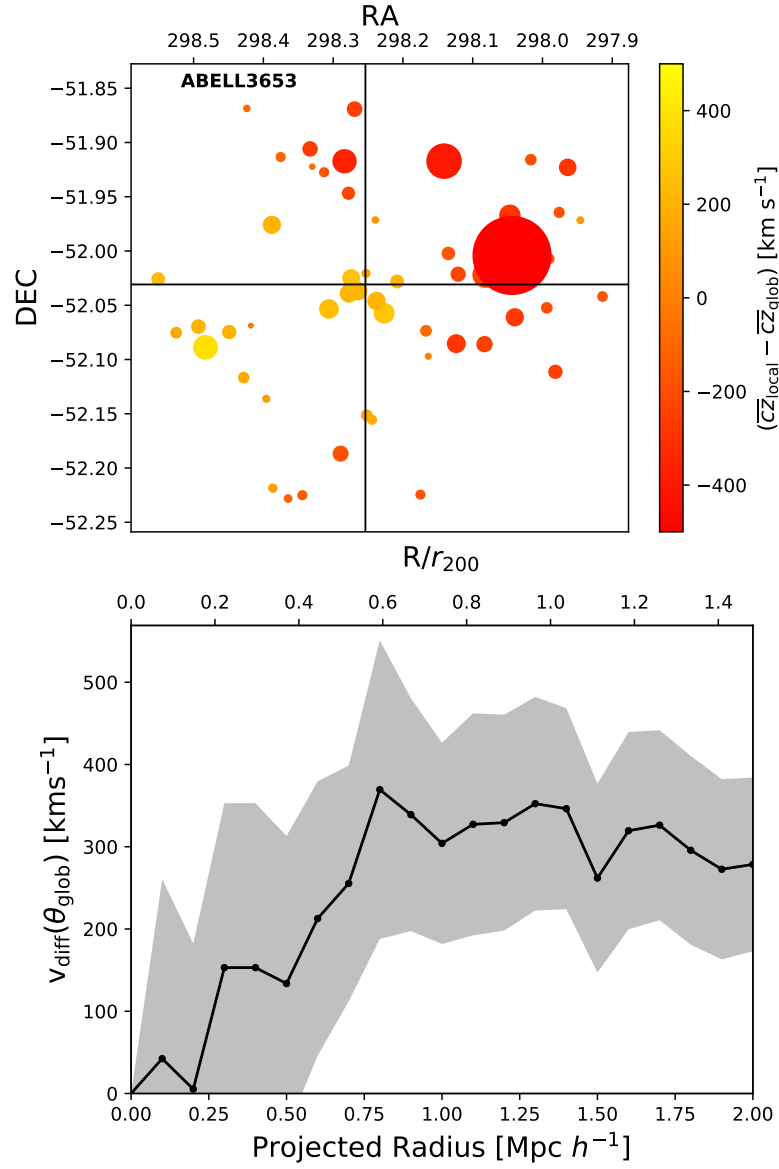
Figure 3.6: Top: bubble plot of Abell 3653 from the Δ-test, where the size of each circle is proportional to $\pi(e^{\delta_i})^2$, the black cross represents the NED-defined centre and the colours representing varying radial velocity differences $[\overline{cz}_{\text{local}} - \overline{cz}_{\text{glob}}]$. Bottom: the rotational profile of Abell 3653.

be seen in Figures 3.5 and 3.6 respectively. The v_{glob} profile of Abell 3716 in particular marries closely to that of Abell 3391, decreasing to a minimum $\lesssim 1.0$ Mpc h^{-1}, before only subtly rising back to dampened levels of rotation where $v_{\mathrm{glob}} \sim 200 \mathrm{km s}^{-1}$. From the bubble plot of Abell 3716 we can see there are some small pockets of deviation from the global values, although, not to the levels found in Abell 3391. We can, therefore, surmise that the Abell 3391 and 3716 are dumbbell hosting clusters in different stages of merging, where the Abell 3391 is in an active phase of merging with intense galaxy-galaxy interactions providing off-axial angular momentum donation. With Abell 3716 in an earlier, less-active phase of merging, where the galaxies are still yet to interact due to their collisionless nature. Abell 3653 presents a v_{glob} profile with a remarkably consistent zero gradient with exception of the bulk increase in rotation at $0.5 \lesssim R \lesssim 1.0$ Mpc h^{-1}. It is also notable how the bubble plot of Abell 3653 has overt displays of substructure towards the west of the sky, where aside from the sizeable peculiar velocity of the BCG addressed in the study of Pimbblet et al. (2006), X-ray analysis conducted by Caglar & Hudaverdi (2017) has shown the location of this substructure to be coincident with another BCG hosting sub-cluster. As further stated within the work of Caglar & Hudaverdi (2017) the presence of harder X-ray emission in the space in-between these two independent BCGs, along with their $\sim 35 \mathrm{kpc}$ off-set from their respective X-ray peaks, is a shock region between their ICM environments indicative of an on-going initial merger phase. Taking into account the projected radial separation between the two BCGs of these sub-clusters ($\sim 500 \mathrm{kpc}$), we can see that the bulk rotation observed $0.5 \lesssim R \lesssim 0.8 \mathrm{Mpc}$ h^{-1} is primarily the result of the foreground BCG towards the west of the sky combined with host sub-cluster's members, as can be seen by the apparent dichotomy in the radial velocities. The clear background and foreground structures, along with the even delineation between them, throughout the projected radius studied creates the impression of a consistent v_{glob} profile, aside from the boost provided by sub-structured west BCG $\sim 0.5 \mathrm{Mpc}$ h^{-1}, which introduces the possibility that the global rotation via our method is merely the result of the z-space difference between the two sub-clusters. With this in mind, however, Caglar & Hudaverdi (2017) have concluded the sub-clusters are gravitationally bound and are in infall at 2400 km s^{-1} with core passage expected in 380 Myr. The peculiar velocities of the dumbbell components of each cluster shown here, along with the two independent Abell 3653 BCG components, are detailed in Table 3.3 for easy comparison. Considering the

Table 3.3: The peculiar velocities of the example dumbbell hosting clusters presented in Figures 3.4, 3.5 and 3.6 within the reference frames of their respective $\overline{cz}$ values, referenced from Pimbblet (2008). The literary values for the BCGs of Abell 3653 are utilised from Caglar & Hudaverdi (2017).

Cluster components	RA (J2000)	DEC (J2000)	$|\Delta cz|$ (km s^{-1})
Abell 3391 DBL1	06 26 20.22	-53 14 57.84	489 ± 133
DBL2	06 26 17.80	-53 14 56.04	68 ± 142
Abell 3653 DBL1	19 53 03.48	-52 07 58.80	736 ± 105
DBL2	19 53 02.76	-52 08 06.00	495 ± 126
BCG1	19 53 01.90	-52 59 13.00	683 ± 96
BCG2	19 52 17.30	-51 59 50.00	43 ± 124*
Abell 3716 DBL1	20 52 00.48	-52 16 18.48	559 ± 92
DBL2	20 51 66.88	-52 16 15.60	255 ± 88

* The uncertainty is propagated through from the literary values.

results from the examples shown here the varying rotation profile, close angular separation between the cores and levels of sub-structuring present in Abell 3391, the cluster must be in a 'post-initial merger' phase; the two cores are relaxing onto a common potential with the surrounding population of galaxies aggressively interacting with one another as a result of their latent friction and global rotation donated from the initial merging phase.

3.4.4   BAX Cluster Stacks

In order to test the dynamical evolution of clusters more generally, we make attempts to observe any contrast in the global rotation profiles across differing cluster environments that could represent different epochs of cluster-cluster merging. Therefore, to build this general picture, we build composite clusters from the BAX sample between those defined as either merging or non-merging, which has the primary benefit of boosting the signal-to-noise for the rotational profiles. For the purposes of calculating $v_{\rm rot}$ using MP17, following the outlined procedure in section 3.4.2, we initiate the following stacking procedure: each cluster is rotated by their respective $\theta_{\rm glob}$ so the rotation axis of each cluster overlaps, we then stack our clusters onto a common RA-DEC grid normalised to each cluster's respective BAX centres along with their normalised ΔV values as per equation 3.3. This
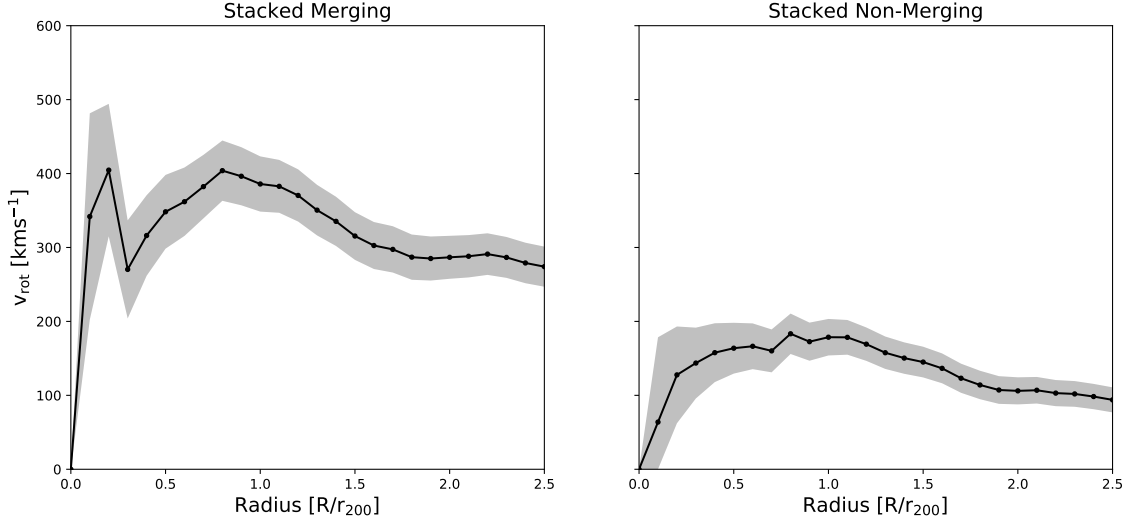
Figure 3.7: Composite rotational velocity profiles of all galaxies as a function of radius (R/r_{200}). The merging rotational profile (*left*) displays a high rotational velocity at the core $\lesssim 0.5R/r_{200}$. In contrast the non-merging rotational profile (*right*) shows dampened core rotation, which collapses close to zero at radii $\geq 0.5R/r_{200}$. The shaded regions represent the uncertainties derived from the propagated standard error as denoted in Equation 3.4.

will lead to the rotational axis of each composite stack becoming $\sim 0°$, which provides, $v_{\text{rot}} = v_{\text{diff}}(\theta = 0)$. The final galaxy contributions to the merging and non-merging stacks are 1286 and 3349 galaxies respectively.

The first result of the complete merging and non-merging composites are highlighted for comparison in Figure 3.7. We can immediately see that the rotational profile of the merging composite in Figure 3.7 possesses very high core rotation peaking up to $\sim 400\text{kms}^{-1}$ within $\lesssim 0.5R/r200$. This result is indicative of the merging sub-sample primarily consisting of relaxing galaxy cluster cores that have undergone recent core-merging processes. The continued high v_{rot} retained throughout to $\lesssim R/r_{200}$ implies this angular momentum donation mechanism is dominant. Where the gradual decline in v_{rot} at $\gtrsim R/r_{200}$ is the result of a decrease in cluster galaxy density, and therefore, interaction probability between them. Contrarily the rotational profile of the non-merging composite presents a dampened core rotation. The immediate inference of this dampening effect presents the non-merging composite to mainly consist of older, more evolved, clusters in more advanced stages of relaxation processes. However, there is the need to consider that the differences in our observations of v_{rot} between the merging and non-merging galaxies are down to their potential difference in mass distributions.
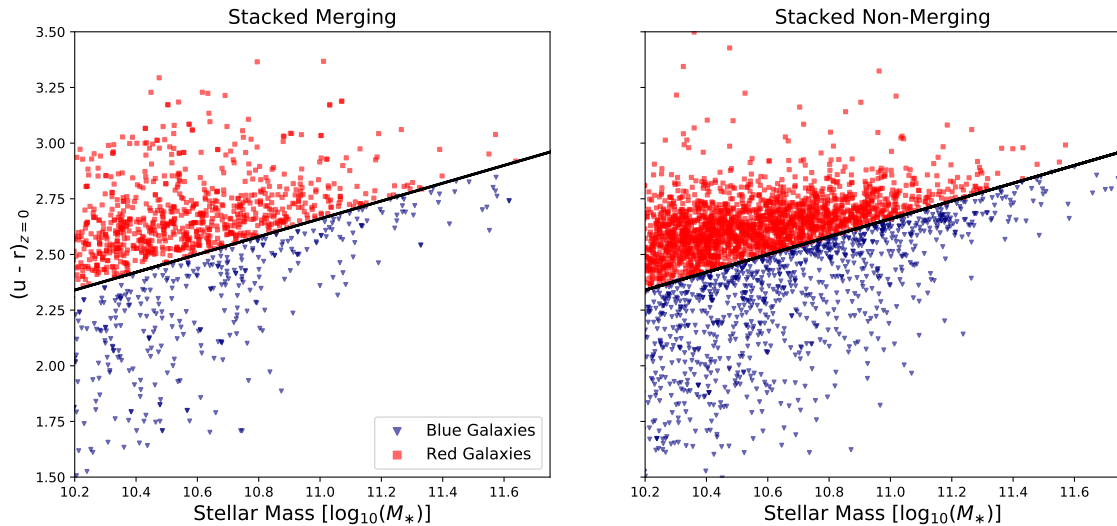
Figure 3.8: The colour distributions of the mass-complete DR8 galaxies between the merging and non-merging samples: $(u-r)_{z=0}$ plotted as a function of $\log_{10}(M_*/M_\odot)$. The black line resembles the linear fit of the centre of the bimodal distribution at quartile increments of $\log_{10}(M_*/M_\odot)$; red galaxies are above the fitted line denoted as red squares; blue galaxies are below the fitted line denoted as blue triangles.

To see how cluster galaxy colour sub-populations respond to the dynamics, activity and environment, the galaxies for the merging and non-merging composites are split into two sub-populations of colour, blue galaxies and red galaxies. In order to account for the biasing of colour distributions with increasing galaxy log stellar mass we find a line of delineation that determines a galaxy's colour, which is computed with a $(u-r)$ colour gradient as a function of the log stellar mass. Following the methodology of Jin et al. (2014), the residual galaxies from the bi-modal $(u-r)$ distribution in bins of increasing stellar mass are used to output the k-corrected linear relation $(u-r)_{z=0} = 0.40[\log_{10}(M_*/M_\odot)] - 1.74$, this is further detailed in equation 4 of Bilton & Pimbblet (2018). We had wished to extend this work to investigate the response between different morphologies similarly to the work of Bilton & Pimbblet (2018), however, for the methodology used to determine the rotational profiles this led to highly incomplete data that did not yield readable results.

All BAX clusters with their member galaxies holding DR8 photometry are k-corrected to the local rest frame ($z = 0$) before being parsed through the linear relation denoted above. Galaxies that lie at greater values from the linear gradient are all classified as red sequence galaxies, with galaxies below classified as blue cloud galaxies. An example of the colour distributions of the galaxies for each stack can be found in Figure 3.8, providing the merging sample with 402 blue galaxies and 862 red galaxies alongside the
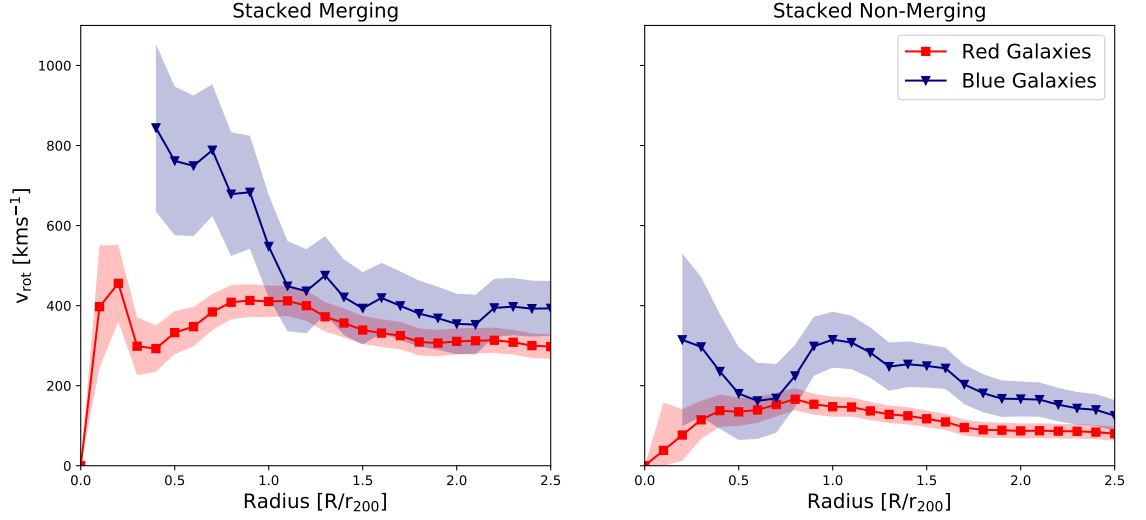
Figure 3.9: Composite rotational velocity profiles split by their colour with the same axes as Figure 3.7. The blue triangle and red square markers of each stack represent the blue and red galaxies respectively. The blue galaxies in the merging cluster stack (*left*) have a high v_{glob} segregation from the red galaxies at $0.4 \lesssim R/r_{200} \lesssim 1.0r_{200}$ before homogenising r_{200}. The non-merging cluster stack (*right*) observes dampened behaviours with 'bumps' $\gtrsim r_{200}$. The shaded regions represent the uncertainties derived from the propagated standard error as denoted in Equation 3.4.

non-merging sample with 1153 blue galaxies and 2184 red galaxies for each stack. The v_{rot} profiles are then calculated for each sub-population, and environment, utilising the same stacking and outputting sequence highlighted previously in the production of Figure 3.7. Figure 3.9 presents the resultant v_{rot} profile with the above implemented methodology. The merging rotational profile in Figure 3.9 depicts the blue sub-population of galaxies with very high segregation of v_{rot} values at $\lesssim R/r200$. However, due to a depletion of blue galaxies towards the core there are no v_{rot} values for the blue sub-population $\lesssim 0.3R/r_{200}$. Consequentially, this implies the observed core rotation from the merging composite in Figure 3.7 is dominated by red sequence galaxies. The immediate conclusion as a result implies that cores of merging clusters consist of evolved, red galaxies in the process of relaxing onto a new common cluster potential via 'back and forth' sloshing motions. The non-merging profile in Figure 3.9 demonstrates a tighter velocity separation between the blue and red galaxy sub-populations, however, there is still a clear segregation in rotational velocity that leads to the connotations of infalling blue galaxies. There is the significant 'bump' in the blue galaxy sub-population at $\sim R/r_{200}$, which could inconclusively be the result of a mixture of infaller and so called 'backsplash' galaxies within the stack (see Pimbblet 2011). The key result from the v_{rot} composite profiles of the
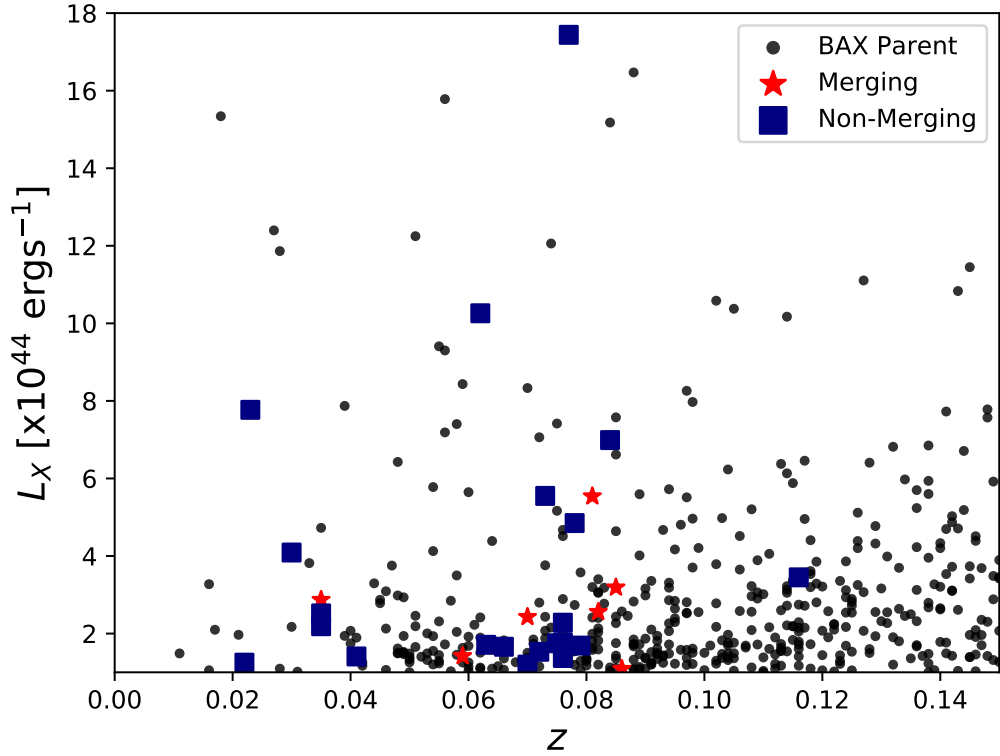
Figure 3.10: The distribution of BAX cluster X-ray luminosities (L_X) against redshift (z). Where the red stars resemble the merging sample and the blue squares depict the non-merging sample.

colour sub-populations is that the two environments are indicative of differing epochs of cluster merging; relaxed galaxies with a population of infalling, or potentially backsplash, blue-galaxies within the non-merging composite and a actively relaxing galaxies onto a common potential from successive merging processes depicting the merging composite.

We show the $L_X - z$ distribution for each BAX sub-sample with comparison to the downloaded BAX catalogue in Figure 3.10 as a proxy for mass distributions present within our BAX sample. Despite some outliers from the non-merging sample, we can see that both the merging and non-merging samples inhabit comparable mass distributions within similar redshifts. However, we briefly test how sensitive the rotational profile composites are to the evolutionary epochs and masses by constraining our BAX samples to those that fall within the redshift range of $0.03 \leq z < 0.09$ and X-ray luminosity values of $< 6 \times 10^{44}$erg s^{-1}, this implementation results in a tighter parity between the two sub-samples. Figures 3.11 and 3.12 illustrate the constrained sample v_{rot} composites.

Despite the tighter constraint, the full composites presented in Figure 3.11 are similar to the unconstrained composite in Figure 3.7, with exception of a dampened core in the merging profile and a general shift in the magnitude of v_{rot} in both merging and non-
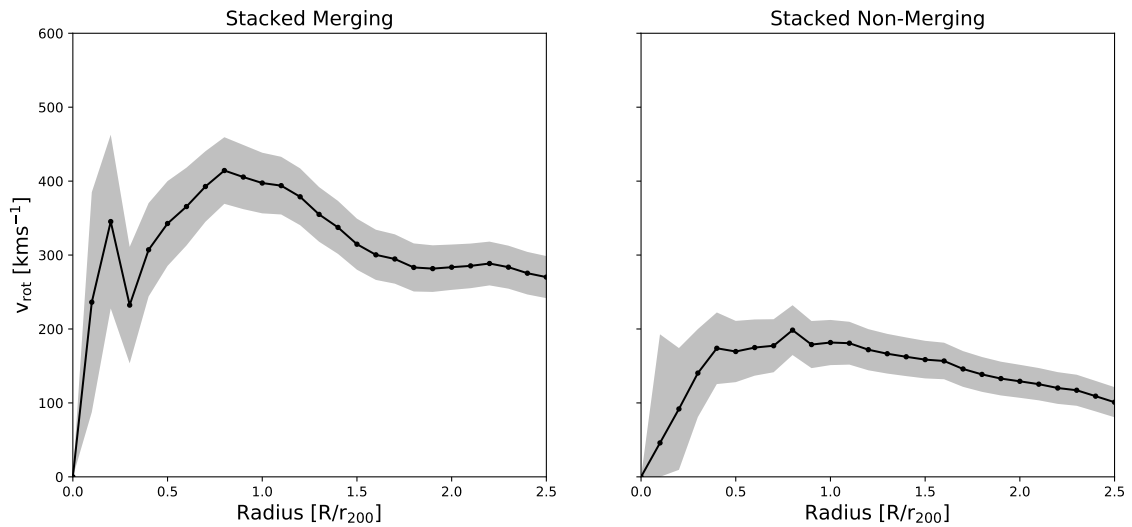
Figure 3.11: Constrained composite rotational profiles, similarly to Figure 3.7, with only BAX clusters lying within redshifts of $0.03 \leq z < 0.09$ and possessing X-ray luminosities in the range $< 6 \times 10^{44}$erg s^{-1}. The overall shape of each of the profiles is retained with some shifts in the magnitude of v_{rot} across both stacks. The shaded regions represent the uncertainties derived from the propagated standard error as denoted in Equation 3.4.
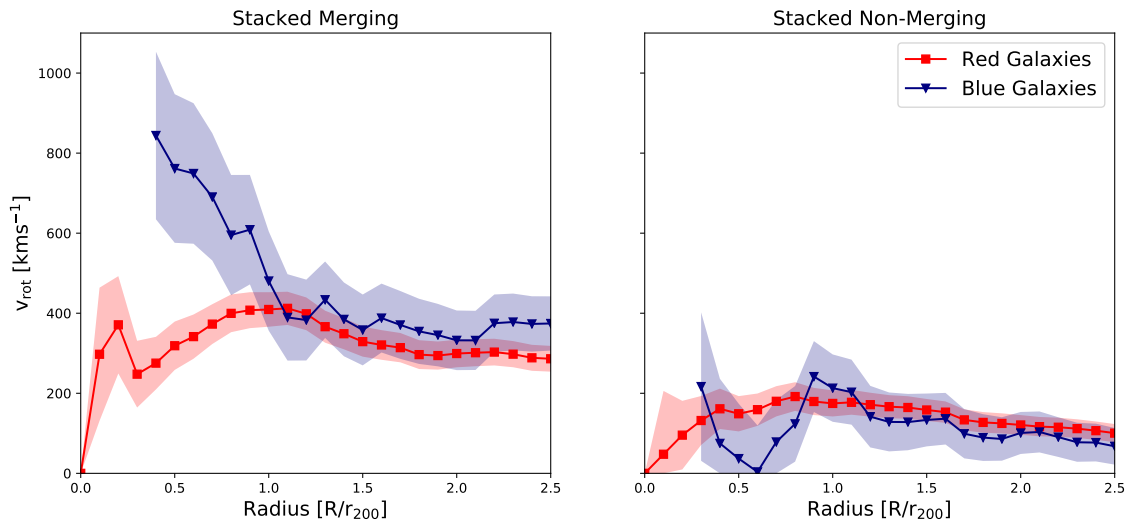
Figure 3.12: Constrained colour composite rotational profiles, similarly to Figure 3.9, with only BAX clusters lying within redshifts of $0.03 \leq z < 0.09$ and possessing X-ray luminosities in the range $< 6 \times 10^{44}$erg s^{-1}. Note the differences in v_{rot} magnitude, especially the blue sub-population in the non-merging composite; loss of signal with a retained shape for values $\lesssim 2.0 r_{200}$. The shaded regions represent the uncertainties derived from the propagated standard error as denoted in Equation 3.4.

merging composites. The most notable difference is found with the constrained colour composite in Figure 3.12 where the blue sub-population of the non-merging stack is subdued with v_{rot} values falling below the red sub-population within the core regions at $\lesssim r_{200}$. The constrained non-merging composite suffers large drops in galaxy numbers contributing to the analysis that leaves 721 blue galaxies and 1365 red galaxies. Although, the general shape of the profile itself is retained with dampened v_{rot} values as has been consistently shown, with the only notable significant loss found at $\sim r_{200}$ with the peak of the retained 'bump' shape of the blue sub-population homogenising with the red sub-population.. With this knowledge, alongside the high uncertainties of the non-merging blue sub-population overlapping with the relatively unaffected red sub-population, indicates that the drop in the rotational velocities within the core regions is not significant in displaying a different picture of non-merging systems as shown in Figure 3.9. This is aided by considering the large omission of non-merging clusters for the constrained composites, it is therefore, no surprise that the non-merging blue sub-population is more sensitive to the constraints. Which is especially the case within the core regions where the number of blue galaxies are fewer. Furthermore, it has already been noted how the shape of the blue sub-population in the non-merging sample is consistent, in addition to the overlapping uncertainties, implies that this is predominantly a signal-noise problem.

3.5   Simulating the Transverse Motions

In this section we describe a 3D simulation of an idealised binary major cluster merger and evaluate how the merger process affects the rotation of the resultant system. We look in particular at how merger phase and viewing angle changes the rotation rate when viewed in an observer-like 2D projection and attempt to draw parallels to the observations.

The simulation is built upon the FLASH Code, a publicly available high performance modular code (Fryxell et al., 2000), utilising the 3D hydrodynamic + N-body capabilities to simulate the gaseous ICM and collisionless dark matter (DM) respectively. Both components being self-gravitating allows the effects of dynamical friction and tidal forces to be captured in the simulation. Taking advantage of the adaptive mesh capabilities of FLASH and refining on particle density results in a maximum resolution in the cluster cores of 19.6 kpc.

The simulation consists of a 1:2 cluster merger with masses of 5×10^{14} M$_\odot$ and 1×10^{15} M$_\odot$ and r_{200} values of 1672 kpc and 2107 kpc respectively. Following the setup procedure described in ZuHone (2011), both clusters are non-rotating cool core clusters possessing spherically symmetric single Hernquist mass profiles (Hernquist, 1990) with a β-profile for the ICM density. The bulk of the mass is provided by 3 million and 6 million DM particles in the smaller and larger cluster respectively. The initial conditions are set such that at the point the two r_{200} cross one another the relative cluster velocity is $1.1V_{\rm c}$ (where $V_{\rm c} = \sqrt{GM_{\rm vir}/r_{\rm vir}}$), in accordance with the average infall velocity onto a cluster found from cosmological simulations by Tormen (1997) and Vitvitska et al. (2002). Following Poole et al. (2006), we use a tangential velocity component equal to $0.25V_{\rm c}$.

To achieve the aims of this section we make the assumption that the simulation's DM particles possess similar motions to that of the galaxies with in the cluster, given that motions of both are collisionless and only feel the effect of dynamical friction. Galaxies would experience higher dynamical friction than a single DM particle given the particles lower mass, however we find that the difference is negligible in this context. Making this assumption allows us to treat the DM particles as galaxies and use their line of sight velocities to calculate the radial rotation rate of the cluster using the same method described previously for the observational data.

Figure 3.13 shows the evolution of projected DM in the simulation. From this we can see that after first core passage each cluster core looses all of its tangential velocity relative to the second cluster. This is as a result of the significant dynamical friction the two cores experience traversing one another. Consequently, all future infalls of the two cores proceed along a straight path that links the two first apocentres. This linear motion has the property of always being perpendicular to the axis of rotation of the merger. The cluster cores oscillate for roughly 2.5 Gyrs after second core passage in which time the pass through one another 6 times, after which they become indistinguishable from one another and hence have merged. If we make the assumption that the BCGs of each cluster remain at the bottom of their respective potential wells throughout the merger then the previous statements regarding the motions of cluster cores can also be considered true for the dumbbell BCGs.

Figure 3.14 shows the radial rotation for the cluster throughout, second passage, from different viewing angles. From this we see that changing the line of sight significantly
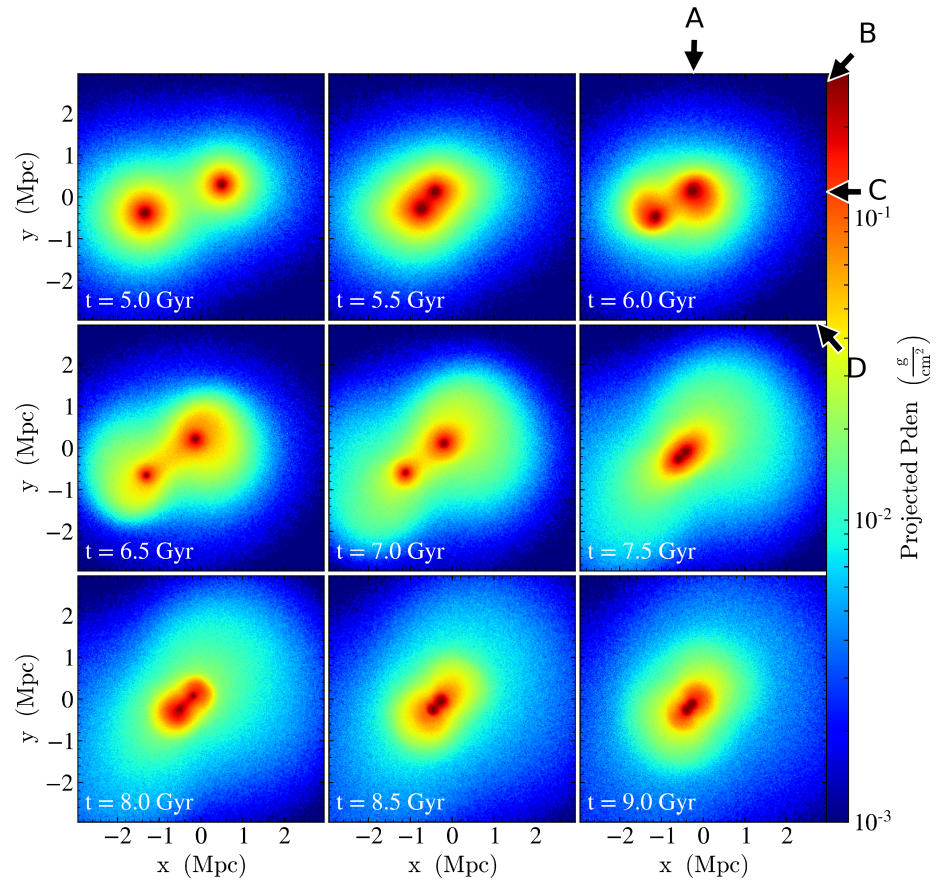
Figure 3.13: Evolution of the simulated cluster merger shown in projected particle density as a proxy for gravitational potential and line of sight galaxy distribution. Labelled arrows depict the four lines of sights from which the rotation of the system is measured throughout the merger. Line of sight A looks down the y-axis axis. B is down the line of second infall, 37 degrees from A. C is aliened with the x-axis. D is perpendicular the line of second infall. All lines of sight are perpendicular the global axis of rotation and are centred on maximum density.
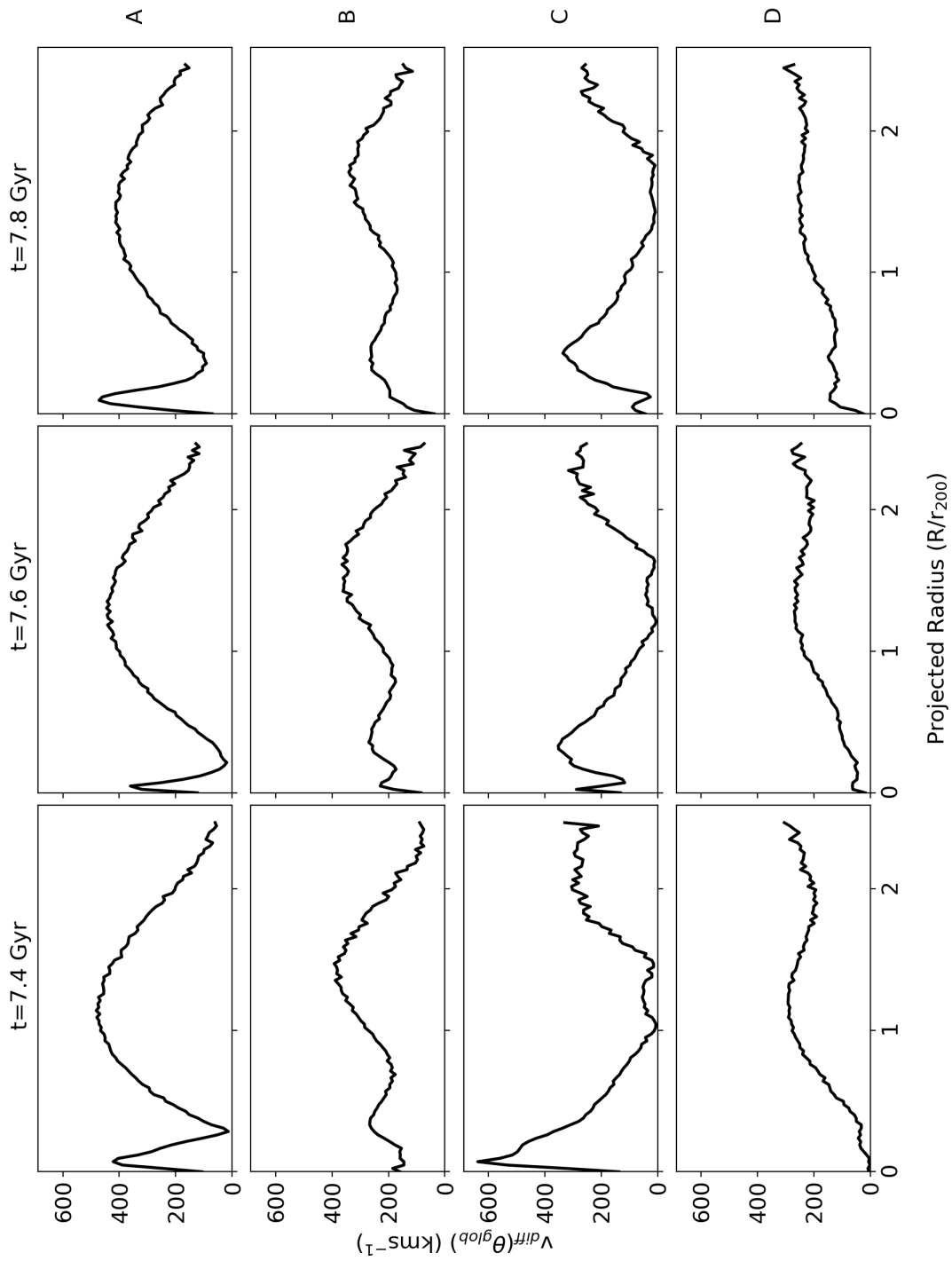
Figure 3.14: Rotational profiles throughout second core passage (7.4 - 7.8 Gyr) from different viewing angles. Radius is normalised to that of the r_{200} of the more massive cluster. Top row shows the evolution for the line of sight down A (as depicted in Figure 3.13) and the second, third and fourth rows are down B. C and D respectively. B and D which are parallel and perpendicular to the line of second infall display relatively continuous profiles where as A and C show significant variation particularly within the core.

alters the effect that second infall has on the measured radial rotation rate of the system. Those viewing angles offset from the linear motion of the cluster cores/dumbbell BCGs (A and C in Figure 3.14) display dramatic changes in the rotation, dropping from maximum to minimum values within one r_{200} and then to increase again at larger radii. Conversely those parallel or perpendicular (B or D in Figure 3.14 respectively) posses far more consistent profiles. The reason for these differences is how the linear motion of the two cores is interpreted via our method of measuring rotation through line of sight motion.

If the merger is viewed such that the line of sight is parallel to the linear motion of the dumbbell BCGs (as with row B) then in the bulk linear motion will average to zero due to the symmetry of the overlapping cores, resulting in it not contributing to the rotation profile. Similarly, a line of sight perpendicular to the linear dumbbell motion would be unable to detect the bulk velocities of the cores due to no fraction of their motion being down the line of sight, this again results in no 'peculiar' increase in rotation whilst still observing the cluster rotation (provided the line of sight was not parallel to the rotation axis where the rotation would not be observable) as can be seen in row D in Figure 3.14.

For mergers viewed with an offset from that of the linear motion of the cluster cores/dumbbell BCGs, such as with rows A and C in Figure 3.14, the linear motion of the cores is incorporated into the radial rotation. This is due to a substantial component of the velocity of the linear motion being along the line of sight, along with the lack of symmetry the projected system possesses, thus resulting in a fraction of the relative velocities of the cores being interpreted as rotation. This manifests itself as high 'peculiar' rotation rates at lower radii.

Rows A and B of Figure 3.14 bear resemblance to the rotation of the dumbbell BCG clusters shown in Figures 3.4 and 3.5, with their rotation rates being high at low radii, but with rapid reductions to minimum values around $0.5r_{200}$ and r_{200}, then finally increasing again at larger radii. The simulation is also in agreement with the prediction for Abell 3391's merger phase drawn from the observations. Based upon observed properties such as angular separation of the cores, rotation profile and the level of sub-structuring, it has been concluded that it is in 'post-initial merger phase' as mentioned above. The simulation supports this conclusion as it is only possible to create a rotation profile similar to that of Abell 3391 during second infall of the clusters (shortly before, during and shortly after second core passage). Beyond this the bulk linear motions of the cores, although
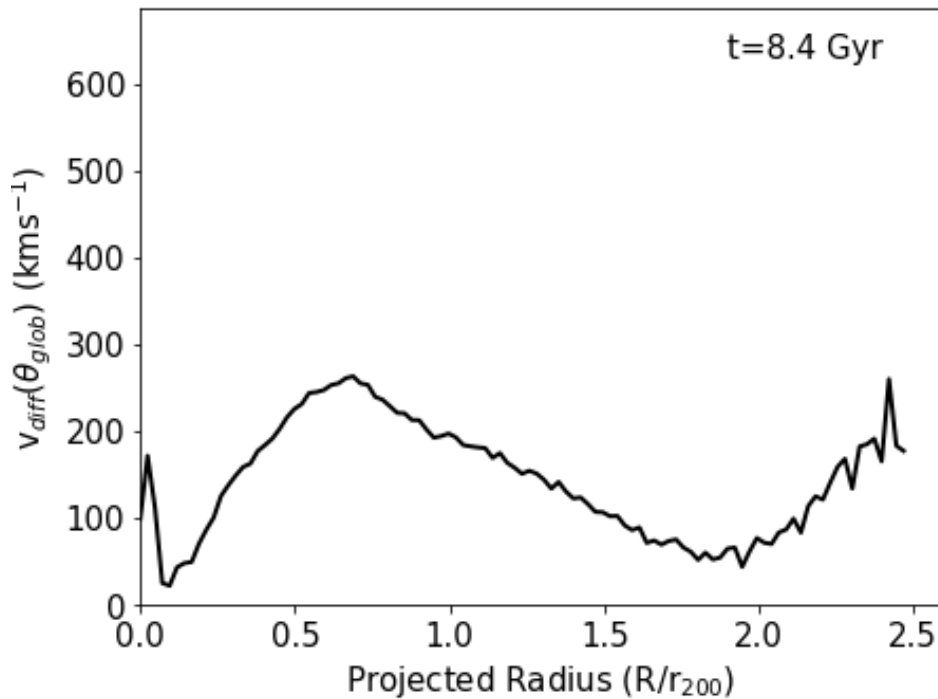
Figure 3.15: Rotational profiles for cluster merger during third core passage from line of sight C (as depicted in Figure 3.13). The effect of the linear infall on the rotation of the cluster has become negligible, contributing only a ~170 kms^{-1} increase in within the very core of the system.

detectable, is only a minor component in the rotation profile, as can be seen in Figure 3.15. Thus comparing Abell 3391 to the simulation suggests that its BCGs are well into their second infall but have not reached second apocentre. This conclusion is in agreement with that made from the observations, however it further constrains what stage the merger has progressed to.

Reverse engineering the previous section gives a framework that could assist observers to further identifying what merger phase a system is in and what angle the observations are being made from. Systems in which dumbbell BCGs are observed suggest an active mergers phase where the two potential wells can have made up to 6 passages through one another. A system that displays 'peculiar' central velocities along with dumbbell BCGs suggests very early phase mergers, in which the central potentials (BCGs) are on their second infall, i.e. shortly before or shortly after second passage. It also means the direction of observation is not perpendicular or parallel to the direction of motion of the dumbbell BCDs, neither is it parallel to the axis of rotation.

This simulation shows that if the viewing angle is favourable then the second infall

of a major merger event, during which dumbbell BCGs would be observable, the linear re-infall of central galaxies creates dramatic changes to the observed radial rotation similar to those seen in the rotational profiles of the dumbbell BCG clusters in Figures 3.4 and 3.5. However it also shows that we should not expect such 'peculiar' rotation in all dumbbell BCG clusters. This is due, in part, to the phase that creates these rotations being relatively short lived (~500 Myr) when compared to the time period in which a dumbbell phase could be observed(~2 Gyr). In addition to this, even if the observation was within the 500 Myr window, any viewing angles aliened perpendicular or parallel to the linear motion of the re-infall are unable to detect the 'peculiar' rotation.

3.6   Discussion & Summary

Despite the obvious caveat in the disparity between our merging and non-merging cluster sample sizes in this work, they still help to provide a consistency in our current understanding on the formation and evolution of galaxies within different cluster environments found in previous works. For example, the observed 'mixing' of the red and blue sub-populations of galaxies we see in Figure 3.9 corresponds to rising velocity dispersion profiles of mixed red and blue ellipticals found in Bilton & Pimbblet (2018); Mixing of sub-populations kinematically suggests sub-structured pre-processed galaxies are on infall as a result of galaxy-galaxy interactions (de Carvalho et al., 2017) either prior, or during, off-axial mergers between two sub-clusters; the pronounced population of late-type galaxies on infall in merging environments as inferred by the blue sub-populations of galaxies gaining angular momentum $\lesssim r_{200}$, chiefly thought to be the result of galaxies with spiral morphology that have survived pre-processing (e.g. Cava et al. 2017; Costa et al. 2018; Bilton & Pimbblet 2018; Nascimento et al. 2019). The study of rotational profiles would have been aided by the addition of understanding how different morphological sub-populations of cluster galaxies contributed to each of the colour profiles. However, due to the limitations on resolving such features for every DR8 galaxy, no meaningful analysis could be conducted via the methodology we use within this work.

A common problem with observational studies of galaxy clusters is the limitation of the apparent 2D plane of sky and trying to ascertain information projected onto that sky. This inherently leads to projection effects due to our inability as observers to comprehend

the precise angular and radial separations, therefore, determining the true direction of the rotational axis is not trivial. The main problem is trying to isolate the true mechanisms behind the observations we record in this work utilising MP17's methods. All current observational techniques (e.g. Kalinkov et al. 2005; Hwang & Lee 2007; Manolopoulou & Plionis 2017) all determine a velocity gradient between some sort of observer defined axis. This observer defined axis within itself can be flawed as a result of our chosen centres, with this caveat in mind, we try and maintain consistency through using literary X-ray centres since they are commonly parallel to a cluster's potential. Therefore, this could potentially indicate that the various techniques we currently have at our disposal are specious, especially when considering we are trying to infer a variety of peculiar motions in a singular z-space. These are the same issues faced with our delineation between merging and non-merging environments via the Dressler & Shectman (1988) Δ-Test, where, substructure is determined through local z-space deviations; does the presence of substructure genuinely infer rotation via angular momentum donation, or, is this a mere deceptive emulation due to overlapping substructures biased by our limited ability to observe galaxy motion? Ideally, studies on global cluster rotation should combine and model observations between the ICM and the member galaxies; the collisional ICM leaves behind stronger markers of interaction and rotation than the more random (and therefore noisy) collisionless galaxies, which both operate on different time scales (Roettiger & Flores, 2000). Furthermore, studies using the kinetic SZ-effect to simulate and analyse the motions of the ICM have shown that the angular momentum and direction between the ICM and dark matter both correlate significantly to imply dark matter dominance (Baldi et al., 2017, 2018).

Overlapping substructures in our projected space at least yields results for interactions of galaxies within the cluster. However, there is still the possibility of interloping substructures from neighbouring clusters. This is in spite the use of caustic techniques (Diaferio & Geller, 1997; Diaferio, 1999) to estimate the mass profiles and membership, as well as removing heavily interloping substructures using the Einasto et al. (2001) catalogue. Some examples of interloping can be found in clusters such as Abell 2061 with possible infalling galaxies via a filament from Abell 2067 (Farnsworth et al., 2013); Abell 2065 is believed to be currently undergoing a merger with evidence of two independent sub-clusters with clear structure due to an unequal core merging event (Chatzikos et al.,

2006); Abell 3391 is in relatively close proximity to Abell 3395, with X-ray observations indicating the presence of a filament between the two clusters, highlighting the possibility of potential foreign foreground structures (Sugawara et al., 2017). Although, the use of the cluster caustics performs reasonably in delineating between cluster and non-cluster members, which offsets the reality of a few stragglers invading our cluster membership. The antithesis to this problem is that by applying our caustics to the more chaotic merging clusters from our sample we result in eliminating genuine cluster members due to the cluster galaxies gaining kinetic energy and increasing their interactions.

In this work we have acquired MPA-JHU DR8 galaxies cross-matched with a sample of galaxy clusters as defined by the BAX cluster database to build their membership, which are stacked in accordance with their environments, as determined by the Δ-test for substructure (Dressler & Shectman, 1988). This is complemented by NED galaxies of dumbbell clusters (Gregorini et al., 1992, 1994) to allow for comparisons of the dynamics from more extreme and complex systems. Finally, we compare our perspective rotation methodology from MP17 between our observational DR8 and NED data against FLASH 3D hydrodynamic and N-body simulations of merging clusters (Fryxell et al., 2000).

The key results are summarised as follows:

(i) Cluster rotation v_{rot} profiles show consistently high rotation until $\sim r_{200}$ with the merging cluster environments (relaxing clusters), whereas non-merging environments commonly depict low v_{rot} profiles indicative of relaxed clusters undergoing a reduction in the sloshing of galaxies caused by dynamical friction.

(ii) Merging cluster environments in our stack exhibit strong core rotation ($\lesssim 0.5r_{200}$) by the red galaxy sub-population, inferring a sloshing of evolved galaxies as they relax onto a common potential.

(iii) The blue galaxy sub-populations in our merging cluster stack have a high v_{glob} segregation from the red galaxy sub-population in the core regions ($0.4 \lesssim R/r_{200} \lesssim 1.0r_{200}$) before homogenising with the red sub-population, this may be a consequence of pre-processed sub-groupings that are on infall.

(iv) The presence of multi-core dumbbell BCGs in clusters displaying variable v_{glob}

profiles as a result of large peculiar velocities, in-situ of the cluster's rest frame, is indicative of a recent core merger between two originally independent sub-clusters.

(v) Peculiar rotation velocities in dumbbell BCGs are a result of second infall of core galaxies along a linear trajectory that is not aligned with or perpendicular to the line of sight.

(vi) The presence of the peculiar rotation velocities are not obligatory in dumbbell BCG clusters due to phases of the dumbbells existence that do not have significant effects on the profile. in addition there are viewing angles that are incapable of measuring the linear motion as the peculiar rotation.

Acknowledgements

4. Cluster Galaxy AGN Kinematics

"The calmer thought is not always the right thought, just as the distant view is not always the truest view."

– Nathaniel Hawthorn

4.1 Prologue

The Chapter presented here is the published work entitled "*The Impact of Disturbed Galaxy Clusters on the Kinematics of Active Galactic Nuclei*", under MNRAS **499**, 3792 (Bilton et al., 2020). The succeeding sections of this Chapter are obtained from the pending article, which was written and led by myself with the following co-authors: Kevin Pimbblet and Yjan Gordon. As the lead author I was the sole contributor to the work by outlining the science case, managing the data, performing the analysis and the formulation of the results into the following article. Any contributions by my co-authors were limited to helping to maintain good standards through scientific feedback, assessing quality and consistency of English used and any minor typographical errors one may casually miss. The article has been slightly altered to fit the format of a thesis, therefore to this end, the abstract has been omitted to avoid repetition of the whole thesis.

4.2 Introduction

In a hierarchical universe clustering is inevitable due to the gradual accretion and accumulation of galaxies through successive merger events as a result of gravitational perturbation from the Hubble flow (Regos & Geller, 1989). Consequentially, the continued coalescing of galaxies leads to an increase in the likelihood of galaxy-galaxy interactions due to the greater number density of galaxies found at low radii towards the centre of their host galaxy cluster (Moore et al., 1996, 1999). Galaxy clusters are therefore harborers of activity and are found to play host to driving the observed evolutionary differences between cluster and field populations of galaxies (Owers et al., 2012). These environment-induced gradual dichotomies in galaxy evolution are illustrated through their morphologies, as early-type

galaxies become ubiquitous within the densest regions of galaxy groups and clusters, vice versa for late-type galaxies(Oemler, 1974; Dressler, 1980; Houghton, 2015). The trend continues with galaxy colours that typically indicate the average ages of the inhabiting stellar population with redder galaxies, commonly associated with early-type galaxies, lying in regions pertaining to higher number densities (Hogg et al., 2003, 2004; Lemaux et al., 2019). The implication of finding redder galaxies at higher densities is the inference of this correlating negatively with their star formation rates and it is indeed shown that increased density leads to relatively quenched levels of star formation (Gómez et al., 2003; van den Bosch et al., 2008; Bamford et al., 2009). Despite these determined relationships between galactic properties and density they are not the dominant cause for the observed galaxy evolution since field populations are generally mixed, indicative of natural galactic evolution (e.g. see Kauffmann et al. 2004; Blanton et al. 2005; Lemaux et al. 2019; Bluck et al. 2020).

The local environment is not purely defined by the greater number densities of cluster galaxies and their interactions with each other however. There is a diffuse hot gas that pervades the space between the cluster galaxies, the Intracluster Medium (ICM), which has been observed to interact with recently harassed, infalling late-type galaxy populations in particular (e.g. Gunn & Gott 1972). As a galaxy gains higher velocities on its passage down into the cluster's deep gravitational potential well, the increasing ICM density will induce ram-pressure stripping of any gas present within the disc and operates on timescales that are inversely proportional to the ICM density (e.g. see Gunn & Gott 1972; Abadi et al. 1999; Quilis et al. 2000; Roediger & Brüggen 2007; Sheen et al. 2017). If an infalling galaxy experiences continuous ram-pressure stripping the ultimate consequence is the impediment of the star formation processes until quiescence is reached. The ICM can also interact with an infalling galaxy's own diffuse hot gas halo, which can be easily stripped and, again, result in the premature quenching of star formation processes as their cold gas fuel reservoirs deplete and strangle the galaxy (Larson et al., 1980).

Aside from the atypical intrinsic properties of cluster galaxies that are studied, more recent works investigate the possible connections between the presence of active galactic nuclei (AGN) hosted by cluster galaxies and their local cluster environment. AGN are themselves a by-product of the accretion of matter into a galaxy's central supermassive black hole, however, not all galaxies possess an active nucleus and this is evident through

the observed evolution of quasars as a function of redshift, which peaks at $z \sim 2$ similarly to the Madau et al. (1998) plot of star formation history (e.g. see also Kauffmann & Haehnelt 2000; Ellison et al. 2011; Kormendy & Ho 2013). The implications of this signify how AGN must play a role in modulating the growth of stellar mass via some sort of co-evolutionary mechanism, an inference which is strengthened by the strong correlations found between supermassive black hole masses and their host stellar bulge masses (see Magorrian et al. 1998; Silk & Rees 1998; Ferrarese & Merritt 2000; Gebhardt et al. 2000). The transient nature of AGN, albeit on long timescales, is indicative that their 'active' nature is dependent on some sort of fuel being accreted onto the central black hole as well as a fuelling mechanism to describe the transport of this fuel. The mechanisms involved in triggering AGN activity are currently not comprehensively understood, however, it is known the fuel supply is in the form of cold gas that could also contribute to the star forming processes within the host galaxy (Reichard et al., 2009). As a result reservoirs of cold gas are needed to continually feed the nucleus to make it active, however, the dense regions of galaxy clusters and groups are relatively poor sources of cold gas, although, evidence shows the AGN that do lie within these dense regions are triggered either by cooling gas flows or galaxy-galaxy mergers (Moore et al., 1996, 1999; Sabater et al., 2013). One recent revelation for a possible origin of AGN triggering within galaxy clusters is the observed correlation between ram-pressure stripped galaxies–known as 'jellyfish galaxies'–and the presence of an AGN residing within these galaxies, implying that the stripped material of an infalling galaxy can cause a migration of fresh cold gas to its supermassive black hole (e.g. Poggianti et al. 2017; Marshall et al. 2018). However, jellyfish galaxies are prevalent in the cores of galaxy cluster (Jaffé et al., 2018), whereas AGN-hosting cluster galaxies are found to preferentially lie within infall regions (Haines et al., 2012; Pimbblet et al., 2013). This corresponds to the reduction in AGN fraction suggesting that AGN are more likely to become quenched in core regions compared to the infall regions (Pimbblet & Jensen, 2012). The AGN reduction seemingly continues to operate across group scales with Gordon et al. (2018) showing a consistent dichotomy in AGN fractions between virialised and infalling regions for group masses $\log_{10}(M_{200}/M_{\odot}) \geq 13$.

Galaxy clusters themselves have less than peaceful histories, with many examples examples of sub-cluster merging processes through interactions in the ICM, the formation of cold fronts and the sub-structuring of the cluster galaxies (e.g. Dressler & Shectman

1988; Markevitch et al. 2002; Ghizzardi et al. 2010; Owers et al. 2011, 2012; Caglar & Hudaverdi 2017). The dynamical states of galaxy clusters can consequently imprint these merger events through their cluster galaxy membership as demonstrated with the aforementioned sub-structuring and grouping of cluster galaxies. Tests for determining the degree of sub-structuring, such as that of Dressler & Shectman (1988), can be used as proxies for delineating between 'merging' and 'non-merging' cluster environments. Analysing the cluster galaxy kinematics of these opposing cluster dynamical states via velocity dispersion profiles (VDPs) and rotational profiles can provide an insight into how cluster galaxies, and their sub-populations, respond kinematically to their environment as a function of radius (Hou et al., 2009, 2012; Bilton & Pimbblet, 2018; Bilton et al., 2019; Morell et al., 2020). In addition, VDPs themselves can independently act as proxies for determining a merging environment if they depict a rising profile as one increases the clustocentric radius within the virial regions, vice versa for non-merging environments (see Menci & Fusco-Femiano 1996; Hou et al. 2009; Bilton & Pimbblet 2018). The AGN activity present within galaxy clusters is found to be commonplace within clusters undergoing merging processes, acting as a repercussion to an increase in ram-pressure stripping as a result of the ICM interactions between two sub-clusters (Miller & Owen, 2003; Sobral et al., 2015; Ruggiero et al., 2019; Ricarte et al., 2020). Therefore, AGN-hosting cluster galaxies should have their own unique kinematic response to their local environment, providing two unique VDP and rotational profile 'signatures' corresponding to the two aforementioned dynamical states of merging and non-merging galaxy clusters.

Within this work we seek to test the kinematic response of AGN-hosting cluster galaxies between the aforesaid two galaxy cluster dynamical states via VDPs, which are determined utilising a weighted Gaussian smoothing kernel as outlined by Hou et al. (2009), and via rotational profiles based upon the work by Manolopoulou & Plionis (2017) and expanded on in Bilton et al. (2019). Thereby allowing for the exploration into whether or not the AGN-hosting cluster galaxy kinematics provide results that correspond to prior studies; AGN activity is predominantly found in infalling galaxies while being encompassed by a merging cluster environment. This is accomplished through obtaining archival galaxy data from the Sloan Digital Sky Survey (SDSS; York et al. 2000) in which to build a sample of clusters as defined by X-ray parameters with an X-ray catalogue. These data and the methodologies in the way they are procured and handled is elaborated within Section

4.3. The computation and output of the AGN kinematics with the VDPs and rotational profiles are detailed in Section 4.4. Which is followed by discussing the interpretation of the cluster galaxy AGN kinematics in Section 4.5. Concluding with a discussion and summary of the results presented throughout the body of this work in Section 4.6.

Throughout the work presented here we assume a ΛCDM model of cosmology with $\Omega_M = 0.3$, $\Omega_\Lambda = 0.7$, $H_0 = 100h$ km s^{-1} Mpc^{-1}, where $h = 0.7$.

4.3   The Data

We briefly outline the methods involved in the procurement and handling of the data used in order to conduct the aims of this work, which follows the same procedures–as well as providing the same cluster sample–used in Bilton et al. (2019). This process involves utilising the X-ray Galaxy Clusters Database (BAX; Sadat et al. 2004) to collate a list of X-ray clusters that is constrained through parameters defined by the authors. The respective coordinates for each galaxy cluster that meet the applied parameter limits are then cross-matched with galaxies from SDSS Data Release 8 (DR8; Aihara et al. 2011) to build their cluster galaxy memberships. To provide a definition for our AGN-hosting cluster galaxies, these DR8 galaxies include the $\sim 9,400$ deg^2 of spectroscopy with a magnitude depth of $m_r \lesssim 17.7$ mag in the r-band (Strauss et al., 2002). Specifically, the DR8 spectra were built from the SDSS spectrograph that was comprised of 640 fibres per plate, with each fibre matching to objects on the focal plane of the sky and which are visible to the SDSS. The spectral resolution ranges from $\lambda/\Delta\lambda = 1500 - 2500$ for the wavelength range of $\lambda = 3800$Å-9000Å. Additionally, stellar mass estimates from the MPA-JHU value added catalogue are cross-matched with the cluster galaxies, which are used in order to maintain completeness of the sample(Kauffmann et al., 2003; Salim et al., 2007).

4.3.1   The Cluster Sample and Their Cluster Galaxies

Utilising the X-ray BAX catalogue we parameterised our sample of clusters to lie within the redshift range $0.0 \leq z \leq 0.15$ to obtain a varied selection of clusters at different epochs of dynamical evolution, while not going too deep so as to impact on the cluster galaxy numbers in order to maintain completeness. We further constrain our cluster sample by

considering only clusters the X-ray luminosity range $1 < L_X \leq 20 \times 10^{44}$ ergs^{-1} so we select the most massive clusters, resulting in a pool of 431 galaxy clusters. The DR8 galaxies are matched to their galaxy cluster environments with an initial ± 0.01 z-space and a ≤ 10 Mpc h^{-1} projected radius cut from the their respective clustocentric coordinates on the plane of the sky; each cluster galaxy candidate's projected radius is scaled from the BAX-defined galaxy cluster redshifts relative to our pre-defined flat cosmology. The key global cluster properties of mean recession velocity ($\overline{cz}_{\mathrm{glob}}$) and velocity dispersion (σ_{glob}) are calculated for each cluster for cluster galaxies that lie ≤ 1.5 Mpc h^{-1} from their cluster centres. The velocity dispersions are deduced using the more robust square-root of the biweight mid-variance as defined by Beers et al. (1990). The uncertainties for the mean recession velocity and velocity dispersion values are derived following the methodology of Danese et al. (1980). We normalise the cluster galaxy redshifts to their respective galaxy cluster mean recession velocities, which is defined as

$$\Delta V = c \left(\frac{z_{\mathrm{gal}} - z_{\mathrm{clu}}}{1 + z_{\mathrm{clu}}} \right), \tag{4.1}$$

where we apply a rather restrained upper limit on the velocity around the cluster mean to $\Delta V = \pm 1500$ kms^{-1} to mitigate against high likelihood of interlopers. To define the cluster galaxy membership we deduce phase-space surface caustic profiles using the methodologies of Diaferio & Geller (1997); Diaferio (1999), which provide an enclosed trumpet-shaped density profile as a function of the projected radius R for each cluster, thereby formalising the galaxy cluster membership to those galaxies confined within these caustic profiles (Gifford & Miller, 2013; Gifford et al., 2013). The consequence of these density profiles, where the density evolves as $\rho(r) = 3M(r)/4\pi r^3$, is in the computation of the r_{200} and M_{200} that correspond to the values of clustrocentric projected radius and cluster mass where $\rho(r) = 200\rho_c$, where $\rho_c = 3H_0^2/8\pi G$ is the critical density of the flat Universe previously defined. Therefore, throughout this work we assume the virial radius of each cluster, which is deemed to be the radial point of virial equilibrium that lies in between galaxies collapsed onto a cluster potential with those that are infalling and beyond, to be approximately $R_{\mathrm{vir}} \sim r_{200}$.

Since we have a sample of clusters across varying redshifts of $z \leq 0.15$ we need to be considerate of the sample of available cluster galaxies and maintain completeness in order

to mitigate against the Malmquist bias (Malmquist, 1925). We therefore find our cluster galaxies to be complete for those that possess stellar masses of $\log_{10}(M_*/M_\odot) \geq 10.2$. The final steps in the curation of the cluster sample involve simple sanity checks against the interlacing between large-scale structures and whether the galaxy clusters themselves are enriched with enough galaxies for analysis; the Einasto et al. (2001) catalogue was cross-matched to the preliminary cluster sample to help remove known closely-spaced cluster-cluster environments in addition to maintaining a high cluster galaxy richness with the omission of $N_{2.5r_{200}} < 50$ galaxies, where $N_{2.5r_{200}}$ is the number of galaxies at $< 2.5r_{200}$. These procedures lend to a total of 33 galaxy clusters in our sample.

4.3.2   Delineating Between Merging and Non-Merging Galaxy Clusters

In order to increase the signal-to-noise of our kinematic analysis between the merging and non-merging dynamical states we will stack cluster galaxies, which are normalised to their respective ΔV (as per equation 4.1) and r_{200} values, into two sub-samples according to their host galaxy cluster's dynamical state. However, we first need to establish what we consider to be a 'merging' (dynamically active or relaxing) or 'non-merging' (dynamically inactive or relaxed) galaxy cluster. If we are to assume that those galaxy clusters currently undergoing merging processes increase the likelihood of their member cluster galaxies to interact with one another, then one could infer the presence of cluster merging through tracing the intensity of galaxy-galaxy interactions within each cluster. We therefore implement the Dressler & Shectman (1988) statistical test for substructure (Δ-test) to determine the strength of these galaxy-galaxy interactions as our proxy for determining if a cluster is indeed a merging system. The Δ-test we employ here compares the differences between the local mean ($\overline{cz}_{\mathrm{local}}$) and local velocity dispersion (σ_{local}) with their global counterparts that are calculated for galaxies ≤ 1.5 Mpc h^{-1} from the cluster centre (see equation 4.2). The local values are computed for each galaxy and its $N_{\mathrm{nn}} = \sqrt{N_{\mathrm{glob}}}$ nearest neighbours, where N_{glob} is the number of galaxies that lie ≤ 1.5 Mpc h^{-1}.

$$\delta_i^2 = \left(\frac{N_{\mathrm{nn}} + 1}{\sigma_{\mathrm{glob}}^2}\right)[(\overline{cz}_{\mathrm{local}} - \overline{cz}_{\mathrm{glob}})^2 + (\sigma_{\mathrm{local}} - \sigma_{\mathrm{glob}})^2], \tag{4.2}$$

where δ_i represents the deviations between the local and global values for a single galaxy and is iterated through for each galaxy ≤ 1.5 Mpc h^{-1} to produce the sum $\Delta = \sum_i \delta_i$.

The Δ-test is found to be very sensitive in determining the presence of substructuring amongst galaxies and its significance can be found at ≥ 99 per cent when weighted against N_{MC} Monte Carlo velocity reshuffles (Pinkney et al., 1996). Therefore, we apply the Δ-test to our cluster sample where substructure is determined to be present at $P \leq 0.01$ with our observational Δ_{obs} weighted against 1000 Monte Carlo velocity reshuffle simulations Δ_{MC}. Where the value of P is computed from the frequency, f_{MC}, in which the condition $\Delta_{\mathrm{obs}} < \Delta_{\mathrm{MC}}$ is met to give $P = f_{\mathrm{MC}}/N_{\mathrm{MC}}$. This results in two sub-samples of clusters, that are originally defined within Bilton et al. (2019), that represent our merging and non-merging dynamical states that hold 8 and 25 clusters respectively. These clusters and their basic properties, including their Δ-test P-values, can be found categorised by their dynamical states within Table 4.1.

4.3.3   AGN determination via WHAN diagrams

In order to derive any analysis of AGN-hosting cluster galaxies from our sub-samples we must first define our AGN selection criteria. Within the confines of optical spectroscopy the selection of AGN has usually been determined by the presence and strength of four narrow emission lines: $H\alpha$, $H\beta$, [N II] $\lambda6584$ and [O III] $\lambda5007$ as per the diagnostic diagrams of extragalactic spectra by Baldwin et al. (1981), commonly referred to as 'BPT' diagrams. However, these BPT diagrams are demanding in requiring all four emission lines to each individually possess a S/N> 3. Preserving this condition is indeed important to maintain high quality data with significant results, although, this benefit is negated by the loss of data through sacrificing the completeness of the galaxies sampled. To be precise, Cid Fernandes et al. (2010) finds that only ~ 40 per cent of the emission line galaxies in the region that AGN usually occupy on BPT diagrams will be detected. Cid Fernandes et al. (2010) notes a proposition to mitigate against this by reducing the number of narrow emission lines used as a diagnostic for emission line galaxies from four to the two strongest lines, $H\alpha$ and [N II] $\lambda6584$.

Using these two narrow emission lines AGN can be selected via comparison of the relative strengths of [N II] $\lambda6584$ and $H\alpha$ with the logarithmic ratio $\log_{10}([\mathrm{N\,II}]/H\alpha)$ against the equivalent width of $H\alpha$, $\mathrm{EW}_{H\alpha}$, in angstroms. These resultant diagnostics, named as 'WHAN' diagrams, define non-passive (i.e. star-forming and AGN dominant) galaxies to lie at $\mathrm{EW}_{H\alpha} > 3\text{Å}$(Cid Fernandes et al., 2011). In spite of this increase in

Table 4.1: The mass-complete BAX cluster sample. The J2000 coordinates and X-ray luminosity values are procured from the literature via BAX. The velocity dispersion at r_{200}, $\sigma_{r_{200}}$, is determined from the square-root of the biweight midvariance Beers et al. (1990). The uncertainties for $\sigma_{r_{200}}$ and $\overline{cz}_{glob}$ are determined using Danese et al. (1980). The values for $N_{r_{200}}$ and N_{AGN} are the number of galaxies at $\leq r_{200}$ and the total number of AGN at all radii respectively, and are determined for where MPA-JHU `galSpec` lines have a SNR ≥ 3, as detailed in section 4.3.3. The $P(\Delta)$ values represent the significance of sub-structuring with respect to the Δ-test in equation 4.2. Where $P(\Delta) \ll 0.01$ depicts a cluster possessing strong sub-structuring with values smaller three d.p.

Cluster	RA (J2000)	DEC (J2000)	L_x ($\times 10^{44}$ erg s^{-1})	$\overline{cz}_{glob}$ (km s^{-1})	$N_{r_{200}}$	$\sigma_{r_{200}}$ (km s^{-1})	N_{AGN}	$P(\Delta)$
				Merging				
Abell 426	03 19 47.20	+41 30 47	15.34[a]	5396±62	82	831^{+40}_{-46}	5	0.010
Abell 1552	12 29 50.01	+00 46 58	1.09[d]	25782±111	38	809^{+64}_{-84}	8	0.003
Abell 1750	13 30 49.94	-01 52 22	3.19[c]	25482±95	21	726^{+55}_{-71}	9	≪0.01
Abell 1767	13 36 00.33	+03 56 51	2.43[c]	20985±78	40	770^{+47}_{-58}	6	0.002
Abell 1991	14 54 30.22	+01 14 31	1.42[d]	17687±61	31	535^{+37}_{-47}	5	≪0.01
Abell 2033	15 11 28.19	+00 25 27	2.56[b]	24582±90	17	589^{+51}_{-69}	7	≪0.01
Abell 2147	16 02 17.17	+01 03 35	2.87[a]	10492±48	38	688^{+30}_{-35}	15	≪0.01
Abell 2255	17 12 31.05	+64 05 33	5.54[a]	24283±107	43	817^{+62}_{-80}	11	≪0.01
				Non-Merging				
Abell 85	00 41 37.81	-09 20 33	9.41[a]	16488±73	28	709^{+44}_{-55}	3	0.853
Abell 119	00 56 21.37	-01 15 46	3.30[a]	13190±77	25	760^{+47}_{-58}	12	0.579
Abell 602	07 53 19.02	+01 57 25	1.12[b]	18587±94	21	626^{+55}_{-75}	8	0.163
Abell 1066	10 39 23.92	+00 20 41	1.20[c]	20985±91	16	714^{+53}_{-69}	5	0.020
Abell 1190	11 11 46.22	+02 43 23	1.75[d]	22484±87	24	669^{+51}_{-66}	13	0.194
Abell 1205	11 13 22.39	+00 10 03	1.77[c]	22784±106	23	748^{+61}_{-82}	7	0.026
Abell 1367	11 44 29.53	+01 19 21	1.25[a]	6595±49	29	660^{+31}_{-37}	3	0.026
Abell 1589	12 41 35.79	+01 14 22	1.53[e]	21585±88	30	751^{+52}_{-66}	7	0.124
Abell 1650	12 58 46.20	-01 45 11	6.99[a]	25182±100	23	670^{+57}_{-77}	10	0.636
Abell 1656	12 59 48.73	+27 58 50	7.77[a]	6895±40	62	817^{+26}_{-29}	6	0.087
Abell 1668	13 03 51.41	+01 17 04	1.71[d]	18886±89	21	639^{+52}_{-69}	9	0.336
Abell 1773	13 42 08.59	+00 08 59	1.37[c]	22784±96	29	687^{+55}_{-73}	7	0.336
Abell 1795	13 49 00.52	+26 35 06	10.26[a]	18587±92	21	785^{+55}_{-69}	4	0.265
Abell 1809	13 53 06.40	+00 20 36	1.69[e]	23683±80	20	618^{+46}_{-60}	5	0.420
Abell 2029	15 10 58.70	+05 45 42	17.44[a]	23084±102	48	893^{+60}_{-76}	15	0.415
Abell 2052	15 16 45.51	+00 28 00	2.52[a]	10492±65	14	619^{+40}_{-50}	4	0.663
Abell 2061	15 21 15.31	+30 39 16	4.85[f]	23383±69	37	630^{+41}_{-51}	11	0.183
Abell 2063	15 23 01.87	+00 34 34	2.19[a]	10492±78	29	785^{+48}_{-59}	8	0.016
Abell 2065	15 22 42.60	+27 43 21	5.55[a]	21884±98	47	873^{+58}_{-73}	15	0.211
Abell 2069	15 23 57.94	+01 59 34	3.45[g]	34775±139	23	910^{+77}_{-104}	10	0.179
Abell 2107	15 39 47.92	+01 27 05	1.41[e]	12291±62	17	615^{+38}_{-47}	6	0.151
Abell 2124	15 44 59.33	+02 24 15	1.66[f]	19786±103	17	751^{+60}_{-80}	4	0.873
Abell 2199	16 28 38.50	+39 33 60	4.09[a]	8993±52	30	649^{+33}_{-39}	23	0.586
Abell 2670	23 54 10.15	-00 41 37	2.28[c]	22784±89	42	799^{+53}_{-66}	8	0.523
ZWCL1215	12 17 41.44	+03 39 32	5.17[a]	22484±86	28	760^{+51}_{-64}	6	0.873

[a] Reiprich & Böhringer (2002)　　[b] Ebeling et al. (1998)　　[c] Popesso et al. (2007)

[d] Böhringer et al. (2000)　　[e] Jones & Forman (1999)　　[f] Marini et al. (2004)

[g] David et al. (1999)

the completeness of the emission line galaxies there is a complication in the form of contamination of 'fake AGN' that would be more appropriately categorised under low-ionisation emission region (LIER), or, star-forming galaxies under the lines of delineation defined by Cid Fernandes et al. (2011). To curb the effects of contamination during the selection of our AGN we opt to use the Gordon et al. (2018) criteria for the WHAN diagram. To segregate the star-forming galaxies from the AGN-hosting galaxies a dividing line is placed on the $\log_{10}([N\,II]/H\,\alpha)$ axis at -0.32, thus, denoting galaxies $\log_{10}([N\,II]/H\,\alpha) \geq$ -0.32 as AGN and vice versa as non-AGN. This has been shown to reduce the sample contamination of AGN by star-forming galaxies from $75.88^{+1.06}_{-1.13}$ per cent to $11.07^{+0.99}_{-0.85}$ for Gordon et al. (2018). The other contaminants, LIERs, host weak hydrogen lines and can therefore easily intrude within the 'weak AGN' regime defined by Cid Fernandes et al. (2011) to be $3\text{Å} \leq EW_{H\alpha} < 6\text{Å}$. Thus, we reduce the contamination of LIERs by adopting the 'strong AGN' criteria of Cid Fernandes et al. (2011) in which we only sample AGN where $EW_{H\alpha} \geq 6\text{Å}$. It is worth noting that during our analysis consideration was made to allay the errors in the stellar mass estimation through the removal of galaxy objects with a significantly broadened Balmer line (see 'Broad-line AGN' in Gordon et al. 2017), by using the MPA-JHU 'SIGMA_BALMER' velocity dispersions in order to deduce $FWHM_{Balmer} = 2\sqrt{2\ln 2} \times [\text{SIGMA\_BALMER}]$, which we were to define by applying a common cut of $FWHM_{Balmer} > 1200$ kms^{-1} seen across the literature (e.g. Hao et al. 2005; Zhang et al. 2013; Gordon et al. 2017). However, we find that the entire MPA-JHU catalogue only yields a maximum $FWHM_{Balmer} \approx 1177$ kms^{-1} from the 'SIGMA_BALMER' column, which implies prior works that implement this particular cut using MPA-JHU data are doing so fruitlessly. Furthermore, the accuracy of the stellar mass values is not paramount for the analysis presented here since they are used purely as a proxy of brightness to maintain completeness.

As a result of ensuring high levels of completeness and data quality, we sample our AGN sample by maintaining that each narrow line measurement possesses S/N> 3; we shield against star-forming galaxies by adopting $\log_{10}([N\,II]/H\,\alpha) \geq -0.32$; we maintain stronger ionisation lines to prevent interloper LIER galaxies through enforcing that $EW_{H\alpha} \geq 6\text{Å}$. Applying this to each of the galaxy cluster sub-samples as a whole provides 70 AGN and 686 non-AGN in the merging sub-sample against 225 AGN and 1713 non-AGN in the non-merging sub-sample, providing an AGN fraction of 10.20 and 13.14 per cent of

the total cluster galaxies respectively. An example of the aforementioned surface caustics produced in section 4.3.2, which define our cluster galaxy membership from each sub-sample, can be found in Figure 4.1 with cluster galaxies possessing MPA-JHU `galSpec` lines of SNR $\geq$ 3. The WHAN diagrams for each stack are shown in Figure 4.2 alongside the distributions of the stellar masses for AGN and non-AGN cluster galaxies.

Additionally, we note that the mass distributions between the AGN and non-AGN in the merging dynamical state show a slight deviance from each other. Therefore, we test whether these distributions are drawn from the same pool of cluster galaxy masses using the two-sampled Kolmogorov-Smirnov test, which yields the p-value $P(\text{KS}) = 0.027$ and the KS statistic $D_{\text{stat}} = 0.187$. Interestingly, for a significance of $\geq$ 95 per cent ($P(\text{KS}) \leq 0.05$) the two-sampled KS-test indicates a rejection of the null hypothesis with the $D_{\text{crit}} = 0.170$, which can be seen in the displacement of the medians between the two distributions with AGN and non-AGN showing 10.52 $\log_{10}(M_*/\text{M}_\odot)$ and 10.62 $\log_{10}(M_*/\text{M}_\odot)$ respectively.
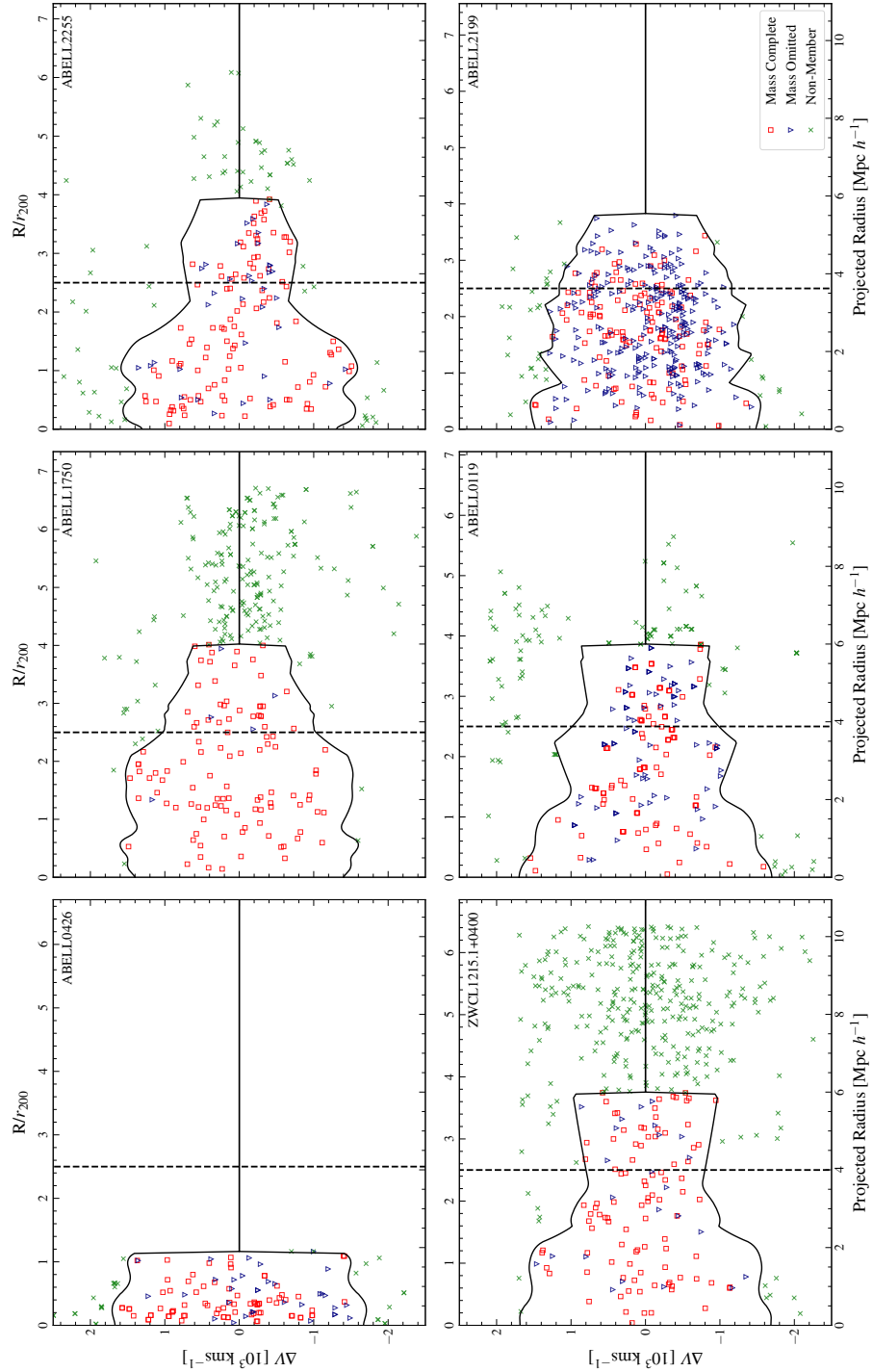
Figure 4.1: Example phase-space surface caustics (black lines) as a function of the projected radius in units of Mpc h^{-1} to determine the cluster galaxy membership for the merging (*top row*) and non-merging (*bottom row*) galaxy clusters in our sample. The hollow red squares indicate the cluster galaxies that are mass complete to $\log_{10}(M_*/M_\odot) \geq 10.2$, where the hollow blue triangles highlight those cluster galaxies that are omitted (not mass complete) and the green crosses illustrate those cluster galaxies that are not cluster members. The vertical dashed line indicates $2.5r_{200}$, the upper limit of our kinematic analysis. The cluster galaxy candidates visualised here possess MPA-JHU `galSpec` lines of SNR ≥ 3.
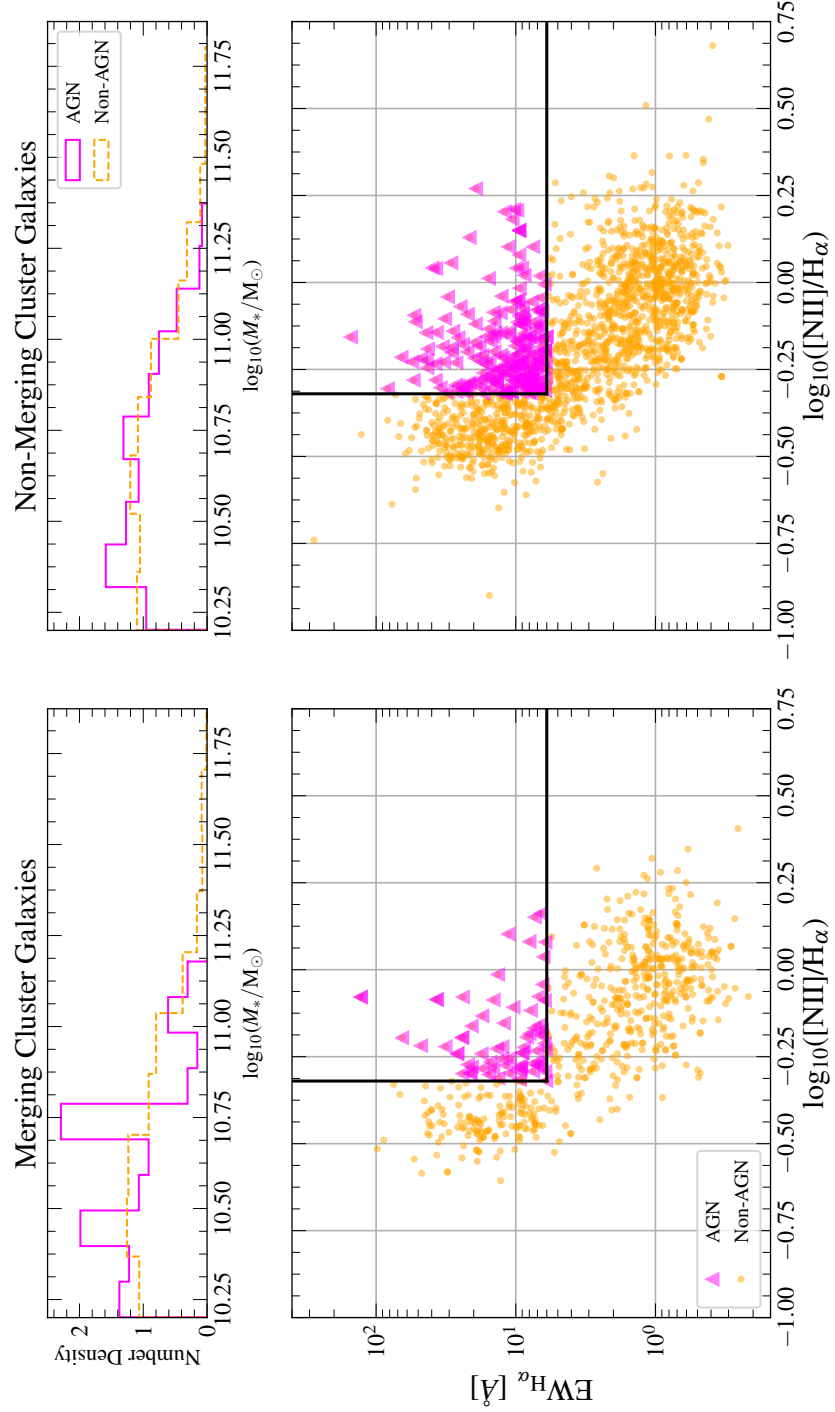
Figure 4.2: The WHAN diagrams (*bottom panels*) for our merging (*left*) and non-merging (*right*) sub-samples demonstrate the AGN selection used, with the magenta triangles representing the AGN and the orange dots depicting non-AGN. The thick vertical line represent the ratio of $\log_{10}([N\,II]/H\alpha) = -0.32$ and the horizontal lines show the line strength of $EW_{H\alpha} = 6\text{Å}$, as per the AGN selection criteria as highlighted in section 4.3.3. The distributions of the stellar masses between AGN and non-AGN are also show for their respective sub-samples (*top panels*). The frequencies per bin in the stellar mass histograms are normalised to their histogram densities, which is defined as $N = f_i/n(c_i - c_{i-1})$, where f_i is the frequency per bin, n is the total size of the histogram sample and $(c_i - c_{i-1})$ is the bin width.

4.4   Cluster Galaxy AGN Kinematics

4.4.1   AGN Velocity Dispersion Profiles

The kinematics of the AGN are derived for each sub-sample via the computation of VDPs, which are elucidated from the data by normalising their host clusters onto a common phase-space and are thereby co-added according to their pre-defined merging or non-merging dynamical states. The VDPs we produce in this work are functions of the projected radius, $\sigma_P(R)$, originally devised by Bergond et al. (2006) for analysing the kinematics of stellar systems but have since been extended to the large-scale structures of galaxy groups and clusters by a variety of authors (e.g. Hou et al. 2009, 2012; Pimbblet et al. 2014; Bilton & Pimbblet 2018; Morell et al. 2020). These VDPs are calculated through cluster galaxy radial velocities at fixed incremental bins of radius, with each bin weighted against a Gaussian window function that is driven exponentially by the square of the difference in radius for each ith galaxy. This window function, corrected by Bilton & Pimbblet (2018), is thus written as

$$\omega_i = \frac{1}{\sigma_R} \exp - \left[\frac{(R - R_i)^2}{2\sigma_R^2} \right],$$ (4.3)

where σ_R is the width of the moving window that weights the window function and $(R - R_i)^2$ is the square of the difference in projected radius. We set the width of the window to $\sigma_R = 0.2R_{max}$ in units of r_{200}. Setting the window width to this size allows for us to elucidate the variation in kinematics to a relatively small scale without becoming too fine to the point of inducing a spurious response in the final profile. Following the calculation of the window function the projected VDP can be deduced, which is written as

$$\sigma_P(R) = \sqrt{\frac{\sum_i \omega_i(R)(x_i - \bar{x})^2}{\sum_i \omega_i(R)}},$$ (4.4)

where $(x_i - \bar{x})^2$ is the square of the difference in the radial velocities between the ith galaxy and the mean recession velocity of the cluster. The result of parsing equation 4.3 through equation 4.4 for each bin of radius is a smoothed radial velocity profile that responds to every galaxy and their proximity to the bin. To maintain the validity of this VDP methodology for analysing the kinematics it is wise to ensure the total number of

cluster galaxies used to output a profile meets the lower limit of 20 members. If too few cluster galaxies contribute to the profile this can lead to an unrealistic response due to the weightings that depend on the projected separation between galaxies and fixed bins with the consequence of large uncertainties.

We incorporate the aforementioned systematic processes for each of our cluster sub-samples so as to be able to partly satisfy the aims of this body of work to compare the kinematic response of AGN-hosting cluster galaxies between different galaxy cluster dynamical states. The procedure we follow for the VDP production is simple, and thus, it outlined here: cluster galaxies are collated from every cluster into their respective merging or non-merging sub-samples as per the definition described in subsection 4.3.2. These cluster galaxies line-of-sight velocities are normalised to their host cluster's mean recession velocities to provide ΔV, which is weighted to the $\sigma_{r_{200}}$, with their projected radii to r_{200} and are co-added onto a common $\Delta V/\sigma_{r_{200}} - r_{200}$ grid to output merging and non-merging phase-space stacks. After the allocation of the cluster galaxies to their appropriate dynamical states, the AGN selection criteria of subsection 4.3.3 is applied to ascertain the AGN present for both sub-samples. Finally, the AGN and non-AGN cluster galaxies for each sub-sample are computed through into equations 4.3 and 4.4 to result in a total of four profiles, two for each dynamical state.

We show the product of our VDP implementation for each dynamical state between AGN and non-AGN cluster galaxies in Figure 4.3. Firstly, focusing on the non-merging VDPs in the right panel of Figure 4.3, we witness the AGN and non-AGN profiles declining in parity with one another as the projected radius increases until $R \sim 2\ r_{200}$ where the AGN profile starts to break away and increase. The near-perfect parity between both of these VDPs suggests that the AGN population has homogenised with the non-AGN population and are not interacting beyond the expected settling of the normalised velocity dispersion to ~ 1, representing a relaxed stack of galaxy clusters. This is not an unexpected result considering this sub-sample marries to the non-merging VDPs of Bilton & Pimbblet (2018), where the cluster galaxy sub-populations of stellar mass, galaxy colour and galaxy morphology consistently demonstrate this decline as a result of the relaxed dynamical state (see also Girardi et al. 1996). This is in contrast to the merging VDPs in the left panel of Figure 4.3, where the AGN-hosting cluster galaxy VDP rises to values of $\sigma_P(R) \sim 1.25$ as $R \to 0$, diverging from the non-AGN cluster galaxy VDP with a significance of $\gtrsim 3\sigma$
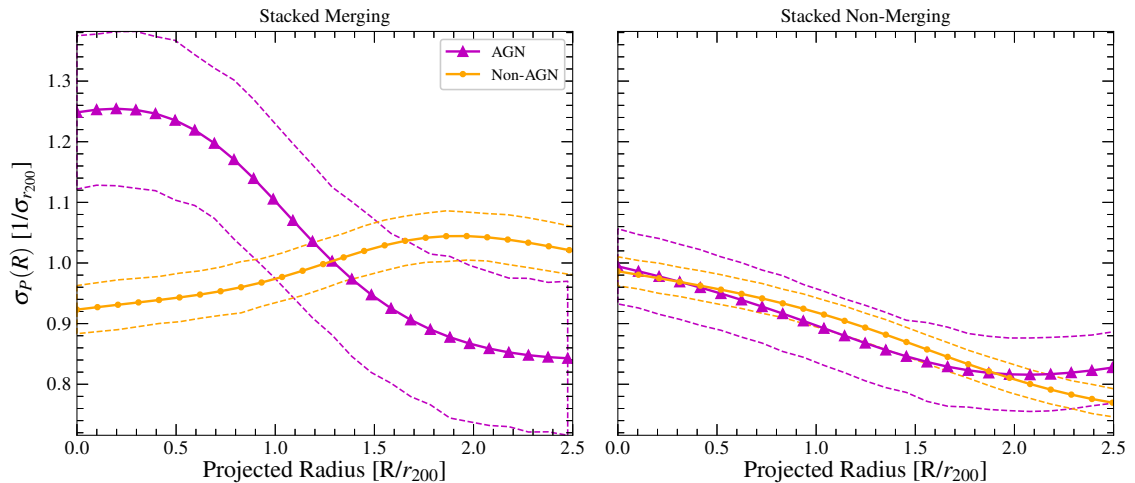
Figure 4.3: The VDPs split by our AGN selection, for the merging (*left*) and non-merging (*right*) dynamical states, produced via co-adding clusters appropriately onto a common phase-space grid. Each stack shows the projected velocity dispersions ($\sigma_P R$), in normalised units of $1/\sigma_{r_{200}}$, for AGN and non-AGN sub-popluations as a function of radius (R/r_{200}); the magenta triangle markers represent the AGN and the orange dot markers non-AGN. The corresponding dashed lines represent the symmetric uncertainty for each profile derived from 1σ of 1000 Monte Carlo resamples.

at $R = 0$. As the projected radius extends outward from the clustocentric regions the AGN sub-population steeply declines in their kinematic activity to equivalent levels seen for a non-merging dynamical state. The increase in the projected velocity dispersion of an AGN sub-population towards the centre of the merging stack implies that these AGN are on their first infall, or, that they are residing within backsplash galaxies (see the VDPs in Figure 13 of Haines et al. 2015). Here backsplash galaxies are recently accreted cluster galaxies that have already passed through their pericentres and are proceeding to journey to their apocentres (Pimbblet, 2011; More et al., 2015, 2016). Although, we should highlight that the number of AGN-hosting cluster galaxies lying at $\leq r_{200}$ in the merging cluster stack is only 15 compared to the 55 found $> r_{200}$, which indicates there is a possibility the rise in the VDP is spurious due to inadequate sampling of the AGN. The non-AGN sub-population, however, illustrates an opposing response where the profile increases steadily with R reaching an apex at $R \sim 1.8\ r_{200}$. This is, again, an unsurprising result considering prior works have shown merging populations of cluster galaxies possess an rise in their kinematic activity as R increases with the red and blue sub-population VDPs inferring strong sub-clustering along with the presence of 'pre-processing' (see Menci & Fusco-Femiano 1996; Hou et al. 2009; Bilton & Pimbblet 2018).

4.4.2   AGN and their Rotation Profiles

Another testable indirect method of determining potential cluster environmental effects that could trigger AGN is analysing the 'rotational profiles' of our selected AGN sample between the two dynamical states, which are naturally contrasted against those that are 'non-AGN'. Galaxy clusters themselves are known to possess some sort of global angular momentum that operates dynamically with respect to the bottom of a cluster's potential well (e.g. see Materne & Hopp 1983; Oegerle & Hill 1992; Hwang & Lee 2007; Manolopoulou & Plionis 2017; Baldi et al. 2018). Indeed, any angular momentum possessed within a galaxy cluster should influence the average motion of the galaxy cluster membership via these very dynamics, which would be imprinted onto the radial velocities of the individual cluster galaxies in z-space. Thus, following the combined methodologies detailed within Manolopoulou & Plionis (2017) and Bilton et al. (2019), we determine the relative rotational profiles of our aforementioned cluster galaxy sub-populations from the 2D plane of sky through the employment of a geometric 'perspective rotation' technique (Feast et al., 1961).

Perspective rotation relies upon the projection of 3D motions of cluster galaxies onto a 2D RA-DEC space relative to a known cluster centre. Thus, with the known BAX defined galaxy cluster coordinates and the known RA and DEC values of each member galaxy one can determine their projected angles with respect to a defined normal. Furthermore, by artificially rotating the cluster galaxies about their respective BAX centres it is possible to determine the planar angle of rotation through finding the maximum difference between the averaged radial velocities for either side of the defined normal. We outline our procedure for determining the cluster galaxy sub-population rotational profiles firstly be making the assumption that the rotational axis of each cluster in our sample lies solely in the plane of the sky so they are perpendicular to our line-of-sight, which leaves the angle of the rotational axis perpendicular to the plane $\phi = 0°$, consequently defining the line-of-sight velocity to be $v_{\mathrm{los}} = \Delta V$ (see Manolopoulou & Plionis 2017). For each galaxy cluster we generate a fixed normal line along their central declination as defined by the X-ray literature with the BAX catalogue, which allows for the calculation of the cluster galaxy's projected angles with respect to this normal, denoted as μ. This fixed normal simultaneously acts as a divide upon which we calculate the averaged v_{los} for the two semicircles $\langle v_1 \rangle$ and $\langle v_2 \rangle$.

These are defined as

$$\langle v_{1,2} \rangle = \frac{1}{N} \sum_{i=1}^{N} \Delta V_i \cos(90° - \mu_i), \tag{4.5}$$

where ΔV_i is the line-of-sight velocity from equation 4.1 for the galaxy $z_{\mathrm{gal},i}$ and μ_i is the angle from the normal operating between $0°$ and $180°$ for each semicircle. Using Equation 4.5 allows to ascertain the difference in averaged velocities with $v_{diff} = \langle v_1 \rangle - \langle v_2 \rangle$ and is, therefore, iterated through rotating the cluster galaxies about their galaxy cluster centre by $\theta = 10°$ until $\theta = 360°$. In addition, we procure the uncertainties of each semicircle by propagating through the standard error for each semicircle at every increment of θ as

$$\sigma_\theta = \sqrt{\frac{\sigma_{v,1}^2}{n_1} + \frac{\sigma_{v,2}^2}{n_2}}, \tag{4.6}$$

where σ_v is the velocity dispersion and n is the galaxy number for each semicircle 1 and 2 at each increment of θ.

To match our global galaxy cluster property definitions we apply Equation 4.5 and 4.6 for all clusters across both merging and non-merging sub-samples for their cluster galaxies at a projected radius of ≤ 1.5 Mpc h^{-1}. We thus take the maximum values of $v_{\mathrm{diff}}(\theta)$ for our global definition of the rotational velocities (v_{glob}) for each galaxy cluster, ergo this proceeds to provide the planar rotational axis θ_{glob}. The global rotational values and statistics for the sample of galaxy clusters presented within the body of this work are defined and catalogued in full in Bilton et al. (2019).

Continuing on from the previously outlined methodology we build two stacks of galaxy clusters from our two sub-samples, where the respective cluster galaxies are co-added onto normalised RA-DEC grids with their X-ray centres set to zero. This is alongside the cluster galaxy radial velocities, which are derived to their respective mean recession velocities as per Equation 4.1 and are normalised by the velocity dispersion $\sigma_{r_{200}}$, similar to the composites produced for subsection 4.4.1. Additionally, each set of cluster galaxies from each galaxy cluster are rotated about their origin by θ_{glob} to align their planar rotational axes along the same normal so as to not overlap opposing dynamics and ensure we enhance the signal of our rotational profiles. This provides a rotational axis of $\theta \sim 0°$, thus, implying the maximum value is consistently found at $v_{\mathrm{diff}}(\theta = 0)$ as we increase incrementally in R where we define $v_{\mathrm{rot}} = v_{\mathrm{diff}}(0)$. Therefore, with each composite of cluster galaxy

sub-populations for each dynamical state we exploit Equation 4.5 to determine the v_{diff} as a function of radius in increments of $0.1r_{200}$ over $0 < R \leq 2.5\, r_{200}$ to maintain consistency.

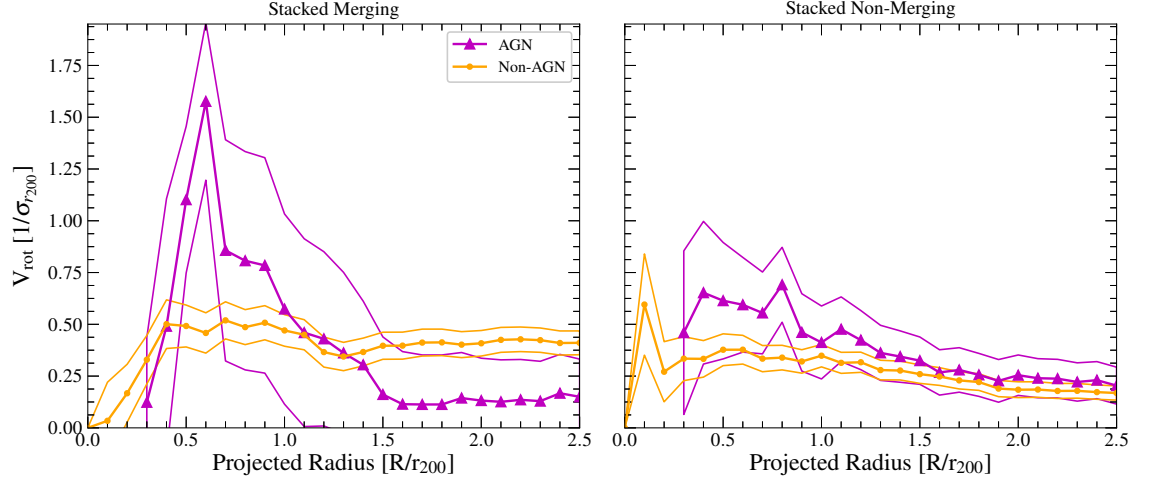**Figure 4.4:** The AGN (magenta triangles) and non-AGN (orange dots) V_{rot} profiles for the cluster galaxies in the merging (left) and non-merging (right) dynamical states. The respective regions around each of the profiles, as shown with the solid lines, represent the uncertainty obtained via propagated standard errors of the mean as per Equation 4.6.

In Figure 4.4 we present the rotational profiles of our selected AGN sample contrasted with the non-AGN for the merging and non-merging dynamical states that were defined in subsection 4.3.2. Concentrating on the non-merging sub-populations both rotational profiles show no significant deviation from one another and appear to be homogenised in a similar fashion to the VDPs in Figure 4.3, with the AGN sub-population lacking detail close to the core regions due to the dwindling numbers that occupy them. If we consider the rotational profiles from Bilton et al. (2019) we can see the general trend of a relatively quenched and decline profile with radius is consistent despite our strict demand for strong and significant line emissions. Although, there is no significant discrepancy between the AGN and non-AGN profiles, which coinciding with the stellar masses presented in Figure 4.2 suggests the AGN within this sample are drawn from the same distribution as the non-AGN, most likely coalescing onto their cluster potentials simultaneously at the same epochs. The co-added merging cluster galaxies almost depict a similar outcome of homogenisation from the analysis, however, the AGN sub-population does briefly spike to a $V_{\text{rot}} \sim 1.5$ at $R \sim 0.6r_{200}$ to a significance of $\sim 2\sigma$ from the non-AGN sub-population. Furthermore, this is followed with a steep declining gradient that flattens at $v_{\text{rot}} \sim 0.1$ at $R \gtrsim 1.5r_{200}$. Overall, the connotations of the observed spike and decline, while noisy,

can corroborate that these AGN either contribute to an infalling or backsplash population of cluster galaxies with the merging AGN sub-population VDP in Figure 4.3. Although, despite the increased variation in the AGN profile, the large uncertainties and insufficient numbers of AGN that contribute to the merging stack impede one's ability to be conclusive about the kinematic independence of the sub-population relative to the non-AGN profile.

4.5   Interpretations of the AGN Kinematics

We have thus far presented how AGN-hosting cluster galaxies respond kinematically as a function of projected radius between unrelaxed and relaxed galaxy cluster dynamical states, however, we are yet to explore what the key results presented in Figures 4.3 and 4.4 imply about the possible origins of AGN in galaxy clusters based upon prior knowledge and works. To elaborate, Poggianti et al. (2017) has shown with MUSE spectra that so-called 'Jellyfish' galaxies–a cluster galaxy with extended tails of gas and stars as a result of ram pressure stripping with the ICM (e.g.Yagi et al. 2010; Kenney et al. 2014; Rawle et al. 2014)–seemingly are more likely to posses and AGN with 5/7 of jellyfish galaxies containing an active nucleus, which is further confirmed with evidence of outflows and ionisation models matching AGN profiles within Radovich et al. (2019). Additionally, increased star formation and AGN activity has been found in cluster-cluster mergers and by extension this includes the jellyfish morphologies, which have been consistently found to harbour within merging cluster environments as well, with the more extreme cases being the result of interactions with high velocity cluster merger shock fronts in the ICM (Miller & Owen, 2003; Owers et al., 2012; McPartland et al., 2016; Ebeling & Kalita, 2019). However, the Abell 901/2 system of simultaneously interacting two sub-clusters and two sub-groups is one of the more plentiful reservoirs of jellyfish galaxies of 70 and only 5 of these galaxies host an AGN, indicating the mechanisms involved in triggering AGN must depend on more parameters than just the coincidence of jellyfish morphologies (Roman-Oliveira et al., 2019). Despite this caveat, the link between ram pressure stripping and an increase in the AGN activities has continued to show promise with simulations by Ricarte et al. (2020), determining galaxies with a mass $\log_{10}(M_*/M_\odot) \gtrsim 9.5$ have spikes in black hole accretion as the star formation is quenched around the strongest regions of ram pressure stripping as the galaxy journeys through its pericentre. Furthermore, the

simulations by Ricarte et al. (2020) seem to illustrate how the quenching of star formation is aided by AGN feedback as a consequence to the spikes on AGN activity and thus producing outflows until the AGN itself runs out of fuel; observational evidence backs this claim of AGN feedback (George et al., 2019). From this brief overview, our Figures 4.3 and 4.4 demonstrate an immediate interpretation that our merging dynamical state represents the AGN sub-population to be hosted by recently accreted cluster galaxies, corroborating the simulations of Ricarte et al. (2020). Placing the current established lines of enquiry on the mechanisms that lead to AGN triggering into consideration we attempt to isolate the nature of their host cluster galaxies; Do AGN-hosting cluster galaxies represent a sub-population of galaxies on their first infall, or, are these galaxies representative of a backsplash population to account for the AGN spikes during the passage though their respective pericentres? We therefore briefly attempt to interpret the VDPs and rotational profiles with complementary analysis, which is detailed in the following sub-section.

4.5.1 Backsplash Cluster Galaxies

AGN-hosting cluster galaxies are commonly found to coincide along the virialised boundaries of galaxy clusters and one explanation for this effect could potentially be that AGN sub-populations are backsplash galaxies, which are described as galaxies that have have already passed through their clustocentric pericentre on first infall and are now journeying towards their respective apocentres. Indeed, Roman-Oliveira et al. (2019) find that their more extreme jellyfish galaxies were more likely to lie along these boundaries, therefore, it is possible to consider that the AGN triggering could occur during the the pericentre passage and this activity continues as a (possibly) weaker AGN remnant of that journey until the activity is eventually quelled. Therefore, in Figure 4.5 we plot a series of $|\Delta V|/\sigma_{r_{200}}$ histograms for our AGN and non-AGN sub-populations for each of the dynamical states at two radial bins for cluster galaxies $\leq r_{200}$ and those $> r_{200}$ (with the upper limit of 2.5 r_{200}), following the same procedures as Gill et al. (2005) and Pimbblet (2011). These procedures involve noting the way in which infaller and backsplash galaxies could be defined. To elaborate, Gill et al. (2005) states that at $\sim R_{\text{virial}}$ a population of cluster galaxies are infallers if they posses the mode value of $|\Delta V| \approx 400 \text{ kms}^{-1}$.

For consistency, we adopt the translation of this to the absolute velocities of cluster galaxies normalised by their respective galaxy cluster velocity dispersions into the range
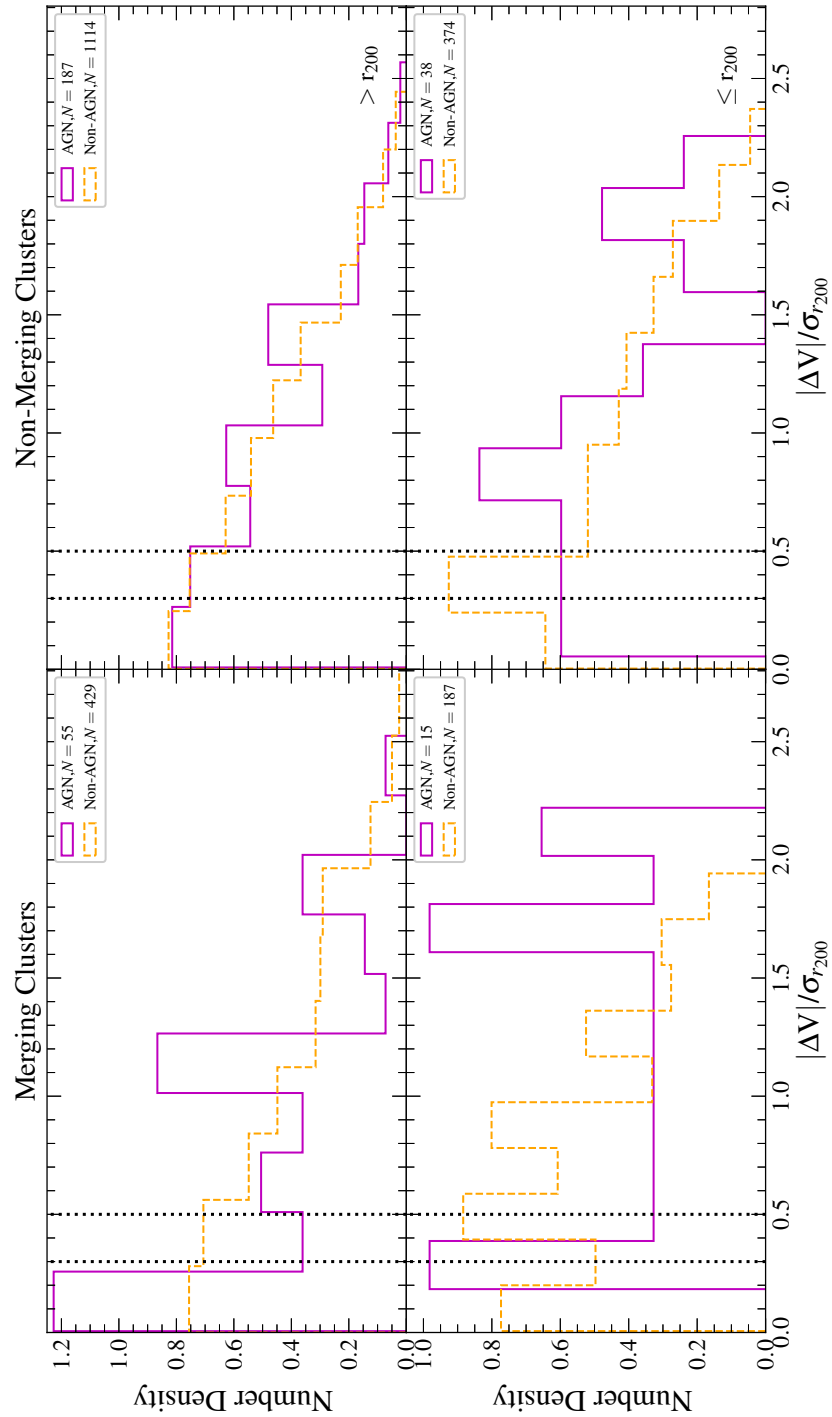
Figure 4.5: Histograms of $|\Delta V|/\sigma_{r_{200}}$ for AGN and non-AGN sub-populations segmented into bins of cluster galaxies that lie $> r_{200}$ (*top row*) and $\leq r_{200}$ (*bottom row*) between merging (*left column*) and non-merging (*right column*) dynamical states. The region occupied by the black dotted vertical lines highlight the range of standardised velocities, $0.3 < |\Delta V|/\sigma_{r_{200}} \sim< 0.5$, which indicate an infaller population if their modal value lies across these velocities and within a reasonable radius. Each sub-population is normalised to their histogram densities, which is defined as $N = f_i/n(c_i - c_{i-1})$, where f_i is the frequency per bin, n is the total size of the histogram sample and $(c_i - c_{i-1})$ is the bin width.

$0.3 < |\Delta V|/\sigma_{r_{200}} < 0.5$ as deduced by Pimbblet (2011). Thus, if the mode of the standardised velocities for a sub-population has its foci at around $0.3 < |\Delta V|/\sigma_{r_{200}} < 0.5$ for values around the virial radius, which we assume to be $R_{\text{virial}} \sim r_{200}$, said sub-population would be classified as infalling. In contrast, a sub-population of backsplash cluster galaxies would be expected to peak significantly at $|\Delta V|/\sigma_{r_{200}} \sim 0$ for values at or beyond our definition of the virial radius, with their fraction reaching zero at some upper limit (e.g. Mamon et al. 2004; Pimbblet 2011; Bahé et al. 2013; Haggar et al. 2020). Therefore, with respect to Figure 4.5, we see that the column of our non-merging sub-populations across both bins of radius do not show any significant difference in the distributions of velocities with the exception of those that lie $\leq r_{200}$, which show the non-AGN sub-population to occupy a mode within the range that nominally represents infallers, most likely for cluster galaxies $0.5 \leq r_{200} < 1.0$ (Gill et al., 2005). Additionally, the AGN sub-population slightly deviates from the non-AGN velocity distribution with a mode centred at $|\Delta V|/\sigma_{r_{200}} \sim 0.8$, which could indicate stronger infalling. In contrast the column of our merging AGN sub-populations show the strongest deviations from the distribution of non-AGN, especially with the $> r_{200}$ bin showing a significant centrally dominated AGN sub-population, where such a central dominance in relative velocity corresponds to a sub-population that were predominantly backsplash cluster galaxies. However, the dependence of this being the true nature of the sub-population relies upon more precise definitions of the radii since there is a natural upper limit a bound cluster galaxy can extend outward to with respect to its galaxy cluster's potential, known as the splashback radius (More et al., 2015, 2016). In addition, Haggar et al. (2020) shows that the fraction of backsplash galaxies diminishes by $2r_{200}$ and $2.5r_{200}$ for massive ($\sim \times 10^{15} M_\odot$) merging and non-merging cluster systems respectively, thus demonstrating that merging cluster environments experience a greater decrease in the fraction of harbouring backsplash galaxies as one continues to extend beyond r_{200}. Indeed, the sub-populations of the merging cluster galaxies present in the $\leq r_{200}$ bin show more variations in their general distributions with the modes of both the AGN and non-AGN sub-populations lying around $0.3 < |\Delta V|/\sigma_{r_{200}} < 0.5$, which eludes to mostly infalling sub-populations rather than those associated with backsplash. Finally, if one considers the equivalent peak of the AGN density histogram at $\Delta V|/\sigma_{r_{200}} \sim 1.7$ it could be possible there is a mix of recently accreted cluster galaxies and those that are relaxing onto a common potential. Although,

Table 4.2: The number and fraction of AGN for the merging and non-merging composites with respect to the total number of cluster galaxies within each phase-space region, as shown in Figure 4.6 with the lines of delineation originally defined by Rhee et al. (2017). The asymmetric uncertainties for each fraction represent the 1σ confidence interval of the binomial distribution (see Cameron 2011).

Region	N_{Merge}	f_{Merge}	$N_{\mathrm{Non-Merge}}$	$f_{\mathrm{Non-Merge}}$
A	42	$0.15^{+0.02}_{-0.02}$	119	$0.15^{+0.01}_{-0.01}$
B	3	$0.14^{+0.09}_{-0.06}$	5	$0.09^{+0.05}_{-0.04}$
C	7	$0.07^{+0.03}_{-0.02}$	30	$0.10^{+0.02}_{-0.02}$
D	8	$0.07^{+0.03}_{-0.02}$	43	$0.16^{+0.02}_{-0.02}$
E	4	$0.04^{+0.03}_{-0.02}$	5	$0.03^{+0.02}_{-0.01}$

it should be noted that not much information can be confidently derived from the AGN sub-populations within the bins that possess small samples size ($N \lesssim 100$), especially with the merging AGN-hosting cluster galaxies at $\leq r_{200}$ that only has $N = 15$.

4.5.2 Phase-Space Analysis

In light of studying the modal absolute velocities between the core regions and the outer most radii for our composites in section 4.5.1 we attempt to make further sense of these distributions and their foci through a projected phase-space analysis. To that end, we use the phase-space region analysis based on the N-body cosmological simulations of Rhee et al. (2017). Exploring the projected phase-space distributions of our cluster galaxy sub-populations for both dynamical states will allow for us to ascertain a cluster galaxy's time since first collapse onto the cluster potential and the likely stage of its journey at our current epoch of $z = 0$. Therefore, in Figure 4.6 we present the Rhee et al. (2017) projected phase-space for each dynamical state alongside the regions A-E, with each representing the space that is occupied by a cluster galaxy chronologically as it journeys through the cluster (e.g. first infall-coalesced onto potential). As a complement to Figure 4.6, we tabulate the numbers and fractions of the AGN sub-population for the merging and non-merging systems relative to each phase-space region in Table 4.2. The fractional uncertainties are computed from the 1σ confidence interval of a binomial distribution as analysed and depicted by Cameron (2011).
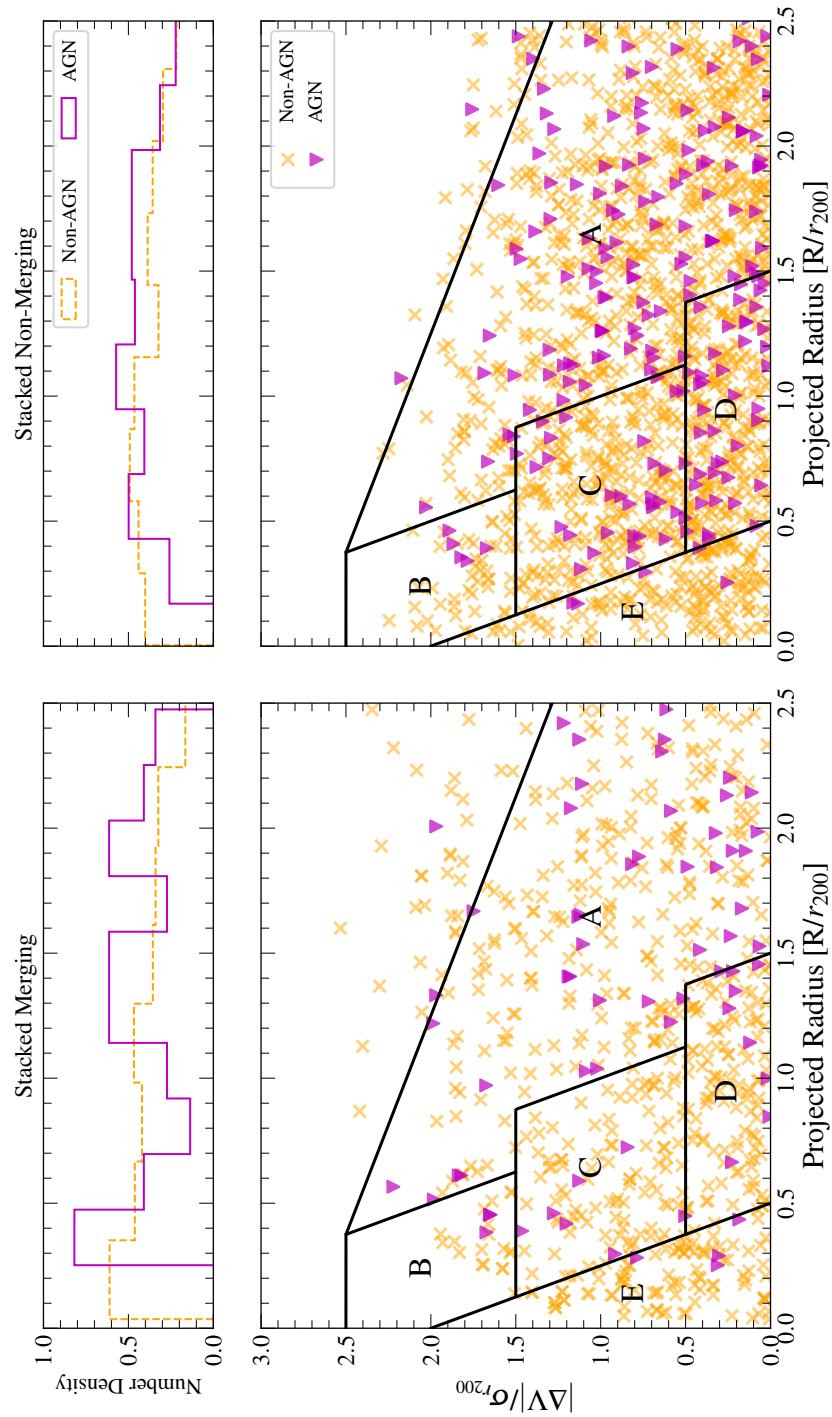
Figure 4.6: The merging (*left column*) and non-merging (*right column*) phase-space composites are depicted on the bottom row, where the absolute radial velocities are normalised as $|\Delta V|/\sigma_{r_{200}}$ and the projected radius as R/r_{200}. The regions A-E represent first, recent, recent-intermediate, intermediate and ancient infallers respectively as prescribed within Rhee et al. (2017). The corresponding histograms on the top row present the radii for each sub-population normalised to their respective histogram densities, which is defined as $N = f_i/n(c_i - c_{i-1})$, where f_i is the frequency per bin, n is the total size of the histogram sample and $(c_i - c_{i-1})$ is the bin width.

Purely by observation of Figure 4.6, there is no obvious concentration of AGN in either dynamical state except by the overt imbalance between the sizes of each cluster sub-sample. This is especially true for the co-added cluster galaxies that lie within the non-merging stack, which show a homogenised distribution of both sub-populations, although with the exception of an elevation of the AGN sub-population $1 \lesssim r_{200} \lesssim 2$. However, the distribution of the radii in the merging stack highlights a peak at $0.25 \lesssim r_{200} \lesssim 0.50$ and cuts through segments of the post-accretion regions B-E. Interestingly, the non-merging regions appear to show a 'cut-off' along the line of delineation for the ancient infaller E region, with the exception of an insignificant number that do invade the region.

More importantly, one should contrast Figure 4.6 with the information in Table 4.2 to better interpret AGN concentration. Thus, we note that region A has the most significant AGN contribution associated with first infallers, where both merging and non-merging stacks have a consistency between each other with ~ 15 per cent across both sub-samples. The merging composite maintains this fraction of AGN consistently into region B, albeit, tenuously so due to the greater uncertainties that do not significantly break away from the non-mergers combined with the difference in the number of galaxy clusters for each sub-sample. Regions C and D are both considerably enriched for the non-merging composite comparatively against the merging composite with fractions of 10 and 16 per cent respectively. Furthermore, in section 4.3.3 we determine the fractions of AGN in the merging and non-merging sub-samples to be 10.20 and 13.14 per cent respectively, which demonstrates an overall decrease in the total merging sub-sample AGN fraction. Again, with reference to the different regions in Table 4.2, it can be seen that the predominant source of this deficiency in merging cluster AGN fraction is in region D when taking into account the uncertainties and suggests AGN are somewhat quenched in merging cluster systems. However, the discrepancy between the cluster sub-samples sizes does mitigate against this as a conclusive explanation for the differences in AGN fraction, especially when comparing clusters from each sub-sample individually in Table 4.1. Additionally, it is estimated by Rhee et al. (2017) that the aforementioned backsplash galaxies would more commonly inhabit the regions C and D. Therefore, implying these non-merging cluster AGN could have survived the first turnaround of their pericentres and potential quenching for up to $\lesssim 3\mathrm{Gyr}$ post-turnaround depending on their distance to their apocentres. Finally, the fractions of AGN-hosting cluster galaxies greatly diminish across both dynamical

states in Region E, and this can be clearly seen in Figure 4.6 when contrasted with the non-AGN sub-populations suggesting AGN cannot survive, or are not commonly triggered, significantly in the ancient virialised regions of clusters.

4.6   Discussion & Summary

The work we present here has the unfortunate discrepancy between our cluster sample sizes as a result of our implementation of the Δ-test to enforce a significance to the 1 per cent level. However, ensuring this strict criterion ensures we are selecting our substructured sub-sample to be a truer proxy of core merging processes and in spite of this we still have sufficient richness in the composites to make a comparative analysis. Of course, the Δ-test itself has its own misgivings operating as a proxy for core merging due to its reliance upon local deviations of cluster galaxies in z-space from the overall mean cluster values, alongside the projection effects due to the limitations of our 2D sky observations where we ultimately are unable to adequately resolve angular and radial separations . Consequentially this results in a proxy of relatively recent cluster-cluster mergers that are in a late relaxing phase compared to systems with initial ICM interactions between two independent sub-clusters (e.g. see Bulbul et al. 2016; Caglar & Hudaverdi 2017). This leads us to ask the question, what do we mean by 'merging'? Merging clusters present processes with a variety of timescales dependent on the epoch of the merger and whether you observe the cluster galaxies or the ICM. This is important when considering the origins of AGN themselves since they have been observed to be prevalent within 'merging' systems as determined via ICM shock fronts (Miller & Owen, 2003; Sobral et al., 2015), as well as 'Jellyfish galaxies' resulting from ram pressure stripping (Owers et al., 2012; Ruggiero et al., 2019; Ebeling & Kalita, 2019), which could in turn be possible conspicuous tracers of AGN due to both being occasionally coincident (see Poggianti et al. 2017; Marshall et al. 2018; Roman-Oliveira et al. 2019). Contrary to this however, it is shown that any minor merging processes indicated by the ICM do not have an immediate impact on the evolution of cluster galaxies (Kleiner et al., 2014).

Considering many clusters in our 'non-merging' sample are actually exhibiting merging processes (e.g. see Nulsen et al. 2013; Wen & Han 2013) in the radio or X-ray implies we may not be capturing the true kinematic effects from AGN triggering due to ram pressure stripping activity, thus, an alternative way of determining merging galaxy clusters may be better suited. In fact our AGN cluster galaxies in this work are optically selected, which therefore means our AGN sample contains the most efficient accretors. To maintain such a high efficiency requires a consistent stream of cold gas funnelled from

a sufficient reservoir, however, denser environments such as of that found towards the inner core regions of galaxy clusters ($\lesssim r_{200}$) do not typically yield such a supply. In contrast, inefficiently accreting AGN may result from 'drip-feeding' of the cold gas due to a variety of either in-situ or ex-situ processes (e.g. see Hardcastle et al. 2007; Ellison et al. 2015). With this in mind the inefficient accretion onto the supermassive black hole could therefore be enough to power an AGN to provide signatures in the radio band, implying that radio selected AGN may provide a greater insight into the interplay between different modes of accretion; radio AGN with a low power output are commonly found in cluster galaxies that pervade the centres of galaxy clusters and groups (Best et al., 2007; Ching et al., 2017). Our selection biasing of accretion efficient AGN can be seen in Figure 4.6 as the numbers depreciate as $r_{200} \rightarrow 0$, especially for cluster galaxies within region E, the slight increase in number for merging states is most likely the result of heavy interactions that displace or 'throw' the cluster galaxies into different regions. Contemplating on this further, we also applied a rather strict criteria to selecting our AGN using the WHAN diagram to maintain high significance in our emission lines while alleviating the loss in data that BPT diagrams would induce. However, restricting our AGN selection to cluster galaxies having a strong $EW_{H\alpha} \geq 6\text{Å}$ emission inevitably removes a sub-sample of weaker AGN that could possibly resemble a relatively ancient trigger in activity due to the local environment. Although, the quid pro quo nature of relaxing this strict criteria would lead to contamination of emissions from AGB stars or LIER hosting cluster galaxies.

There is the additional possibility that our application of surface caustics to the cluster sample is too restrictive for those possessing merging environments leading to the omission of genuine members that are temporarily thrown out of the system before collapsing back onto the cluster. However, there the cautious approach is often required to prevent lingerers from pervading the galaxy cluster membership for our sub-samples at the expense of potentially losing members in our merger. Indeed, this is a problem that becomes more apparent for galaxy clusters in our sample in relative close proximity to other large, and independent, structures such as Abell 2065 which is currently undergoing merging processes with another cluster core (Markevitch et al., 1999; Belsole et al., 2005; Chatzikos et al., 2006); Abell 1750 is a part of a triple cluster system with ICM interactions that is < 1000 kms^{-1} from the central sub-cluster, risking overlapping cluster galaxies from these other structures due to our line-of-sight limitations (Molnar et al., 2013; Bulbul et al.,

2016).

Within this work we have obtained a sample of 33 galaxy clusters collated with the BAX cluster database that were split into two sub-samples of 8 merging (relaxing) and 25 non-merging (relaxed) dynamical states from the Δ-test for substructure Dressler & Shectman (1988). Compiling each of their memberships with MPA-JHU DR8 galaxies via the mass estimations methods of surface caustics (Diaferio & Geller, 1997; Diaferio, 1999) sub-populations between AGN and non-AGN-hosting cluster galaxies were determined adhering to the strict criterion of $\log_{10}([N\,II]/H\,\alpha) \geq -0.32$ and $EW_{H\alpha} \geq 6$Å to the WHAN diagram (Cid Fernandes et al., 2010, 2011; Gordon et al., 2018). This results in a kinematic analysis through the VDPs, rotational profiles and their respective positions in phase-space for each dynamical state. The summary of our findings are as follows:

(i) Merging cluster dynamical states on average, as determined by the Δ-test, present kinematically active AGN within core regions ($< r_{200}$) that implies they are a first infaller and recently accreted sub-population of merging systems. This is coincident within regions where ram pressure is strongest for first pericentre passage (see Ricarte et al. 2020).

(ii) Non-merging cluster dynamical states on average illustrate an AGN sub-population that is kinematically inactive and is homogenous with the non-AGN sub-population, with their VDPs being atypical for a relaxed galaxy cluster system, suggesting there is no unique behaviour that could infer mechanisms that affect AGN activity.

(iii) Phase-space analysis exhibits a fractional enrichment of AGN in non-merging cluster dynamical states in regions associated with 'backsplash' cluster galaxies, which resemble galaxies that have made their first passage through their pericentre.

Acknowledgements

Data Availability

The SDSS DR8 and MPA-JHU data utilised within this work are publicly available to examine and download from the SQL-based SkyServer CasJobs service, which can be accessed via http://skyserver.sdss.org/CasJobs.

5.   Summary & Future Work

"All truly great thoughts are conceived while walking."

– Friedrich Nietzsche, *Twilight of the Idols (1889)*

5.1   Prologue

The Chapter that follows presents a summary of the last three science Chapters (2-4) and how each provides a window to the answers of the three main questions asked within them, and thus, the answering of the questions to the theme of this thesis; How do cluster galaxy sub-populations respond to their environment and sub-structuring activity? How does a galaxy cluster's angular momentum evolve? Can we infer the evolutionary history of a galaxy cluster through their angular momentum histories? Additionally, there is a brief discussion on potential future work to expand upon what has already been compiled here alongside upcoming future missions and facilities that will be online within the next few years. Of particular relevance to this thesis, the UK Schmidt Telescope in Australia and the Vera Rubin Observatory (VRO) in Chile will host the prospective Taipan galaxy survey (da Cunha et al., 2017) and the Legacy Survey of Space and Time (LSST; Ivezić et al. 2019) respectively in hope of improving survey completeness at greater magnitude depths, granting access to larger galaxy sample sizes at higher resolutions. Furthermore, other instruments in the near future will provide complementary data sets such as the Dark Energy Spectroscopic Instrument (DESI; Aghamousa et al. 2016) and the Square Kilometre Array (SKA; Dewdney et al. 2009).

5.2   Summary

We have presented within this thesis three science Chapters that have used observational data chiefly taken from the well-established Sloan Digital Sky Survey to aspire to understanding the environmental effects of cluster galaxies on galaxy evolution. Specifically, each Chapter individually seeks to answer questions on how cluster galaxy sub-populations respond to their environment as a function of the presence of core merging processes and

their radius from the cluster centre through their peculiar kinematics and dynamics within large-scale structures. Therefore, as a reminder, here are the main questions addressed by the three science Chapters of this thesis:

1. How do proxies for galaxy evolution, on average, drive the kinematics as a function of radius between unrelaxed and relaxed galaxy clusters?

2. How do these same proxies for galaxy evolution drive the rotational profiles as a function of radius and can these rotational profiles be used to determine galaxy cluster evolutionary histories?

3. Can we infer the likely triggering mechanisms of AGN in hostile galaxy cluster environments via the kinematics of their host cluster galaxies?

Where each question (1-3) is individually addressed sequentially from Chapter 2 to Chapter 4. While there have been previous works that have focused on the variations in proper motions of cluster galaxies utilising a variety of techniques (e.g. Hou et al. 2009; de Carvalho et al. 2017; Cava et al. 2017), none had comprehensively explored how more in-depth kinematic responses as continuous functions of radius could influence multiple sub-populations, including AGN-hosting cluster galaxies.

Velocity dispersion profiles are robust tools for assessing the spread in the cluster galaxy line-of-sight velocity distribution as a function of projected radius, however, traditional binning of cluster galaxies in incremental radius is limited for use to sufficiently large sample sizes consistently across all binned radii for a valid result. In Chapter 2 we utilise the weighted velocity dispersion profile that was introduced to star cluster systems by Bergond et al. (2006) and later adapted to galaxy clusters by Hou et al. (2009) to address the sample size problem; weighted VDPs typically only need ~ 20 cluster galaxies in total to produce a reasonable profile (Hou et al., 2009, 2012). This weighted VDP methodology is used on cluster galaxies of differing evolution-based sub-populations of morphology, colour and stellar mass pooled from relaxed (non-merging) and unrelaxed (merging) galaxy clusters in order to determine – on average – what drives the kinematics across these aforementioned cluster environments, where the VDPs are a proxy for the kinematics. Therefore Chapter 2 finds, in answer to question 1, cluster galaxies from unrelaxed cluster environments contribute to an increase in kinematic activity with projected radius from

evolved cluster galaxy sub-populations, most likely the result of galaxy-galaxy interactions; increase in kinematic activity by those sub-populations commonly attributed to younger galaxies demonstrate first time infallers that are yet to be 'spoiled' via processes that lead to their premature evolution.

In Chapter 3 we take the methodology of Manolopoulou & Plionis (2017) for determining the presence of rotation in galaxy clusters via their cluster galaxies and incorporate it into produce a 'rotational profile' as a function of radius. To answer question 2, we use this adapted methodology in Chapter 3 to again split our cluster galaxies into sub-populations based on colour, drawn from the relaxed and unrelaxed cluster states in order to see how this proxy for galaxy evolution contributes to the overall rotational profile which is compared against simulated rotational profiles using FLASH (Fryxell et al., 2000). In addition, we derive a sample of 'Dumbbell BCG' hosting galaxy clusters from the NASA/IPAC Extragalactic Database (NED) to enable us to answer the rest of question to see if we can infer galaxy cluster evolutionary histories based on the assumption these particular clusters resemble an earlier epoch in a cluster-cluster merging system. Consequently, Chapter 3 answers question 2 by finding that redder cluster galaxies in unrelaxed systems possess a high core rotation velocity as the result of residual sloshing from recent a core merger. Additionally, it is found that some galaxy clusters hosting dumbbell BCGs possess an offset peculiar velocity between the BCG components, resulting in a characteristic rotation profile which can be replicated within simulations of unequal core mergers; simulations show the most active dumbbell BCG hosting galaxy clusters present an second-core passage after inital collapse of the two cores.

Finally, in Chapter 4 we build upon what had already been established within Chapters 2 and 3 and applying our prior kinematic analysis onto AGN sub-populations from AGN-hosting cluster galaxies procured from unrelaxed and relaxed galaxy cluster sub-samples. In answering question 3, we consider the recent works that have shown an increase in AGN activity that appears to be coincident with ram-pressure stripping mechanisms during a galaxy's infall into a galaxy cluster (Poggianti et al., 2017; Ricarte et al., 2020). Therefore, by analysing the kinematics of their host cluster galaxies with VDPs and rotational profiles we find that unrelaxed galaxy clusters host kinematically active AGN lying within the core regions, leading to the implication they are an infalling sub-population where the local environment is perturbing enough gas to fall into their supermassive black holes.

Therefore, with this brief summary of each of the science Chapters 2, 3 and 4 we exemplify the important role cluster galaxy kinematics has to the full understanding of their evolution inside a galaxy cluster at two epochs identifiable from their relative 'clumpiness'; from analysing differing cluster galaxy sub-population peculiar velocities we can observe and infer, on average, how their evolutionary fates came to pass based upon two historical snapshots of a galaxy cluster's dynamical state.

5.3 Future Work

To build on the scope of this thesis we have to take into consideration the limitations of the SDSS instrumentation, despite its continued success and persistent scientific output, as well as other ways to approach the analysis. The SDSS, as outlined in section 1.4, was a multi-object survey that contributed over $\sim 15,000$ deg^2 and $\sim 9,000$ deg^2 of photometric and spectroscopic data respectively with a mixture of intergalactic and extragalactic sources. Developing a survey that collates data both from relatively local ($z \sim 0$) stellar populations and the more time consuming deeper galaxy populations is in itself challenging to manage. This is further compounded by the stark contrast in obtaining spectra between bright point-like stars and the deeper, diffuse galaxies; tackling with fibre collisions for galaxies ≤ 55" apart by making multiple exposures; ensuring the selected galaxies have sufficient surface brightness to obtain a good signal-to-noise; Contending with $\sim 3 \times 15$ minute exposures, assuming good seeing conditions, to maintain consistency in data quality (Strauss et al., 2002). Other drawbacks include the limiting magnitude and resolving power of the optical and imaging systems from a relatively small aperture meaning limits being applied on our sampling of galaxies at greater redshifts. Although, these limitations are mostly the result of concessions made during the initial proposal stages for designing such a survey – as well as current technological limitations – where the scope of the science goals are firmly established. Broadly speaking, as an example of such a concession in survey-based astronomy, one should consider if the scientific proposal wants to focus surveying 'wide and shallow' (volume-limited) or 'narrow and deep' (magnitude-limited). Once it is known what the main focus of such a survey is to be it makes it easier to constrain the requirements to obtain high efficiencies in observations (e.g. Maximise sky coverage and depth from optimising exposure and observing times) depending on the feasibility and

availability of the required technology. One such example of a new, up and coming, facility is the Vera Rubin Observatory[1] (VRO) on Cerro Pachón in Chile that will be running the LSST science programme (Abell et al., 2009; Ivezić et al., 2019).

5.3.1   The Vera Rubin Observatory and the Legacy Survey of Space and Time

The VRO and the LSST programme is considered as the spiritual successor to the SDSS at Apache Point Observatory, with construction currently ongoing at the time of writing, the anticipated first light is estimated to be 2021 and science operations commencing in 2022. However, the telescope will be lacking the inclusion of a full spectrograph that is designed for observing distant objects such as galaxies. In spite of this, there are numerous improvements that build on the SDSS instrumentation and optical system in regards to its imaging and photometric capabilities. The most notable improvement is the increase in size of the collecting area with the 8.4 m primary mirror (mean effective aperture of 6.423 m), helping to provide greater magnitude depth as well as faster optics (f/1.234) that allow for the main 'deep-wide-fast' survey mode that dominates the programme to cover $\sim 18,000$ deg^2 of sky ($\sim 44\%$) 800 times, which increases the effective collective area by an order of magnitude on from SDSS with its considerably smaller 2.5 m primary (York et al., 2000; Gunn et al., 2006). The main imaging system of the VRO consists of 189 CCDs, each possessing 1.6×10^7 pixels, encased into a mosaic that contribute the total of 3.2×10^9 pixels with an automatic filter-changing mechanism that allows the the swapping between the photometric bands on the fly. There are six photometric bands for the VRO/LSST photometric system defined as *u, g, r, i, z, y* with estimated median wavelengths of 357, 476, 621, 754, 870 and 1004 nm respectively.

Each of the six photometric bands aim to match magnitude depths to maintain completeness across all bands, with the magnitude depth in the r-band expecting to reach 'single visit' and 'co-added' depths of $r \lesssim 24.7$ mag and $r \lesssim 27.5$ mag respectively with the latter being achievable after the 10 year survey is complete (Ivezić et al., 2019). Not only does this allow for the procurement of galaxies at even greater redshifts, it additionally grants improved sampling of dimmer galaxies at lower redshifts, allowing for a broader population of galaxies at comparative redshifts from SDSS data. Additionally, while spectroscopic redshifts of galaxies would not be possible, the LSST run will be able

---

[1]https://www.lsst.org/

to produce photometric redshifts of galaxies accurate to 2% ($0.3 < z < 3.0$) as a result of the high frequency and distribution of visits per filter (Ivezić et al., 2019). Furthermore, the LSST run at the VRO will consequently lead to an increase in the sampling of low redshift AGN, similarly to those AGN sampled in our relatively low redshift galaxy cluster samples. The AGN selection from the VRO relies upon several methods to build a valid catalogue; determination from colours; identification from omission of proper motion; Recognition of variability associated with AGN; comparisons made with other surveys from multiple wavelengths. Making these thorough assessments of the survey data in comparison with other surveys is especially important due to the absence of spectroscopic measurements, with the implication that the atypical BPT (Baldwin et al., 1981) and WHAN (Cid Fernandes et al., 2010) diagrams cannot be used specifically with data from the VRO LSST run. It is estimated that the census of AGN from the LSST run alone will yield $\sim 20 \times 10^6$, increasing by an order of magnitude to $\sim \times 10^8$ once the final data release is compared to the multiwavelength data (Ivezić et al., 2014).

Therefore, future projects that build upon the work within this thesis will be able to have an enriched sample of galaxies, improving the signal-to-noise as well as opening up to the possibility of more cluster galaxy sub-populations. Maximising the seeing depth of the LSST run will enable observers to garner significant samples of older populations from earlier epochs, where galaxy cluster sampling will provide a median redshift of cluster galaxies at $z \sim 1.2$, which can be useful in determining the evolutionary histories of galaxy clusters and how their membership behaves across varying cosmologies. Broadening the sample of cluster galaxies to higher magnitudes – thereby lower redshifts to maintain completeness – will expand breadth of sub-populations that can be explored to better understand their role in galaxy cluster; low mass galaxies and galaxies with low surface brightness such as dwarf galaxies.

5.3.2   The Taipan Galaxy Survey

Considering the main VRO instrumentation for the LSST run does not contain a dedicated ability to obtain galaxy spectra that advances upon the SDSS, there is a considerable gap in the data acquisition to complement the photometry. The Taipan galaxy survey is an up and coming optical spectroscopic survey ($370 - 870$ nm) that involves the use of the instrument of the same name under the acronym TAIPAN (Transforming Astronomical

Imaging Through the Polychromatic Analysis of Nebulae; Kuehn et al. 2014) being fitted to the recently refurbished 1.2m UK Schmidt Telescope at Siding Spring Observatory in Australia. Therefore, the Taipan survey can provide additional complementary multiwavelength data to the LSST with both covering the southern hemisphere with similar coverage and high level of crossover. The TAIPAN instrument itself will possess so-called 'Starbug' fibre technology that will enable fast, parallel, repositioning of 150 spectral fibres within a 6 degree field of view $\leq$ 5 minutes, which operates $\sim$ 12 times quicker than prior fibre positioning systems from previous equivalent surveys such as 6dFGS (Jones et al., 2004; Lorente et al., 2015; da Cunha et al., 2017). Shortly after TAIPAN receives first light the Taipan main survey run will focus obtaining a magnitude-limited sample of 1.2×10^6 galaxy spectra, which will be complete at $i \leq 17$, with an even deeper sample of 8×10^5 red galaxy spectra that will reach redshifts of $z = 0.4$ across $\sim 20,600$ deg^2 ($\sim 50\%$) of the sky (da Cunha et al., 2017).

While the magnitude limit and galaxy sample size will be equivalent to what was obtainable with the SDSS, comparatively, the key benefits are the adaptability of the fibre positioning system to quickly align the objects in the field; the fibre collision limit is reduced to $\lesssim 25$"; improved resolving power with spectral resolutions of $R = \lambda/\Delta\lambda 1960 - 2740$; larger coverage of the sky and improving the footprint in the southern hemisphere. In particular, the reduction in the improved fibre collision limit will yield the observation of greater galaxy numbers due to the removal of any confusion and disentanglement of closely grouped galaxies, where it is modelled that $N = 131428 \pm 3914$ pairings of galaxies ≤ 55" improving on SDSS by an order of magnitude (Gordon, 2018). The spectral resolution is within the same bounds as the SDSS ($R \sim 1500 - 2500$), however, it is still improved on from the bluer and redder ends of the wavelength coverage of Taipan granting higher sensitivity to finer emission (or absorption) lines. Taipan will cover over $\sim 15\%$ more of the sky compared to SDSS, furthermore, it will enhance the spectroscopic footprint for galaxies that lie prominently in the southern hemisphere allowing for the final phase of Taipan to yield a total of 2×10^6 galaxies with a median redshift of $z_{med} = 0.17$ compared to the median of SDSS $z_{med} = 0.10$ and $\sim \times 10^6$ galaxies (Aihara et al., 2011; da Cunha et al., 2017). Furthermore, Taipan will improve on the existing Galaxy And Mass Assembly survey (GAMA; Driver et al. 2011), which has already significantly improved the completeness of individual clusters from SDSS (e.g. see Owers et al. 2013),

by improving on the ability to resolve pairings and tight groupings of galaxies by a factor of 9 (Gordon, 2018).

Therefore, it would be possible to cross-match the future LSST photometric data releases with that of Taipan's spectral data to procure more precise definitions of our sub-populations, including further constraints on the AGN population that will pervade the galaxy data. As a bonus to improving cluster galaxy sample sizes this would consequently improve our AGN sample size, thus their signal-to-noise, as well as significantly improve the accuracy – while lowering our uncertainties – of the AGN fractions for composite clusters. Combined with other multiwavelength surveys would allow to probe the less accretion efficient AGN, considering what is known about 'accretion boosts' that trigger AGN within infall regions (Haines et al., 2012; Pimbblet et al., 2013) along with pre-processing of cluster galaxies within these same regions (Haines et al., 2015; Bilton & Pimbblet, 2018), there could be a dichotomy with less-efficient AGN being present within regions where ram-pressure against the ICM is at its strongest (Poggianti et al., 2017; Ricarte et al., 2020). Reductions in fibre collisions will improve the observing capacity of the survey, which allows for a significant lowering of any confusion limit for identifying the individual galaxy spectra within closely bound groupings of galaxies, equating to a greater number of objects with spectra in the Taipan catalogue. This, combined with the improved spectral resolution, will be especially important in improving the assembly of galaxies into galaxy groups and galaxy clusters enabling the ability to isolate their evolutionary properties and with Taipan's greater median redshift the potential to provide more complete samples from older galaxy cluster evolutionary epochs to help constrain a more comprehensive picture of the motions of different cluster galaxy sub-populaitons. Additionally Taipan will provide redshift measurements for galaxies in the southern hemisphere with greater accuracy and therefore, specifically for the work conducted here, would permit greater accuracy in determining cluster galaxy peculiar velocities relative to their host galaxy cluster that would present truer kinematic values alongside constrained values for cluster velocity dispersions and mean recession velocities.

Finally, there is plenty of future potential for the studying of large-scale structures in the Universe. For example, additional data could be complemented with the LSST from future instrument projects such as the upcoming DESI instrument, an optical spectroscopic survey being retrofitted to the Mayall Telescope on Kitt Peak in the USA (Aghamousa et al.,

2016). While DESI will primarily perform in the northern hemisphere there will be some overlap with the southern LSST and Taipan surveys of $\sim \times 10^3$ deg^2, therefore, allowing for further constraints to be applied to photometric redshifts and the mass estimates of galaxy clusters. Other instruments such as the SKA hope to probe the Universe in the radio with very high resolution (thanks to the 1km^2 collecting area as its namesake suggests) to very high depths Dewdney et al. (2009). The SKA's precursor instrument, the Australian SKA Pathfinder (ASKAP; Johnston et al. 2008), has already demonstrated sensitivities of $\sim 10 \mu Jy$ with up to 6 times the resolution of the NRAO VLA Sky Survey with Evolutionary Map of the Universe survey (EMU; Norris et al. 2011). Complementary radio data that can reach equivalent resolutions and depths of their optical survey counterparts would enable the improved selection of further sub-populations of cluster galaxies, for example, finding radio cluster galaxies down to low surface brightness levels or procuring radio AGN cluster galaxies that are indicative of weak and inefficient accreting processes as noted in Chapter 4. Therefore, the avenues for which the work presented in this thesis can be advanced upon are certainly plentiful for the next decade of astronomy.

Bibliography

Abadi M. G., Moore B., Bower R. G., 1999, MNRAS, 308, 947

Abazajian K. N., et al., 2009, ApJS, 182, 543

Abdullah M. H., Ali G. B., Ismail H. A., Rassem M. A., 2011, MNRAS, 416, 2027

Abell G. O., 1958, ApJS, 3, 211

Abell G. O., 1959, Leaflet of the Astronomical Society of the Pacific, 8, 121

Abell P. A., et al., 2009, arXiv e-prints, p. arXiv:0912.0201

Aghamousa A., et al., 2016, arXiv e-prints, p. arXiv:1611.00036

Agulli I., Aguerri J. A. L., Sánchez-Janssen R., Dalla Vecchia C., Diaferio A., Barrena R., Dominguez Palmero L., Yu H., 2016, MNRAS, 458, 1590

Aihara H., et al., 2011, ApJS, 193, 29

Akamatsu H., et al., 2017, A&A, 600, A100

Aragón-Calvo M. A., van de Weygaert R., Jones B. J. T., 2010, MNRAS, 408, 2163

Baade W., Zwicky F., 1934, Contributions from the Mount Wilson Observatory, 3, 73

Bahcall N. A., 1988, ARA&A, 26, 631

Bahé Y. M., McCarthy I. G., Balogh M. L., Font A. S., 2013, MNRAS, 430, 3017

Baldi A. S., De Petris M., Sembolini F., Yepes G., Lamagna L., Rasia E., 2017, MNRAS, 465, 2584

Baldi A. S., De Petris M., Sembolini F., Yepes G., Cui W., Lamagna L., 2018, MNRAS, 479, 4028

Baldwin J. A., Phillips M. M., Terlevich R., 1981, PASP, 93, 5

Balogh M. L., Morris S. L., Yee H. K. C., Carlberg R. G., Ellingson E., 1999, ApJ, 527, 54

Balogh M. L., Baldry I. K., Nichol R., Miller C., Bower R., Glazebrook K., 2004, ApJL, 615, L101

Bamford S. P., et al., 2009, MNRAS, 393, 1324

Barrena R., Biviano A., Ramella M., Falco E. E., Seitz S., 2002, A&A, 386, 816

Baxter E., et al., 2017, ApJ, 841, 18

Beers T. C., Flynn K., Gebhardt K., 1990, AJ, 100, 32

Bell E. F., et al., 2004, ApJ, 608, 752

Belsole E., Sauvageot J.-L., Pratt G. W., Bourdin H., 2005, Advances in Space Research, 36, 630

Bergond G., Zepf S. E., Romanowsky A. J., Sharples R. M., Rhode K. L., 2006, A&A, 448, 155

Berrier J. C., Stewart K. R., Bullock J. S., Purcell C. W., Barton E. J., Wechsler R. H., 2009, ApJ, 690, 1292

Best P. N., von der Linden A., Kauffmann G., Heckman T. M., Kaiser C. R., 2007, MNRAS, 379, 894

Bilton L. E., Pimbblet K. A., 2018, MNRAS, 481, 1507

Bilton L. E., Hunt M., Pimbblet K. A., Roediger E., 2019, MNRAS, 490, 5017

Bilton L. E., Pimbblet K. A., Gordon Y. A., 2020, MNRAS, 499, 3792

Binggeli B., Sandage A., Tammann G. A., 1988, ARA&A, 26, 509

Blake C., et al., 2011, MNRAS, 418, 1707

Blanton M. R., Lupton R. H., Schlegel D. J., Strauss M. A., Brinkmann J., Fukugita M., Loveday J., 2005, ApJ, 631, 208

Bluck A. F. L., Maiolino R., Sánchez S. F., Ellison S. L., Thorp M. D., Piotrowska J. M., Teimoorinia H., Bundy K. A., 2020, MNRAS, 492, 96

Blumenthal G. R., Pagels H., Primack J. R., 1982, Nature, 299, 37

Blumenthal G. R., Faber S. M., Primack J. R., Rees M. J., 1984, Nature, 311, 517

Böhringer H., et al., 2000, ApJS, 129, 435

Bond J. R., Szalay A. S., Turner M. S., 1982, Phys. Rev. Lett, 48, 1636

Bond J. R., Kofman L., Pogosyan D., 1996, Nature, 380, 603

Botteon A., Gastaldello F., Brunetti G., 2018, MNRAS, 476, 5591

Boylan-Kolchin M., Springel V., White S. D. M., Jenkins A., Lemson G., 2009, MNRAS, 398, 1150

Brinchmann J., Charlot S., White S. D. M., Tremonti C., Kauffmann G., Heckman T., Brinkmann J., 2004, MNRAS, 351, 1151

Bulbul E., et al., 2016, ApJ, 818, 131

Caglar T., Hudaverdi M., 2017, MNRAS, 472, 2633

Cameron E., 2011, PASA, 28, 128

Cava A., et al., 2017, A&A, 606, A108

Chabrier G., 2003, PASP, 115, 763

Chatzikos M., Sarazin C. L., Kempner J. C., 2006, ApJ, 643, 751

Chilingarian I. V., Zolotukhin I. Y., 2012, MNRAS, 419, 1727

Chilingarian I. V., Melchior A.-L., Zolotukhin I. Y., 2010, MNRAS, 405, 1409

Ching J. H. Y., et al., 2017, MNRAS, 469, 4584

Chon G., Böhringer H., Zaroubi S., 2015, A&A, 575, L14

Cid Fernandes R., Stasińska G., Schlickmann M. S., Mateus A., Vale Asari N., Schoenell W., Sodré L.,
    2010, MNRAS, 403, 1036

Cid Fernandes R., Stasińska G., Mateus A., Vale Asari N., 2011, MNRAS, 413, 1687

Clowe D., Gonzalez A., Markevitch M., 2004, ApJ, 604, 596

Clowe D., Bradač M., Gonzalez A. H., Markevitch M., Randall S. W., Jones C., Zaritsky D., 2006, ApJL,
    648, L109

Colberg J. M., et al., 2000, MNRAS, 319, 209

Coles P., Lucchin F., 2002, Cosmology: The Origin and Evolution of Cosmic Structure, Second Edition.
    John Wiley & Sons Ltd

Colless M., et al., 2001, MNRAS, 328, 1039

Collins C. A., et al., 2009, Nature, 458, 603

Cortese L., et al., 2007, MNRAS, 376, 157

Costa A. P., Ribeiro A. L. B., de Carvalho R. R., 2018, MNRAS, 473, L31

Croton D. J., et al., 2006, MNRAS, 365, 11

Curtis H. D., 1917, PASP, 29, 206

Curtis H. D., 1920, JRASC, 14, 317

Danese L., de Zotti G., di Tullio G., 1980, A&A, 82, 322

David L. P., Forman W., Jones C., 1999, ApJ, 519, 533

Davis M., Huchra J., Latham D. W., Tonry J., 1982, ApJ, 253, 423

Dawson K. S., et al., 2013, AJ, 145, 10

Deshev B., et al., 2017, A&A, 607, A131

Dewdney P. E., Hall P. J., Schilizzi R. T., Lazio T. J. L. W., 2009, IEEE Proceedings, 97, 1482

Di Matteo T., Springel V., Hernquist L., 2005, Nature, 433, 604

Diaferio A., 1999, MNRAS, 309, 610

Diaferio A., Geller M. J., 1997, ApJ, 481, 633

Dicke R. H., 1961, Nature, 192, 440

Diener C., et al., 2013, ApJ, 765, 109

Dopita M. A., Pereira M., Kewley L. J., Capaccioli M., 2002, ApJS, 143, 47

Dressler A., 1980, ApJ, 236, 351

Dressler A., Shectman S. A., 1988, AJ, 95, 985

Driver S. P., et al., 2011, MNRAS, 413, 971

Dubinski J., 1998, ApJ, 502, 141

Dyson F., 2005, Nature, 435, 1033

Ebeling H., Kalita B. S., 2019, ApJ, 882, 127

Ebeling H., Edge A. C., Bohringer H., Allen S. W., Crawford C. S., Fabian A. C., Voges W., Huchra J. P., 1998, MNRAS, 301, 881

Eddington A. S., 1924, MNRAS, 84, 308

Einasto M., Einasto J., Tago E., Müller V., Andernach H., 2001, AJ, 122, 2222

Einasto M., et al., 2012, A&A, 540, A123

Elbaz D., et al., 2011, A&A, 533, A119

Ellison S. L., Patton D. R., Mendel J. T., Scudder J. M., 2011, MNRAS, 418, 2043

Ellison S. L., Patton D. R., Hickox R. C., 2015, MNRAS, 451, L35

Fabian A. C., 2012, ARA&A, 50, 455

Farnsworth D., Rudnick L., Brown S., Brunetti G., 2013, ApJ, 779, 189

Farrah D., et al., 2007, ApJ, 667, 149

Feast M. W., Thackeray A. D., Wesselink A. J., 1961, MNRAS, 122, 433

Ferrarese L., Merritt D., 2000, ApJL, 539, L9

Fitchett M., Webster R., 1987, ApJ, 317, 653

Freedman W. L., Madore B. F., 2010, ARA&A, 48, 673

Frenk C. S., et al., 1999, ApJ, 525, 554

Friedmann A., 1922, Zeitschrift fur Physik, 10, 377

Fryxell B., et al., 2000, ApJS, 131, 273

Gavazzi G., Boselli A., Mayer L., Iglesias-Paramo J., Vílchez J. M., Carrasco L., 2001, ApJL, 563, L23

Gebhardt K., et al., 2000, ApJL, 539, L13

Geller M. J., Beers T. C., 1982, PASP, 94, 421

George K., et al., 2019, MNRAS, 487, 3102

Ghizzardi S., Rossetti M., Molendi S., 2010, A&A, 516, A32

Gifford D., Miller C. J., 2013, ApJL, 768, L32

Gifford D., Miller C., Kern N., 2013, ApJ, 773, 116

Gill S. P. D., Knebe A., Gibson B. K., 2005, MNRAS, 356, 1327

Giovannini G., Bonafede A., Feretti L., Govoni F., Murgia M., Ferrari F., Monti G., 2009, A&A, 507, 1257

Girardi M., Fadda D., Giuricin G., Mardirossian F., Mezzetti M., Biviano A., 1996, ApJ, 457, 61

Godłowski W., Szydłowski M., Flin P., Biernacka M., 2003, Gen. Relativ. Gravit., 35, 907

Godłowski W., Szydłowski M., Flin P., 2005, Gen. Relativ. Gravit., 37, 615

Gómez P. L., et al., 2003, ApJ, 584, 210

Gordon Y. A., 2018, PhD thesis, University of Hull, doi:10.5281/zenodo.1466127, http://adsabs.
    harvard.edu/abs/2018PhDT........60G

Gordon Y. A., et al., 2017, MNRAS, 465, 2671

Gordon Y. A., et al., 2018, MNRAS, 475, 4223

Gorski K., 1988, ApJL, 332, L7

Gregorini L., Vettolani G., de Ruiter H. R., Parma P., 1992, A&A, 95, 1

Gregorini L., de Ruiter H. R., Parma P., Sadler E. M., Vettolani G., Ekers R. D., 1994, A&A, 106, 1

Gunn J. E., Gott III J. R., 1972, ApJ, 176, 1

Gunn J. E., et al., 2006, AJ, 131, 2332

Haggar R., Gray M. E., Pearce F. R., Knebe A., Cui W., Mostoghiu R., Yepes G., 2020, MNRAS, 492, 6074

Haines C. P., et al., 2009, ApJ, 704, 126

Haines C. P., et al., 2012, ApJ, 754, 97

Haines C. P., et al., 2015, ApJ, 806, 101

Hao L., et al., 2005, AJ, 129, 1783

Hardcastle M. J., Evans D. A., Croston J. H., 2007, MNRAS, 376, 1849

Hart R. E., et al., 2016, MNRAS, 461, 3663

Hernquist L., 1990, ApJ, 356, 359

Herschel W., 1802, Philosophical Transactions of the Royal Society of London Series I, 92, 477

Hertzsprung E., 1909, Astronomische Nachrichten, 179, 373

Hickson P., 1982, ApJ, 255, 382

Hickson P., 1997, ARA&A, 35, 357

Hogg D. W., 1999, arXiv e-prints, pp astro–ph/9905116

Hogg D. W., et al., 2003, ApJL, 585, L5

Hogg D. W., et al., 2004, ApJL, 601, L29

Hooper E. J., Impey C. D., Foltz C. B., Hewett P. C., 1995, ApJ, 445, 62

Hou A., Parker L. C., Harris W. E., Wilman D. J., 2009, ApJ, 702, 1199

Hou A., et al., 2012, MNRAS, 421, 3594

Houghton R. C. W., 2015, MNRAS, 451, 3427

Hubble E. P., 1926, ApJ, 64

Hubble E. P., 1927, The Observatory, 50, 276

Hubble E., 1929a, Proceedings of the National Academy of Science, 15, 168

Hubble E. P., 1929b, ApJ, 69

Hwang H. S., Lee M. G., 2007, ApJ, 662, 236

Ivezić Ž., Brandt W. N., Fan X., MacLeod C. L., Richards G. T., Yoachim P., 2014, in Mickaelian A. M., Sanders D. B., eds, IAU Symposium Vol. 304, Multiwavelength AGN Surveys and Studies. pp 11–17

Ivezić Ž., et al., 2019, ApJ, 873, 111

Jackson J. C., 1972, MNRAS, 156, 1P

Jaffé Y. L., et al., 2018, MNRAS, 476, 4753

Jin S.-W., Gu Q., Huang S., Shi Y., Feng L.-L., 2014, ApJ, 787, 63

Johnston S., et al., 2008, Experimental Astronomy, 22, 151

Jones C., Forman W., 1999, ApJ, 511, 65

Jones D. H., et al., 2004, MNRAS, 355, 747

Jones M. H., Lambourne R. J. A., Serjeant S., 2015, An Introduction to Galaxies and Cosmology. Cambridge University Press

Kaiser N., 1987, MNRAS, 227, 1

Kalinkov M., Valchanov T., Valtchanov I., Kuneva I., Dissanska M., 2005, MNRAS, 359, 1491

Kant I., 1755, Allgemeine Naturgeschichte und Theorie des Himmels

Kauffmann G., Haehnelt M., 2000, MNRAS, 311, 576

Kauffmann G., et al., 2003, MNRAS, 341, 33

Kauffmann G., White S. D. M., Heckman T. M., Ménard B., Brinchmann J., Charlot S., Tremonti C., Brinkmann J., 2004, MNRAS, 353, 713

Kenney J. D. P., Geha M., Jáchym P., Crowl H. H., Dague W., Chung A., van Gorkom J., Vollmer B., 2014, ApJ, 780, 119

Kennicutt Robert C. J., 1998a, ARA&A, 36, 189

Kennicutt Robert C. J., 1998b, ApJ, 498, 541

Kennicutt R. C., Evans N. J., 2012, ARA&A, 50, 531

Kennicutt R. C. J., Kent S. M., 1983, AJ, 88, 1094

Kewley L. J., Geller M. J., Jansen R. A., Dopita M. A., 2002, AJ, 124, 3135

Kim M., Choi Y.-Y., Kim S. S., 2020, MNRAS, 491, 4045

King A., 2003, ApJL, 596, L27

Kleiner D., Pimbblet K. A., Owers M. S., Jones D. H., Stephenson A. P., 2014, MNRAS, 439, 2755

Kolb U., 2010, Extreme Environment Astrophysics. Cambridge University Press

Kormendy J., Ho L. C., 2013, ARA&A, 51, 511

Kravtsov A. V., Borgani S., 2012, ARA&A, 50, 353

Kuehn K., et al., 2014, in Ground-based and Airborne Instrumentation for Astronomy V. p. 914710, doi:10.1117/12.2055677

Lacey C., Cole S., 1993, MNRAS, 262, 627

Laine S., van der Marel R. P., Lauer T. R., Postman M., O'Dea C. P., Owen F. N., 2003, AJ, 125, 478

Lakhchaura K., Singh K. P., Saikia D. J., Hunstead R. W., 2013, ApJ, 767, 91

Lambourne R. J. A., 2010, Relativity, Gravitation and Cosmology. Cambridge University Press

Larson R. B., Tinsley B. M., Caldwell C. N., 1980, ApJ, 237, 692

Lauer T. R., 1988, ApJ, 325, 49

Lemaître G., 1927, Annales de la Société Scientifique de Bruxelles, 47, 49

Lemaître G., 1931, MNRAS, 91, 483

Lemaux B. C., et al., 2019, MNRAS, 490, 1231

Lewis I., et al., 2002, MNRAS, 334, 673

Li L.-X., 1998, Gen. Relativ. Gravit., 30, 497

Lonsdale Persson C. J., Helou G., 1987, ApJ, 314, 513

Lorente N. P. F., Vuong M., Satorre C., Hong S. E., Shortridge K., Goodwin M., Kuehn K., 2015, in Taylor A. R., Rosolowsky E., eds, Astronomical Society of the Pacific Conference Series Vol. 495, Astronomical Data Analysis Software an Systems XXIV (ADASS XXIV). p. 265

Lubin L. M., Cen R., Bahcall N. A., Ostriker J. P., 1996, ApJ, 460, 10

Madau P., Pozzetti L., Dickinson M., 1998, ApJ, 498, 106

Magorrian J., et al., 1998, AJ, 115, 2285

Majewski S. R., et al., 2017, AJ, 154, 94

Malmquist K. G., 1925, Meddelanden fran Lunds Astronomiska Observatorium Serie I, 106, 1

Mamon G. A., Sanchis T., Salvador-Solé E., Solanes J. M., 2004, A&A, 414, 445

Manolopoulou M., Plionis M., 2017, MNRAS, 465, 2616

Marini F., et al., 2004, MNRAS, 353, 1219

Markevitch M., Sarazin C. L., Vikhlinin A., 1999, ApJ, 521, 526

Markevitch M., et al., 2000, ApJ, 541, 542

Markevitch M., Gonzalez A. H., David L., Vikhlinin A., Murray S., Forman W., Jones C., Tucker W., 2002, ApJL, 567, L27

Markevitch M., Gonzalez A. H., Clowe D., Vikhlinin A., Forman W., Jones C., Murray S., Tucker W., 2004, ApJ, 606, 819

Marshall M. A., Shabala S. S., Krause M. G. H., Pimbblet K. A., Croton D. J., Owers M. S., 2018, MNRAS, 474, 3615

Materne J., Hopp U., 1983, A&A, 124, L13

McGee S. L., Balogh M. L., Wilman D. J., Bower R. G., Mulchaey J. S., Parker L. C., Oemler A., 2011, MNRAS, 413, 996

McNamara B. R., Nulsen P. E. J., 2007, ARA&A, 45, 117

McNamara B. R., Nulsen P. E. J., Wise M. W., Rafferty D. A., Carilli C., Sarazin C. L., Blanton E. L., 2005, Nature, 433, 45

McPartland C., Ebeling H., Roediger E., Blumenthal K., 2016, MNRAS, 455, 2994

Menci N., Fusco-Femiano R., 1996, ApJ, 472, 46

Merritt D., 1985, ApJ, 289, 18

Messier C., 1781, Connoissance des Temps ou des Mouvements Célestes, for 1784, p. 227-267, pp 227–267

Miller N. A., Owen F. N., 2003, AJ, 125, 2427

Minkowski R. L., Abell G. O., 1963, The National Geographic Society-Palomar Observatory Sky Survey. p. 481

Mitchell P. D., Lacey C. G., Baugh C. M., Cole S., 2013, MNRAS, 435, 87

Molnar S. M., Chiu I.-N. T., Broadhurst T., Stadel J. G., 2013, ApJ, 779, 63

Moore B., 1994, Nature, 370, 629

Moore B., Katz N., Lake G., Dressler A., Oemler A., 1996, Nature, 379, 613

Moore B., Lake G., Quinn T., Stadel J., 1999, MNRAS, 304, 465

More S., Diemer B., Kravtsov A. V., 2015, ApJ, 810, 36

More S., et al., 2016, ApJ, 825, 39

Morell D. F., Ribeiro A. L. B., de Carvalho R. R., Rembold S. B., Lopes P. A. A., Costa A. P., 2020, MNRAS, 494, 3317

Mulchaey J. S., 2000, ARA&A, 38, 289

Mulroy S. L., McGee S. L., Gillman S., Smith G. P., Haines C. P., Démoclès J., Okabe N., Egami E., 2017, MNRAS, 472, 3246

Munari E., Biviano A., Mamon G. A., 2014, A&A, 566, A68

Nascimento R. S., Lopes P. A. A., Ribeiro A. L. B., Costa A. P., Morell D. F., 2019, MNRAS, 483, L121

Nature 1949, Nature, 164, 97

Navarro J. F., Frenk C. S., White S. D. M., 1995, MNRAS, 275, 56

Navarro J. F., Frenk C. S., White S. D. M., 1996, ApJ, 462, 563

Navarro J. F., Frenk C. S., White S. D. M., 1997, ApJ, 490, 493

Netzer H., 2015, ARA&A, 53, 365

Newman P. R., et al., 2004, Mass-producing spectra: the SDSS spectrographic system. SPIE Astronomical Telescopes + Instrumentation, pp 533–544, doi:10.1117/12.541394, https://ui.adsabs.harvard.edu/abs/2004SPIE.5492..533N

Norris R. P., et al., 2011, PASA, 28, 215

Nulsen P. E. J., et al., 2013, ApJ, 775, 117

Oegerle W. R., Hill J. M., 1992, AJ, 104, 2078

Oemler Jr. A., 1974, ApJ, 194, 1

Oh S.-H., et al., 2015, AJ, 149, 180

Ostriker J. P., Tremaine S. D., 1975, ApJL, 202, L113

Owers M. S., Couch W. J., Nulsen P. E. J., 2009, ApJ, 693, 901

Owers M. S., Randall S. W., Nulsen P. E. J., Couch W. J., David L. P., Kempner J. C., 2011, ApJ, 728, 27

Owers M. S., Couch W. J., Nulsen P. E. J., Randall S. W., 2012, ApJL, 750, L23

Owers M. S., et al., 2013, ApJ, 772, 104

Pan D. C., Vogeley M. S., Hoyle F., Choi Y.-Y., Park C., 2012, MNRAS, 421, 926

Paul S., John R. S., Gupta P., Kumar H., 2017, MNRAS, 471, 2

Pearson D. W., Batiste M., Batuski D. J., 2014, MNRAS, 441, 1601

Peebles P. J. E., 1969, ApJ, 155, 393

Peebles P. J. E., 1982, ApJL, 263, L1

Peeters E., Spoon H. W. W., Tielens A. G. G. M., 2004, ApJ, 613, 986

Percival W. J., et al., 2002, MNRAS, 337, 1068

Pimbblet K. A., 2008, PASA, 25, 176

Pimbblet K. A., 2011, MNRAS, 411, 2637

Pimbblet K. A., Jensen P. C., 2012, MNRAS, 426, 1632

Pimbblet K. A., Smail I., Edge A. C., O'Hely E., Couch W. J., Zabludoff A. I., 2006, MNRAS, 366, 645

Pimbblet K. A., Shabala S. S., Haines C. P., Fraser-McKelvie A., Floyd D. J. E., 2013, MNRAS, 429, 1827

Pimbblet K. A., Penny S. J., Davies R. L., 2014, MNRAS, 438, 3049

Pinkney J., Roettiger K., Burns J. O., Bird C. M., 1996, ApJS, 104, 1

Planck et al., 2018, arXiv e-prints, p. arXiv:1807.06209

Poggianti B. M., et al., 2017, Nature, 548, 304

Poole G. B., Fardal M. A., Babul A., McCarthy I. G., Quinn T., Wadsley J., 2006, MNRAS, 373, 881

Popesso P., Biviano A., Böhringer H., Romaniello M., 2007, A&A, 461, 397

Postman M., Geller M. J., 1984, ApJ, 281, 95

Press W. H., Schechter P., 1974, ApJ, 187, 425

Price-Whelan A. M., et al., 2018, AJ, 156, 123

Quilis V., Moore B., Bower R., 2000, Science, 288, 1617

Quintana H., Lawrie D. G., 1982, AJ, 87, 1

Quintana H., Ramirez A., Way M. J., 1996, AJ, 112, 36

Radovich M., Poggianti B., Jaffé Y. L., Moretti A., Bettoni D., Gullieuszik M., Vulcani B., Fritz J., 2019, MNRAS, 486, 486

Rawle T. D., et al., 2014, MNRAS, 442, 196

Regos E., Geller M. J., 1989, AJ, 98, 755

Reichard T. A., Heckman T. M., Rudnick G., Brinchmann J., Kauffmann G., Wild V., 2009, ApJ, 691, 1005

Reiprich T. H., Böhringer H., 2002, ApJ, 567, 716

Rhee J., Smith R., Choi H., Yi S. K., Jaffé Y., Candlish G., Sánchez-Jánssen R., 2017, ApJ, 843, 128

Ribeiro A. L. B., de Carvalho R. R., Trevisan M., Capelato H. V., La Barbera F., Lopes P. A. A., Schilling A. C., 2013, MNRAS, 434, 784

Ricarte A., Tremmel M., Natarajan P., Quinn T., 2020, ApJL, 895, L8

Ricker P. M., 1998, ApJ, 496, 670

Rines K., Diaferio A., 2006, AJ, 132, 1275

Rines K., Geller M. J., Kurtz M. J., Diaferio A., 2003, AJ, 126, 2152

Roberts I. D., Parker L. C., 2017, MNRAS, 467, 3268

Robertson H. P., 1935, ApJ, 82, 284

Robitaille T. P., et al., 2013, A&A, 558, A33

Roediger E., Brüggen M., 2007, MNRAS, 380, 1399

Roettiger K., Flores R., 2000, ApJ, 538, 92

Roettiger K., Loken C., Burns J. O., 1997, ApJS, 109, 307

Roman-Oliveira F. V., Chies-Santos A. L., Rodríguez del Pino B., Aragón-Salamanca A., Gray M. E., Bamford S. P., 2019, MNRAS, 484, 892

Rubin V. C., Ford W. Kent J., 1970, ApJ, 159, 379

Ruggiero R., Machado R. E. G., Roman-Oliveira F. V., Chies-Santos A. L., Lima Neto G. B., Doubrawa L., Rodríguez del Pino B., 2019, MNRAS, 484, 906

Russell H. N., 1914, Popular Astronomy, 22, 331

Saadeh D., Feeney S. M., Pontzen A., Peiris H. V., McEwen J. D., 2016, Phys. Rev. Lett, 117, 131302

Sabater J., Best P. N., Argudo-Fernández M., 2013, MNRAS, 430, 638

Sadat R., Blanchard A., Kneib J.-P., Mathez G., Madore B., Mazzarella J. M., 2004, A&A, 424, 1097

Salim S., et al., 2007, ApJS, 173, 267

Salpeter E. E., 1955, ApJ, 121, 161

Sanchis T., Mamon G. A., Salvador-Solé E., Solanes J. M., 2004, A&A, 418, 393

Schawinski K., Thomas D., Sarzi M., Maraston C., Kaviraj S., Joo S.-J., Yi S. K., Silk J., 2007, MNRAS, 382, 1415

Schawinski K., et al., 2014, MNRAS, 440, 889

Schechter P., 1976, ApJ, 203, 297

Schmidt B., 1938, Mitteilungen der Hamburger Sternwarte in Bergedorf, 7, 15

Schmidt M., 1959, ApJ, 129, 243

Schmitt H. R., Calzetti D., Armus L., Giavalisco M., Heckman T. M., Kennicutt R. C. J., Leitherer C., Meurer G. R., 2006, ApJS, 164, 52

Schneider P., 2015, Extragalactic Astronomy and Cosmology. Springer Berlin Heidelberg, doi:10.1007/978-3-642-54083-7

Schwinn J., Baugh C. M., Jauzac M., Bartelmann M., Eckert D., 2018, MNRAS, 481, 4300

Scrimgeour M. I., et al., 2012, MNRAS, 425, 116

Serjeant S., 2010, Observational Cosmology. Cambridge University Press

Shan H., Qin B., Fort B., Tao C., Wu X.-P., Zhao H., 2010, MNRAS, 406, 1134

Shapley H., Curtis H. D., 1921, Bulletin of the National Research Council, Vol. 2, Part 3, No. 11, p. 171-217, 2, 171

Sheen Y.-K., et al., 2017, ApJL, 840, L7

Silk J., Rees M. J., 1998, A&A, 331, L1

Slipher V. M., 1915, Popular Astronomy, 23, 21

Smith G. P., Kneib J.-P., Smail I., Mazzotta P., Ebeling H., Czoske O., 2005a, MNRAS, 359, 417

Smith G. P., Treu T., Ellis R. S., Moran S. M., Dressler A., 2005b, ApJ, 620, 78

Sobral D., Stroe A., Dawson W. A., Wittman D., Jee M. J., Röttgering H., van Weeren R. J., Brüggen M., 2015, MNRAS, 450, 630

Sohn J., Geller M. J., Zahid H. J., Fabricant D. G., Diaferio A., Rines K. J., 2017, ApJS, 229, 20

Song H., Hwang H. S., Park C., Tamura T., 2017, ApJ, 842, 88

Song H., Hwang H. S., Park C., Smith R., Einasto M., 2018, ApJ, 869, 124

Springel V., Di Matteo T., Hernquist L., 2005a, MNRAS, 361, 776

Springel V., et al., 2005b, Nature, 435, 629

Strateva I., et al., 2001, AJ, 122, 1861

Strauss M. A., et al., 2002, AJ, 124, 1810

Struble M. F., Rood H. J., 1999, ApJS, 125, 35

Sugawara Y., Takizawa M., Itahana M., Akamatsu H., Fujita Y., Ohashi T., Ishisaki Y., 2017, PASJ, 69, 93

Tadhunter C., 2008, , 52, 227

Tormen G., 1997, MNRAS, 290, 411

Tovmassian H. M., 2015, Astrophysics, 58, 328

Tremonti C. A., et al., 2004, ApJ, 613, 898

Tucker W., et al., 1998, ApJL, 496, L5

Vitvitska M., Klypin A. A., Kravtsov A. V., Wechsler R. H., Primack J. R., Bullock J. S., 2002, ApJ, 581, 799

Walker A. G., 1937, Proceedings of the London Mathematical Society, 42, 90

Walker S. A., Fabian A. C., Sanders J. S., George M. R., Tawara Y., 2012, MNRAS, 422, 3503

Walker S. A., Fabian A. C., Kosec P., 2014, MNRAS, 445, 3444

Wall J. V., Jenkins C. R., 2012, Practical Statistics for Astronomers, 2nd edn. Cambridge University Press

Wen Z. L., Han J. L., 2013, MNRAS, 436, 275

Wetzel A. R., Tinker J. L., Conroy C., 2012, MNRAS, 424, 232

White D. A., Fabian A. C., 1995, MNRAS, 273, 72

White S. D. M., Navarro J. F., Evrard A. E., Frenk C. S., 1993, Nature, 366, 429

Willett K. W., et al., 2013, MNRAS, 435, 2835

Woodley K. A., Harris W. E., Beasley M. A., Peng E. W., Bridges T. J., Forbes D. A., Harris G. L. H., 2007, AJ, 134, 494

Wright E. L., 2006, PASP, 118, 1711

Yagi M., et al., 2010, AJ, 140, 1814

Yanny B., et al., 2009, AJ, 137, 4377

York D. G., et al., 2000, AJ, 120, 1579

Yun M. S., Reddy N. A., Condon J. J., 2001, ApJ, 554, 803

Zabludoff A. I., Huchra J. P., Geller M. J., 1990, ApJS, 74, 1

Zhang Y.-Y., Andernach H., Caretta C. A., Reiprich T. H., Böhringer H., Puchwein E., Sijacki D., Girardi M., 2011, A&A, 526, A105

Zhang Z. T., Liang Y. C., Hammer F., 2013, MNRAS, 430, 2605

ZuHone J. A., 2011, ApJ, 728, 54

Zwicky F., 1933, Helvetica Physica Acta, 6, 110

Zwicky F., Rudnicki K., 1963, ApJ, 137, 707

da Cunha E., et al., 2017, PASA, 34, e047

de Bernardis P., et al., 2000, Nature, 404, 955

de Carvalho R. R., Ribeiro A. L. B., Stalder D. H., Rosa R. R., Costa A. P., Moura T. C., 2017, AJ, 154, 96

van Maanen A., 1916, ApJ, 44

van Weeren R. J., Brüggen M., Röttgering H. J. A., Hoeft M., Nuza S. E., Intema H. T., 2011, A&A, 533, A35

van den Bosch F. C., Aquino D., Yang X., Mo H. J., Pasquali A., McIntosh D. H., Weinmann S. M., Kang X., 2008, MNRAS, 387, 79

von der Linden A., Wild V., Kauffmann G., White S. D. M., Weinmann S., 2010, MNRAS, 404, 1231